CHEMISTRY AND PHYSICS OF THE CERAMIC CORE LEACHING PROCESS

by

DANIEL ADETUNJI

A thesis submitted to the
University of Birmingham
for the degree of
DOCTOR OF ENGINEERING

School of Chemical Engineering
College of Engineering and Physical Sciences
University of Birmingham
September 2018

Abstract

The ceramic core leaching process is one of the final steps used in the investment casting process to manufacture air cooled turbine blades. The core is primarily composed of cristobalite and in a highly alkaline environment, depolymerisation of the tetrahedral SiO_2 structure via siloxane cleavage is the chemical process via which leaching occurs. Industrially, this process is carried out in a low pressure autoclave using either NaOH or KOH solutions at 160 ^oC and 600 kPag with a pressure swing cycle. The products from this reaction are either sodium or potassium silicates. The type of Group IA metal cation present had a significant influence on the dissolution process and the properties of the reaction products. Potassium silicates were found to be several orders of magnitude more viscous than sodium silicates at high concentrations. This led to a diffusion film controlled process in KOH and a chemical reaction controlled process in NaOH. A fluid film layer was formed on the cristobalite surface and consisted of potentially layered silicates which can absorb water, expand and cause cracking in the brittle ceramic core. The expansive nature of this gel has not been proven and requires some amount of calcium which exists only in trace amounts in the ceramic core. This is however still likely to be the primary physical mechanism responsible for core removal and is known as the Alkali Silica Reaction (ASR) cracking process.

Table of Contents

List of Figures

List of Tables

1 INTRODUCTION AND BUSINESS CASE

This project was carried out as a joint partnership between Roll-Royce plc and LBBC Technologies. Rolls-Royce plc is a global engineering company which operates through three business segments: Civil Aerospace, Defence and Power Systems. The Civil Aerospace segment has consistently accounted for a majority of the group's revenues (1). It also has considerable market share averaging 25% in recent years for narrow and wide body aircraft. For wide body aircraft, the group has a dominant 50% market share (2). For the company to maintain and expand its market position, a significant amount of money has been invested into research and development (R&D). From 2007-2017, R&D spend has accounted for 5% of the group's revenues which is in line with the median R&D spend in the aerospace industry (1).

The civil aerospace segment is responsible for the manufacture of jet engines for aircraft propulsion. The high pressure (HP) and intermediate pressure (IP) turbine blades are responsible for extracting power from the hot exhaust gases leaving the combustion chamber. The blades are made from nickel-based single crystal superalloys and operate in a gas stream which is higher than the melting point of the metal alloy. To prevent failure during operation, thermal barrier coatings and internal cooling channels are incorporated into the blade design. The cooling channels are

created using a ceramic core during the investment casting process. Cooler air at about 800 ^{o}C from the front of the engine is diverted to the turbine blade to actively cool it during operation. Heat is transferred via conduction from the hot exhaust gases through the turbine blade and then by convection into the cooler air flowing through the channels. The air then exits at carefully positioned holes on the blade surface creating a thin film of air which further protects the blade against the high temperatures of the exhaust gases and allows the blade to operate at temperatures higher than its melting point (3).

Additionally, the ceramic core creates a hollow turbine blade component which reduces the weight of the blades and the disc it is mounted on. Several turbine blades are attached to a single disc and lighter blades have the added benefit of requiring a lighter and slimmer disc because of the reduced centripetal forces. This reduction in blade and disc mass improves engine efficiency by increasing the power to weight ratio of the engine (3).

After the metal has been cast, the ceramic core is typically removed in a low pressure autoclave manufactured by LBBC Technologies – the sole supplier to Rolls-Royce for pressurised leaching autoclaves. Founded in 1876, LBBC Technologies is a family run engineering company that manufactures process equipment for foundries all over the world. The company was initially focused on producing boilers for local

crane suppliers, tar stills and brewing pans. Over its long history and through several generations, it has repositioned itself to be a key supplier of process equipment to foundries. LBBC Technologies also manufactures fast sealing doors used in submarines and other pressure vessels (4).

1.1 Business Case

As of 2017, the USA accounted for 27% of Rolls-Royce's revenue – the largest share by any region. While the developed world accounted for most of the group's revenues, growth rates in these regions are slower relative to the developing world. Over the past 3 years, revenue in the developed regions grew at 9% whereas developing regions of Africa and the Middle East had growth rates of 94% and 99% respectively (1). As the middle class expands in these regions, larger disposable incomes mean more discretionary spending on travel. This implies increased demand for the civil aerospace segment which means production will need to be increased.

As previously mentioned, the turbine is one of the most critical parts of the gas turbine engine. Turbine components are manufactured via the investment casting process. Figure 1.1 shows some of the different investment casting operations and the typical normalised times for each step.

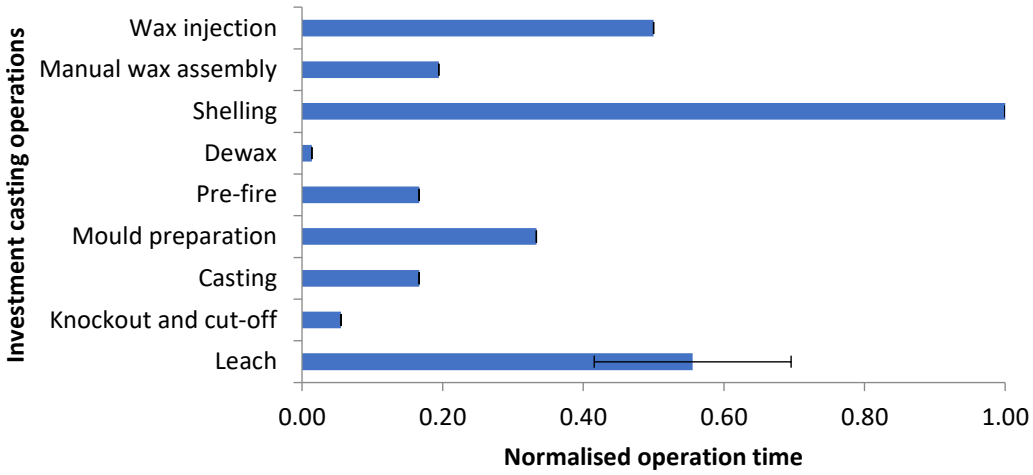

Figure 1.1 Normalised times for some investment casting operations (5)

The operations in Figure 1.1 are arranged in chronological order. The core leaching process is one of the final steps of the investment casting process. It is batch process and the second slowest operation in the entire investment casting process. However, because over a 100 turbine components are leached simultaneously, the operation time on a part basis is about 99% lower than the normalised batch time shown in Figure 1.1.

Different casting facilities also have different leach times as shown by the error bar in Figure 1.1. This relatively wide spread in leach times exists because of differences in leaching chemicals (leachant) used. This in turn arises for legacy reasons – casting facilities have their own preferred leachants. One of the aims of this project is to understand the reasons for these differences and recommend an ideal leachant.

Rolls-Royce plc manufactures several different turbine components which all have unique cooling channel geometries created using a ceramic core. The ceramic core is made from primarily silica and zircon.

The silica in the pre-fired core exists in its amorphous phase and undergoes a phase transition at casting temperatures into cristobalite – a crystalline phase of silica. Cristobalite improves the creep resistance of the core by suppressing sintering shrinkage at high temperatures. However, the highly ordered structure of cristobalite significantly reduces its dissolution rate in an alkaline solution by sterically blocking the OH^- from penetrating into the inner SiO_2 tetrahedral framework and limiting the reaction to the crystal surface (6).

The complex cooling channel geometry created by the ceramic core brings an added layer of difficulty in determining the optimal leach times for the different blades. This is coupled with the fact that inspection of the turbine blade component post leach to ensure 100% core removal is difficult to access. Fiberscopes and ophthalmoscopes are routinely used to ensure no core is present in the cooling channels after leaching. However, some parts of the geometry are inaccessible without cutting up the blade which increases scrap. In order to have an adequate margin of safety, the turbine components are leached for extended periods in the autoclave to ensure complete core removal. Residual core in the cooling channel post leach can be catastrophic

to the safe operation of the jet engine. Any unremoved core within the cooling channels will reduce heat transfer by blocking film cooling holes and could create localised regions where the metal blade will experience temperatures in excess of its melting point.

LBBC Technologies manufacture the core leaching autoclaves used by Roll-Royce plc. They are manufactured from 316L stainless steel due to its excellent resistance to stress corrosion in a highly alkaline environment. The autoclave operates on a pressure swing cycle which consists of a high pressure dwell, vent and low pressure dwell phases. An external air supply pressurises the autoclave up to 600 kPag.

1.2 Project Aims & Thesis Structure

This project had 3 primary aims:

I. To develop an understanding of the chemistry of silica dissolution in highly alkaline environments
II. To develop an understanding of the underlying physics of the core removal process for complex geometries in an autoclave utilising a pressure-swing system
III. To utilise the knowledge gained from I. and II. to drive improvements in the industrial core leach process

While some of the primary objectives of the two participating parties were different, there was considerable overlap as illustrated in Figure 1.2.

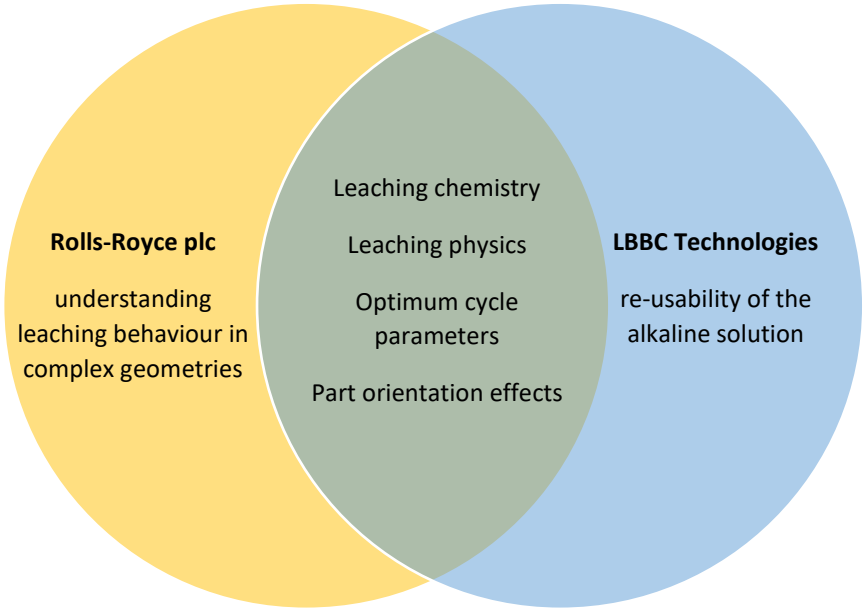

Figure 1.2 Primary objectives of Rolls-Royce plc and LBBC Technologies

Excluding this chapter, the thesis is split into seven other chapters:

1. Chapter two – literature review
2. Chapter three – experimental methods and materials
3. Chapter four – silica dissolution chemistry
4. Chapter five – physics of the ceramic core leaching process
5. Chapter six – industrial leaching trials
6. Chapter seven – recommendations for improving the process based on the understanding developed in the preceding three chapters
7. Chapter eight – conclusion and recommendations for future work

2 LITERATURE REVIEW

2.1 The Jet Engine

The core principle of aircraft propulsion stems from Newton's third law of motion which states that *for every action, there is an equal but opposite re-action*. This principle is illustrated in Figure 2.1.

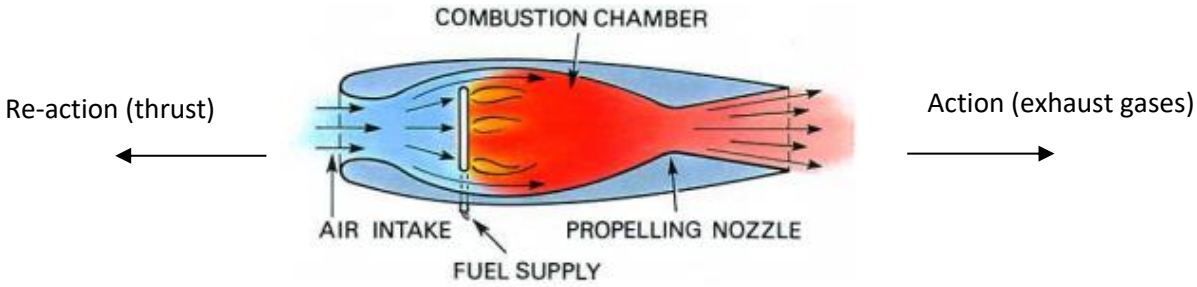

Figure 2.1 Newton's third law – the basis of jet propulsion (3)

A jet engine bears some similarity to internal combustion engines in terms of operating principles. Compression, combustion and expansion are processes that occur in both. In the internal combustion engine, these processes occur in a single component whereas in a jet engine they occur in different sections (3). A simple schematic showing the operation of a jet engine is shown in Figure 2.2.

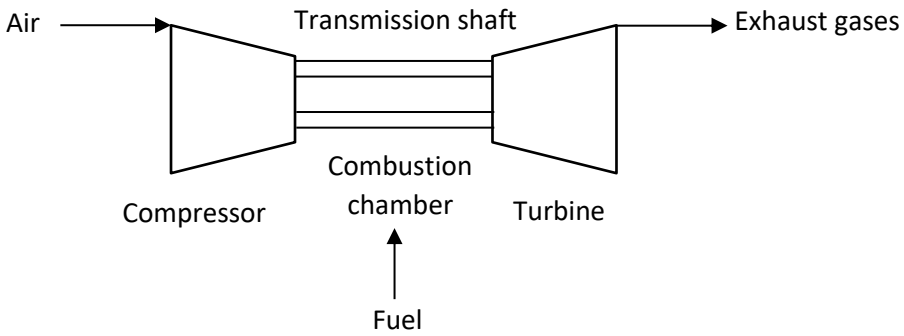

Figure 2.2 Simplified schematic of a jet engine

The process begins with air being compressed reaching pressures of up to 4000 kPag. This compressed air is a source of oxidation for the combustion reaction which takes place in the combustion chamber. Hot exhaust gases are produced during combustion and this drives the turbine blade. As the exhaust gases expand through the turbine blade stages, heat energy is transformed to mechanical energy causing the turbine blades to rotate. Some of the mechanical energy from the turbine blades is then transferred through a transmission shaft which in turn drives the compressor at the front of the engine. As the exhaust gases leave the turbines, its discharge to the atmosphere provides a propulsive jet (3).

Two main factors are critical for achieving optimal jet engine performance (7):

- Component efficiencies
- Turbine entry temperature

This is of course an oversimplification of an inherently complex process. In reality, several factors contribute to engine performance. The turbine entry temperature is of particular importance as it relates to the maximum theoretical efficiency of a heat engine.

The gas turbine engine operates on a Brayton cycle which consists of four steps (7):

- Isentropic compression through a series of axial compressors
- Isobaric heat addition in the combustion chamber
- Isentropic expansion through a series of turbine stages

- Isobaric heat rejection to the atmosphere

These processes are summarised in the P-V and T-S diagrams in Figures 2.3a and 2.3b respectively.

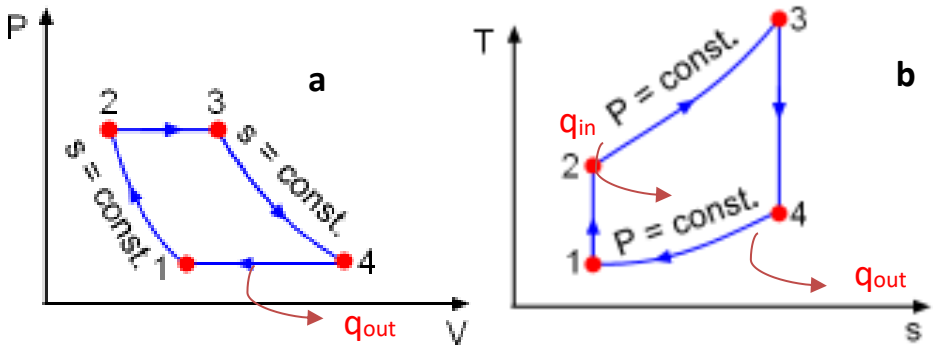

Figure 2.3 P-V (a) and T-S (b) diagrams for an ideal Brayton cycle (7)

The maximum theoretical thermal efficiency of a gas turbine operating under a Brayton cycle is (7):

$$\eta = \frac{W_{net}}{q_{in}} = 1 - \frac{q_{out}}{q_{in}} = 1 - \frac{C_P(T_4 - T_1)}{C_P(T_3 - T_2)} = 1 - \frac{T_1\left(\frac{T_4}{T_1} - 1\right)}{T_2\left(\frac{T_3}{T_2} - 1\right)} \quad (2.1)$$

Since steps 1-2 and 3-4 are isentropic, and $P_2 = P_3$; $P_4 = P_1$

$$\frac{T_2}{T_1} = \left(\frac{P_2}{P_1}\right)^{\frac{\gamma-1}{\gamma}} = \left(\frac{P_3}{P_4}\right)^{\frac{\gamma-1}{\gamma}} = \frac{T_3}{T_4} \quad (2.2)$$

$$\eta = 1 - \frac{T_1}{T_2} = 1 - \frac{T_4}{T_3} \quad (2.3)$$

where, W is work, P is the pressure, q is heat energy, C_p is the heat capacity, γ is the specific heat ratio and η is the thermal efficiency.

T_3 is the maximum temperature in the cycle, which in the case of the jet engine is equivalent to the turbine entry temperature, i.e. the temperature of the exhaust gases leaving the combustion chamber to the turbine stages and T_4 is the cold reservoir, which represents ambient atmospheric conditions. Therefore, higher engine efficiencies can be achieved by operating at a higher turbine entry temperature.

There are metallurgical restrictions to increasing the turbine entry temperatures. Turbine blades manufactured by Rolls-Royce are composed of single crystal nickel-based superalloys. These have a melting point range (solidus and liquidus respectively) of 1593 K and 1656 K (8) depending on the alloy. Current turbine entry temperatures are approximately 350 K higher than this (8). To operate the blades above this temperature without mechanical failure, Rolls-Royce implement two technologies:

- Thermal barrier coating – using ceramic coatings to improve heat resistance properties of the turbine component
- Internal cooling channels – Internal cooling channels within the turbine blade actively cool the blade during operation. This ensures that the melting point of the turbine blade is not exceeded. Cooling air is diverted from the compressor stages to the turbine blade (3). This is depicted in Figure 2.4. Heat is transferred via conduction from the hot exhaust gases in contact with the turbine blade and then by convection into the cooler air flowing through the channels. This air then exits at carefully positioned holes on the turbine blade surface creating a thin film

of air which further protects the blade from the high temperature exhaust gases (9).

The cooling channels also reduce the overall weight of the engine. This improves fuel consumption and makes the engine more efficient through an increase in the output power to weight ratio of the engine (9, 10).

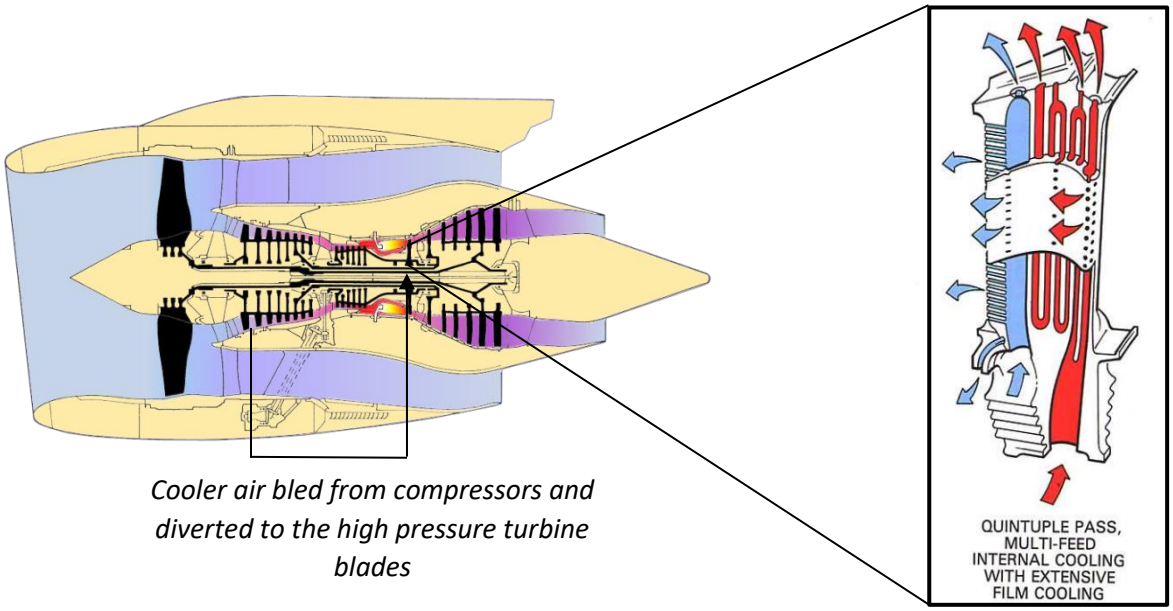

Figure 2.4 Jet Engine Profile showing internal cooling channels courtesy of Rolls-Royce plc (3, 11)

These cooling channels are created using a ceramic core during the investment casting process which is described in Section 2.2.

2.2 The Investment Casting Process

Investment casting is a multi-step metal forming processes. It was used in ancient Egypt to make gold jewellery and as one can imagine, products with complex geometries were often produced (12). In the present day, it is used widely for the manufacture of various metals and alloys with complex geometries.

The investment casting process is used by Rolls-Royce for the manufacture of nickel-based superalloys. A summary of the process is shown in Figure 2.5. It should be noted that the process shown in Figure 2.5 is not exhaustive. After core removal, the turbine blades go through a series of inspections, machining, heat treatment and final inspection before the final product is complete.

Figure 2.5 Summary of the investment casting process for air cooled turbine blade manufacture (12, 13)

1. Wax Pattern

The wax geometry incorporates a special design that only allows the formation of single crystals when the metal to be cast is poured. A ceramic core is inserted into the wax pattern to create the internal cooling channels.

2. Assembly

Large and complex wax components are assembled into a tree and runner system. This allows multiple patterns to be cast simultaneously

3. Investment

(a) Coating – Wax pattern is dipped in ceramic slurry to reproduce every detail of the wax

(b) Stuccoing – Coarse particles are applied to the initial coating used to improve structural integrity of the slurry. This prevents run-off and fracturing of initial cast

(c) Hardening – Each coating is left to set before the application of subsequent layers

Process repeated until desired thickness achieved

4. Dewaxing

After solidification of the slurry, the wax pattern is melted. Autoclave dewaxing is the industrial standard using saturated steam

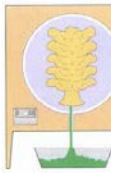

5. Firing

After the wax pattern is removed, residual moisture and organics present in the ceramic mould are removed. This step also serves as a means of preheating the mould in preparation of casting. Burnout furnaces often used and operated in the 870 ^{o}C -1095 ^{o}C temperature ranges with 10% excess air to ensure complete combustion

6. Melting and Casting

Vacuum melting is usually used for turbine blade components as it prevents oxidation of the reactive alloy. The molten metal is poured into the mould and withdrawn from the furnace hot zone allowing the crystals to grow

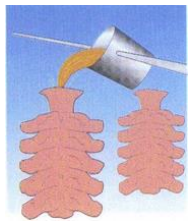

7. Core removal

After the shell mould has been removed, the ceramic core used to create the cooling channels needs to be removed as well. This core removal process takes place in a low pressure leaching autoclave

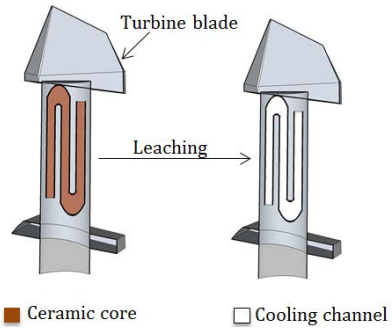

The turbine blade is made of a nickel based single crystal superalloy. At normal temperatures, Nickel (Ni) is resistant to atmospheric corrosion. Nickel is resistant to most basic but not acidic attack. It dissolves in mineral acids but relatively faster in dilute HNO_3 (14). This resistance to attacks from bases is a very useful property that is taken advantage of in the core removal process.

Turbine blades need to withstand large centrifugal loads during rotation at high speeds. They must also be resistant to fatigue and thermal shock (3). Casting the metal alloy in a single crystal helps to improve these properties by eliminating grain boundaries which are points of weakness in the crystal structure. The three relevant types of crystal structures are shown in Figure 2.6.

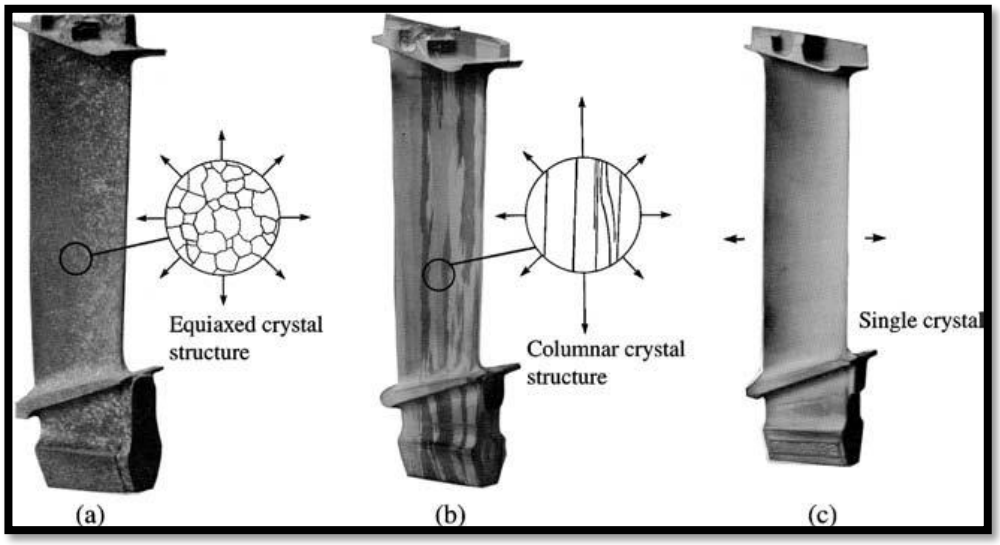

Figure 2.6 Possible Crystal Structures of Turbine Blades (14)

The equiaxed structure is formed as a result of the cast component only temporarily being held under vacuum (during the metal pour phase) after which

they are allowed to cool at room temperature. This cooling leads to the production of uniform three-dimensional crystal growths with many grain boundaries (14).

The columnar structure has better mechanical properties than the equiaxed structure but will still be insufficient to handle the large pressures and temperatures an aircraft engine experiences over prolonged time periods. The columnar structure is formed by directional solidification of the crystal grains (15).

The single crystal structure is present in some turbine castings manufactured by Rolls-Royce. This structure lacks any grain boundaries thereby improving the creep resistance of the alloy (15).

Figure 2.7 shows the manufacture of a turbine blade and how its geometry changes from the initial wax model to the final machined part that goes into the jet engine.

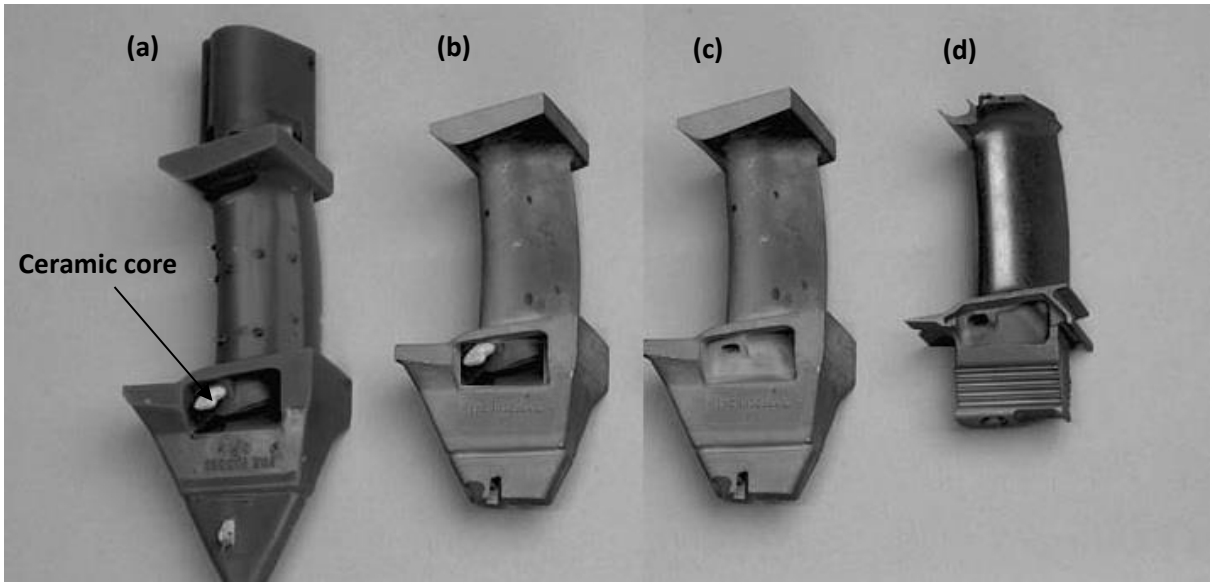

Figure 2.7 Production Stages of a high pressure turbine blades during the investment casting process. (a) Wax model of blade with ceramic core (b) Cast metal with ceramic core (c) Cast metal without ceramic core (d) Heat treated and machined turbine blade (16)

2.3 The Ceramic Core

Ceramic cores are used to create the internal cooling passages within the turbine blades. The ceramic core used by Rolls-Royce is primarily composed of silica and zircon. Silica has a high melting point of 1700 ^{o}C, a low coefficient of thermal expansion and dissolves in caustic solutions (17). These properties make silica an ideal component from which to fabricate the ceramic core.

The ceramic core typically contains silica and zircon in approximately 3:1 mass ratio and 5wt. % additives to control phase growth.

2.3.1 Silica

Silica (SiO_2) is the second most abundant compound on earth after water. Bonding is approximately 60% covalent and 40% ionic with average bond energies of 468 kJ mol^{-1} (18). Silica consists of a 3-dimensional framework of $(SiO_4)^{4-}$ units. This unit is a closely packed tetrahedron with Si^{4+} at the centre (18). Silica has a high melting point of 1700 ^oC and a low coefficient of thermal expansion (17). These properties make it ideal for a ceramic core because the melting point is in excess of the casting temperatures of about 1500 ^oC.

Silica exists in amorphous and crystalline forms. The principal forms of amorphous silica are pyrogenic silica, precipitated silica, silica gel and colloidal silica sols whereas the principal crystalline forms are quartz, tridymite and cristobalite at atmospheric pressure (18). The crystalline polymorphs are shown in Figure 2.8.

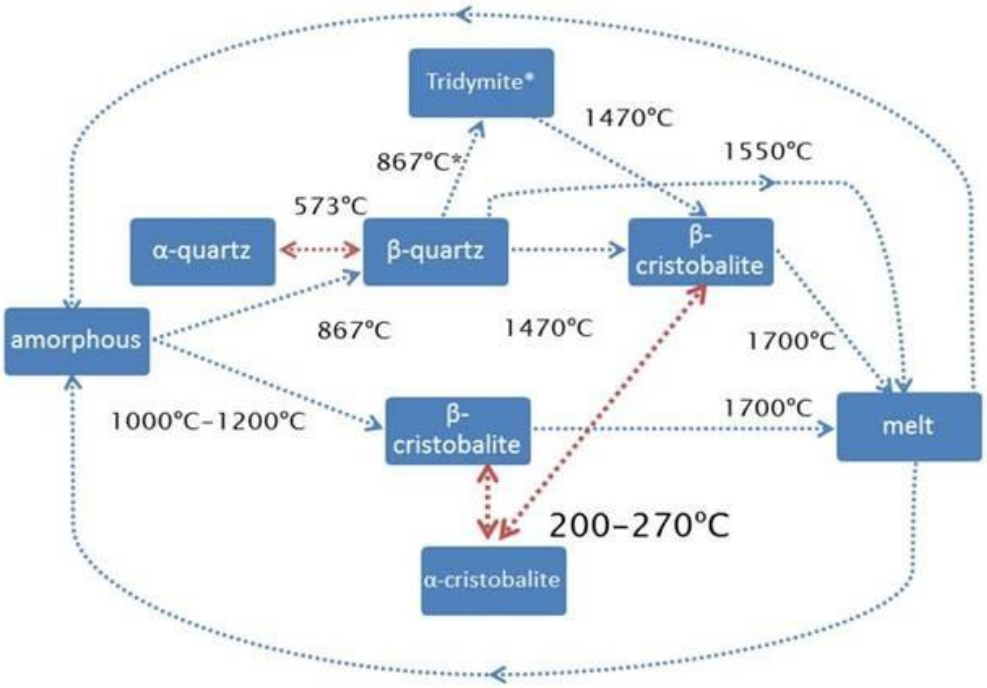

**Only in the presence of certain mineralisers. Red arrows indicate a reversible transition*

Figure 2.8 Crystalline silica polymorphs (17)

Upon heating, α-quartz undergoes a phase transition at 573 °C becoming β-Quartz. At 867 °C, tridymite is formed. This step is skipped if β-Quartz is pure as trace amounts of mineralisers are necessary for the formation of tridymite (17). At 1470 °C, β-cristobalite forms and is stable up 1700 °C and metastable down to 268 °C whereas α-cristobalite is metastable to below 200 °C (18).

2.3.2 Zircon

Zircon ($ZrSiO_4$) is used extensively in the investment casting industry. It is used in most ceramic cores for high temperature application. It has a low coefficient of

thermal expansion, low coefficient of heat conductivity, high chemical stability, high resistance to melt corrosion and high thermal shock resistance. Zircon is relatively inert however; it does dissolve in strong solutions of LiOH, NaOH and KOH above 573 K (17).

2.3.3 Life of a Core

Before a core is leached, it goes through a series of physical and chemical transformations during the various stages of the investment casting process – from core formulation to casting.

The ceramic core formulation consists of two main components – the powder and the binder. These are mixed together to form a homogenous mixture. The homogeneity of the mixture is important for several stages of the process. A poorly mixed core formulation will lead to localised pockets of high solids loading during core injection. This will lead to a non-uniform burn out of the binder and it will also affect the sintering properties of the powder at casting temperatures (17). More importantly for this project, any inhomogeneities in the formulation could lead to localised high concentration of zircon grains which will affect the leachability of the core as a result of the chemical inertness of zircon in strong alkaline solutions.

The pre-fired core is an amorphous phase of silica which undergoes a phase transition into cristobalite during casting temperature cycle. The temperature ramp experienced by the core during the casting process is approximately as follows (19):

- Ramp at 10 ^{o}C min^{-1} to 1500 ^{o}C
- Hold at 1500 ^{o}C for 20 min
- Cool at 7 ^{o}C min^{-1} to 1300 ^{O}C
- Cool at 10 ^{o}C min^{-1} to room temperature

Cristobalite formed during the casting cycle improves the creep resistance of the core by suppressing sintering shrinkage at the high temperatures experienced during casting which improves the dimensional stability of the core (19). The main drawback of forming cristobalite in the core is its slower dissolution rate in alkaline solutions relative to amorphous silica. This is because the well-ordered cristobalite structure blocks the OH^- from reaching the inner tetrahedral SiO_4^{4-} framework thereby limiting the reaction to the silica surface. In amorphous silica, the disordered structure allows penetration of the OH^- into the inner framework which leads to faster dissolution rates via a higher frequency of siloxane (≡Si-O-Si≡) bond cleavage (6). It has been reported that the activation energy for the dissolution of amorphous silica is less than the activation energy of crystalline silica (6).

The ceramic core is primarily composed of α-cristobalite at room temperature. Even when taken up to leach temperature of 160 ^{o}C, α-cristobalite is still the

predominant silica phase in the core. The porosity of the ceramic core also changes during casting. Figure 2.9 shows the pore distribution of V core after a simulated cast cycle. It can be seen that before the cast cycle, the pore distribution of the material is centred at around 5 µm (large pores) and 0.5 – 2 µm (small pores). The larger pores are between silica grains whereas the smaller pores are between the smaller silica and zircon grains. After the simulated cast cycle, the pore distribution is centred on 10 µm. This increase in pore radius probably exists because of liquid phase sintering which transports material into the smaller pores thereby increasing the size of the larger pores (17). The V core highlighted in Figure 2.9 is one of the core formulations used by Rolls-Royce.

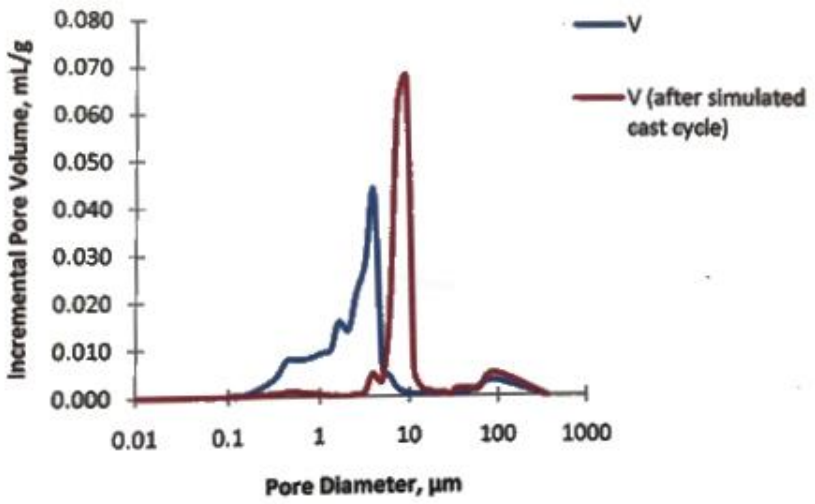

Figure 2.9 V material pore distribution before and after a simulated cast cycle (17)

2.4 Core Leaching Autoclave

LBBC Technologies manufactures the core leaching autoclaves used by Rolls-Royce for leaching ceramic cores. The core leaching autoclave can be thought of as a batch reactor with a pressure swing system.

Components to be leached are loaded into baskets, then into the autoclave. The Quicklock door - a pneumatically powered swing door is operated on a localised control panel to prevent accidentally trapping someone within the autoclave. Once the door is locked, caustic is pumped into the vessel to a specified height and the leach cycle is started. The leach cycle involves cyclic pressurisation and depressurisation of the system at a temperature of about 160 ^{o}C.

Three variables control the leach cycle: the pressure, vent and dwell times. After the leach cycle, the caustic is drained out into a vent tank. Water is then pumped to the top of the autoclave to wash down any lumps of undissolved core material which is then flushed out of the autoclave into the dump tank. Finally, neutralisation of the system with citric acid is sometimes performed internally within the autoclave or externally (20).

Figure 2.10 shows the steps in the core leaching process and Figure 2.11 shows the piping and instrumentation diagram (PID) of the autoclave.

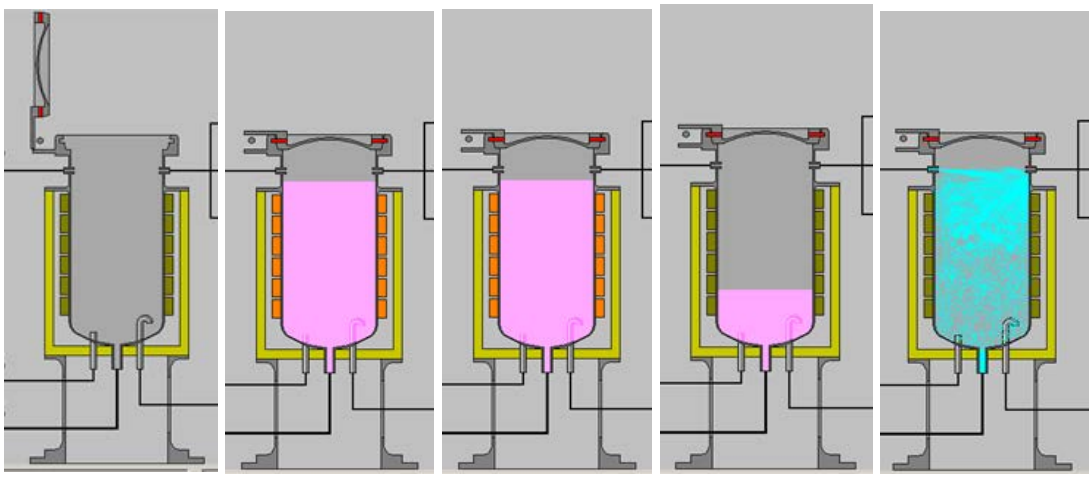

(1) Load components (2) Fill with caustic and heat up (3) Pressure and vent cycle initiated (4) Caustic drained to dump tank (5) Flush with water

Figure 2.10 Summary of the leaching process (20)

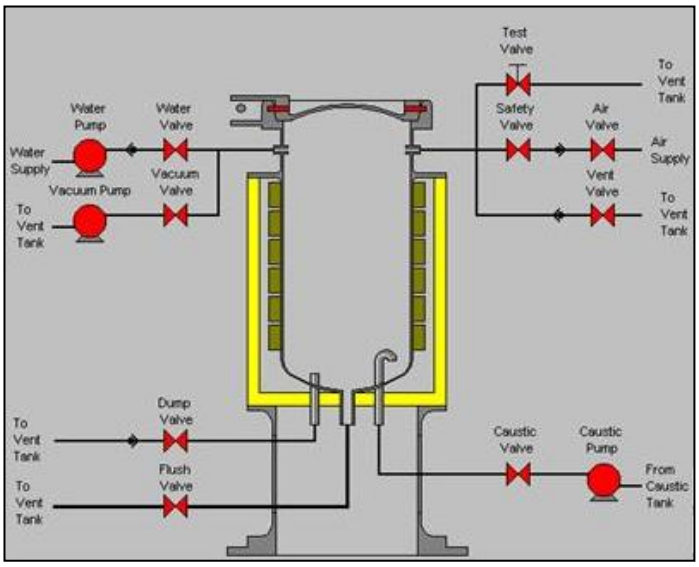

Figure 2.11 Core leaching autoclave PFD (20)

2.5 Chemistry of Core Removal

The literature on the chemistry of silica dissolution in highly alkaline solutions is very broad. This section will give an overview of the mechanics of both amorphous and crystalline silica dissolution, with a greater focus on the latter. The effect of pH and the influence of different alkali metal cations on the dissolution process will also be covered. Finally, the complex rheological behaviour of silicates and its effect on the rate determining step of the dissolution process will be considered.

2.5.1 Alkaline Solution Properties

NaOH and KOH are used by Rolls-Royce across its various casting facilities for core leaching. These two bases have similar physical and chemical properties. They are both strong bases, i.e. they dissociate completely into their constituent ions when dissolved in water as shown in equation 2.4 where M is the Group IA metal cation.

$$MOH_{(s)} + H_2O_{(l)} \leftrightarrow M^+{}_{(aq)} + OH^-{}_{(aq)} + H_2O_{(l)} \quad (2.4)$$

To understand the chemistry of bases, one must understand the chemistry of acids as well, since they complement each other. There are three main theories on acids and bases (21).

- Arrhenius theory – An acid produces H^+ and a base produces OH^- when dissolved in a solvent

- Bronsted-Lowry theory – Acids are proton donors whereas bases are proton acceptors
- Lewis theory – Acids are electron pair acceptors whereas bases are electron pair donors. With this theory, a Lewis acid is an electrophile and a Lewis base is a nucleophile

A weak base does not fully dissociate when dissolved in water. An example of this is ammonia as shown in equation 2.5.

$$NH_3 + H_2O \leftrightarrow {NH_4}^+ OH^- \quad (2.5)$$

A strong base like NaOH or KOH completely dissociates in water. Equation 2.4 can be simplified as:

$$MOH \leftrightarrow M^+ + OH^- \quad (2.6)$$

The rate dissociation constant is given as:

$$K_b = \frac{[M^+][OH^-]}{[MOH]} \quad (2.7)$$

Strong bases fully dissociate in solution, K_b approaches a constant value as [MOH] approaches 0 (22, 23).

$$pK_b = -log_{10}K_b \quad (2.8)$$

Thus, a smaller pK_b equates to stronger base. LiOH, NaOH and KOH are all strong bases with a $pK_b < 1$ (23).

At high concentrations however, Raman spectral investigations have shown the formation of clusters between the metal cation and hydroxide ions (24). This is relevant because concentrations used in the autoclave often exceed 5 M

NaOH/KOH. At such high concentrations, clustering will reduce the concentration of free hydroxides which are the catalyst for silica dissolution.

Once the M-OH bonds are broken to form M^+ and OH^-, noncovalent interactions with polar water molecules lead to a highly structured hydrated cation and anion. The strength of these interactions is dependent on the ionic potential of the ion, which is in turn dependent to its charge density (25). This is illustrated in Figure 2.12.

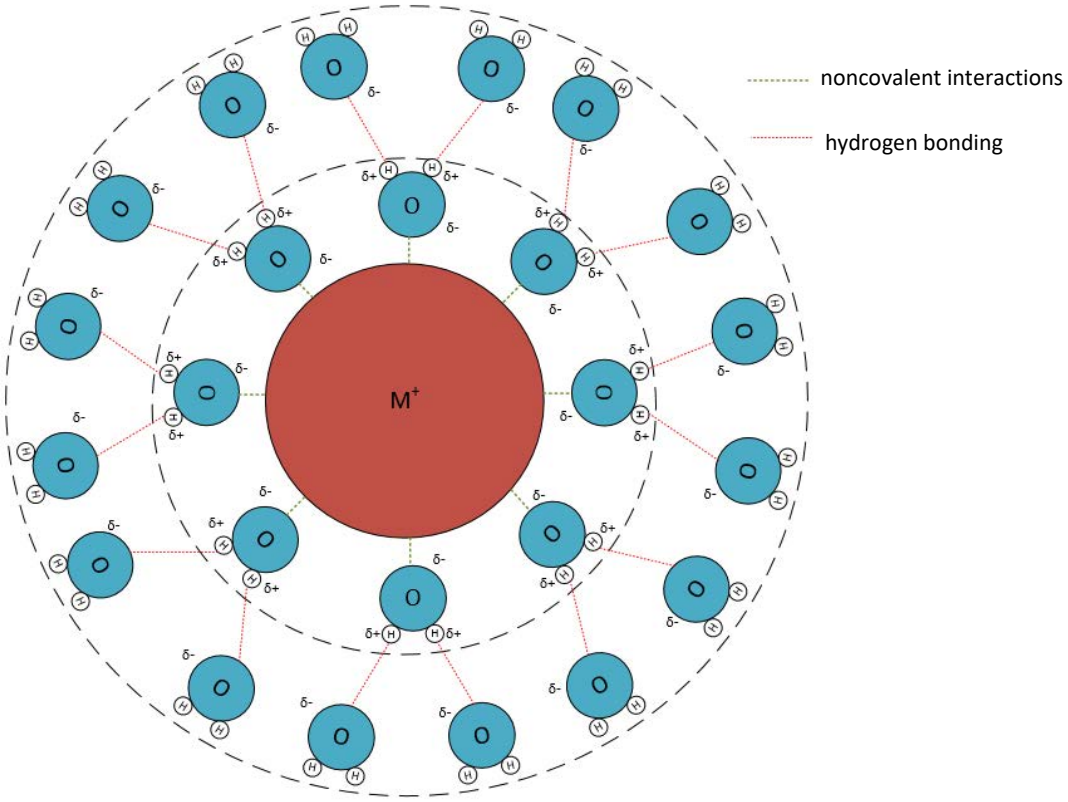

Figure 2.12 Primary and secondary hydration spheres around a metal cation

The formal positive charge on the metal cation attracts the highly polar water molecules which has a partial negative charge on the oxygen atom. This creates a primary hydration sphere around the metal cation. The size of the hydrated

metal cation depends on the charge density of the central cation. Water cluster binding studies show that ions with larger charge densities bind water clusters more strongly than ions with a low charge density. If the charge density of the cation is large enough, i.e. cations with smaller ionic radii, then hydrogen bonding between the hydrogen from water molecules in the primary hydration sphere and oxygen molecules from nearby water molecules form a secondary hydration sphere (25). It should be noted that at very high concentrations used in the autoclave (> 5M MOH) there will be less water available to form hydration spheres around the metal cation.

The hydroxide anion will also interact with nearby water molecules forming a hydration sphere. The hydrated radii of anions will however be smaller than cations with similar atomic numbers. The anion can hold fewer water molecules in its hydration sphere because the orientation of water molecules towards the central anion limits hydrogen bonding and precludes the formation of a secondary hydration sphere (25). The water molecules in the hydration sphere are constantly exchanged with the water in the solution bulk at rates less than 10^9 s^{-1} (25). Birk (26) using NMR on ^{17}O showed that the solvent exchange rate increased from Li^+ to Na^+ to K^+ with values of $10^{8.8}$ s^{-1}, 10^9 s^{-1} and $10^{9.2}$ s^{-1} respectively indicating, as expected that K^+ would have the highest exchange frequency because of its lower charge density relative to Na^+ and Li^+. Kinrade (27) showed that the silicon atom had solvent exchange rates that were 5-8 orders of magnitude less than the metal cations listed previously. The slow rate associated with the silicon atom is indicative of its ability to orient and constrain the water molecules around it.

Table 2.1 shows the hydrated radii of some Group IA, IIA and IIIA cations as well as the hydroxide anion.

Table 2.1 Solvation properties of some ions in aqueous solutions

Ion	Ionic radius (pm)	Hydration radius (pm)	Hydration free energy (kJ mol^{-1})	Charge density (x $10^{-3}pm^{-1}$)
Li^+	55 [28]	340 [29]	-515 [30]	12.7
	76 [30]	380 [28]	-544 [31]	
	78 [32]	382 [30]		
	90 [31]			
	94 [33]			
Na^+	94 [28]	276 [34]	-365 [28]	9.36
	98 [32]	299 [29]	-398 [35]	
	101 [36]	358 [33]	-405 [30]	
	102 [30]	360 [28]	-435 [31]	
	116 [31]			
	117 [33]			
K^+	133 [28]	201 [37]	-271 [29]	6.91
	138 [29]	232 [34]	-295 [28]	
	149 [33]	275 [32]	-321 [30]	
	151 [38]	331 [33]	-343 [34]	
	152 [31, 34]		-351 [31]	
Rb^+	148 [28]	330 [28]		6.54
	149 [39]			
	152 [40]			
	163 [33]			
Cs^+	170 [28]	329 [32]	-376 [41]	5.63
	174 [42]			
	181 [34]			
	186 [33]			
Mg^{2+}	72 [33]	300 [37]	-1828 [28]	62.0
		428 [33]	-1992 [30]	
Ca^{2+}	100 [37]	412 [33]	-1306 [35]	37.5
	106 [32]	420 [39]	-1504 [28]	
	114 [31]		-1592 [32]	
Zn^{2+}	74 [33]	430 [30]		54.1
OH^-	133 [43]	300 [37]		8.23
	110 [44]			

The different values reported in literature arise because of different experimental methods, the assumptions made in theoretical methods and differences in coordination numbers of the hydrated ions (25).

Figure 2.13 shows the average ionic and hydrated radii of Lithium, sodium, potassium, rubidium and caesium ions calculated from the sources in Table 2.1. It can be seen that the ionic radii increases as you go down group from lithium to caesium. However, size of the hydrated radius decreases from lithium to potassium and then increases again in rubidium and caesium. The reason for trend is unclear as the size of the hydrated radius has been reported to be proportional to the charge density – defined as Z^2/r where Z is the ionic charge and r is the ionic radius (25).

From Table 2.1, it can be seen that the charge density is dependent on the hydrated radius of Li, Na and K. However for Rb and Cs, there is a break in the trend as the charge density is lower for these atoms but the hydrated radii increases. This could be because the hydrated radii values for Rb and Cs were derived from two and one sources respectively which could magnify any random error whereas the values for Li, Na and K are averaged from more than three sources.

It is also possible that the magnitude of the standard deviation of the hydrated radii is related to the number of sources from which that value was derived from, i.e. the values for potassium and sodium were derived from 4 sources whereas lithium was derived from 3 sources. Rubidium and caesium were derived from 2 and 1 sources respectively leading to less variability in the data.

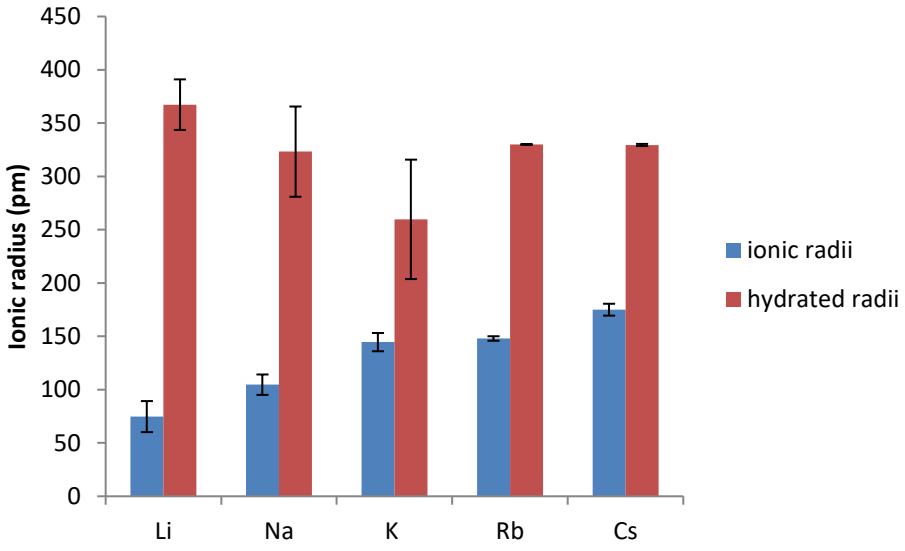

Figure 2.13 Ionic and hydrated radii of Group IA cations

Figure 2.14 shows the hydration free energy for Li, Na and K averaged from the values in Table 2.1. Data for Rb and Cs was not included because of insufficient sources of data from other sources.

It should be noted that different methods were used by the different authors to obtain the ionic and hydration radii shown in Table 2.1. These include neutron diffraction, EXAFS (Extended X-ray Absorption Fine Structure), Photoluminescence, infrared spectroscopy etc. More recent work carried out by Binder and Zschörnig (35) used infrared spectroscopy to measure the ionic and hydrated radii of some Group IA cations.

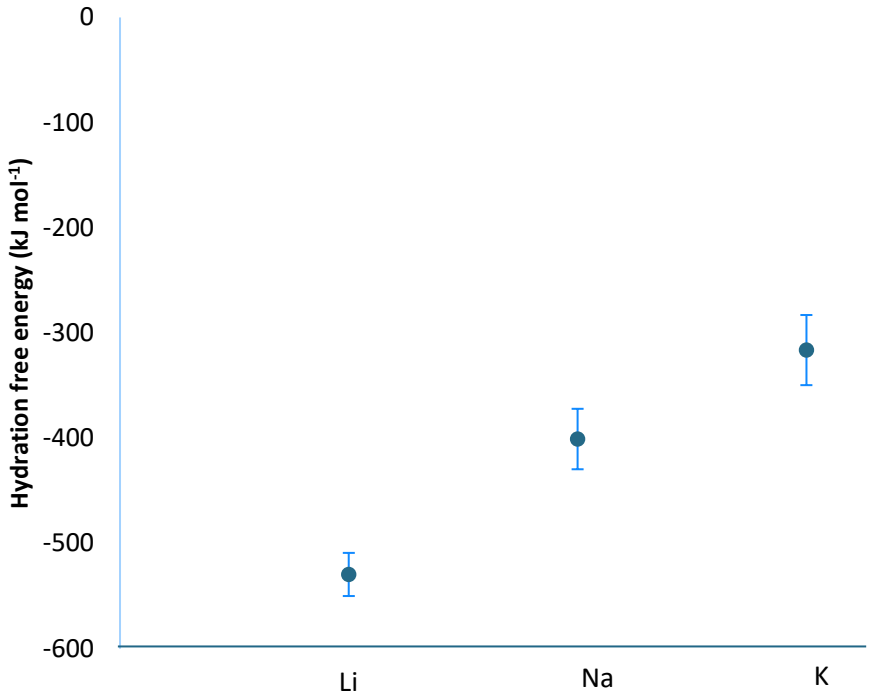

Figure 2.14 Hydration free energy of some Group IA alkali cations

Lithium has the most negative hydration free energy hence the strongest hold on its hydration waters whereas potassium has the least negative hydration free energy of the ions considered.

The physical properties of LiOH, NaOH and KOH are also important for the core leaching process. Figure 2.15 shows the viscosity as function of molar concentration at 25 ^{o}C. A molar concentration (mol L^{-1}) basis is used for comparison because it is a more accurate representation of the concentration of molecules in solution as opposed to the more widely used weight % which is prevalent in industry. Also, all of the laboratory dissolution experiments are carried out on a molar basis to allow for easy comparisons with the literature.

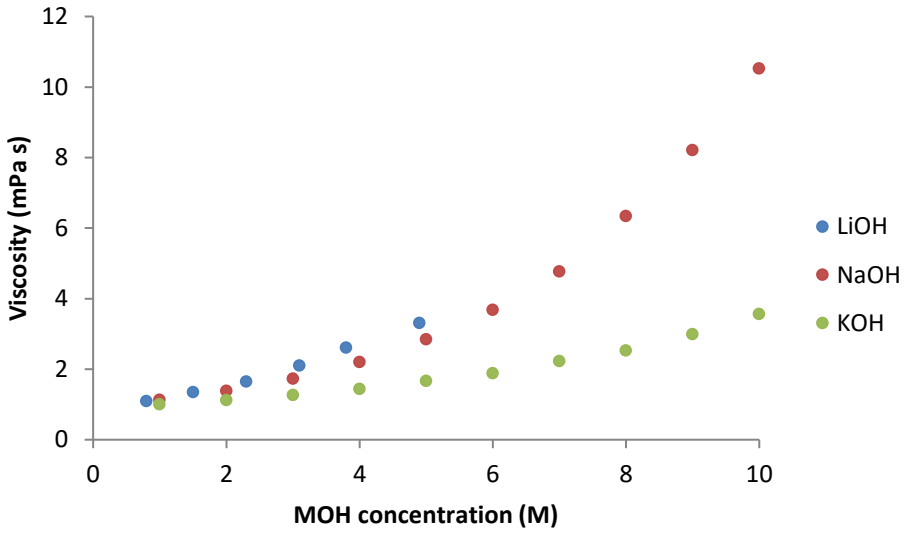

Figure 2.15 Viscosity of different alkali hydroxides as a function of concentration (45)

KOH is the least viscous of the three bases whereas LiOH is the most viscous. All three alkali hydroxides exhibit Newtonian behaviour up to the concentrations considered. At higher concentrations up to 100 wt%, i.e. molten caustic; it is possible that that the rheological behaviour will deviate from Newtonian since no water is present. There is, however, no literature evidence for this. In any case, it is not of importance as industrial concentrations for leaching do not exceed MOH of about 50 wt% which is 13.5 M and 19.1 M for KOH and NaOH respectively (5).

Figure 2.16 shows the viscosity of approximately equimolar solutions of NaOH and KOH as a function of temperature from 20 ^{o}C – 70 ^{o}C.

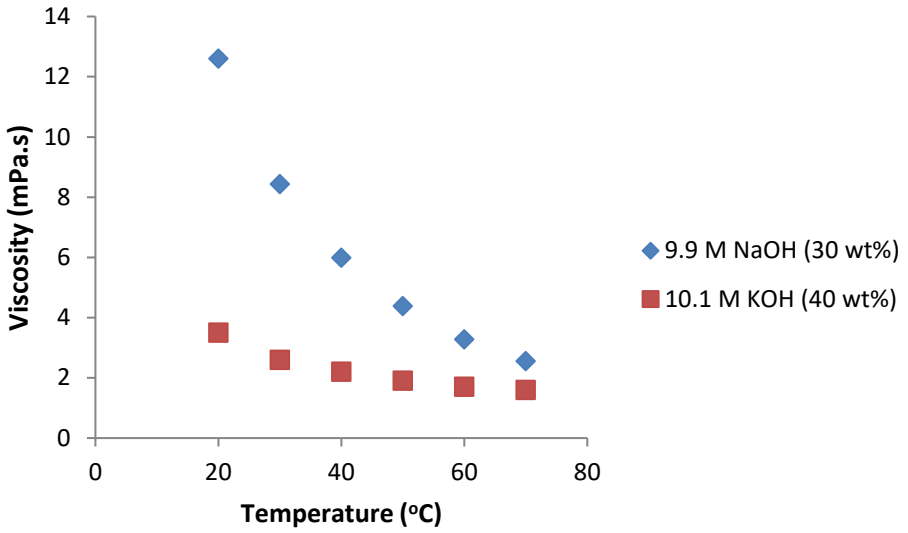

Figure 2.16 Viscosity of NaOH and KOH solutions at approximately equimolar concentrations as a function of temperature (45-47)

From the data, the viscosity of the NaOH solution is 3.6 times larger than KOH at 20 °C. However, at 70 °C, this viscosity spread reduces to 1.6 thus indicating that at operating temperatures of about 160 °C in the autoclave, the difference in viscosity may well be negligible.

2.5.2 Silica Dissolution Mechanism

Silica consists of a 3-dimensional framework of SiO_4^- units. This unit is a closely packed tetrahedron with Si^{+4} at the centre. Silica dissolution can be regarded as the depolymerisation of the three dimensional covalent silica network via siloxane bond cleavage (48, 49). There are five main factors that determine the rate of silica dissolution:

a) pH

b) Silica polymorph

c) Temperature

d) Cationic effects

e) Surface area

The process is further complicated by the fact that these factors are not independent of each other. For example, cationic effects are enhanced by a high pH (48-50). However, higher temperatures (150 ^{o}C) seem to reduce the rate enhancing effects of the cations (50). Other minor factors that affect the dissolution rate include porosity, the state of internal hydration of the silica structure and the presence of impurities (50).

2.5.2.1 pH effects

According to several authors (51-55) the dissolution rate of silica is accentuated at pH extremes, especially at a higher pH and is slowest at a neutral pH. Figure 2.17 shows the solubility of amorphous silica as a function of pH.

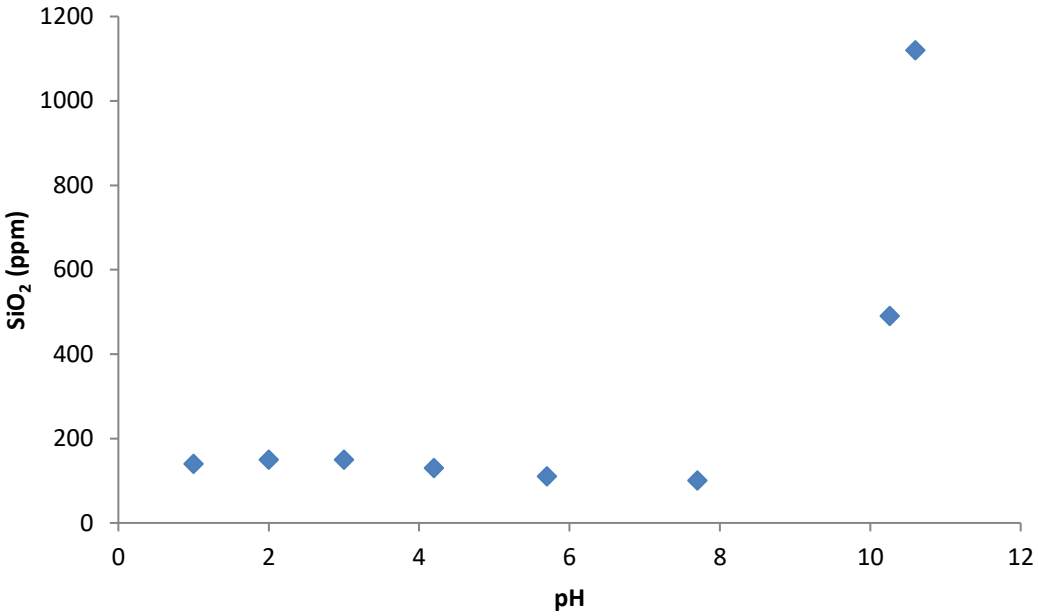

Figure 2.17 Amorphous silica solubility in water at 25 °C as a function of pH (56)

Under acidic conditions (pH < 7) the maximum solubility is at a pH of 3 (150 ppm). Overall, the minimum solubility is at a pH of 7.7 (100 ppm) and the maximum solubility of 1120 ppm is at a pH of 10.6 (57). The limitation of Figure 2.17 is that it does not include solubility data at higher pH values which is relevant for in this study.

Ab initio quantum mechanical studies of the kinetics of quartz dissolution where H_3O^+ and OH^- act as catalysts by reducing the activation energy barrier from 121.3 kJ mol^{-1} in H_2O down to 100.4 kJ mol^{-1} and 79.1 kJ mol^{-1} for H_3O^+ and OH^- respectively (51, 52). The quantum mechanical studies were however performed on quartz which has a much lower solubility limit than amorphous silica in water. This will be expanded upon in section 2.5.2.2.

Under neutral conditions, i.e. silica in pure water; dissolution leads to the formation of monosilicic acid. Its structure consists of a silicon atom coordinated with four hydroxyl groups as $Si(OH)_4$.

$$SiO_{2(aq)} + H_2O_{(l)} \leftrightarrows Si(OH)_{4(aq)} \quad (2.9)$$

Monosilicic acid is stable in water at 25 ºC up to its solubility limit of about 100 ppm (53, 57). Above this concentration, polycondensation reactions between two monosilicic acid molecules leads to the formation of a dimer with the simultaneous release of H_2O – the leaving group.

$$Si(OH)_{4(aq)} + Si(OH)_{4(aq)} \leftrightarrows Si_2O(OH)_{6(aq)} + H_2O_{(l)} \quad (2.10)$$

Quantum mechanical studies on the mechanism of quartz dissolution in H_2O performed by Xiao and Lasaga (52) show that the attack of H_2O on a negatively charged silica surface is identical to OH^- attack on a neutral surface, i.e. they both form the same initial surface complex. This is in agreement with work by Tamada et al. (58), Schwartzentruber (59), Brady and Walter (60), Dove and Crerar (61) and Gratz and Bird (62).

In the studies by Xiao and Lasaga (52) were carried out in the gas phase. Disilicic acid was used as a neutral quartz surface and deprotonated disilicic acid was used to create a negatively charged quartz surface.

H_2O attack on a negative silica surface yields the same surface complex as OH^- attack on a neutral surface as shown in equations 2.11 and 2.12 respectively.

$$Si_2O_2(OH)_5^- + H_2O \rightarrow Si(OH)_4 + Si(OH)_3^- \quad (2.11)$$

$$Si_2O(OH)_6 + OH^- \rightarrow Si(OH)_4 + Si(OH)_3{}^- \quad (2.12)$$

Figures 2.19 a-f show the detailed mechanism of OH^- adsorption unto a neutral silica surface which is somewhat representative of what happens to the silica based ceramic core during the leaching process at high pH. Two important distinctions between the mechanism shown here and what in an aqueous solution is the lack of cation adsorption on the silica surface and more importantly, the fact that the silica surface used in the simulations were all Q^1 Si, i.e. each Si atom is joined to only one other Si via siloxane bonds.

In reality, the surface of a crystalline silica phase such as quartz or α-cristobalite (as present in the core) would be composed of predominantly Q^2 and Q^3 Si (57, 63). A Q^2 Si atom is connected to two other Si atoms via siloxane bonds while a Q^3 Si atom is connected to three other Si atoms via siloxane bonds. Computational studies carried out by Pelmenschikov et al. (64) showed that lower activation energies were linked to Si atoms with a lower degree of connectivity.

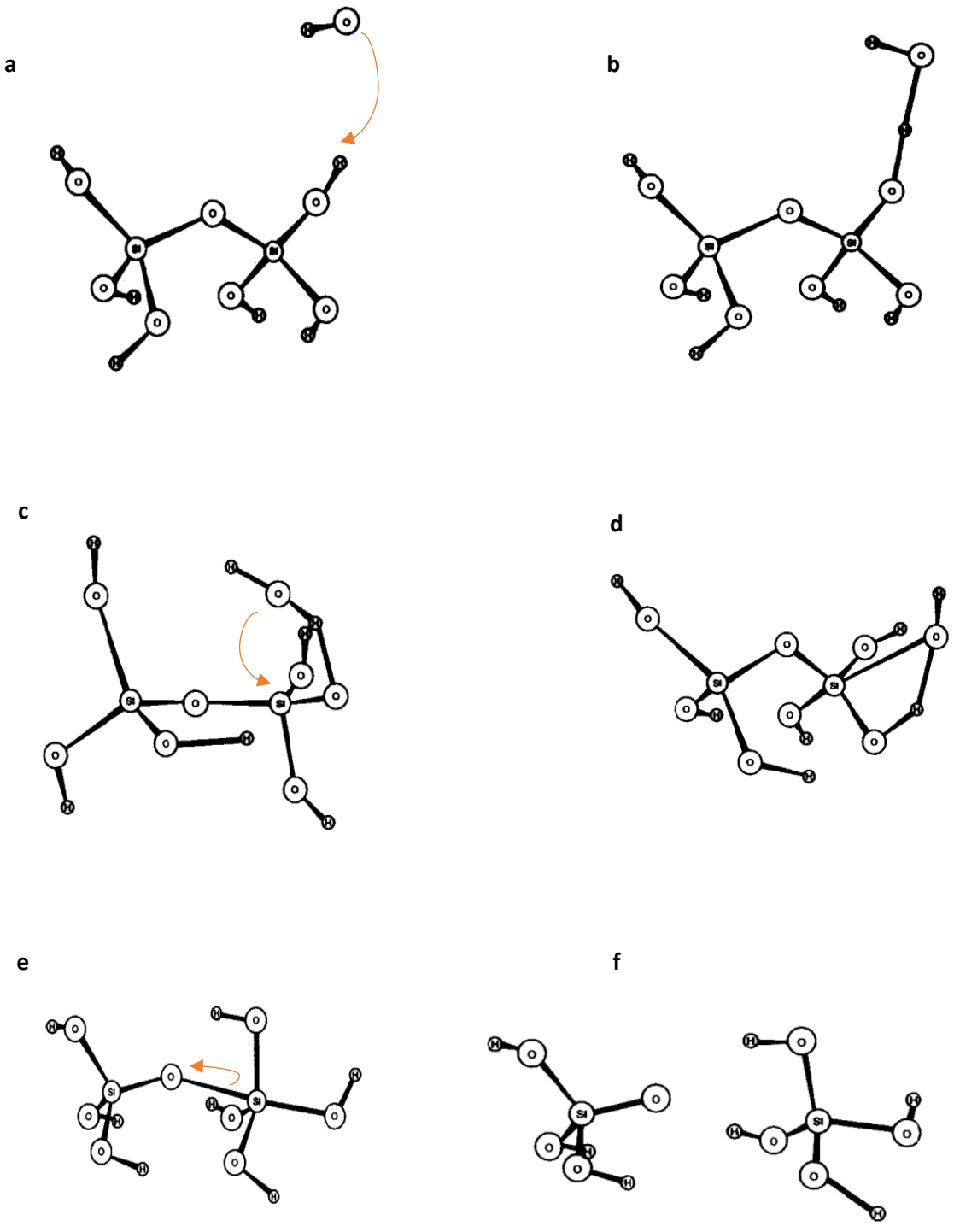

Figure 2.18 Mechanism of OH- attack on a simulated quartz surface - modelled as disilicic acid (52)

Figure 2.18a shows the hydroxide approach the disilicic acid molecule. A hydrogen bond is formed with one H from $Si_2O(OH)_6$ as shown in Figure 2.18b, which is identical to water adsorption on a negatively charged silica surface. In Figure 2.18c, a five-fold coordinated Si is formed which is the first transition state (TS1) which is optimised in Figure 2.18d in its second transition state (TS2). Finally in Figure 2.18e, cleavage of the siloxane bond occurs to yield the hydrolysed products shown in Figure 2.18f.

Figures 2.19 and 2.20 show the bond lengths (in angstroms) of the fully optimised initial simulated quartz molecule (disilicic acid) and the fully optimised five-fold coordinated Si species respectively. It can be seen that the Si-O bond adjacent to the five-fold coordinated Si atom has elongated by 4.9 %. This elongation is hypothesised to be the precursor to Si-O cleavage (52, 65).

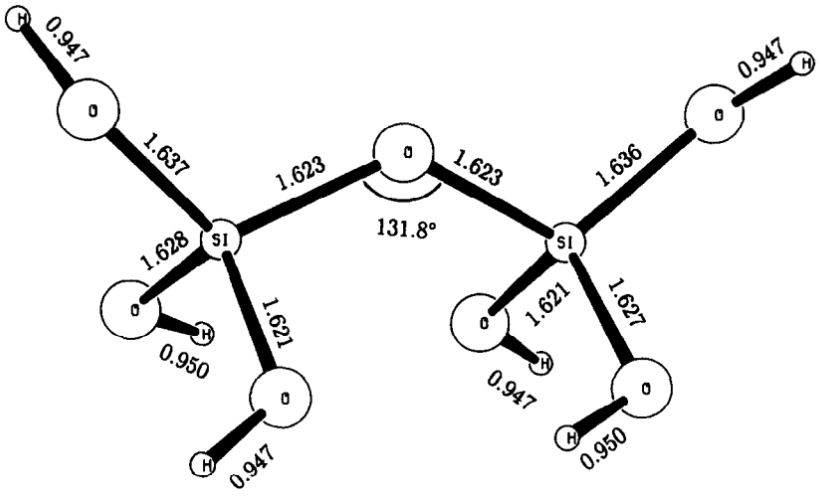

Figure 2.19 Fully optimised disilicic acid geometry (52)

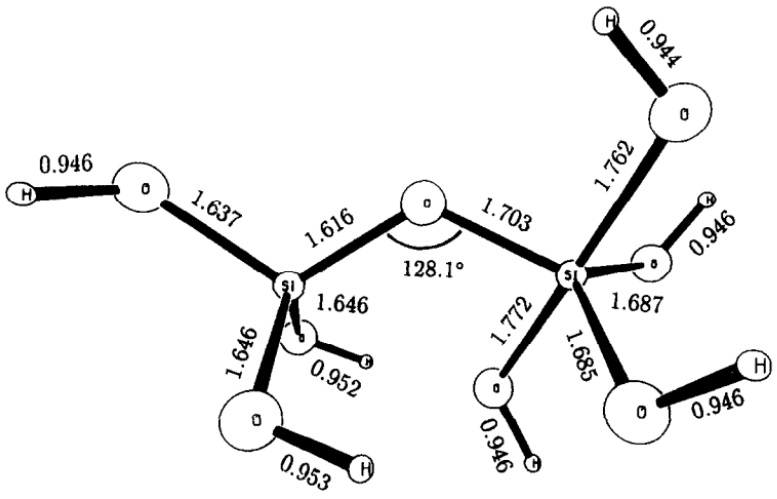

Figure 2.20 Fully optimised five-fold Si coordinated geometry prior to cleavage (52)

According to calculations by the same author (52), the formation of the five-fold coordinated species, i.e. TS1, has to overcome an energy barrier of 79.1 kJ mol^{-1} whereas the formation of the hydrolysed products via siloxane cleavage shown in Figure 2.19f has to overcome an energy barrier of only 18.8 kJ mol^{-1}. This is in agreement with more recent computational work done by Tamada et al. (58) where it was reported that the energy barrier associated with TS1 formation was 63 kJ mol^{-1} whereas the breakdown of TS2 into its hydrolysed products had an energy barrier between 22-29 kJ mol^{-1}. Tamada et al. (58) accounted for cation adsorption (Na^{+}) on the crystalline silica surface as well as a more realistic transformation from Q^3 Si to Q^1 Si which is more representative of what happens at the surface of crystalline silica during dissolution.

The work carried out by both authors (52, 58) shows that the rate controlling step of quartz dissolution in a high pH environment is the formation of a five-fold

coordinated Si species, not the cleavage of siloxane bonds holding the structure together. Detailed computational studies of α-cristobalite dissolution have not been carried out but it can be assumed that the mechanism would be similar to that in quartz since they are both crystalline phases of silica.

The mechanism of silica dissolution at a low pH is similar to the mechanism at a neutral or high pH in that it ultimately involves siloxane bond cleavage. However, in the case of H_3O^+ catalysed dissolution, the first step is the attack of the H_3O^+ on the bridging oxygen (Si-O-Si) which elongates and weakens the siloxane bond holding the structure together. In the H_3O^+ catalysed reaction, the cleavage of the siloxane bond has the largest energy barrier of 100.4 kJ mol^{-1} and is the rate controlling step of the process as opposed to adsorption of H^+ and H_2O or H_3O^+ on the bridging oxygen of the Si-O-Si structure which has an energy barrier of -16.2 kJ mol^{-1} (51). This differs significantly from the activation energy of 45 kJ mol^{-1} calculated by Criscenti et al. (65) where solvation effects on the bridging oxygen atom where accounted for.

Tables 2.2 and 2.3 show the computational and experimental values, respectively, for the activation energy of silica dissolution. Q^n is the standard nomenclature in silicate chemistry where n is an integer between 1 and 4 and is indicative of the number of siloxane bonds (Si-O-Si) bonded to the Si atom.

Table 2.2 Computational activation energies of SiO_2 dissolution

Activation energy (kJ mol^{-1})	Summary
100.4 (51)	Quartz simulated as a cluster of disilicic acid in the presence of H_3O^+. Dissolution proceeds via Q^1 to Q^0 transformation. Activation energy of siloxane cleavage
79.1 (52)	Quartz simulated as a cluster of disilicic acid in the presence of OH^-. Dissolution proceeds via Q^1 to Q^0 transformation.
122.6 (66)	Amorphous silica in H_2O. Dissolution proceeds via Q^1 to Q^0 transformation.
116.8 (66)	Amorphous silica in H_2O. Dissolution proceeds via Q^2 to Q^1 transformation.
75 (67)	β cristobalite simulated as a cluster of disilicic acid in H_2O. Dissolution proceeds via Q^1 to Q^0 transformation.
92 (64)	β cristobalite simulated as a cluster of disilicic acid in H_2O. Dissolution proceeds via Q^2 to Q^1 transformation.
138 (64)	β cristobalite simulated as a cluster of disilicic acid in H_2O. Dissolution proceeds via Q^3 to Q^2 transformation.
205 (64)	β cristobalite simulated as a cluster of disilicic acid in H_2O. Dissolution proceeds via Q^4 to Q^3 transformation.
142 (68)	Cluster of disiloxane in H_3O^+. Dissolution proceeded via Q^1 to Q^0 transformation
115-125 (63)	Cluster of $Si_4O_3(OH)_{10}$ and H_3O^+. Dissolution proceeded via Q^3 to Q^2 transformation.
152-157 (69)	Protonated, deprotonated and neutral silica clusters in H_2O. Dissolution proceeds via Q^1 to Q^0 transformation.
82 (58)	Quartz simulated as $Si_4O_6(OH)_4$ in NaOH. Dissolution proceeds via Q^3 to Q^1 transformation.
41.8 ± 17.0 (69)	Amorphous silica in H_2O. Dissolution proceeds via Q^4 to Q^3 transformation
59 ± 12.1 (69)	Amorphous silica in H_2O. Dissolution proceeds via Q^3 to Q^2 transformation
58.6 ± 10.5 (69)	Amorphous silica in H_2O. Dissolution proceeds via Q^2 to Q^1 transformation
52.7 ± 3.8 (69)	Amorphous silica in H_2O. Dissolution proceeds via Q^1 to Q^0 transformation.
54 ± 7.0 (69)	Q^4 to $Q^{0.}$ Average value calculated from activation energies of individual transformations from Q^4 to Q^3 to Q^2 to Q^1 by the same author.
138.9 (70)	Quartz simulated as a cluster of $Si_6O_{16}H_8$ in H_2O and Mg^{2+}. Dissolution proceeds via Q3 to Q^2 transformation.
156.4 (70)	Quartz simulated as a cluster of $Si_6O_{16}H_8$ in H_2O and Ca^{2+}. Dissolution proceeds via Q3 to Q^2 transformation.

Table 2.3 Experimental activation energies of SiO_2 dissolution

Activation energy (kJ mol^{-1})	Summary
46.0 [60]	Quartz in water from 25 °C to 60 °C and pH of 7.5
67.4 – 76.6 [71]	Quartz in water from 25 °C to 300 °C
68.7 [72]	α-cristobalite in water from 25 °C to 300 °C
65 [72]	β-cristobalite in water from 25 °C to 300 °C
71.3 ± 8.7 [64]	Quartz in water from 100 to 300 °C
72 [73, 74]	Quartz in water from 175 to 295 °C
72.8 [75]	Quartz in dilute aqueous organic acids between 25 to 70 °C
87 – 94 [76]	α-cristobalite in 1 M NaOH between 80 °C and 130 °C
89 [71]	Quartz in water from 25 to 625 °C

Four important points to note from the computational and experimental activation energy values are:

a) The computational activation energies of crystalline silica dissolution shown in Table 2.2 are predominantly larger than the experimentally determined energies shown in Table 2.3. According to Pelmenschikov (64) this can be attributed to the fact that the experimental activation energies measure Q^1 to Q^0 transformation, i.e. the final siloxane bond cleavage which is systematically lower than higher order transformations, i.e. Q^4 to Q^3 or Q^3 to Q^2 under identical initial conditions.

b) For crystalline silica phases there, is a reduction in the computational activation energy as the connectedness of the silica atom decreases continuously from 205 kJ mol^{-1} to 138 kJ mol^{-1} to 92 kJ mol^{-1} to 75 kJ mol^{-1} for Q^4 to Q^3, Q^3 to Q^2, Q^2 to Q^1 and Q^1 to Q^0 transformations respectively (64, 67).

c) The computational activation energy for the amorphous phases do not seem to show any trend with the degree of connectedness of the Si atom as indicated by Kagan et al. (69) and Walsh et al. (66). The former found that the activation energy for the initial Q^4 to Q^3 transformation was 41.8 kJ mol^{-1} which increased to 59 kJ mol^{-1} for Q^3 to Q^2, slightly decreased to 58.6 kJ mol^{-1} for Q^2 to Q^1 and decreased again for the final Q^1 to Q^0 transformation (69). Walsh et al. found that the activation energy for Q^1 to Q^0 (122.6 kJ mol^{-1}) transformation was actually higher than Q^2 to Q^1 (116.8 $kJmol^{-1}$).

d) The inclusion of metal cations in the computational calculations has a significant effect on the activation energy as can be seen by the addition of Mg^{2+} calculated by Wallace et al. (70) which had an activation energy of 156.4 kJ mol^{-1}, which is 13% higher than the identical transformation of Q^3 to Q^2 as calculated by Pelmenschikov et al. (64) which had an activation energy of 138 kJ mol^{-1}.

Going back to Figure 2.17, an increase or decrease in the pH from 7 leads to an increase in the solubility limit of $Si(OH)_4$ in solution. This increase is more pronounced at a higher pH for two reasons. Firstly, as the pH of the solution increases, the larger concentration of hydroxyl groups in solution will lead to an increase in the depolymerisation rate of the silica structure producing monosilicic acid in the process until its equilibrium concentration is reached. Because of the lower activation energy of silica dissolution in the presence of OH^- (79.1 kJ mol^{-1} according to Xiao and Lasaga (52)), more collisions between OH^-

and Si will have sufficient energy required to surmount the activation energy barrier relative to the depolymerisation process in H_3O^+ (100.4 kJ mol^{-1}). Polycondensation of the monomer to form dimers will increase causing a decrease in monomer concentration. The equilibrium (in equation 2.9) will shift to the right to produce more $Si(OH)_4$ counteracting the reduction in $Si(OH)_4$ concentration as a result of the polycondensation reaction. The formation of higher order oligomers beyond the dimer will continuously reduce the concentration of $Si(OH)_4$ in solution causing even more SiO_2 to be dissolved so that equilibrium between the silicate species can be maintained (50, 53, 57).

Secondly, silica has a zero surface charge at a pH of approximately 2, i.e. there are equal amount of positive and negative charges on the silica surface at this pH (50). As the pH is increased, the surface silanol groups (≡Si-OH) are deprotonated creating a negatively charged surface (≡Si-O^-) (50). Allen et al. (77) conducted titration of suspended amorphous silica and confirmed the presence of predominantly ≡Si-O^- on the silica surface above a pH of 12. Cationic adsorption is favoured at a higher pH because of electrostatic interactions (50, 53). Cationic adsorption onto the negatively charged surface creates an electrically neutral silica surface. There is also an increase in Si-O bond lengths from 165 pm to 175 pm as a result of Na adsorption (58). The elongation of Si-O bond distances is a prerequisite for silixoane bond cleavage, similar to the elongation that arises as a result of the formation the five-fold coordinated silicon shown in Figure 2.20. In the case of Na adsorption, Si-O bond lengths were

elongated by 6% compared with 4.9% elongation during the formation of a five-fold coordinated Si (52, 58).

2.5.2.2 Silica polymorph and temperature effects

Amorphous silica in neutral pH has an equilibrium concentration of silica in solution (existing as silicic acid – $Si(OH)_4$) of 70-150 ppm whereas for crystalline silica (quartz), the concentration of silica in solution is 6 ppm, which is an order of magnitude smaller (50). The experimental and computational activation energies shown in Tables 2.4 and 2.5 also show that the activation energy of amorphous silica dissolution in water is consistently lower than its crystalline equivalent.

Glasser (6) attributed this to the ease of accessibility of the H_2O or OH^- molecule (in the case of dissolution at a higher pH) into the tetrahedral silica framework. Attack on a well crystallised framework takes place mainly at the surface where mainly Q^3 Si sites are present. These have been shown to have larger activation energies relative to the more strained Q^2 and Q^1 sites which are more reactive and more prevalent on the surface of an amorphous silica particle (74).

Figure 2.21 shows the solubility of various silica polymorphs as a function of temperature at 1 bar. Solubilities were calculated from dissociation constant values provided by Sjoberg (53). At 25 ^oC, α-cristobalite has a solubility limit that is larger than quartz by a factor of approximately 3.5. This is reduced to 2.6 at

100 °C. The explanation for this is not given but may be due to slight differences in bond angles and length of the two crystalline polymorphs which will have an effect on the activation energy of siloxane bond cleavage. Also, the solubility limit is proportional to the temperature. This is expected as higher temperatures equate to higher molecular energies for effective collisions between H_2O or OH^- and SiO_2 molecules thereby increasing the probability of siloxane bond cleavage (76).

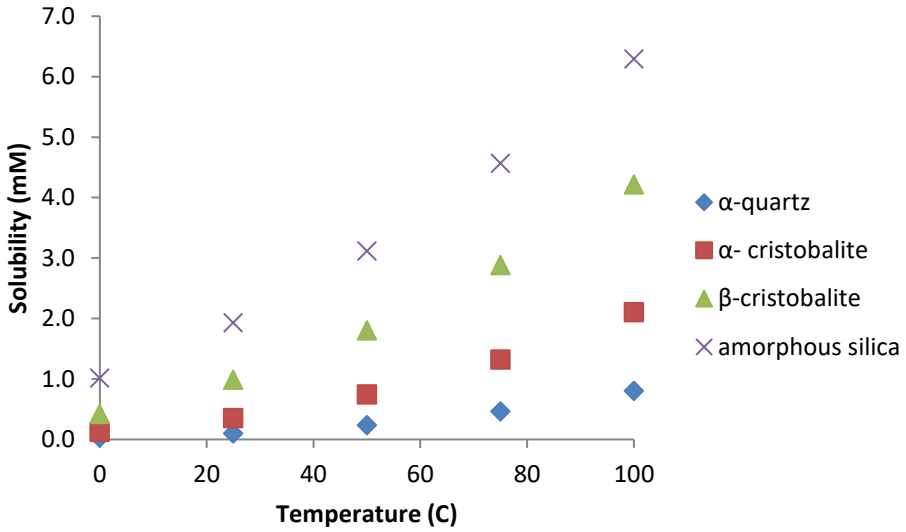

Figure 2.21 Solubility of various silica polymorphs in water as a function of the temperature (53)

2.5.2.3 Metal cation effect

In the cristobalite crystal, the Si–O distance is 159 pm and the Si–O–Si bond angle is 150° (55). As previously mentioned, cristobalite consists of a 3-dimensional framework of $(SiO_4)^{4-}$ units. At the surface, both silicon and oxygen atoms can be present. It was hypothesised by Papirer (48) that oxygen will

preferentially protrude out of the surface because of its lower charge and higher polarizability.

In a low pH or neutral environment, the negatively charged oxygen atoms protruding from the silica surface will be neutralised via adsorption of protons forming silanol groups (48, 53).

$$\equiv Si\text{–}O^{-} + H + \leftrightarrows \equiv Si\text{–}OH \qquad (2.13)$$

Equation 2.13 (53) shows a single proton adsorbing unto the negatively charged oxygen atom. This is known as a single silanol group. If two protons adsorb unto the surface oxygen, a geminal silanol is formed as shown in equation 2.14 (53).

$$\equiv Si\text{–}OH + H^{+} \leftrightarrows \equiv Si\text{–}OH_2{}^{+} \qquad (2.14)$$

The protonation constants of the single and geminal silanol groups were found to be 9.7 and -4.61 respectively. This means that ≡Si–OH is quite stable between pH 2 – pH 7 whereas ≡Si–OH_2 forms only in highly acidic media < pH 1(48, 53, 77).

At a pH above 7, the excess hydroxide ions deprotonate the surface silanol groups leaving the surface negatively charged (48, 53).

$$\equiv Si\text{–}OH + OH- \leftrightarrows \equiv Si\text{–}O^{-} + H_2O \qquad (2.15)$$

Allen et al. (77) reported that above a pH of 12, the entire silica surface consists of ≡Si-O^{-} sites. Brady and Walter (60) found that the dissolution rates of quartz were proportional to [≡Si-O^{-}]. Cations adsorb unto the negatively charged sites via electrostatic interactions and this has been reported to have a very significant effect on the subsequent dissolution process.

Dove and Crerar (61) determined that quartz dissolution rate in near neutral pH solutions in the presence of 0.05 molal NaCl or KCl was enhanced by a factor of 33 relative to the dissolution rate in deionised water. Even at a higher pH, Na^+ was found to still enhance the dissolution rate.

Tamada et al. (58) attributes this rate increase to the elongation of the Si-O bonds during cation adsorption which reduces the activation energy of siloxane cleavage. The problem with the explanation put forward by Tamada et al. (58) for the rate increase is that in his model, adsorption of Na^+ is assumed to occur on the bridging oxygen. This may be possible in amorphous silica however, in the well-ordered structure of cristobalite and quartz, accessibility of Na^+ to the bridging oxygen will be difficult and the doubly-coordinated bridging oxygen has a protonation constant at -16.9; significantly lower than the geminal silanol groups (48, 53).

Another mechanism proposed by Dove et al. (61, 74) is that the adsorbed cations (Na^+ and K^+) passively enhance dissolution rate by promoting the frequency of successful siloxane cleavage and not altering the mechanism via a reduction in activation energy.

Equation 2.16 shows the Arrhenius equation used to describe the dissolution rate of a reaction as a function of its various dependencies:

$$K = Ae^{-\frac{E_a}{RT}} \tag{2.16}$$

where E_a is the activation energy, R is the molar gas constant, T is the absolute temperature and A is the pre-exponential constant. According to Dove and Crerar (61) the activation energy of quartz dissolution is 71.3 kJ mol^{-1} in deionised water,

71.2 kJ mol^{-1} in NaCl and 71.5 kJ mol^{-1} in KCl which are all identical. The reason for the 33-fold rate increase in the solutions containing these ions was therefore attributed to an increase in reaction frequency through the pre-exponential term (A) in the Arrhenius equation.

In a heterogeneous reaction, the process occurring at the surface is not a one-step reaction and the morphology of the solid is constantly modified. This changes the mechanism of the reaction as the degree of conversion increases. This complex behaviour is described by the isoconversion model. The activation energy will change as a function of the degree of conversion (76).

Other cations have been shown to retard or completely prevent silica dissolution, even at a high pH. At a near neutral pH, the rate enhancing trend increases in the order (78):

$$Mg^{2+} < Ca^{2+} \approx Li^{+} \approx Na^{+} \approx K^{+} < Ba^{2+}$$

Some aluminium and lithium compounds have also been reported to retard silica dissolution at pH > 12.5 (79-82). This retardation is not polymorph specific as it was reported for both amorphous and crystalline (quartz) phases.

2.5.3 Metal Cation Effects

Structural engineers sometimes encounter cracking in concrete. This is caused by alkali silica reaction (ASR). The alkaline environment leads to OH^{-} attacking

any reactive aggregates (silica) in the concrete paste. This creates a gel which swells as it absorbs water. The pressure build up within the brittle concrete matrix then leads to cracking. LiOH, LiCl, $LiNO_3$ and $AL(OH)_3$ have all been shown to reduce ASR. There three main theories as to why the cations in these compounds retard the reaction (80).

a) Formation of insoluble Si-Li or Si-Al products on the silica surface which acts as a barrier against further OH^- attack (79, 80). Figure 2.22 shows the formation of Li_2SiO_3 on rhyolite (65 % SiO_2) in 1 M NaOH with 0.74 M $LiNO_3$

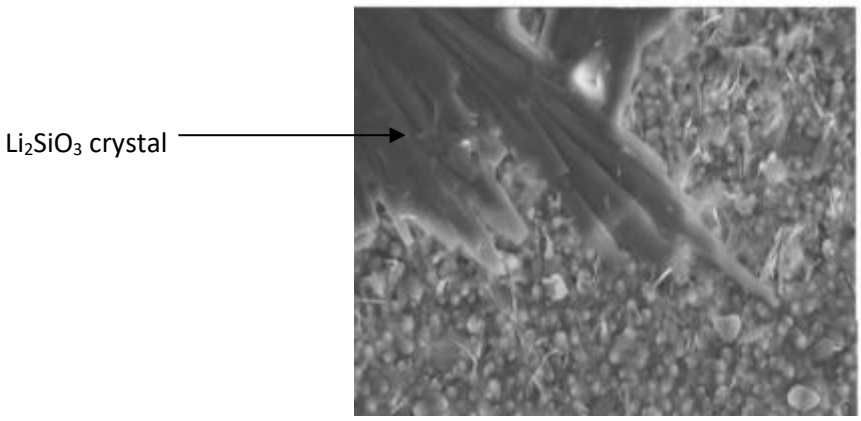

Figure 2.22 $LiSiO_3$ crystals forming on rhyolite (79)

b) Increased stability of the silica surface as a result of cation adsorption (79, 83)
c) Formation of a less expansive gel (79, 81). Li^+ tend to form less polymerised silica gels which diminishes its water absorbing properties

From Table 2.1, it can be seen that the ions with the larger hydrated radii and charge densities are the same ions which have been shown to retard the silica

dissolution process. Another possibility proposed by Dove (74) is that the water of hydration associated with the monovalent cations can re-orient themselves into more constructive positions thereby ensuring hydroxyl formation at the silica surface which subsequently attack the Si atom. The divalent and trivalent cations (group IIA and IIIA) have a stronger hold on the water molecules, i.e. more negative hydration free energies thus limiting re-orientation of the water molecules into more favourable positions.

2.6 Rheology and the Nature of Silicates in Solution

The viscosity of silicate solutions at constant temperature is dependent on three factors (84, 85):

a) Nature of the stabilising metal cation
b) SiO_2 weight %
c) SiO_2:M_2O molar ratio (where M is the metal cation).

Figure 2.23 shows the silicate viscosity as a function of the SiO_2:M_2O molar ratio for both sodium and potassium silicate solutions at constant SiO_2 wt%

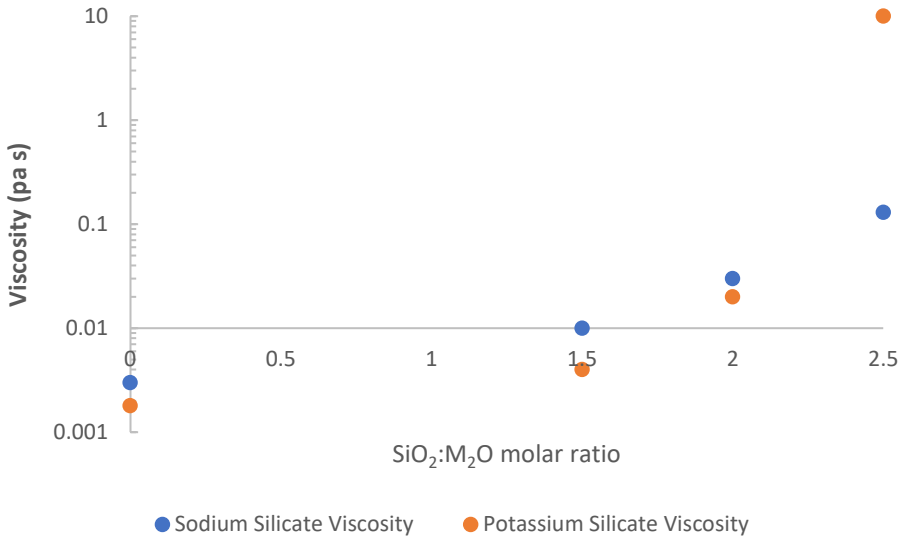

Figure 2.23 Viscosity of sodium and potassium silicates as a function of SiO_2:M_2O molar ratio at 20 wt.% SiO_2

Adapted from Weldes and Lange (84) and Sipos (45)

At higher SiO_2:M_2O ratios, potassium silicates are significantly more viscous than sodium silicates. One explanation for this is the influence of the hydrated metal cation. Weldes and Lange (84) found that lithium silicates have a stable and low viscosity even at very high SiO_2:Li_2O molar ratio of 8:1. This was attributed to the large hydrated lithium cation – $[Li(H_2O)_n]^+$ which stabilises the silicates. This is in agreement with NMR studies carried out by Leeman et al. (81) and Mitchell and Grattan (86) who reported that the introduction of Li^+ ions into the ASR gel led to structural transformations from mainly branched Q^3 site to more linear Q^2 and Q^1 sites. Wijnen (87) performed ^{29}Si-NMR on equimolar solutions of lithium, sodium, potassium, rubidium and caesium silicates at a SiO_2:M_2O = 1:1. The NMR spectra are shown in Figure 2.24.

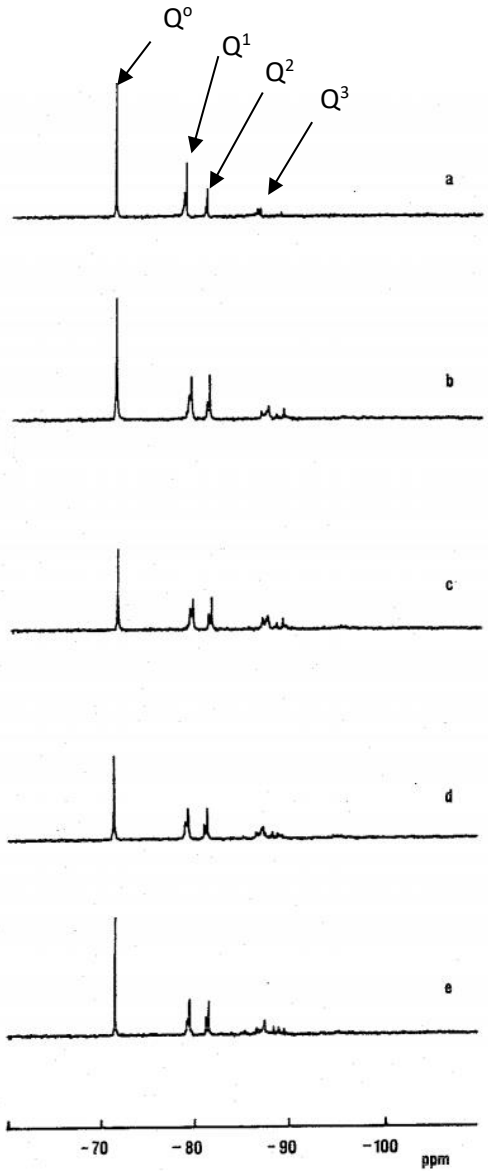

Figure 2.24 ^{29}Si-NMR spectra of silicates stabilised by a) Li^+ b) Na^+ c) K^+ d) Rb^+ and e) Cs^+ (87)

From Li^+ to K^+, there is a constant decrease in Q^o concentration accompanied with an increase in Q^3 concentration whereas from K^+ to Cs^+, there is an increase in Q^0 accompanied by a slight decrease in Q^3. This trend matches the hydration radii trend shown in Figure 2.13 where K^+ has the smallest hydrated radii of the Group IA cations considered.

Yang et al. (85) described the rheological properties of silicates and found that they display dual properties of both suspensions and polymers depending on the SiO_2:M_2O molar ratio and SiO_2 wt%. In the low shear regime, up to 10 s^{-1}, it was reported that sodium silicates display Newtonian behaviour whereas at higher shear rates, shear thickening was reported (85).

2.7 Reaction Controls

The ceramic core leaching process is a heterogeneous fluid-solid reaction. Such reactions experience different resistances which inhibit the reaction. The largest resistance experienced by the reacting species is known as the rate controlling step since the reaction rate is in essence, largely controlled by that step. According to Levenspiel (88), there are three main rate controlling steps for such reactions:

a) Diffusion through fluid film controlled
b) Diffusion through ash layer controlled
c) Chemical kinetics controlled

Table 2.4 summarises the equations for the different rate controlling mechanisms.

Table 2.4 Theoretical models for diffusion and chemical reaction controls (89)

Control mechanism	Summary	Equation	Equation number
Diffusion control	One-dimensional	$kt = \alpha$	2.17
	Two-dimensional	$kt = (1-\alpha)\ln(1-\alpha) + \alpha$	2.18
	Three-dimensional	$kt = \left[1-(1-\alpha)^{1/3}\right]^2$	2.19
	Ginstling-Brounshtein	$kt = \left(1-\frac{2\alpha}{3}\right) - (1-\alpha)^{2/3}$	2.20
	Kröger & Ziegler	$\ln t = \left[1-(1-\alpha)^{1/3}\right]^2$	2.21
	Small shrinking spherical particle	$kt = \frac{t}{\tau} = 1-(1-\alpha)^{2/3}$	2.22
	Large shrinking spherical particle	$kt = 1-(1-\alpha)^{1/2}$	2.23
Chemical reaction control	Zero order	$kt = \alpha$	2.24
	First order	$kt = (1-\alpha)^{1/3}$	2.25
	Second order	$kt = (1-\alpha)^{-1}$	2.26
	Avrami-Erofeev	$kt = [-\ln(1-\alpha)]^n$ where n = 0.25 – 0.75	2.27
	Interface (contracting area)	$kt = 1-(1-\alpha)^{1/2}$	2.28
	Interface (contracting volume)	$kt = 1-(1-\alpha)^{1/3}$	2.29
	Exponential	$kt = \ln \alpha$	2.30
	Prout-Tompkins	$kt = \ln\left(\frac{\alpha}{1-\alpha}\right)$	2.31

2.8 Physics of core removal

Two different variations of the core removal process are used across industry; an open bath process and a closed process. One important safety advantage of the closed system over an open vessel is the containment of chemicals during the leaching process. Another advantage of the closed system is the ability to pressurise the alkaline leaching solution above its boiling point which increases the maximum operating temperature of the process (20). The leaching autoclave manufactured by LBBC technologies operates on a pressure swing system as shown in Figure 2.25. independently controlled by the operator.

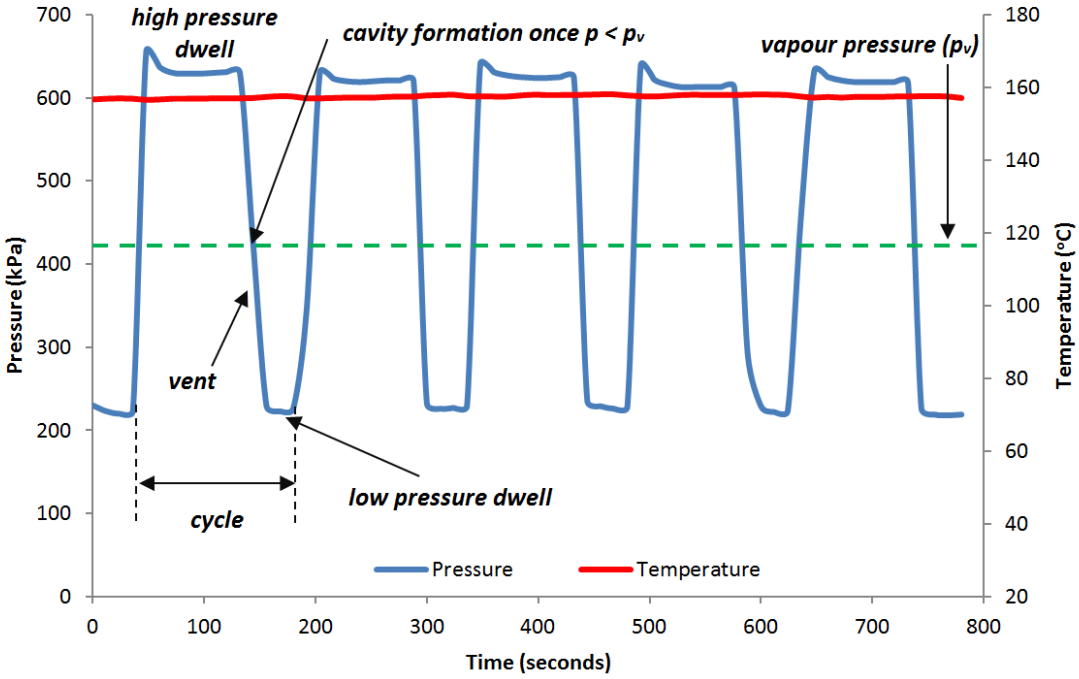

Figure 2.25 Typical LBBC Autoclave pressure-swing cycle (20)

Once the pressure drops below the vapour pressure line (P_v), cavities form in the fluid. Boiling and cavitation can both be defined as the tensile force created in a liquid causing rupture and creating of vapour bubbles (20). The difference between the two processes is the preceding method via which the subsequent tensile force was created.

Boiling is initiated by addition of heat which causes the temperature and vapour pressure of the liquid to increase until it exceeds the ambient pressure whereas cavitation is caused by a drop in the ambient pressure below the vapour pressure at constant temperature (90). This is illustrated in Figure 2.26.

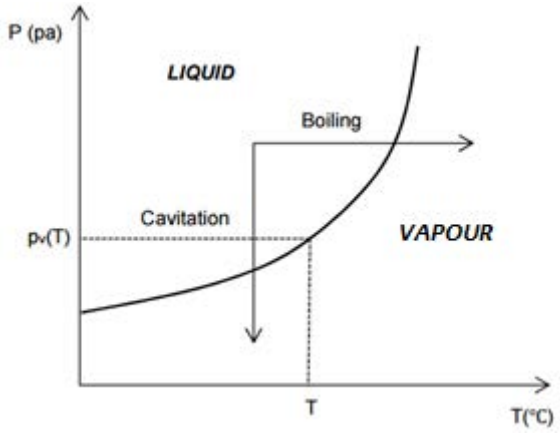

Figure 2.26 Mechanism of phase change in boiling and cavitation (90)

From Figures 2.25 and 2.26, it can be seen that the pressure swing cycle is technically a cavitation process since vapour bubble formation is induced by a drop in autoclave pressure. However, it may not be useful to call it cavitation because it is unlikely that the subsequent bubble collapse process occurs during the pressure recovery phase of the cycle.

Cavities form once the ambient pressure equals the vapour pressure (91) i.e.:

$$P_{external} = P_{internal} \quad (2.32)$$

$$P_A = P_V + P_G \quad (2.33)$$

where P_A is the ambient pressure, P_V is the vapour pressure and P_G is the gas pressure.

Cavities form because of the presence of nuclei in the liquid. These nuclei are created by weak spots in the liquid which reduce the tensile stresses required for the liquid to rupture once the ambient pressure drops below the vapour pressure. Typical sources of nuclei are microbubbles of air, solid impurities and trapped

pockets of air on a solid surface (91). The gas pressure (P_G) arises from entrapped air bubbles in the liquid.

Once the ambient pressure drops below the vapour pressure, the internal cavity pressure ($P_{internal}$) starts to exceed the external ambient pressure and the cavity grows. The liquid in direct contact with the vapour and gas within the cavity now experiences an additional tensile force because of the difference in cohesive forces between the liquid molecules and the adhesive force between the liquid and the vapour, i.e. surface tension. This is illustrated in Figure 2.27.

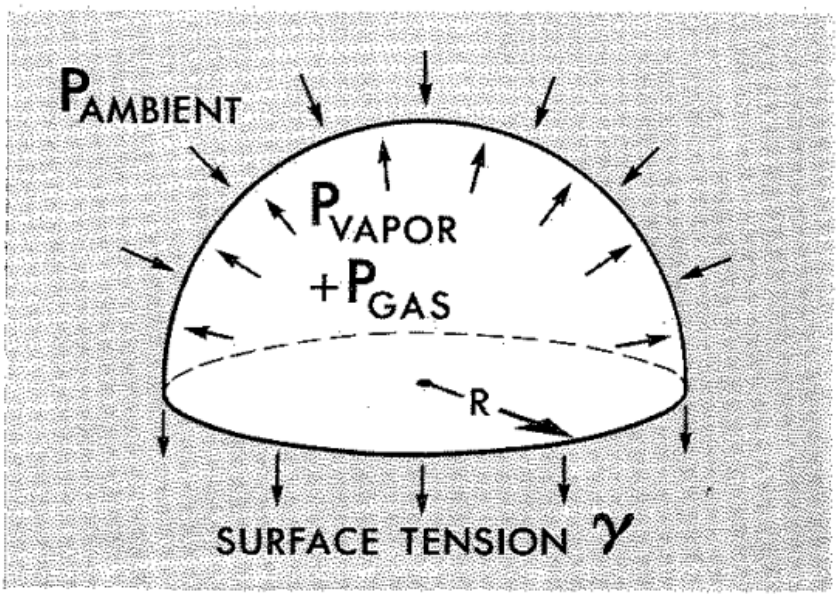

Figure 2.27 Forces acting on a growing cavity (91)

From Figure 2.27, it can be assumed that equation 2.33 is a slight oversimplification of the forces present during cavitation inception because it does not consider the effects of surface tension and this is quite important in

understanding what is happening in the fluid film layer during the vent phase of the pressure cycle. Accounting for surface tension effects, equation 2.33 is modified to (91):

$$P_A + \frac{2\gamma}{R} = P_V + P_G \tag{2.34}$$

$$P_{ci} = P_V - \frac{4\gamma}{3R} \tag{2.35}$$

where γ is the surface tension, R is the cavity radius and P_{ci} is the critical inception pressure.

For vapour cavities to form, the ambient pressure needs to drop below the vapour pressure by an additional $\frac{4\gamma}{3R}$. From Figure 2.27, it can be seen that during the vent phase, the ambient pressure drops significantly below the vapour pressure thus ensuring a wide margin of safety for cavitation inception to occur.

2.9 Conclusion

While the chemistry of silica dissolution and the role of different metal cations has been well covered in the literature, much of the research is focused on one particular part of the process. This thesis focuses on a broader picture to understand the process and gain insights that can be used to enhance its industrial application. Literature on the physics of core removal does not explicitly exist because it involves a combination of different physical processes.

3 EXPERIMENTAL METHODS

This chapter describes the various methods used in understanding the dissolution of silica in concentrated alkaline solutions. These experiments were carried out at the University of Birmingham, Rolls-Royce facilities in Rotherham and Bristol and LBBC Technologies in Leeds.

Experiments on understanding the chemistry and physics of the core removal process were performed on three orders of complexity. The first simply considered the dissolution of cristobalite powder on a laboratory scale with a simple reflux set-up. This was done to understand the chemistry of the dissolution process.

The second set of experiments involved leaching simple rectangular prism of ceramic core which had been cast within an equiaxed Nickel superalloy. The core material used in these test was the V formulation used for cores in several Rolls-Royce high pressure turbine blade geometries. Since core leaching is one of the final steps in the investment casting process, making these parts involved going through the entire investment casting process. These parts were leached in a 30 L pilot scale autoclave manufactured by LBBC Technologies. The autoclave operates on a pressure swing cycle and the objective of these experiments was to understand what happens at the leach front during the different stages of the pressure swing for a simple geometry. These trials were also used to determine optimal part orientation during leaching, i.e. in which orientation should the core opening face in the autoclave for maximum core removal.

The final set of experiments focused on understanding the leaching process for actual core geometries; these are complex, multi-pass, serpentine geometries with elliptical and airfoil cross-sections.

3.1 Cristobalite Powder Properties

Cristobalite M006, M3000 and M6000 obtained from Sibelco (Antwerp, Belgium) was reacted with equimolar solutions of NaOH and KOH solutions at 0.5 M, 1 M, 2 M, 5 M and 10 M in simple reflux set-up at 95 ^{o}C ± 2^{o}C. Table 3.1 summarises the granulometric data and physical characteristics of the cristobalite powder provided by Sibelco.

Table 3.1 Granulometric and physical properties of cristobalite powder (92)

Property	Powder name		
	M006	**M3000**	**M6000**
D10 (µm)	5	4.5	1.5
D50 (µm)	40	17	4
D90 (µm)	100	40	8
Density (kg m^{-3})	2350	2350	2350
Bulk density (kg m^{-3})	900	700	420
BET surface area (m^2 kg^{-1})	700	1500	5000

D10, D50 and D90 values were measured using a Malvern MS 2000 particle size analyser (Malvern instruments, Malvern, UK). Three powders with different particle size distributions and surface areas were used to understand the

relationship between the surfaced area of the particle exposed to the alkaline solution and the dissolution rate.

In all the dissolution experiments discussed in this Chapter, cristobalite M006 was used unless stated otherwise.

3.2 Cristobalite Dissolution

Cristobalite dissolution was carried out at 95 ^{o}C in a reflux set up as shown in Figure 3.1.

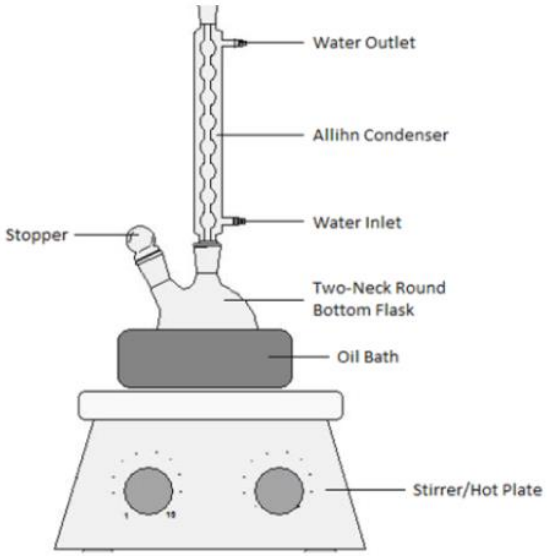

Figure 3.1 Laboratory set-up for cristobalite dissolution experiments

LiOH, NaOH, KOH and CsOH pellets obtained from Sigma-Aldrich (Gillingham, UK) were used to make hydroxide solutions by mixing the alkali metal hydroxides pellets with deionised water. Concentrations of 0.5 M, 1 M, 2 M, 5 M and 10 M were prepared for NaOH and KOH to determine the effect of OH^- concentration on the dissolution rate. 5 M concentrations of LiOH and CsOH were also prepared

using deionised water to understand the role of Group IA metal cations on the dissolution process.

For each experiment, 10 g of cristobalite was reacted with 100 mL of MOH at the molar concentrations stated above. A 20 mm magnetic stirrer obtained from Sigma-Aldrich operating at 300 rpm was used to agitate the mixture and prevent settling of the fine cristobalite powder. The experiments were run for 6 hours at each concentration.

The 150 mL round bottom flask was made of borosilicate glass which is relatively inert. However, after several dissolution experiments, it was observed that the vessel began to etch as a result of repeated exposure to highly alkaline solutions at 95 ^{o}C. The rate of etching was observed to increase rapidly once the initial etch marks appeared; probably due to increased surface area available for the OH^- to attack as the degree of etching increased. To prevent contamination of the reactants with an external source of silicates from the borosilicate glass vessel, replacements were made after three sets of 6 hour dissolution experiments. No etch marks were visible after the elapsed time so it could be safely assumed that minimal contamination from the borosilicate glass vessel occurred. No dissolved silica was observed when running a 5 M NaOH solution without cristobalite for 6 hours using the titrimetric method.

The dissolution of silica in alkali solutions at high pH leads to the formation of soluble silicates. The measurement of silicates in solution was carried out using titrimetric analysis in the presence of methyl red indicator and analysis grade

sodium fluoride (99% NaF) obtained from Sigma-Aldrich. The titrimetric method described is adapted from a method outlined in the Treatise of Analytical Chemistry (93).

The detailed step by step procedure for the measurement of silicates in solution and validation of the method is as follows:

3.2.1 Extracting Aliquots

- At 5 minutes to the hour, the magnetic stirrer was stopped allowing the undissolved cristobalite to settle out
- Three 1 g aliquots were extracted. This was done every hour for the first 6 hours

3.2.2 Determining M_2O content

M represents the alkali component of the silicate where M is the metal cation stabilising the silicate anions and could be Li^+, Na^+, K^+ or Cs^+ depending on which alkali metal hydroxide was used.

- Each 1 g aliquot was transferred into a 50 mL conical flask
- 5 drops of methyl red indicator (Sigma-Aldrich) in 1% ethanol to accentuate the colour change was added to the sample. The solution changed from colourless to clear yellow
- 1 M HCl was prepared from a 37 wt.% stock solution obtained from Sigma-Aldrich. This was titrated against the silicate aliquot. Once the equivalence point was reached, the solution turned red instantaneously, indicating a sharp end point. The silicate solution consists of a mixture of monomer, dimer, trimer

and even tetramer silicates. As HCl is added to the mixture, the pH of the solution starts to decrease and these higher order silicate oligomers were depolymerised forming monomeric silicates. These become fully protonated as more acid is added. Once the pH falls below 8, the silicates exist primarily as $Si(OH)_4$. The reaction is shown as follows:

$$H_2SiO_4^{2-} + 2H^+ \rightarrow Si(OH)_4 \quad (3.1)$$

or

$$H_3SiO_4^- + H^+ \rightarrow Si(OH)_4 \quad (3.2)$$

- The H^+ ions displace the metal cation (M^+) adsorbed unto the silicate anions. The amount of H^+ required for this is proportional to the M content. This is calculated as:

$$M_2O \text{ wt.}\% = \frac{T_1 \text{ x } M_r \text{ x } C_{HCl}}{10 \text{ x M x } 2} \quad (3.3)$$

- Where T_1 is the HCl titre volume (L), M_r is the relative molecular mass of M_2O (g mol^{-1}), C_{HCl} is the molar concentration of HCl (mol L^{-1}) and M is the sample mass (g)

3.2.3 Determining SiO_2 content

- After the first equivalence point was reached, 5 g of analytical grade NaF (99%) obtained from Alfa Aesar (Lancashire, UK) was added to the solution. This turned the solution cloudy yellow.

- NaF undergoes hydrolysis forming Na^+ and F^- in solution. The F^- ions displaced the OH^- from $Si(OH)_4$ as follows:

$$Si(OH)_4 + 6F^- \rightarrow (SiF_6)^{2-} + 4OH^- \quad (3.4)$$

- Silicon exists in six-fold coordination as $(SiF_6)^{2-}$ liberating OH^-. This is why the solution became yellow again after the addition of NaF. The amount of OH^- liberated is proportional to the amount of $Si(OH)_4$ present which, in turn, is the amount of silica in solution.
- 1 M HCl was added to the solution again to neutralise the liberated OH^-. However, the colour change from yellow to red was not as sharp as before. This was probably because of the buffering capacity of the $(SiF_6)^{2-}$. 1 M HCl was continually added while the solution was vigorously stirred using a magnetic stirrer and swirling action simultaneously until the colour was reasonably stable. The reaction is:

$$4OH^- + 4H^+ \rightarrow 4H_2O \quad (3.5)$$

- The overall reaction is:

$$Si(OH)_4 + 6F^- + 4H^+ \rightarrow (SiF_6)^{2-} + 4H_2O \quad (3.6)$$

- The colour change sequence observed for the two part titration in the presence of methyl red indicator is summarised in Figure 3.2

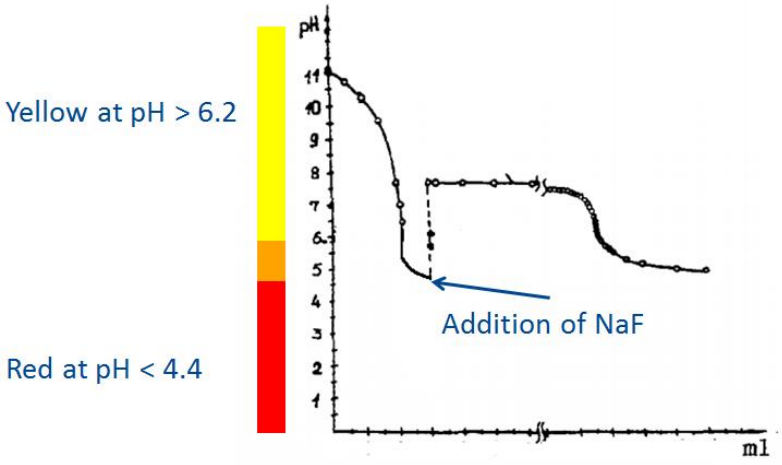

Figure 3.2 pH curve of two-part titrimetric analysis of silicates (94)

SiO_2 wt.% is given by:

$$SiO_2 \text{ wt.}\% = \frac{(T_1 - B) \text{ x } M_r \text{ x } C_{HCl}}{10 \text{ x } M_S \text{ x } 2} \quad (3.7)$$

where T_1 is the HCl titre volume (L), B is the NaF blank volume (L) and M_r is the relative molecular mass of SiO_2 (g mol^{-1}).

3.2.4 Titration Blanks

Before analysing each sample, titration blanks were carried out by titrating a known concentration of titrant – 1 M HCl into a solvent in the absence of the analyte (silicate solution). This was done to determine if hydrolysis of NaF would change the pH of the solution.

- 5 g of NaF was mixed with 20 mL deionised water in the presence of methyl red indicator. A cloudy yellow solution was formed

- 1 M HCl was titrated against this solution. A sharp colour change from yellow to red was observed after 0.2 mL of acid was added

  NaF gives a slight alkaline reaction through hydrolysis, as:

$$NaF \rightarrow Na^{+} + F^{-} \quad (3.8)$$

$$F^{-} + H_2O \leftrightarrow HF + OH^{-} \quad (3.9)$$

- A correction of 0.2 mL was made for every titration to account for the slight alkalinity produced during NaF hydrolysis. This is the same correction suggested by Banks et al. (93)

3.2.5 Validation of the Titrimetric Method using Standard Silicate Solutions

To ensure that the titrimetric method of determining %M and %Si content was accurate and precise, standard sodium silicate solutions from Sigma-Aldrich and Mistral (Antrim, UK) which both had different SiO_2 wt.% and SiO_2:M_2O molar ratios and anhydrous potassium silicate powder from Alfa Aesar were used as benchmarks.

- Five 1 g aliquots of each sodium silicate solution were analysed using the method described from Section 3.3.2 and 3.3.3 to determine the SiO_2 wt.% and SiO_2:M_2O molar ratio
- The potassium silicate powder was mixed with water at 80 ^{o}C to determine the SiO_2:K_2O molar ratio of the powder. Because the potassium silicate powder was very siliceous, (SiO_2:K_2O = 3.9 molar ratio) it could not be

dissolved in the water. The potassium silicate powder was then dissolved in a 0.5 M KOH solution which reduced the SiO_2:K_2O molar ratio to 3.7

Tables 3.2 and 3.3 show the accuracy and precision of the titrimetric method.

Table 3.2 Precision and accuracy of the titrimetric method for measuring sodium silicates in solution

Supplier name	Actual SiO_2 wt%	Experimental SiO_2 wt%	Actual SiO_2:Na_2O molar ratio	Experimental SiO_2:Na_2O molar ratio
Sigma Aldrich	26.5	26.6 ± 0.3	2.6	2.50 ± 0.03
Mistral	28.0	27.9 ± 0.5	3.27	3.30 ± 0.06

Table 3.3 Precision and accuracy of the titrimetric method for measuring potassium silicates in solution

Supplier name	Actual SiO_2 wt%	Experimental SiO_2 wt%	Actual SiO_2:K_2O molar ratio	Experimental SiO_2:K_2O molar ratio
Alfa Aesar	-	-	3.9	3.70 ± 0.06

The actual values SiO_2 wt.% and SiO_2:M_2O shown in Tables 3.2 and 3.3 are sourced from the supplier MSDS. Also, the uncertainty in the experimental molar ratios are calculated as standard deviations.

The titrimetric method is accurate and precise. For the sodium silicate solution, the experimentally determined SiO_2 wt. % falls within the same range as the actual SiO_2 wt. % stated by the manufacturer. The experimental SiO_2:Na_2O molar ratio is 97% accurate.

The measurement accuracy in the potassium silicate solution comparing the experimental and actual SiO_2:K_2O molar ratios was 95% accurate. This was lower than the accuracy observed in the sodium silicate solution because it was not reagent grade potassium silicate.

The low standard deviation measured for five samples shows the titrimetric method is also precise.

3.2.6 Activation Energy

The activation energy of cristobalite dissolution and the temperature dependency of the rate constant were determined by repeating the experiments outlined in Section 3.2 at different temperatures. The dissolution experiment was carried out in 5 M NaOH and 5M KOH solutions at 50 ^oC, 70 ^oC and 105 ^oC. The relationship between the activation energy (E_a) and the rate constant (k) is:

$$k = Ae^{-\frac{E_a}{RT}} \tag{3.10}$$

A graph of ln k against 1/T gives a straight line with a gradient of $-E_a/R$. The activation energy can be found by multiplying the gradient of the straight line by the molar gas constant R (8.314 J mol^{-1} K^{-1}).

This however proved to be an inaccurate way of determining the activation energy because of the constant modification of the solid surface as the reaction proceeded. An isoconversion model was used to determine the activation energy as a function of the degree of conversion.

Equation 3.11 shows the isoconversion model (76).

$$ln(t) = \frac{E_a}{RT} + ln\left(\frac{g(\alpha)}{A}\right) \quad (3.11)$$

At a particular mole conversion, $ln\left(\frac{g(\alpha)}{A}\right)$ is constant (76) therefore the gradient of a plot of ln(t) versus 1/T gives the activation energy.

The temperature range for determining the activation energy was limited to a narrow range between 50 ^{o}C – 105 ^{o}C. Lower temperatures could not be used because of the strong dependence of cristobalite dissolution on temperature therefore the experiment would have to last for an impractically long time to reach the desired conversion. Higher temperatures were not used because external pressure would be required to heat up the solution above its boiling point.

For the activation energy experiments, cristobalite M6000 was used because of its larger surface area compared to cristobalite M006. This ensured that the desired conversions were reached in a within a few hours.

The experimental procedure is as follows:

- 100 mL of 5 M NaOH was placed in the 150 mL round bottom flask and the reflux set-up was arranged as shown in Figure 3.1
- The hot plate temperature was set at 50 ^{o}C. A thermocouple was inserted into the alkaline solution to ensure its temperature reached 50 ^{o}C

- The 20 mm magnetic stirrer was placed in the round bottom flask. The stirrer speed was set at 300 rpm
- Cristobalite M6000 was then transferred into the round bottom flask. 1 g samples were withdrawn every hour and the time taken to reach the desired conversion of 0.2, 0.4 and 0.6 were recorded
- A plot of ln(t) where t is the time taken to reach the desired conversion was plotted against 1/T at conversions of 0.2, 0.4 and 0.6. The gradient of each plot multiplied by the molar gas constant gave the activation energy at different conversions
- This was repeated at 70 ^{o}C and 105 ^{o}C using 5 M NaOH. It was also repeated at 50 ^{o}C, 70 ^{o}C and 105 ^{o}C for 5 M KOH solutions

3.3 X-ray Diffraction

X-ray diffraction (XRD) analysis was carried out on the cristobalite samples after dissolution experiments to determine if the undissolved powder present in the round bottom flask after 6 hours of dissolution was precipitated amorphous silica, undissolved cristobalite or a new reaction product.

When X-rays are scattered from successive planes in a crystal structure at a specified incidence angle, they will travel distances differing by exactly one wavelength. Reflected X-rays are produced when the wavelengths of the scattered X-rays interfere constructively. The relationship between the wavelength of the incident X-rays, angle of incidence and spacing between the

crystal lattice planes of atoms is expressed as Bragg's Law where θ is the incident ray angle, λ is the wavelength, d is the spacing between atomic layers and n is an integer, referred to as the order of diffraction (36):

$$n\lambda = 2dsin(\theta) \quad (3.11)$$

The samples were analysed on an Equinox X-ray diffractometer (Thermo Scientific, UK) with copper X-ray tube powered to 35 kV and 25 mA. The XRD patterns were analysed using Match software which contains a database of reference patterns.

3.4 Formulation of Potassium and Sodium Silicates Solutions

Sodium and potassium silicate solutions were made at three different SiO_2:M_2O molar ratios: 3:1, 2.5:1 and 2:1. Higher SiO_2:M_2O ratios are more siliceous whereas lower ratios are more alkaline. At each of these ratios, SiO_2 wt. % concentrations of 20%, 25%, 26.5%, 28% and 30% were also made. At the same SiO_2:M_2O molar ratio and SiO_2 wt. %, the sodium and potassium silicate concentrations are identical. The only differentiator between the two is the type of metal cation present. Therefore, any difference in silicate properties can be attributed to the behaviour of the metal cation.

Increasing the SiO_2:M_2O molar ratio can be achieved by increasing SiO_2 content or by reducing the Na_2O content. These can be achieved by dissolving more silica or via ion exchange processes to remove the alkali respectively. Decreasing the SiO_2:Na_2O molar ratio can be achieved by adding more alkali.

For the sodium silicate solutions, adjusting the SiO_2:Na_2O ratio was achieved by starting with the most siliceous solution i.e. the highest SiO_2:Na_2O molar ratio (obtained from Mistral which had a 3.3 molar ratio) and adding more NaOH to make it more alkaline. This was easier than starting with a more alkaline silicate solution and trying to make it more siliceous by dissolving silica because the dissolution process is strongly dependent on pH; it would therefore become progressively harder to obtained higher SiO_2:Na_2O molar ratios by this method because of the drop in pH as the solution became more siliceous.

Adjusting the SiO_2 wt. % was done after the required SiO_2:Na_2O molar ratio was reached. This was done by simply evaporating or adding water to increase or decrease SiO_2 wt. % and using a mass balance accurate to 3 decimal places to measure the water vapour loss. The detailed process of making sodium silicate solutions at 4 different molar ratios – 2:1, 2.5:1, 3:1 and 3.3:1 as well as SiO_2 wt. % at 20%, 25%, 26.5%, 28%, 30% at each of these ratios is outlined in Section 3.4.1.

3.4.1 Sodium Silicate Solutions

- A 200 g stock solution of SiO_2:Na_2O with a molar ratio = 2.5 which is equivalent to a weight ratio of 2.4 composed of 26.6 wt. % SiO_2 and 11.2 wt. % Na_2O was reacted with 7.1 g of NaOH to reduce the SiO_2:Na_2O weight ratio to 1.94:1 (2:1 molar ratio)
- Conversion between molar and weight ratios of sodium silicates:

$$\text{weight ratio} = \frac{\text{molar ratio}}{1.03} \tag{3.12}$$

where 1.03 is the ratio of molecular weights of Na_2O (62 g mol^{-1}) and SiO_2 (60 g mol^{-1})

- The titrimetric method of measuring SiO_2 and Na_2O wt.% was used to confirm that the required molar ratio of 2:1 was achieved
- Adjusting the SiO_2 wt.% at constant molar ratio was achieved by first separating the 207.1 g solution of sodium silicate at 2:1 molar ratio and 26.5 SiO_2 wt. % into four 20 g solutions and one 100 g solution of sodium silicate solution
- Each of the 20 g sodium silicate aliquots were used to create solutions of varying SiO_2 wt. %. For a 25 wt. % solution, 1.21 g of deionised water was added. For 26.5 wt. %, no water was added or removed. For 28 wt. % and 30 wt. %, 1.04 g and 2.3 g respectively of water was evaporated. This was done by intermittently heating and weighing the sample until the mass dropped by the required amount.
- 32.75 g of deionised water was added to the 100 g sodium silicate aliquot at 26.5 wt.% SiO_2; reducing the SiO_2 wt.% to 20%.

- Sodium silicate solution of 2.5: 1 molar ratio was the stock solution so making solutions with different SiO_2 wt.% was achieved in same steps as for the 2:1 sodium silicate solution
- Sodium silicate solution of 3:1 molar ratio was made by adding 2.45 g of NaOH to a 200 g stock solution which had an initial molar ratio of 3.3:1 and 28 wt.% SiO_2 (from Mistral). Adjusting the SiO_2 wt.% was achieved by adjusting the water content via addition or evaporation of water. For 20 g aliquots of 25% and 26.5% SiO_2 wt.%, 2.4 g and 1.13 g of deionised water were added respectively. For 28%, the solution was kept constant and for 30%, 1.33 g of water was evaporated. For the 20% solution, 100 g of the 28% solution was mixed with 40 g of deionised water
- Sodium silicate solution of 3.3:1 molar ratio was available as a stock solution. Adjusting the SiO_2 wt.% was done by adjusting water content via addition or evaporation of water as mentioned above
- All sodium silicate solutions were then stored in PTFE bottles for further analysis

3.4.2 Potassium Silicate Solutions

Potassium silicate solutions were made by dissolving potassium silicate powder (SiO_2:K_2O = 3.9:1 molar ratio) from Alfa-Aesar in water at 80 ^oC. KOH pellets were added to reduce the SiO_2:K_2O molar ratios down to 2:1, 2.5:1 and 3:1.

Ratios above these could not be made above 26.5 wt.% SiO_2 because of viscosity constraints. The titrimetric method described in Section 3.2.3 and 3.3.3 was used to check that the required ratios were met.

The method for preparing potassium silicates was similar to that for sodium silicates. Once the desired ratio of SiO_2:K_2O was made; the SiO_2 wt.% was adjusted by adding or evaporating water in order to decrease or increase the SiO_2 wt.% respectively.

3.5 Reusability Experiments

Determining the dissolution rate as a function of SiO_2:M_2O ratio at a relatively high solids loading of 20 wt.% SiO_2 for both potassium and sodium silicates were carried out in order to elucidate the role of Na^+ and K^+ in the dissolution process.

Quantifying the re-usability of NaOH and KOH was determined in the laboratory by dissolving 10 g of cristobalite in 100 mL sodium and potassium silicate solutions at 2:1 SiO_2:M_2O molar ratios and 20 wt.% SiO_2. Titrimetric analysis (outlined in Section 3.2.3) was used to determine the change in SiO_2 wt.% from the base 20% over 6 hours. The solutions were heated up to 95 ^oC in the reflux set-up shown in Figure 3.1 and stirred with a magnetic stirrer at 300 rpm.

3.6 Rheology of Silicates

The rheological properties of silicates are important for understanding the physics of the pressure cycles used in the autoclave. Silicate solutions which have a high viscosity can slow down the mass transfer rate of reactants and products crossing the fluid film boundary layer within the cooling channels during leaching.

An AR500 rheometer (Texas Instruments) with a 60 mm stainless steel cone and plate was used to measure the dynamic viscosity of sodium and potassium silicates as a function of SiO_2:M_2O ratio and SiO_2 wt%. The viscosity at a low to high shear regime (0.1 s^{-1} to 1000 s^{-1}) was determined.

The viscoelastic properties of the silicates were also measured by determining the linear viscoelastic range at constant oscillation frequency with various amplitudes and at constant amplitude with varying frequencies. The latter method gave G' and G'' – which are the elastic and viscous modulus respectively. Another advantage of the second method is that it prevented the destruction of the silicate structures by using sufficiently low amplitudes.

Determining the viscoelastic properties of the non-Newtonian potassium silicate solutions which were observed at 28 wt. % and 30 wt. % SiO_2 and SiO_2:K_2O molar ratios of 3:1 involved a two-step process.

In the first step, an oscillatory strain sweep was used to determine the linear viscoelastic region of the potassium silicate solutions. In the second step, a

frequency sweep below the critical strain, i.e. in the linear viscoelastic region (determined in step 1) was used to determine the storage and loss moduli as a function of the angular frequency.

3.7 Silicon NMR

The nucleus of an atom consists of protons and neutrons. Any atomic nuclei which consists of either odd atomic or mass numbers has a spin angular momentum and magnetic moment. The nuclear spin represents the total angular momentum of the nucleus (95).

When a nucleus of non-zero nuclear spin is placed in a magnetic field between 1 T – 10 T, its nuclear spin energy levels become non-degenerate. This resulted in a net magnetisation vector which is parallel to the direction of the magnetic field. Introducing electromagnetic energy into the system at a particular frequency in the form of radio waves led to a resonant absorption between the higher nuclear spin energy level (unstable) and the stable lower nuclear spin energy level states (95). This is illustrated in Figure 3.3.

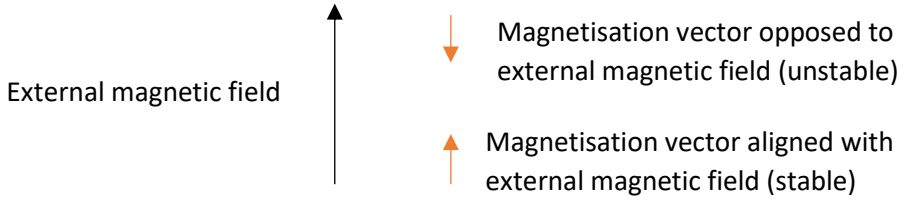

Figure 3.3 Stable and unstable nuclear spins

Sodium and potassium silicate samples as described in Section 3.4 were analysed by measuring the chemical shifts as a function of SiO_2:M_2O molar ratio

and the type of metal cation present – either Na^+ or K^+ for sodium and potassium silicates respectively. The purpose of this analysis was to determine the structure of silicate oligomers formed at different SiO_2:M_2O molar ratios and the effect of that the type of metal cation on the formation of these oligomers.

Silicon-29 spectra on 4 solutions of silicates at SiO_2:M_2O molar ratios of 2.5:1 and 3:1 for both sodium and potassium silicates were obtained on a Bruker 400 NMR spectrometer (Coventry, UK) with a 9.4 T magnet. These experiments were carried out by the NMR technician in the Chemistry department at the University of Birmingham.

Of the naturally occurring isotopes of silicon, only ^{29}Si has a spin of ½ therefore a magnetic moment. The ^{29}Si resonance frequency is 79.4 MHz and 2300 scans were made. The relaxation time of Si is between 5 – 150 seconds (95). The relaxation time was multiplied by a factor of 5 to determine the number of seconds per scan. Using the upper range of the relaxation time of 150 seconds would mean that a scan would be taken every 750 seconds and the experiment would last 19 days making it practically unfeasible. Using the lower range of 5 seconds meant that scans were taken every 25 seconds and the entire experiment lasted 16 hours.

Samples were placed into 5 mm diameter 500 MHz Wilmad NMR tubes obtained from Sigma-Aldrich. Since the NMR tubes were made of glass, this interfered with the results because the tube, probe and sample all had silicon atoms present.

This problem was solved by running a blank spectrum and subtracting from the regular spectrum, removing the broad background signal from the glass tube in the process.

Referencing was done relative to Tetramethylsilane (TMS) because of its chemical inertness and short relaxation time.

3.8 Test bar Manufacture

The investment casting process was used to manufacture 100 samples consisting of a ceramic core encapsulated within a metal with a single opening as shown in Figure 3.4. The purpose of this was to understand the physics of the leaching process for a simple, rectangular prism core geometry and to determine the layer etch rate (mm^2 min^{-1}) of the leaching process. The core material formulation used here is the same as what is used in actual turbine blade components – consisting of approximately silica and zircon in a 3:1 mass ratio.

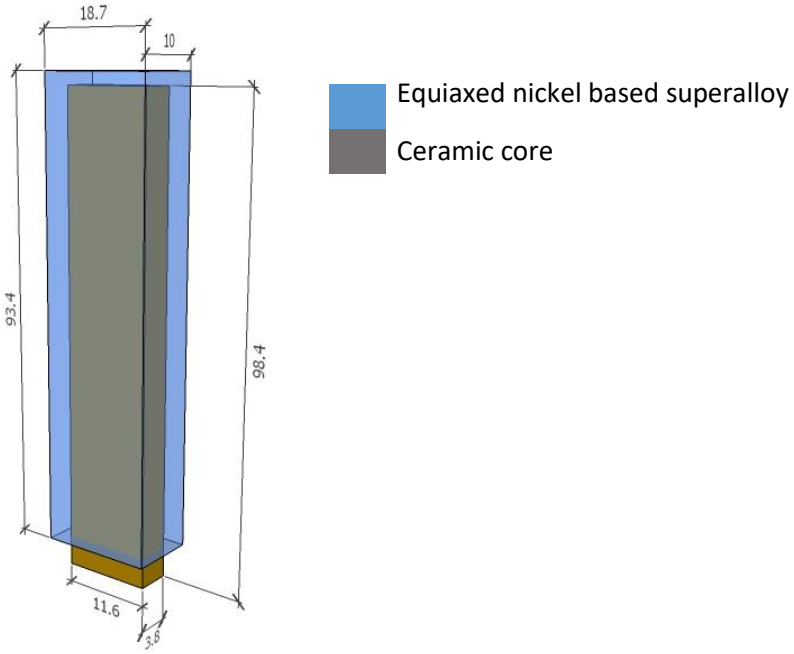

Figure 3.4 Rectangular prism ceramic core within an equiaxed nickel based superalloy casting (dimensions in mm)

3.8.1 Wax Injection

Rectangular core samples measuring 11.6mm by 3.8 mm by 98.4 mm were obtained from Ross Ceramics, a subsidiary of Rolls-Royce plc. A 100 of these samples were obtained. The first step was the injection of wax around the core. A 5 cavity aluminium die was obtained from Derwent Valley Tooling. Draft angles were included in the die design to allow for easy ejection of the parts after wax injection. A CAD model of the die is shown in Figure 3.5 and 3.6.

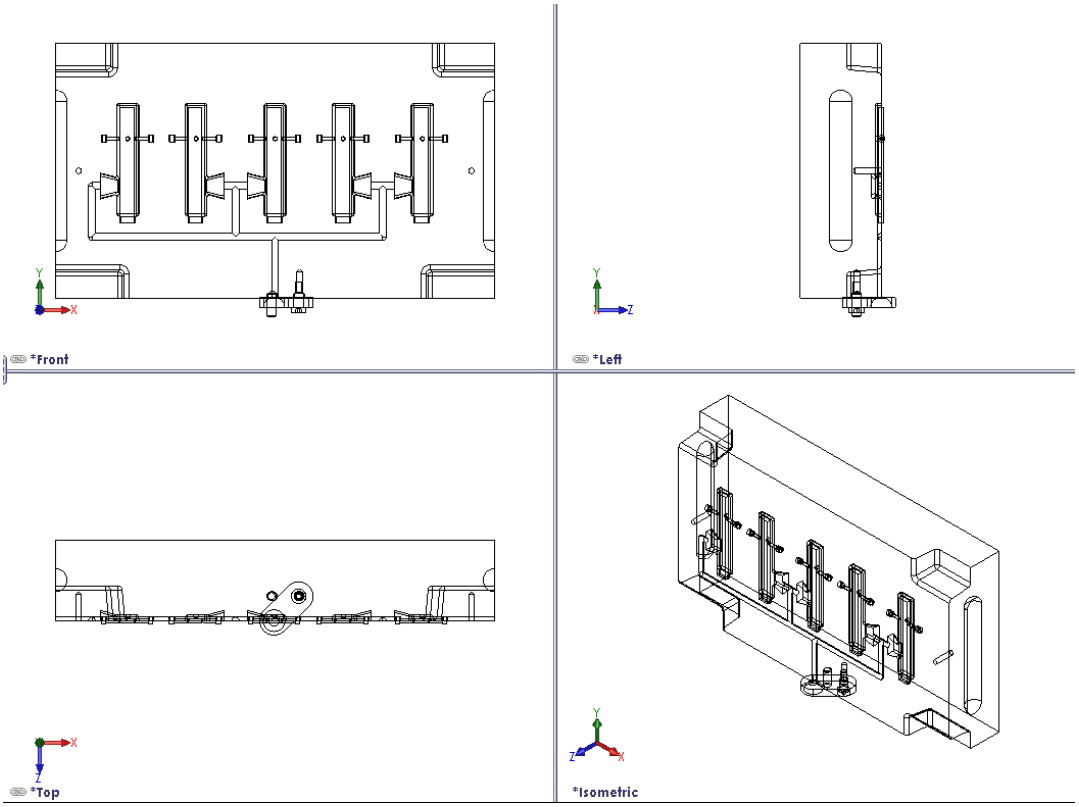

Figure 3.5 CAD model of the 5 cavity die (96)

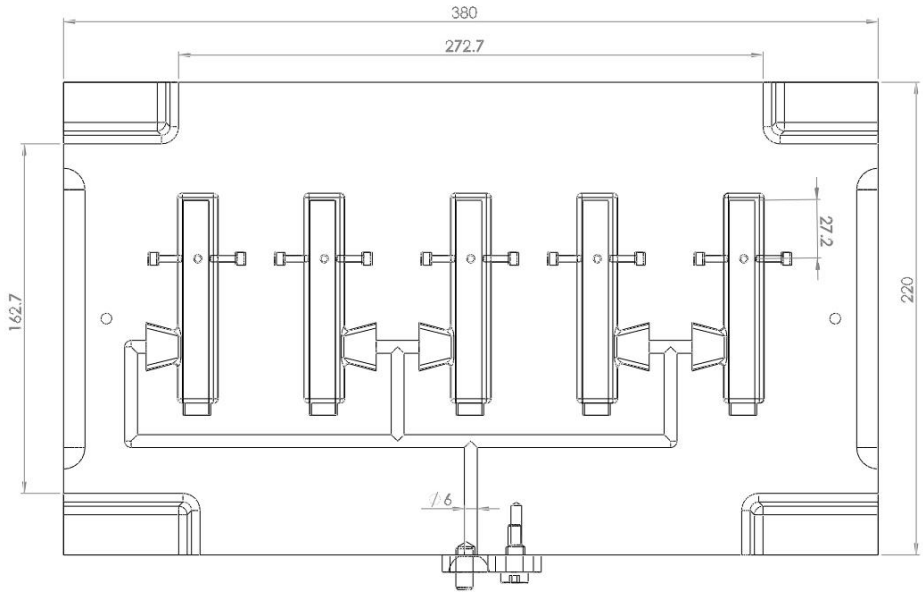

Figure 3.6 Detailed front elevation of 5 cavity die cross-section (96)

Holding pins were located 27.2 mm from the base of the core to hold it in place during injection.

Wax injection was carried out using an MP1 model 55 wax injector. The pack pressure of the wax was 2000 kPag. Blaysons A7 FR/60 virgin wax pellets were melted and injected at 63 ^{o}C into the die.

The pins shown in Figure 3.6 were used to hold the core in place during wax injection. These created a recess in the wax pattern as shown in Figure 3.7.

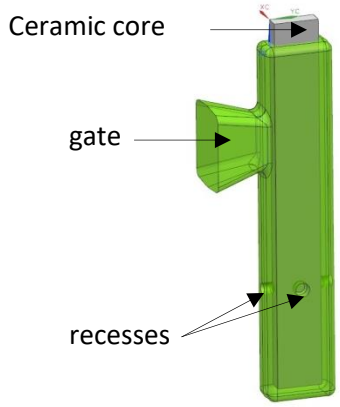

Figure 3.7 Wax pattern around ceramic core (97)

Figure 3.7 shows the ceramic core after wax injection. The recess was filled with wax post injection to create a smooth, flat surface. 20 patterns were then arranged around an adour runner as shown in Figure 3.8. The gate connected the runner with the mould cavity.

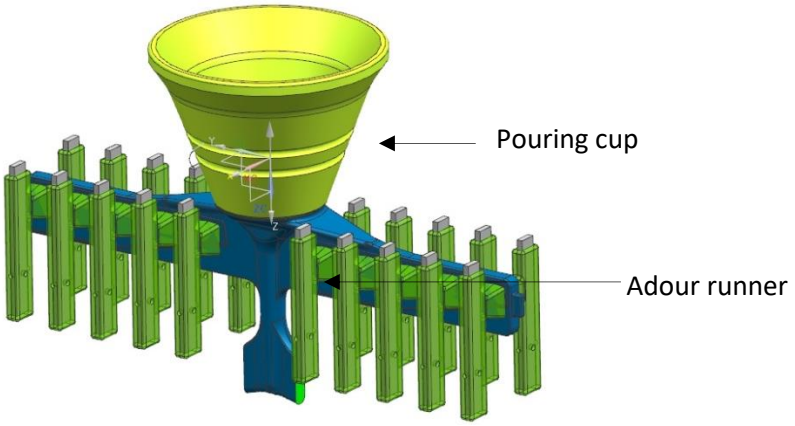

Figure 3.8 Wax assembly with 20 ceramic cores (97)

3.8.2 Shell Mould

Application of the shell mould was carried at the BTC (Rolls-Royce's casting facility in Bristol). The wax assembly was dipped into a ceramic slurry to form a shell coat. This was repeated 8 times to create a shell mould. The slurry consisted of colloidal silica binder and fine refractory powder. After each dip of the wax pattern into the slurry, coarse refractory grains were rainfall sanded onto the pattern and allowed to dry before the application of subsequent coats. The exposed part of the ceramic core not covered in wax (5 mm x 11.6 mm x 3.8 mm) was the only point of contact between the core and the shell mould. This was necessary to keep the core in place during the next step of the process, where the wax was melted out. This is described in the next section.

3.8.3 De-wax, Cast and Post Cast Operations

The ceramic shell and wax pattern were placed in a dewaxing boilerclave to remove the wax pattern leaving behind the shell mould and the ceramic core. This was placed in a tunnel oven where the parts moved between 6 temperature-controlled zones before being cast at 1500 ^{o}C and then cooled in air.

A high pressure water jet was then used to remove the shell mould leaving behind an equiaxed, nickel based superalloy casting with a ceramic core as shown in Figure 3.4. Some residual shell material remained on the metal surface after shell removal. This was however inconsequential to the subsequent trials described in Section 3.9.

3.9 Pilot Scale Trials With Test Bars

Pilot scale leach trials were carried out using the test pieces manufactured as described in Section 3.8. This was done at LBBC Technologies using a 30 L capacity autoclave as shown in Figure 3.9.

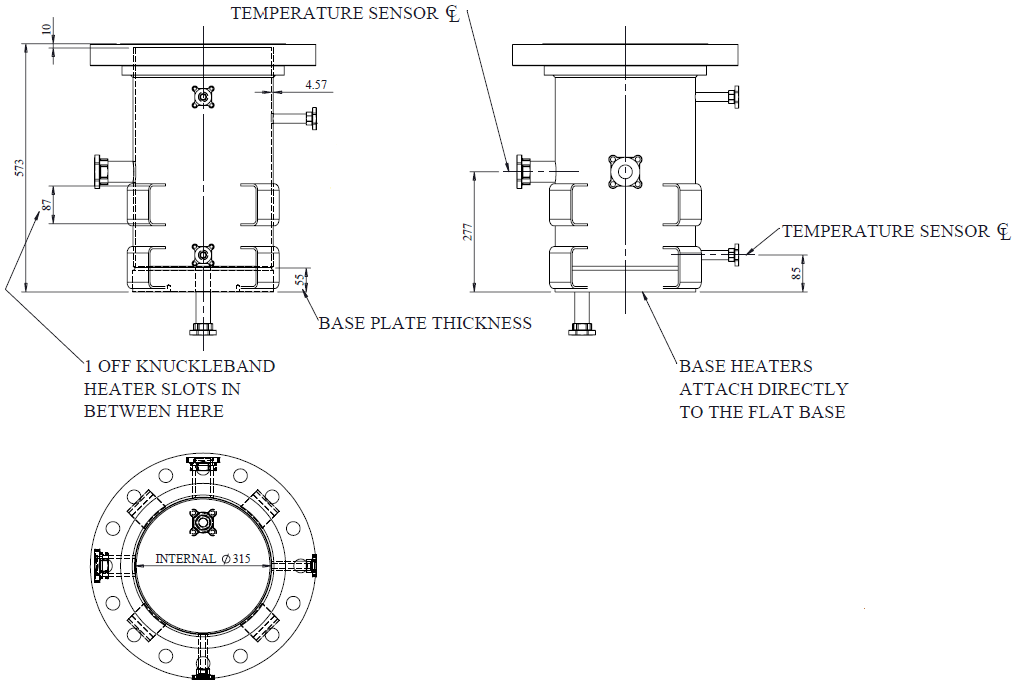

Figure 3.9 Detailed dimensions of the pilot scale autoclave (98)

Parts were placed into a holding basket which rested at the bottom of the autoclave. Two temperature sensors were used to monitor the alkaline solution temperature at the bottom and mid-section of the autoclave. The temperature sensor at the mid-section, located 192 mm from the base was used to control the temperature through a PID controller. Heat was supplied via 3 kW knuckle band heaters and a 3.2 kW base heater.

The autoclave temperature was set at 160°C. Pressurised factory air was supplied at 600 kPag to the top of the autoclave. The autoclave operates on a pressure swing cycle where the high-pressure dwell, vent and low pressure dwell times were all independently controlled. Pressurisation took approximately 2

seconds to 600 kPag. This was then held for a specified amount of time (high pressure dwell). After this, the vent valve was opened which led to aggressive boiling for a specified time (vent). The vapour consisted of wet steam, i.e. steam with entrained alkaline solution droplets. This was vented off into a dump tank. After this, the vent valve was closed and the solution was held at a lower pressure of approximately 200 kPag for a specified time (low pressure dwell). The autoclave was then re-pressurised again and the cycle of pressure swings was continuously repeated over the entire leach time.

Figure 3.10 shows the piping and instrumentation diagram (PID) for the leaching process at the pilot plant.

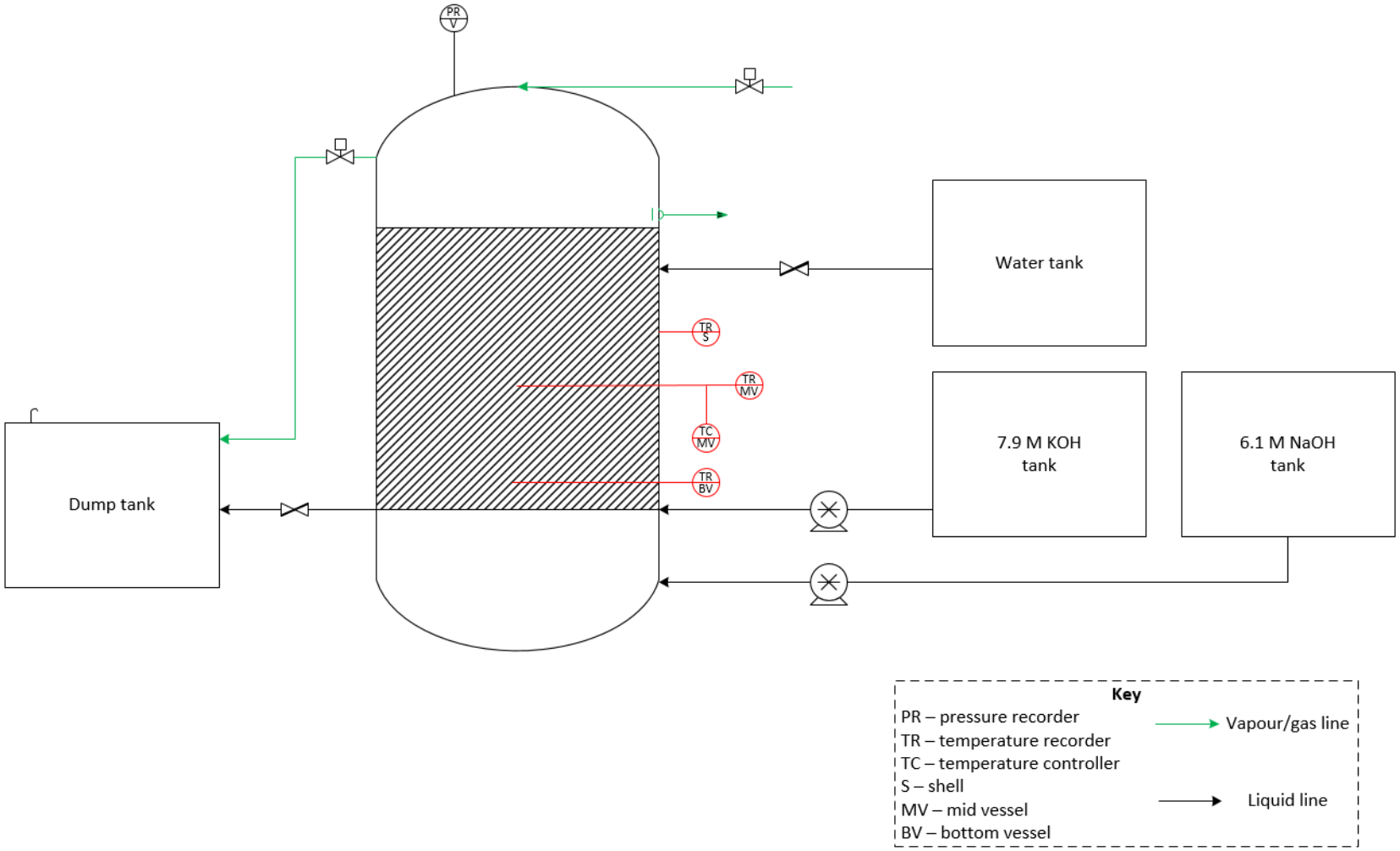

Figure 3.10 Piping and instrumentation diagram (PID) for the leaching process at the pilot plant

For each run using either 1 M NaOH or KOH, 10 test bars were placed in the autoclave as shown in Figure 3.11. Each test bar was aligned with the opening facing down. The pressure, vent and dwell times were set to 60 seconds pressure, 5 seconds vent and 60 seconds dwell. The vent time was limited to only 5 seconds to prevent excessive liquid loss. Total cycle times were 30 minutes, 60 minutes and 120 minutes. After each cycle, the alkaline solution was sent to the dump tank. Pressurised air was used to force any remnant alkaline solution out of the autoclave. The alkaline solution was dumped immediately after each cycle to prevent further dissolution of the core. Water was then pumped into the autoclave to rapidly cool the autoclave and the test bars. Once the autoclave shell temperature (TR S) reached 50 ^{o}C, the vessel was opened and the parts were taken out.

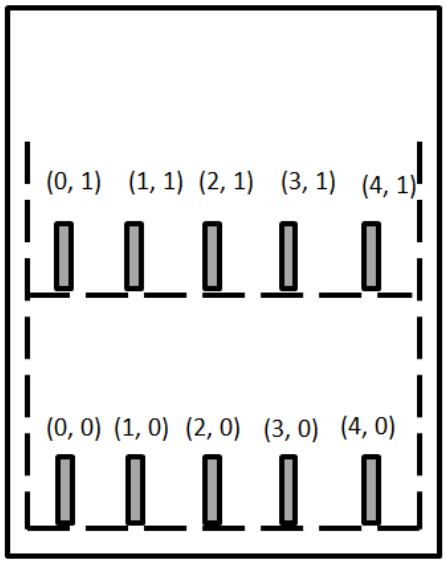

Figure 3.11 Test bar positions in the autoclave

The effect of 3 variables on leach rate where examined – the type of metal cation present, the orientation of the test bar in the autoclave and the effect of total boil time (which is the sum of the vent and low pressure dwell times) on the amount of core removed.

3.9.1 Metal Cation Effect

All NaOH and KOH solutions were obtained from Caldic (Chesterfield, UK). For NaOH, a 1M solution was made from a 20 wt.% stock solution of NaOH (6.1 M). For KOH, a 1 M concentration was made from a 33 wt.% stock solution of KOH (7.9 M) by diluting with water. Because of the relatively large size of the autoclave, volume measurements were imprecise, and the actual concentrations had an error of ± 0.1 M. This was measured by extracting a 5 mL sample from the autoclave (after thoroughly mixing the solution by bubbling air into the autoclave) and titrating against 1 M HCl with methyl red indicator.

The 1 M NaOH solution was made by marking the inner wall of the autoclave at 40 mm and 284 mm from the base. 6.1 M NaOH and water were then filled up to these respective heights. This is shown in Figure 3.12.

Calculation:

$C_1V_1 = C_2V_2$

$C_1 = 6.1\,M$

$C_2 = 1.0\,M$

$V_1 = \pi r^2 h_1 = \pi(0.1575)^2 0.04 = 3.12\text{x}10^{-3}\ \text{m}^3 = 3.12\ \text{L}$

$V_2 = \frac{C_1V_1}{C_2} = 19.0\ \text{x}\ 10^{-3}\ \text{m}^3 = 19\ \text{L}$

$$h_2 = \frac{V_2}{\pi r^2} = 0.244 \text{ m} = 244 \text{ mm}$$

where C_1 is the starting concentration, V_1 is the starting volume of the solution at 1 M concentration, C_2 is the desired concentration and V_2 is the final volume with h_2 being the water level required to achieve the desired concentration.

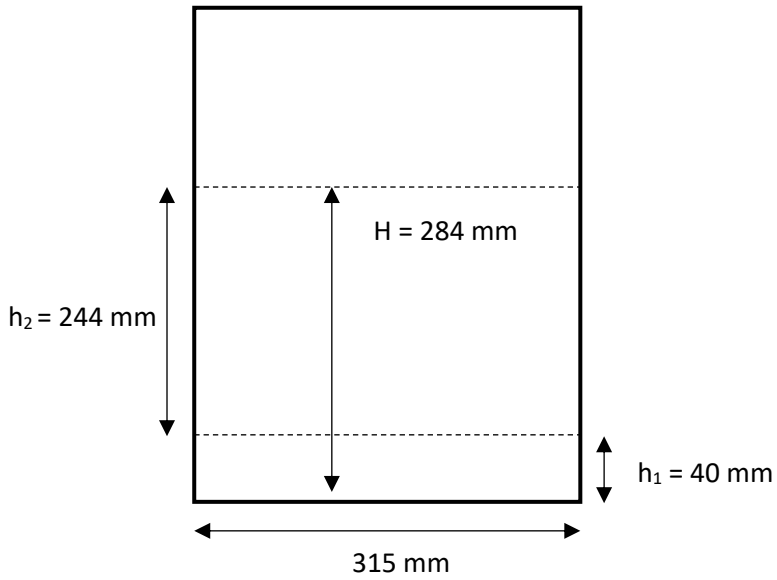

Figure 3.12 Height markings for a 1 M NaOH solution

The 1 M KOH solution was made by marking the inner wall of the autoclave at 40 mm and 356 mm from the base. 7.9 M KOH and water were then filled up to these respective heights. This is shown in Figure 3.13.

Calculation:

$$C_1V_1 = C_2V_2$$

$$C_1 = 7.9\ M$$

$$C_2 = 1\ M$$

$$V_1 = \pi r^2 h_1 = \pi(0.1575)^2 0.04 = 3.12\text{x}10^{-3}\ \text{m}^3 = 3.12\ \text{L}$$

$$V_2 = \frac{C_1V_1}{C_2} = 24.7\ \text{x}\ 10^{-3}\ \text{m}^3 = 24.65\ \text{L}$$

$$h_2 = \frac{V_2}{\pi r^2} = 0.316 \text{ m} = 316 \text{ mm}$$

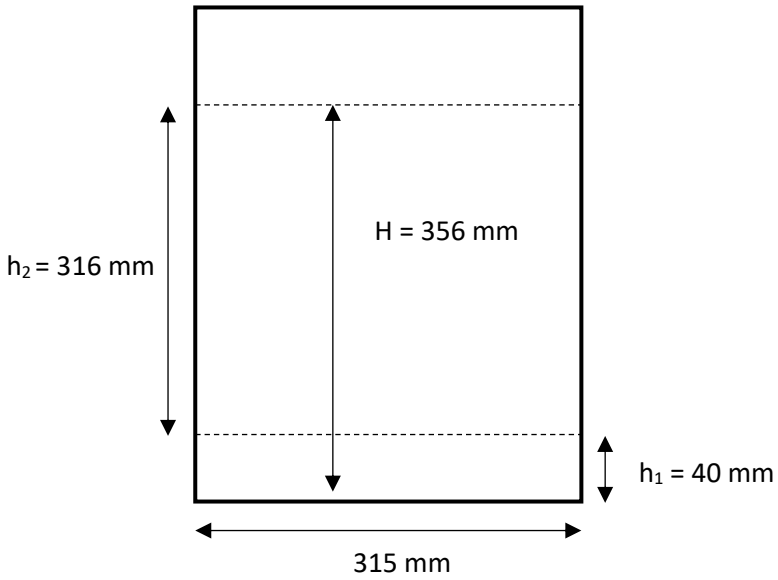

Figure 3.13 Height markings for a 1 M KOH solution

It was necessary that the liquid level in the autoclave was significantly above the position of the knuckle band heaters which were located 222 mm from the base. This was done to ensure a sufficient margin of safety to prevent the shut-down of the heaters if the liquid level dropped below 222 mm during venting of the autoclave.

The total alkaline volume used for the 1 M KOH cycle was 25% larger than that used for 1 M NaOH. This slightly altered the %SiO_2 dissolved and the viscosity of the solution but was ultimately insignificant because the total mass of the core available to dissolve is very small relative to the mass of the alkaline solution in the autoclave.

3.9.2 Part Orientation

The amount of core removed from parts with the core opening at 0º, 90º and 180º relative to the bottom of the autoclave as shown in Figure 3.14 was determined by leaching in the autoclave for 1 hour and comparing the amount of core removed in each orientation. For each orientation, 10 test bars were used and arranged in the autoclave as illustrated in Figure 3.11.

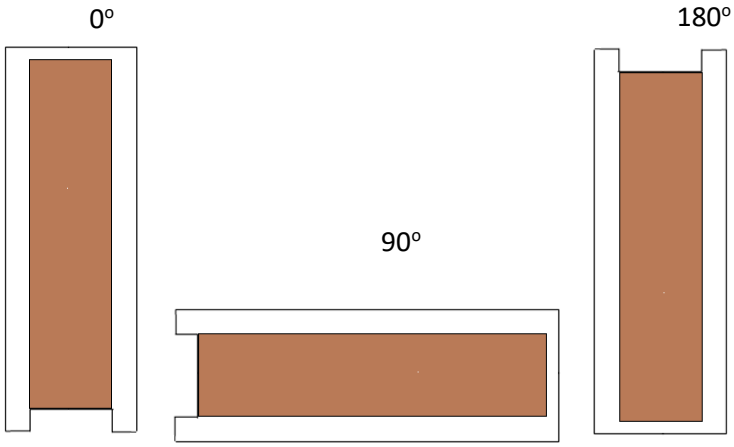

Figure 3.14 Test bar orientations in the autoclave

3.9.3 Total Boil Time

The amount of core removed as a function of the total boil time was determined by measuring the volume of core removed under different high pressure dwell, vent and low pressure dwell times. The amount of core removed in a 30 minute cycle using the standard high pressure dwell, vent and low pressure dwell times of 60 seconds, 5 seconds and 60 seconds was compared with an accelerated cycle operating with 5 seconds high pressure dwell, 5 seconds vent and 10

seconds low pressure dwell. The total boil time (vent + low pressure dwell times) for the accelerated cycle was 1.4 times that of the standard cycle and the total aggressive boil time (vent time) for the accelerated cycle was 6.3 times that of the standard cycle aggressive boil time.

3.10 Post Leach Inspection

After leaching, the volume of core removed was measured. Also, the surface of the leached area was analysed under an SEM.

3.10.1 Volume of Core Leached

The volume of core leached from the test bars was determined by measuring the volume of water needed to fill the leached volume. A 1000 mm^3 syringe was filled with water. This was then injected into the test bar and the volume loss % was calculated by simply dividing the water volume by the test bar volume.

$$Volume\ loss\ \% = \frac{water\ volume}{test\ bar\ volume}\ \text{x}\ 100 \qquad (3.13)$$

The test bar volume (4117 mm^3) is the volume of the core (4337 mm^3) less the core volume removed with the ceramic shell during shell removal (220 mm^3) as shown in Figure 3.4 where core prism sticking out of the cast superalloy measures 11.6 mm by 3.8 mm by 5 mm.

3.10.2 Scanning Electron Microscopy (SEM)

Jeol 6060 scanning electron microscope was used to examine the core surface post leach. The secondary electron image was used to observe any physical damage on the core surface. The samples were prepared by first sawing off the excess metal up to the leach front as shown in Figure 3.15. An IsoMet 4000 linear precision saw was used to cut-up the sample. The total sample length was 20 mm from the leach front. The samples were also cut across half-way through the core width of 3.8 mm at 1.9 mm to reveal the exposed leach profile. The samples were then coated in gold for SEM analysis

.

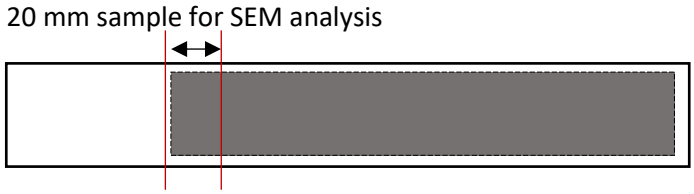

Figure 3.15 Test bar cut-off points for SEM analysis

3.11 Pilot Scale trials With Turbine Blades

Trent 1000 HP and IP blades were leached in the pilot scale autoclave as shown in Figure 3.10. Two blades were used in each experiment. There were limitations with the number of blades available for the pilot scale trials. This made planning in advance very difficult and reduced the amount of experiments carried out.

The autoclave temperature was set at 160 ^{o}C and pressurised factory air was supplied at 600 kPag to suppress boiling of the alkaline solution. Three trials were carried out:

3.11.1 Tracking Leach Rate for a Complex Geometry

5 M KOH (22.6 wt%) was made from a stock solution of 7.9 M (33 wt%). This was done by filling the autoclave up to 150 mm from the base with the 7.9 M stock solution and adding water up to 387 mm.

For each cycle, the pressure, vent and dwell times were 60 seconds, 5 seconds and 60 seconds respectively. The 3 blades were loaded into a holding basket with the largest opening facing down. The total cycle times were 1, 2 and 3 hours and each set of blades were leached at these respective times in order to track leach progress. It took approximately 1 hour for the temperature to reach the target temperature of 160 ^{o}C after which the cycle commenced.

After the cycle was completed, the alkaline solution was dumped and the vessel temperature was allowed to reach 50 ^{o}C before it was opened and the blades were taken out for analysis as described in Section 3.10. Water was pumped into the autoclave to increase the rate of cooling and to remove any residual alkaline solution from the blade surface.

The leach depth was measured by inserting a 1 mm diameter steel wire into each channel and measuring the depth of penetration. The leach depth across each channel was then used to measure the corresponding volume loss using the CAD file of the blade.

The average cross-sectional area over which the core volume loss was registered was also measured using the CAD file. This was done by measuring the surface area of the top and bottom of the leached core segment and taking an average. This average cross-sectional area is approximately representative of the core surface area exposed to the alkaline solution.

In reality, this surface area underestimates the actually surface area exposed to the alkaline solution because of the non-linear leach fronts. However, this underestimation does not affect comparisons in leach rates between different channels because there will be a systematic underestimation.

3.11.2 Effect of Pressure Swing Cycle

The amount of core removed as a function of the high pressure dwell, vent and low pressure dwell times was used to determine optimum cycle parameters for NaOH and KOH. Table 3.4 shows the pressure sing parameters used for the pilot scale trials.

Table 3.4 Autoclave cycle parameters for pilot scale trials

	Standard cycle	Extended high pressure dwell	Extended low pressure dwell 1	Extended low pressure dwell 2	Extended vent
High Pressure dwell (s)	60	60	30	5	30
Vent (s)	5	5	5	5	5
Low pressure dwell (s)	60	5	90	26	30
High Pressure dwell %	48	86	24	14	46
Vent %	4	7	4	14	8
Low pressure dwell %	48	7	72	72	46

In every cycle, the extended vent time did not change from 5 seconds because excess vapour loss could lead to the liquid level dropping below the height of the knuckle band heaters causing the autoclave to overheat and shut down.

3.11.3 Mixed Cation Solutions

The amount of core removed in a mixture of Na^+ and K^+ at a 1:4 ratio at 5 M OH^- concentration was determined in a 1 hour leach cycle using the standard pressure swing parameters – 60 seconds high pressure dwell, 5 seconds vent, 60 seconds low pressure dwell. The amount of core removed was determined using the same method outlined in Section 3.10.1.

4 SILICA DISSOLUTION CHEMISTRY

Cristobalite dissolution in alkaline solutions is a significant process in the investment casting industry. The ceramic cores used by Rolls-Royce plc are primarily composed of cristobalite and zircon. Cristobalite is the reactive component of the core which dissolves in highly alkaline solutions whereas zircon is considered to be chemically inert. Therefore, this chapter will focus on the chemistry of cristobalite dissolution in highly alkaline environments. Strong alkaline solutions dissolve the silica based ceramic core without damaging the metal casting.

Crystalline silica dissolution in strong alkaline solutions has been shown to be a very complex process (59-62, 64). This problem is further compounded by the fact that in the leaching autoclave, the physical and chemical processes occur simultaneously and the difference between the two processes is arbitrary. For example, diffusion can be considered to be a purely chemical process because it arises from a concentration gradient. It can also be considered to be a physical process because the diffusion rate through a fluid film will be affected by its rheological properties. For the purpose of simplicity and because the aim of the project was to understand the chemistry and physics of the core leaching process, any phenomenon that does not directly lead to a mechanical breakdown of the ceramic core will be classed as a chemical process.

The first few sections will detail the surface chemistry of cristobalite in strong alkaline solutions, i.e. what happens at the start of the reaction once the alkaline solution contacts the ceramic core surface. The final sections will investigate the rheological properties of the reaction products and the effects of this on the rate determining step of the reaction.

4.1 Silica Structure and Surface Chemistry

At the surface, both silicon and oxygen atoms can be present. It was hypothesised by Papirer (48, 64) that oxygen will preferentially protrude out of the surface because of its lower charge and higher polarizability; this is illustrated in Figure 4.1.

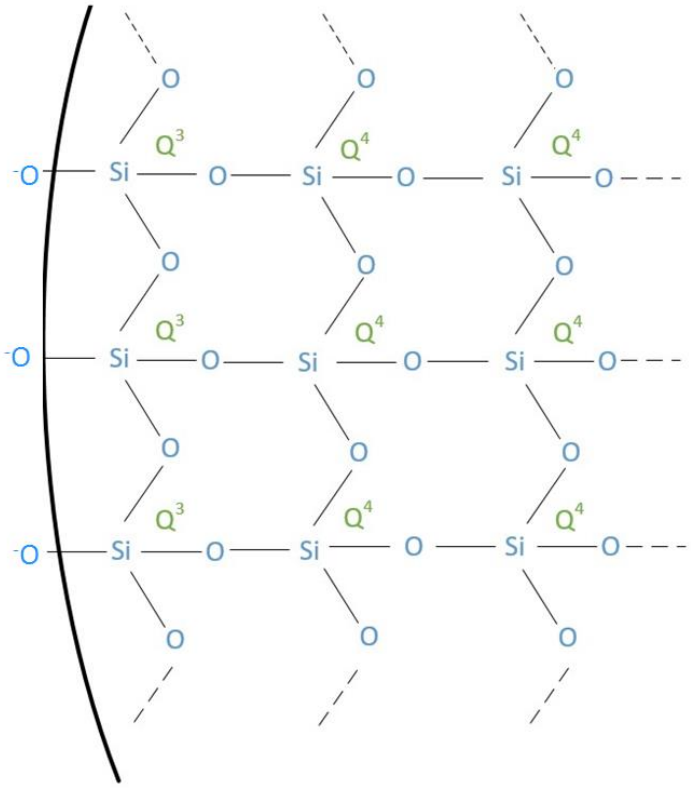

Figure 4.1 Crystalline silica structure with protruding oxygen atoms

The number of siloxane bonds linked to any Si atom is donated by Q^n where n is the number of siloxane bonds (53). The surface of a smooth silica particle is composed of mainly Q^3 Si atoms whereas the inner Si atoms have four siloxane bonds attached – denoted as Q^4. This is the standard nomenclature used in silica chemistry and will be important for the discussion going forward.

In a low pH or neutral environment, the negatively charged oxygen atoms protruding from the silica surface will be neutralised by adsorption of protons forming silanol groups (48).

$$\equiv Si–O^- + H^+ \leftrightarrows \equiv Si–OH \qquad (4.1)$$

Reaction 4.1 shows the formation of a single proton adsorbing onto the negatively charged oxygen atom. This is known as a single silanol group. If two protons adsorb onto the surface oxygen, a geminal silanol is formed as shown in reaction 4.2 (48).

$$\equiv Si–O^- + 2H^+ \leftrightarrows \equiv Si–OH_2^+ \qquad (4.2)$$

The protonation constants of the single and double geminal silanol groups were found to be 9.7 and -4.6 respectively (48) . This means that ≡Si–OH is quite stable between pH 2 – pH 7 whereas $\equiv Si–OH_2^+$ forms only in highly acidic media < pH 1 (48).

The doubly coordinated oxygen atoms within the 3-dimensional silica framework will not be protonated because their protonation constant of -16.9 is much lower than even the geminal silanol groups (48, 53). This leads to the conclusion that at pH 7, the silica surface is electrically neutral and consists of single silanol groups as can be seen in Figure 4.2.

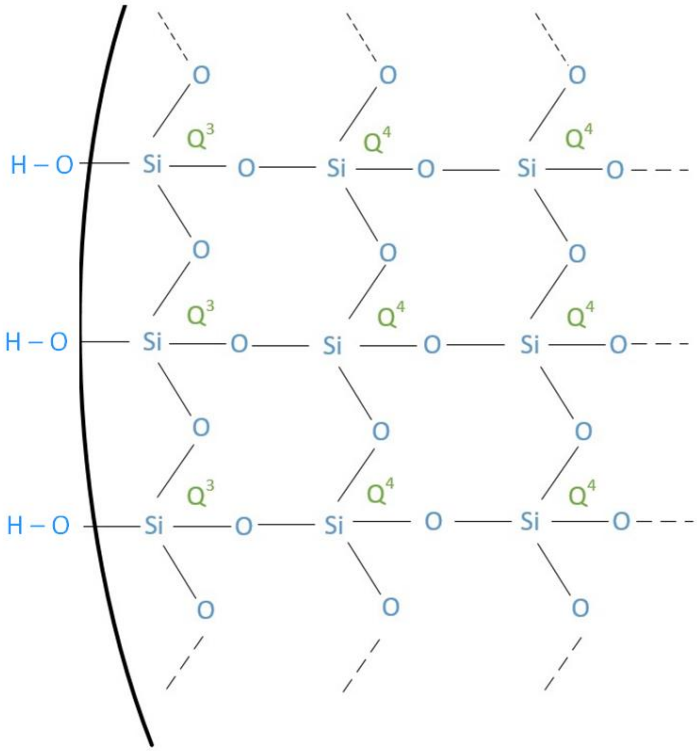

Figure 4.2 Single silanol groups on the silica surface at neutral pH

At a pH above 7, the excess hydroxide ions (OH^-) deprotonate the surface silanol groups leaving the silica surface negatively charged (48, 53).

$$\equiv Si–OH + OH^- \leftrightarrows \equiv Si–O^- + H_2O \qquad (4.3)$$

The deprotonation mechanism of surface silanol groups is shown in Figure 4.3.

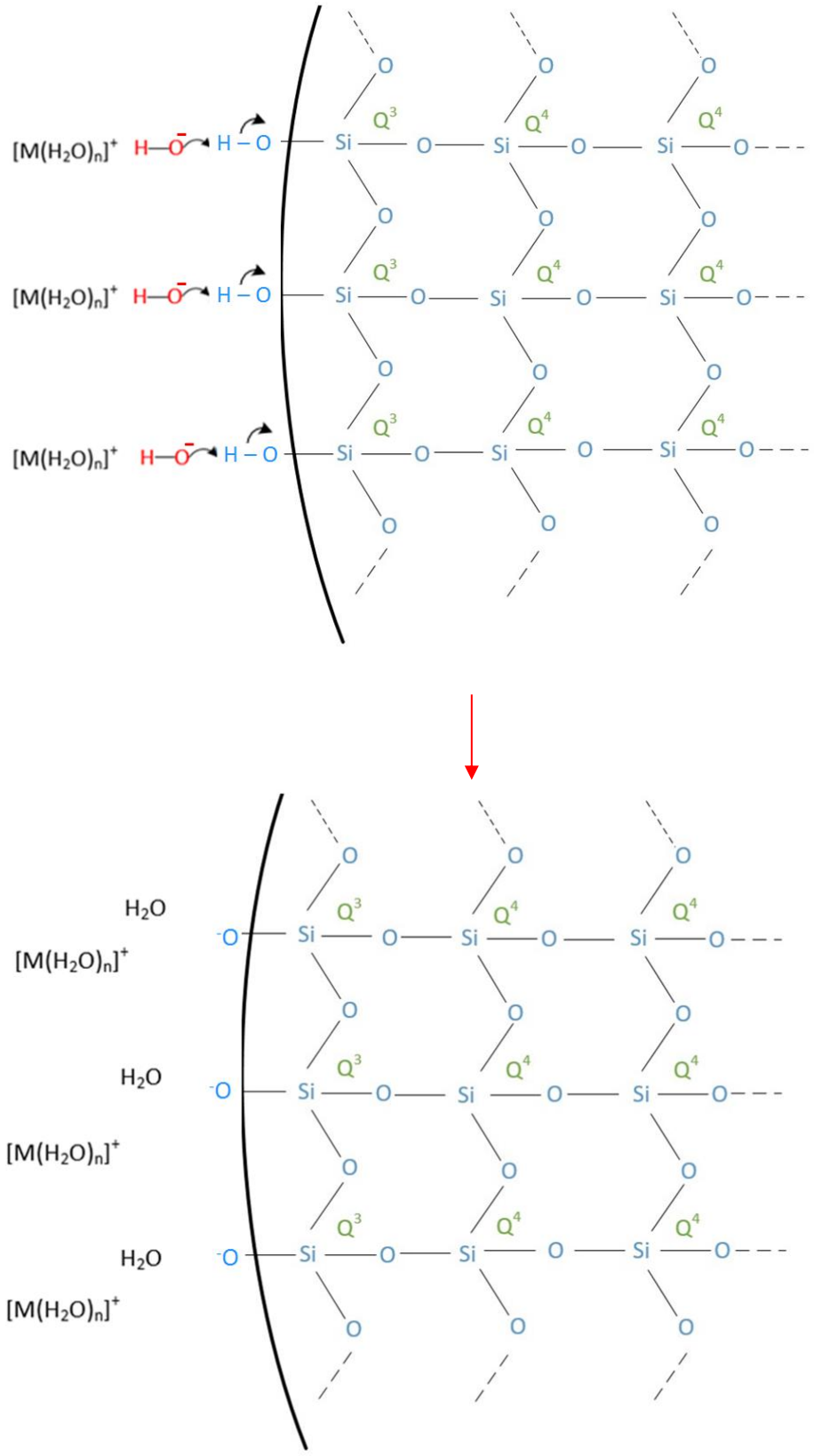

Figure 4.3 Deprotonation of surface silanol groups

Deprotonation of the surface silanol groups leads to the formation of a negatively charged silica surface. This charge is immediately neutralised by the adsorption of positively charged Group IA alkali metal counterions. These counterions don't exist in isolation and have associated hydration spheres.

In Figure 4.3, M denotes the metal cation and n is the number of water molecules that form a hydration sphere around it. This is expanded upon in section 4.2.

4.2 Cationic Adsorption on the Negatively Charged Silica Surface

Group IA metal hydroxides are all strong bases that completely dissociate into their constituent ions in aqueous solutions.

$$MOH + H_2O \rightarrow M^+ + OH^- + H_2O \qquad (4.4)$$

The metal cation and hydroxide anion do not exist in isolation in aqueous solutions. They interact with nearby water molecules forming hydration spheres as explained in Chapter 2. The metal cation therefore exists as – $[M(H_2O)_n]^+$ where n is the number of water molecules forming noncovalent interactions with the metal cation. The net charge of the hydrated metal cation is still positive because the formal positive charge on the metal cation is not neutralised by the partial negative charge of the oxygen atom in the polar water molecule. Figure 4.4 shows the metal cation with its hydration sphere.

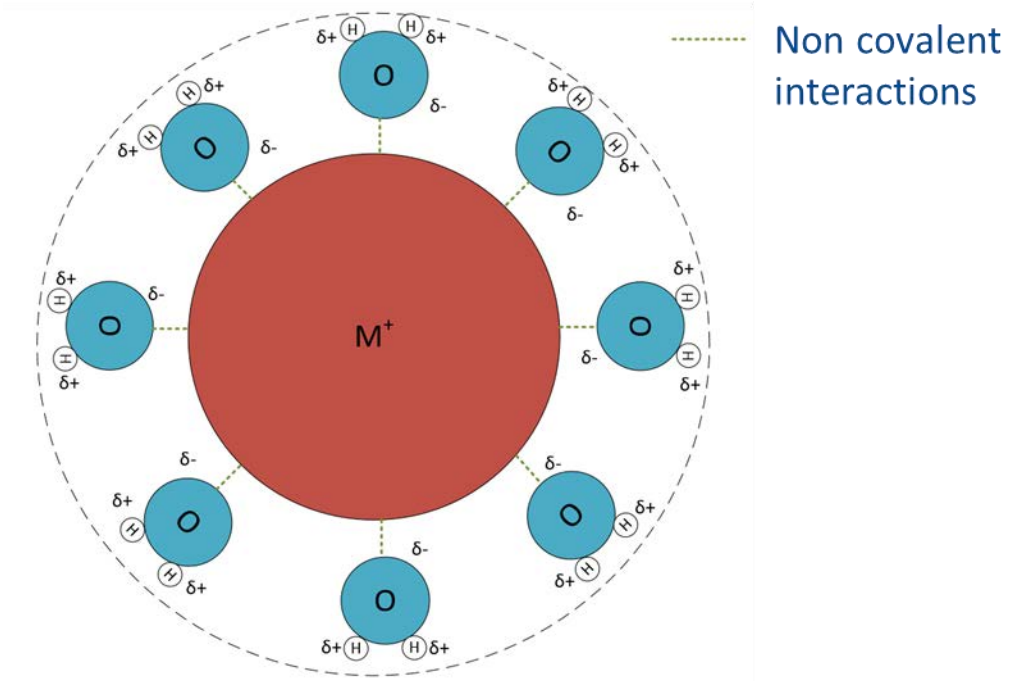

Figure 4.4 Hydration sphere around metal cation

The formal positive charge on the metal cation causes the oxygen atom in the water molecule to face inwards because of its partial negative charge. This leaves the hydrogen atoms facing outward. If the charge density of the metal cation is large enough (where charge density is defined as Z^2/r where Z is the ionic charge and r is the ionic radius) then hydrogen bonding between the hydrogen from water molecules in the primary hydration sphere and oxygen molecules from nearby water molecules form a secondary hydration sphere (25).

The hydrated metal cations adsorb onto the negatively charged silica surface creating an electrically neutral Stern layer. It was reported by Dove and Icenhower (55) and Iler (50) that these cations remain at least partially hydrated

at the silica-solution interface. Table 2.1 shows the ionic radii and charge densities and hydration radii of some Group IA and IIA cations.

In the laboratory experiments, cristobalite M006 (Sibelco, Belgium) was reacted with prepared 5 M solutions of LiOH, NaOH, KOH and CsOH in a reflux set-up at 95 ^{o}C (described in Chapter 3) to understand the effect of different metal cations on the surface chemistry of cristobalite. This was further complicated because the different metal cations affect the rheology of the reaction products, which in turn affects the diffusion rate of the hydroxide through the fluid film layer. As a result of this, isolating the cation specific interaction on cristobalite surface chemistry is complicated.

Reaction 4.5 shows the adsorption of the metal cation on the negatively charged silica surface, which is illustrated in Figure 4.5.

$$\equiv Si–O^- + [M(H_2O)_n]^+ \leftrightarrows \equiv Si–O^-.....[M(H_2O)_n]^+ \quad (4.5)$$

Combining reactions 4.3 and 4.5, the overall surface reaction at the instant the alkali hydroxide contacts the silica surface is (48):

$$\equiv Si–OH + OH^- + [M(H_2O)_n]^+ \leftrightarrows \equiv Si–O^-.....[M(H_2O)_n]^+ + H_2O \quad (4.6)$$

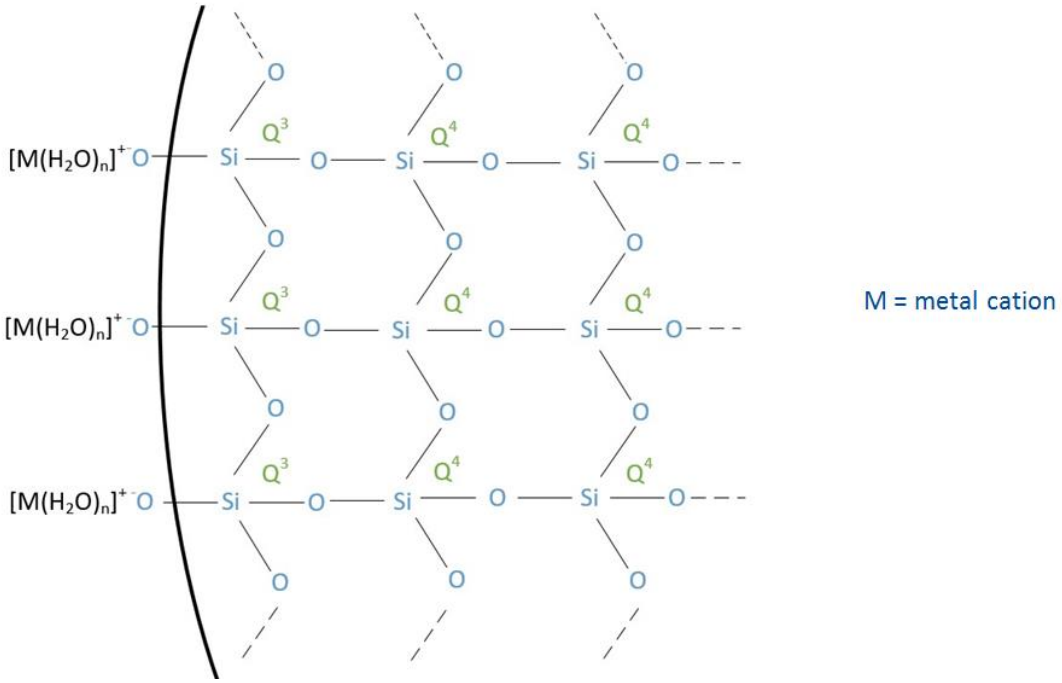

Figure 4.5 Adsorption of hydrated metal cation on the silica surface

It should be noted that while Equations 4.1 – 4.6 are reversible, the rate of the forward reaction exceeds the rate of the backward reaction (48).

Adsorption of the hydrated metal cations is a necessary precursor for the next step of the process – siloxane bond cleavage (discussed in Section 4.3). Without this step, the silica surface will remain negatively charged and electrostatically repel the approach of the hydroxide ion.

4.2.1 Effect of Metal Cations on Dissolution Rate

100 g equimolar solutions of LiOH, NaOH, KOH and CsOH at 5 M and 95 ^{o}C were reacted with 10 g of cristobalite M006 for 6 hours. A magnetic stirrer at 300 rpm was used to agitate the system and percent the cristobalite powder from settling. Equally weighted aliquots were extracted every hour to determine the amount of

silica in solution via the titrimetric method outlined in Chapter 3. Figure 4.6 shows the amount of cristobalite dissolved as the reaction progressed.

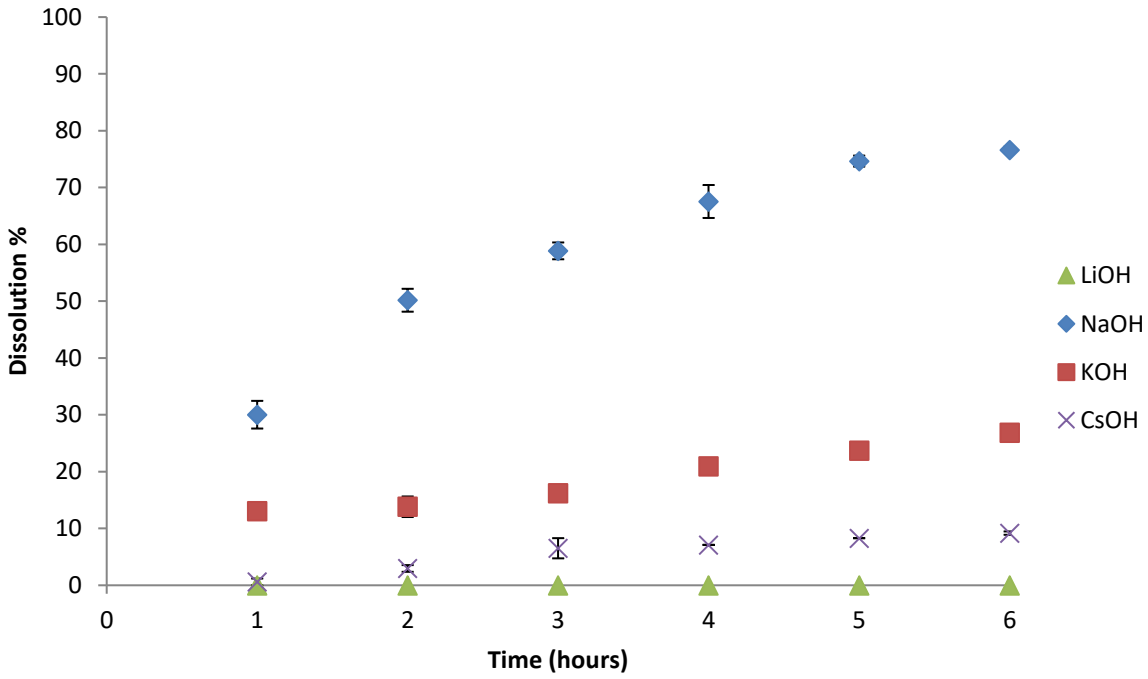

Figure 4.6 Cristobalite dissolution in 100 g of equimolar Group IA alkali metal hydroxides at 95°C

Three samples were analysed every hour and the error bars represent the standard deviation of silica dissolved. From Figure 4.6, it can be seen that the type of metal cation present in solution has a significant impact on the amount of cristobalite dissolved. The experimental conditions were all identical and the only variable that changed was the type of metal cation present. Therefore, any difference in the amount of silica dissolved and the dissolution rate is attributed to the influence of the metal cation.

Numerous studies have shown that the presence of alkali cations increase the dissolution rate of both crystalline and amorphous silica. At near neutral pH and

ambient temperatures, Bennett (75) showed the NaCl and KCl increased rates by approximately 5-8 times. Dove and Crerar (61) and Berger (99) showed rate increases by a factor of 6 in the presence of these ions. At higher temperatures, Na^+ and K^+ increased dissolution rates by a factor of 33 (61). This has been proven more recently at higher pH by Ali et al. (83) who studied the effect of Na^+, K^+ and Ca^+ on quartz dissolution from a near neutral pH of 6.5 up to highly alkaline pH of 12.5. Every solution had equimolar concentrations of the metal cation – 0.05 M, the reaction temperature was 70 ^oC and the only variable was the pH. It was found that even up to a pH of 12.5, the rate enhancing properties of Na^+ and K^+ were still observed in the following order (83):

$$Ca^{2+} < Na^+ < K^+$$

While some cations have rate enhancing effects, others were shown to retard crystalline silica dissolution. According to several authors (78, 80-82, 100), cations that retard the dissolution process are Li^+, Al^{3+} and Mg^{2+}. There was some disagreement between Dove and Nix (78) and the other authors about the role of Li^+ with the former stating that Li^+ has the same rate enhancing properties as Na^+ and K^+. This was not in agreement with the experimental results shown in Figure 4.6 – no detectable amount of cristobalite dissolved in the presence of Li^+. Even after 24 hours in 5 M LiOH, none of the cristobalite had dissolved.

The role of CsOH in crystalline silica dissolution literature is more muted. Wijnen et al. (87) showed that silica gel dissolution followed the trend:

$$LiOH \approx CsOH < RbOH \approx NaOH < KOH$$

This is not an ideal comparison because the dissolution of silica gel was studied by the author, which is amorphous. However, this trend is partially in agreement with the results shown in Figure 4.6 which is:

$$LiOH << CsOH < KOH < NaOH$$

From the literature highlighted thus far, it seems that monovalent cations are generally rate enhancing with the exception of Li^+ whereas divalent and trivalent cations such as Mg^{2+}, Ca^{2+} and Al^{3+} are rate retarding. Possible reasons for this trend are detailed as follows:

a) Hydrated radii shielding

The cations which retard silica dissolution the most, i.e. Li^+ and Cs^+, have the largest hydrated radii as shown in Table 2.1. Li^+ and Cs^+ have average hydrated radii of 367 pm and 329 pm respectively. Also, the other cations which were reported in literature to slow down the dissolution reaction have the largest average hydrated radii: Mg^{2+} = 364 pm, Ca^{2+} = 416 pm and Al^{3+} = 400 pm.

It was initially expected that cations with a larger hydrated radius adsorb onto the negatively charged silica surface and sterically block the approach of the hydroxide ion thereby preventing the subsequent siloxane bond cleavage from occurring. Dove (74) cites that the cations enhance dissolution rates in proportion to solvation properties which control water mobility and surface shielding. This seems plausible given that the hydration radii and hydration free energies are larger in the trivalent and divalent ions as well as lithium – all the cations which retard dissolution. However, the hydration spheres forming around these cations

are not static but are in constant exchange with water in the bulk solution (78). A constant known as the solvent exchange frequency (K_{ex}) measures the rate of exchange of water molecules in the primary hydration sphere around the metal cation with water in the bulk fluid. The value of K_{ex} in Mg^{2+},Ca^{2+}, Li^{+}, Na^{+}, K^{+} and Si^{4+} are summarised in Table 4.1.

Table 4.1 Solvent exchange frequency of different cations (78)

Cation	K_{ex} (S^{-1})
Mg^{2+}	$10^{5.2}$
Ca^{2+}	$10^{8.5}$
Li^{+}	$10^{8.8}$
Na^{+}	$10^{9.0}$
K^{+}	$10^{9.2}$
*Si^{4+}	$10^{0.52}$

*Si^{4+} in $H_3SiO_4^-$

The divalent, higher charge density metal cations – Mg^{2+} and Ca^{2+} have lower solvent exchange frequencies than Li^{+}, Na^{+} and K^{+} implying that the monovalent cations have a weaker hold on their hydration waters since they are constantly in exchange with water in the bulk solution. The difference in K_{ex} between Li^{+} and the other monovalent cations can be considered negligible. The large difference in the dissolution behaviour of cristobalite in the presence of Li^{+} compared with the other monovalent cations is therefore unlikely to be caused by the metal cation blocking the approach of the OH^{-} towards the silica surface.

The solvent exchange frequency of the silicon cation on the other hand is orders of magnitude lower than all the metal cations, i.e. it has a strong hold on its hydration water molecules. The initial hypothesis that the adsorbed hydrated metal cations with larger radii - Li^{+}, Ca^{2+} and Mg^{2+} leads to surface shielding is unlikely to be the cause of dissolution retardation. The cations have a weak hold on the water molecules around them and are in constant flux with the water molecules in the bulk and will not be able to 'shield' against the approaching hydroxide ion.

The temperature at which dissolution takes place has also been reported to influence the behaviour of the cation hydration spheres. At 25 ^{o}C, it was reported (99) that the hydration sphere of sodium interacts weakly with the silica surface whereas at 150 ^{o}C (more representative of temperatures used in the autoclave) the hydration sphere interaction with the silica surface is limited, possibly because of thinning of the hydration sphere at higher temperatures.

Based on the evidence provided so far and the dissolution trends with respect to the metal cation present in solution, it is implausible that surface shielding by the hydrated metal cations is responsible for the results shown in Figure 4.6.

b) Hydration water orientation aiding siloxane cleavage

The K_{ex} of the Si^{4+} in $H_3SiO_4^-$ (shown in Table 4.1) is orders of magnitude larger than that of the metal cations. The K_{ex} determined by ^{17}O-NMR was shown to be $10^{0.52}$ s^{-1} = 3.3 s^{-1} (78).

Silicon has a larger charge density than the metal cations because it has four valence electrons spread out over a smaller ionic radius, i.e. a high charge density. Literature values for the charge density of Si^{4+} are not available but is calculated as (25):

$$Charge\ density\ = \frac{Z^2}{r} \tag{4.7}$$

$$Si\ charge\ density\ = \frac{4^2}{26\ pm} = 615 \times 10^{-3}\ pm^{-1}$$

where r = Si radius = 26 pm (101)

The Si charge density is an order of magnitude larger than the monovalent cations K^+ and Na^+. Dove and Nix (78) suggested that the high charge density of the silicon atom strongly orients nearby hydration water molecules to a favourable position allowing water to act as a nucleophile. This is illustrated in Figure 4.7.

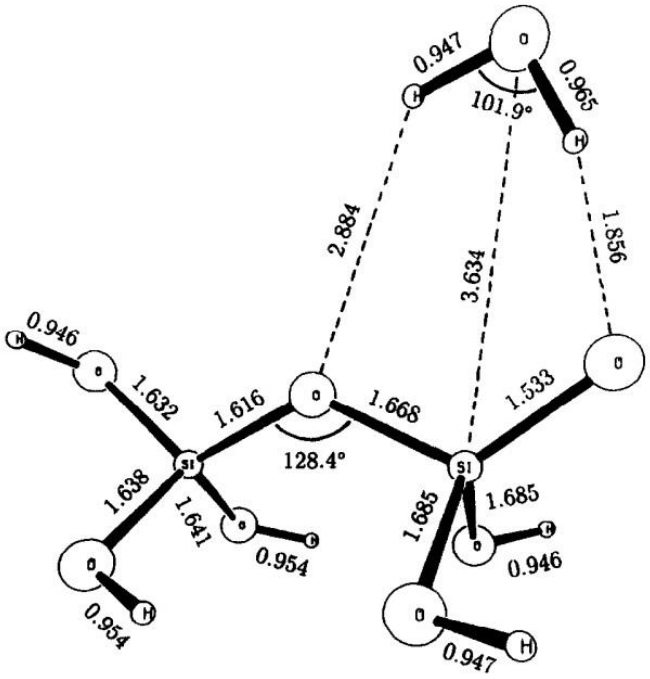

Figure 4.7 Water acting as a nucleophile under favourable conditions (52)

The authors of Figure 4.7 used Ab initio quantum mechanical simulations to model approach of a water molecule towards a crystalline silica (quartz) surface. Disilicic acid was used to represent the quartz surface and the metal cations were not included in the study. The oxygen in the polar water molecule acts as a nucleophile and attacks the Si atom creating a five-fold coordinated silica compound which, as explained in the literature review, is the prerequisite step before siloxane cleavage occurs. This is better illustrated in Figure 4.8.

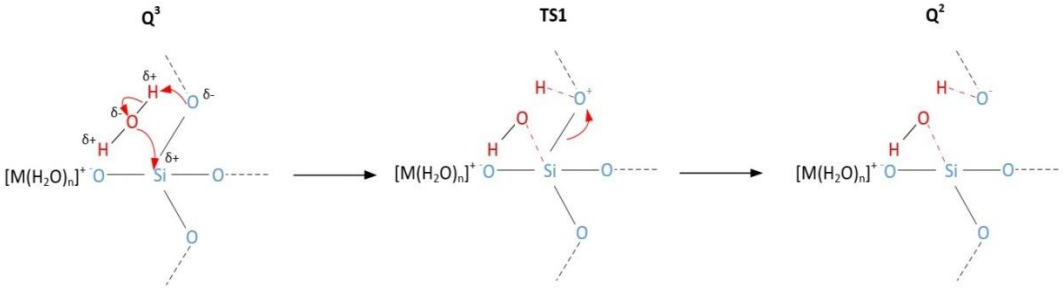

Figure 4.8 Detailed mechanism of water behaving as a weak nucleophile at the silica surface with adsorbed hydrated metal cations

Figure 4.8 shows the transformation of a Q^3 surface Si atom (three siloxane bonds) to Q^2 (two siloxane bonds) via the transition state – TS1. One of the two lone electron pairs from the oxygen forms a bond with the silicon atom creating a five-fold coordinated compound. This time, only one of the hydrogens in the water molecule forms a bond with the bridging oxygen atom. The surface oxygen atom is inaccessible because of the adsorbed metal cation which was not accounted for in Figure 4.7.

The surface Si atom now has a five-fold coordination (TS1) with two silanol (Si-OH) groups attached. While the first silanol group is formed by nucleophilic attack of the oxygen in the water molecules, the second silanol group is expected to form between the bridging oxygen atom (partial negative charge) and hydrogen from the water molecule as shown in Figure 4.8 (TS1). The formation of the second silanol group creates positively charged oxygen coordinated with three other atoms. This is unstable and ultimately yields to cleavage of the siloxane bonds forming a Q^2 Si. This reaction mechanism is similar to the nucleophilic substitution reactions of halogenoalkanes with water acting as a weak nucleophile (102).

Based on the reaction mechanism shown in Figure 4.8, it is plausible that metal cations with the following properties will allow for re-orientation of their hydration waters into more favourable positions when in proximity with the high charge density Si atom:

- Small hydration free energy
- Large solvent exchange frequencies

The dependency of cristobalite dissolution on the type of metal cation present in solution (Figure 4.6) supports the hypothesis that cations with a small hydration free energy and large solvent exchange frequencies (Na^+ and K^+) enhance dissolution whereas the cations with larger hydration free energy and smaller solvent exchange frequencies (Li^+) retard the reaction. The literature on Cs^+ is sparse but experimental work covered in Section 4.2.2 will discuss this further.

The wider literature covering the metal cations that retard silica dissolution also supports this hypothesis. The rate retarding properties of Al^{3+} and Mg^{2+} have been widely cited (79-81, 103) and a plausible reason for this could be that these higher charge density cations have a stronger hold in their hydration waters thus, any re-orientation of the water molecules into more favourable positions to aid silica dissolution is more difficult to achieve.

c) Formation of insoluble products

From the literature (79-82, 103, 104), the formation of insoluble reaction products on the silica surface is the most likely explanation for the retarding effect of some cations. This is true for cations with large charge densities, i.e. trivalent and divalent ions. Al^{3+}, Mg^{2+} and Ca^{2+} have all been shown to retard silica dissolution. For the monovalent cations, only Li^{+} has been reported to significantly retard silica dissolution.

The most plausible reason for this, based on the literature review and evidence covered in section 4.2.2 is that the metal cations with large charge densities are strongly attracted to the negatively charged cristobalite surface at a high pH and form insoluble products as discussed in Section 4.2.2. These cations withdraw some electrons from the cristobalite surface, forming an insoluble complex: Si-O-M (74, 104).

On the other hand, the cations with lower charge densities which enhance dissolution (K^+ and Na^+) form complexes that are soluble because of the weaker attraction of the metal cation to the cristobalite surface (104).

The Eisenman model assumes that both the binding site (O^-) and the Group IA cations are charged spheres. The smaller the ionic radii, the larger it's affinity for the negatively charged binding site (105).

The Eisenman binding selectivity sequence for the 5 Group IA cations have 11 possible permutations. The sequence most frequently observed is (105):

$$Li^+ > Na^+ > K^+ > Rb^+ > Cs^+$$

According to a recent study (105), this permutation of the selectivity trend was observed 61% of the time – a significant majority. The next frequent permutation was observed only 9.3% of the time. The binding selectivity trend depends on the concentration of O^- on the silica surface and larger O^- concentrations favour this trend. As previously mentioned, the silica surface becomes increasingly negatively charged as the pH increases. Above a pH of 12, the entire silica surface is negatively charged (77) and consists of ≡Si-O^-. At the 5 M OH^- concentration used in this experiment, the pH is 14.7 and it can be safely assumed that any silanol groups (Si-OH) are deprotonated. Therefore, the Eisenman binding selectivity sequence highlighted is the likely adsorption trend for the metal cations on the silica surface.

The binding selectivity sequence follows the same trend as the ionic radii trend with Li^+ being the smallest and Cs^+ the largest. Ignoring Rb^+ which wasn't used in the experiments, the binding selectivity sequence for the cations considered is:

$$Li^+ > Na^+ > K^+ > Cs^+$$

The cations at either extreme – Li^+ and Cs^+, completely arrested or retarded (respectively) cristobalite dissolution even at a very high pH. Dissolution was fastest in Na^+ followed by K^+. The reason for this is examined in Sections 4.2.2 and 4.2.3.

4.2.2 X-Ray Diffraction Analysis of Undissolved Cristobalite

X-Ray diffraction (XRD) analysis of partially dissolved cristobalite samples in equimolar concentrations of different alkaline solutions was used to determine the presence of any insoluble products on particle surface. The XRD pattern of undissolved cristobalite after reacting with 5 M LiOH, NaOH, KOH and CsOH for 6 hours is shown in Figures 4.9 – 4.12.

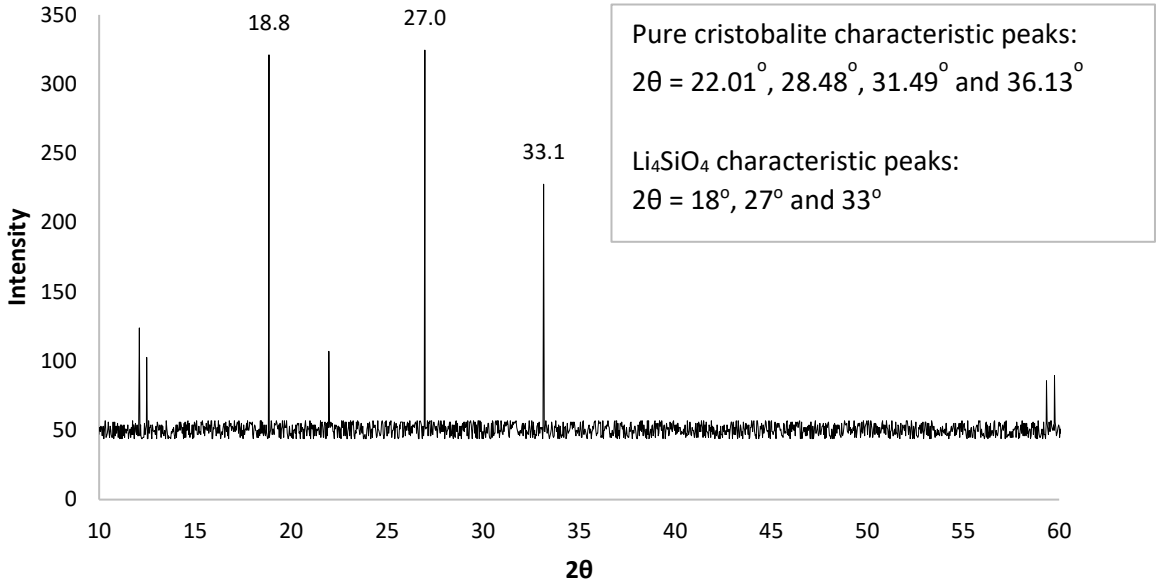

Figure 4.9 XRD pattern of cristobalite after dissolution in 5 M LiOH for 6 hours [source: Cristobalite peaks (106), lithium silicate peaks (107)]

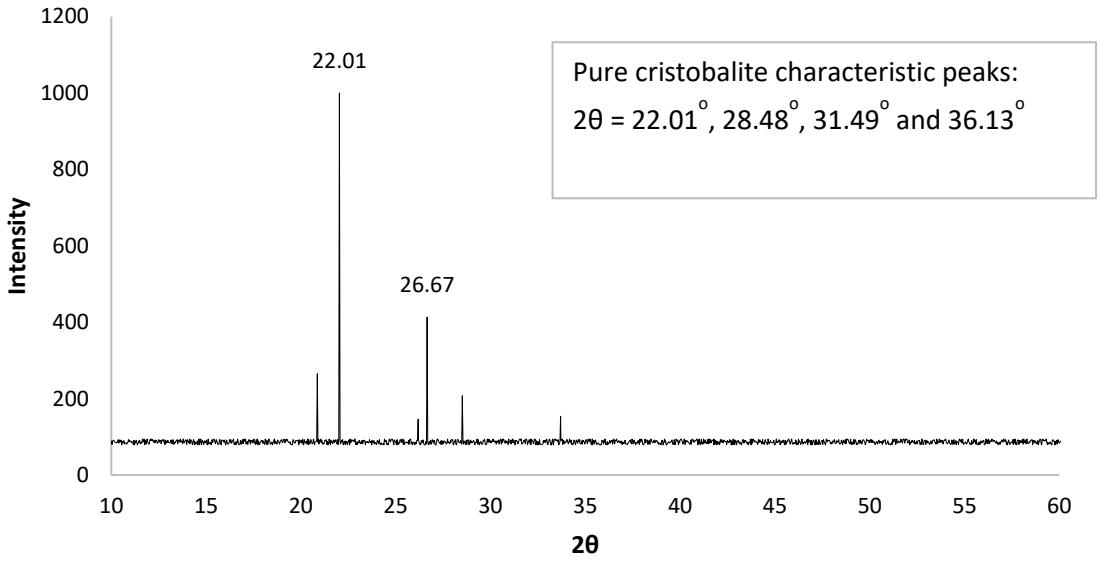

Figure 4.10 XRD pattern of cristobalite after dissolution in 5 M NaOH for 6 hours [source: Cristobalite peaks (106)]

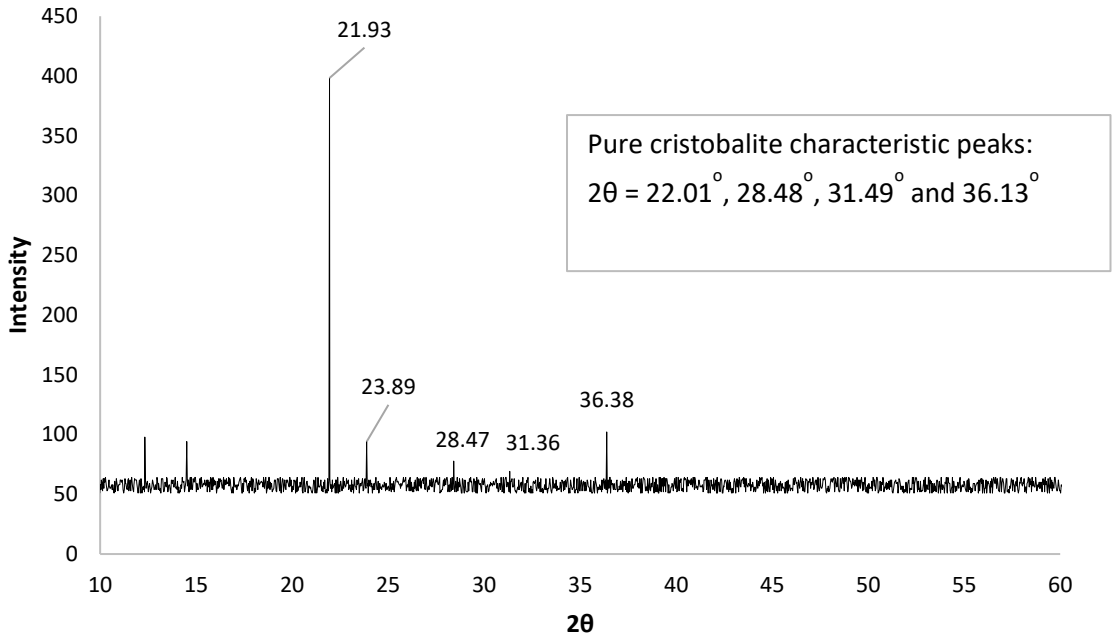

Figure 4.11 XRD pattern of cristobalite after dissolution in 5 M KOH for 6 hours [source: Cristobalite peaks (106)]

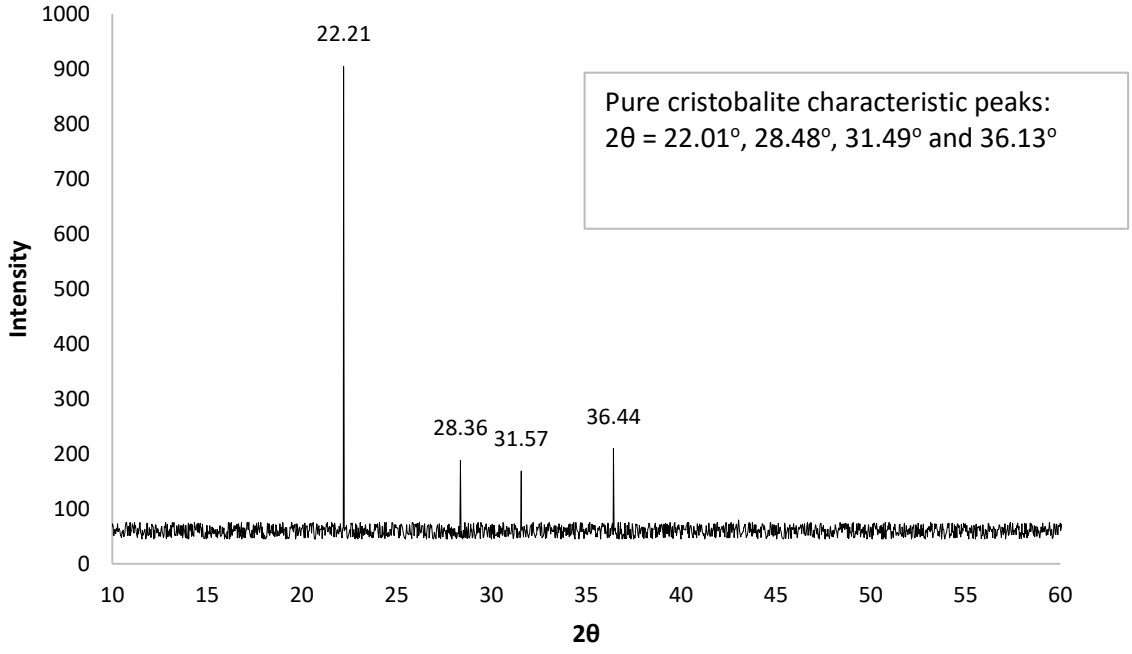

Figure 4.12 XRD pattern of cristobalite after dissolution in 5 M CsOH for 6 hours [source: Cristobalite peaks (106)]

The XRD pattern of partially dissolved cristobalite in LiOH has the largest deviation from pure cristobalite. Initially, it was hypothesised that a layer of

insoluble lithium silicates formed on the cristobalite surface and arrested the dissolution. However, XRD is not surface sensitive. Therefore, a more likely explanation is that the cristobalite has fully converted to insoluble lithium silicates, based on characteristic peaks of Li_4SiO_4 (107).

The surface structure of cristobalite dissolved in NaOH and KOH remained unchanged after 6 hours in solution. In NaOH, there was a slight deviation of the XRD pattern from a pure cristobalite sample. The secondary peaks at 28°, 31° and 36° were not observed, instead a secondary peak at 26.7° was observed. This is unlikely to be sodium silicate on the cristobalite surface because sodium silicates are water soluble. Also, the primary peak for a sodium silicate sample was found (108) to be at 2θ of 31° and no secondary peaks between 25° and 28°. The lack of the characteristic secondary peaks on the cristobalite sample dissolved in NaOH is likely to be an experimental error and not indicative of sodium silicate formation on the cristobalite surface. The secondary peak at 26.7° could be indicative of quartz however it is unclear why quartz would form on the surface of cristobalite after dissolution in NaOH.

Cristobalite dissolved in CsOH had the same XRD pattern as shown in samples dissolved in NaOH and KOH. Cs^+ ions did not form an insoluble complex as in LiOH. This was expected because of the relatively larger ionic size and lower charge density of the cation. The Eisenman binding selectivity sequence predicts that smaller ions are more strongly attracted to the silica surface whereas larger

ions such as Cs^+ are less strongly attracted therefore less likely to form an insoluble complex.

During cristobalite dissolution, a five-fold coordinated Si compound is formed as a result of the nucleophilic attack of OH^- on the Si atom; this is expanded upon in Section 4.3. This five-fold coordinated compound is the transition state that exists prior to siloxane bond cleavage. It was hypothesised (58) that the adsorbed metal cations increase the Si-O bond length thereby weakening the strength of the siloxane bond and reducing the activation energy of the subsequent siloxane cleavage. The cations at the extremes of the Eisenman binding selectivity sequence – Li^+ and Cs^+ completely arrest or retard the dissolution process respectively. In the case of Cs^+, It has the lowest charge density of the four cations considered and did not form an insoluble surface complex of caesium silicates.

One possible reason for dissolution retardation in CsOH is that the lower sorption strength of Cs^+ does not lead to a significant elongation of the Si-O bond. This would imply that Na^+ and K^+ have an ideal sorption strength onto the silica surface, not too strong like Li^+ and other divalent and trivalent cations which form an insoluble surface compound and not too weak like Cs^+ which may limit siloxane bond elongation and increase the activation energy of siloxane cleavage (58).

4.2.3 Mixed Cation Solutions

Cristobalite dissolution in mixed cation solutions was used to understand the sorption preferences of the negative charged cristobalite surface in the presence of competing cations. The reaction temperature was 95 ^{o}C and all solutions had the same OH^- concentration.

Cristobalite dissolution in NaOH was the fastest whereas in LiOH, no dissolution occurred. A 5 M OH^- solution with 2.5 M Na and 2.5 M Li mixture was prepared. The pH and ionic strength of the mixture is the same as a pure solution of NaOH or LiOH therefore, any deviation of the dissolution curve of the mixture compared to the pure solutions is primarily caused by sorption behaviour of the competing ions.

It was initially expected that cristobalite dissolution in a mixture of Na^+ and Li^+ would exhibit rates that were disproportionately controlled by Li^+ since it is the smaller ion with a larger charge density and stronger sorption strength. The results are shown in Figure 4.13.

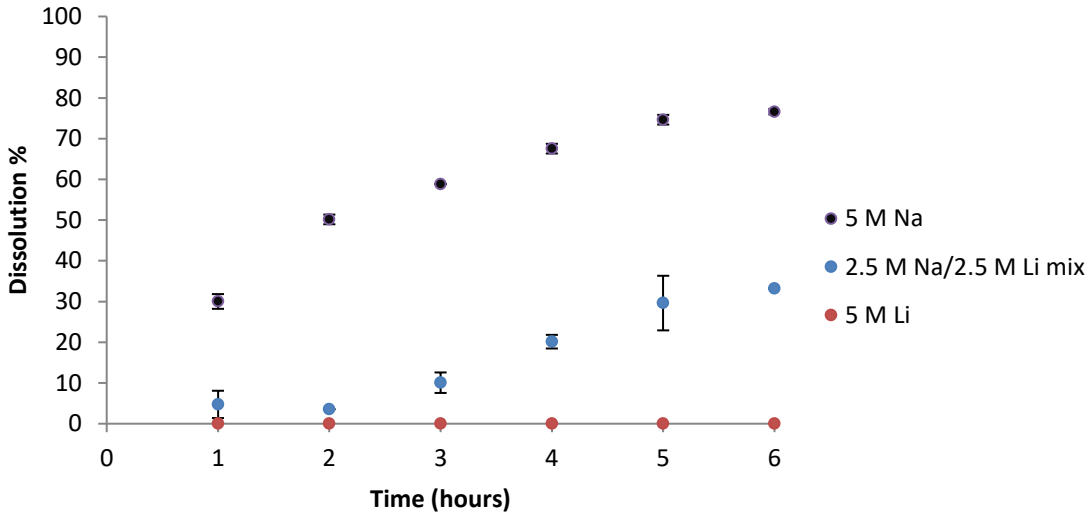

Figure 4.13 Cristobalite dissolution in mixed cation solutions of Na+ and Li+ and 5 M OH^-

After 6 hours, the amount of cristobalite dissolved in the mixed cation solution was more than halved from 77% in pure NaOH down to 33% in the presence of Li^+. This is in agreement with the literature where it was found that addition of rate retarding cations like Ca^{2+} and Mg^{2+} reduced the amount of dissolved crystalline silica by about 37% (74). Li^+ acts as an inhibitor to the reaction because it is preferentially adsorbed onto the silica surface thereby reducing the rate enhancing ability of Na^+. The silica grain is however not completely converted into insoluble lithium silicates because dissolution is not completely arrested in the mixed cation solution.

The dissolution curve in the mixed cation solution is sigmoidal – an initial induction period exists in the first two hours with limited dissolution followed by an increase in the dissolution rate over the next four hours. The cause of this is unclear but could be because of an initial saturation of the silica surface with Li^+ with only a small portion of Na^+ being adsorbed. As the silica particles are gradually dissolved, surface roughness on a molecular scale increases the

concentration of Q^2 Si atoms which are easier to detach from the silica structure. The precise mechanism behind this is expanded upon in Section 4.3.5.

Dissolution in mixed cation solutions containing Na^+ and K^+ produced more surprising results. Two solutions were prepared – an equimolar mix of Na^+ and K^+ at 2.5 M each (same ratio as the Na^+ and Li^+ mix) and another solution with 4 M K and 1 M Na. The dissolution curves are shown in Figure 4.14.

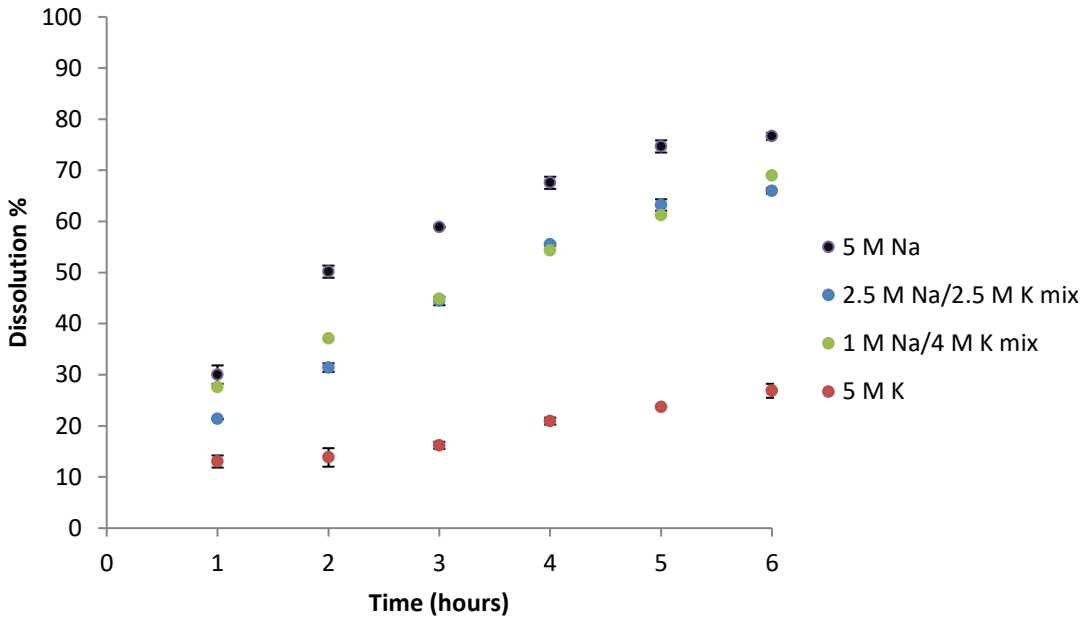

Figure 4.14 Cristobalite dissolution in mixed cation solutions of Na+ and K+ and 5 M OH^-

The addition of Na^+ increased the amount of cristobalite dissolved after 6 hours by a factor of 2.5. This was still below the amount dissolved in a pure NaOH solution but nevertheless, significantly larger compared to a pure KOH solution. Also, the dissolution curves for the 2.5 M Na/2.5 M K solution and the 1 M Na/4 M K solutions were almost identical.

This implies that Na^+ ions are likely to have a disproportionate effect on the dissolution rate relative to their concentration. This cannot be attributed to preferential binding of the smaller Na^+ ion alone. This is probably due to viscosity differences in the reactions products – potassium silicates have been shown, both experimentally and in literature, to be more viscous than sodium silicate solutions at identical concentrations. Adding Na^+ ions into a potassium silicate solution was expected to reduce the viscosity of the overall solution. The rheological properties of the silicate solutions will be detailed in Section 4.5.

Another interesting observation from the 1 M Na/ 1 M K solution was that the dissolution rate was constant over the 6 hour period, similar to the pure 5 M KOH solution whereas in the pure 5 M NaOH solution, the initial rate is fast but slows down after 6 hours. As shown in Chapter 7, mixed cation solutions in the pilot scale trials were undertaken to determine if the rate increase using a 1:4 molar ratio of Na^+ to K^+ in the lab would be observed using real cores in an autoclave.

The limitation of the mixed cation dissolution experiments is that it is difficult to isolate a single variable, i.e. the surface chemistry effect of the cations and how they affect the dissolution process. The reaction products – aqueous solutions of lithium, sodium and potassium silicates form a fluid film layer around individual silica particles and the rheological properties of this layer will inadvertently affect the dissolution rates. A highly viscous fluid film layer enveloping the silica particle will slow down the diffusion of OH^- and $[M(H_2O)]^+$ towards the silica surface.

4.2.4 Conclusion

XRD analysis showed that the cristobalite surface remained unchanged after 6 hours of dissolution at 95 ^{o}C in equimolar aqueous solutions of NaOH, KOH and CsOH. After dissolution in NaOH, quartz seemed to form on the cristobalite surface however the reason behind this remains unclear. In LiOH, the cristobalite grains are converted into insoluble lithium silicate crystals effectively arresting the dissolution process.

Crystalline silica has been reported to dissolve 33 times faster in the presence of $Na^{+}$and K^{+}, relative to dissolution in de-ionised water (61). The precise mechanism of this rate enhancement is not fully understood and the literature is often contradictory. However, some of the evidence from literature and the experiments covered in this section are in agreement. Dissolution of crystalline silica is enhanced by the presence of Na^{+} and K^{+}, retarded in Cs^{+} and arrested in Li^{+}.

In the presence of Na^{+} and K^{+}, it was expected that these cations passively improve dissolution rates without reducing the activation energy (74). As explained in Chapter 2, this can be attributed to a change in the pre-exponential constant (A) in the Arrhenius Equation.

According to Bickmore el a. (82) these cations passively increase the dissolution rate by increasing the reaction frequency. The precise mechanism of the rate increase in the presence of some cations is unclear. It was proposed (60) that adsorption of Na^+ led to elongation of the siloxane bonds thereby making it easier for the attacking OH^- to form the five-fold coordinated complex – a prerequisite for siloxane cleavage. Cations with a lower charge density have weak interactions with the silica surface and could be the reason for dissolution retardation in the presence of Cs^+.

As a result its small ionic radius and high charge density, lithium forms an insoluble complex (Si-O-Li) on the cristobalite surface as shown by the XRD analysis. This insoluble layer acts as a resistance to dissolution by preventing further nucleophilic attack of OH^- on the Si (detailed in Section 4.3).

4.3 Nucleophilic Attack on Si and Siloxane Cleavage

The crystalline silica structure shown in Figure 4.5 shows a smooth surface comprised of Q^3 Si and adsorbed metal cations, which retain some of their hydration waters. In order to remove a single $(SiO_4)^{4-}$ unit from the silica surface into solution, three siloxane (Si-O-Si) bonds need to be broken. The Si atom will transform from one that has three siloxane bonds attached to zero, i.e. Q^3 to Q^0 with three transition states (TS) between each transformation:

$$Q^3 \xrightarrow[TS1]{} Q^2 \xrightarrow[TS2]{} Q^1 \xrightarrow[TS3]{} Q^0$$

OH^- acts as a nucleophile and is attracted to the partial positive charge on the Si atom. For a Si atom to transform from Q^3 to Q^0, three scenarios of attack by OH^- are possible. A single OH^- could attack one Si with another two OH^- ions attacking the two adjacent Si atoms, three OH^- ions could attack a single Si atom or two OH^- could attack a single Si with another OH^- attacking the adjacent Si. This third scenario is illustrated as an example in Figure 4.15.

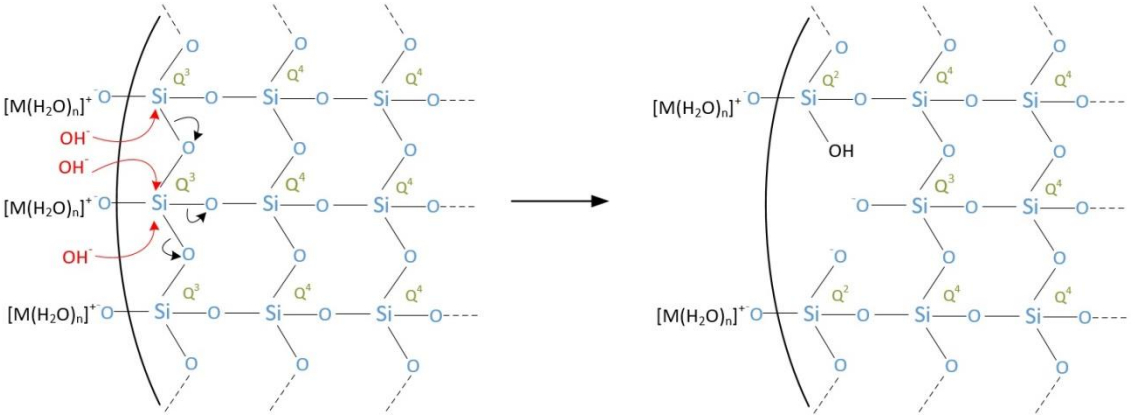

Figure 4.15 Nucleophilic attack of OH- and siloxane cleavage

Any Si atom that is attacked and not detached from the silica surface is left with a silanol group (Si-OH) as shown in Figure 4.15. The precise mechanism as to whether three OH^- ions attack a single Si or two attack the Si atom and another attacks the adjacent Si is not of any great importance. From the perspective of the Si atom detached from the silica surface, three transformations occur during the cleavage of its three siloxane bonds. Each transformation involves the formation of a five-fold coordinated compound followed by a siloxane cleavage.

This section will cover the dissolution rate of cristobalite in alkaline solutions, the different variables that influence it, the rate determining step of the process and

a detailed reaction mechanism. The activation energy of the process is also covered using an isoconversion model which account for changing surface morphologies as the reaction proceeds.

4.3.1 Effect of [OH] on Dissolution Rate

Allen et al. (77) reported that above a pH of 12, the entire silica surface consists of ≡Si-O^- sites. Brady and Walther (60) found that the dissolution rates of quartz were proportional to [≡Si-O^-]. Dissolution experiments were carried out at OH^- concentrations of 0.5 M – 10 M. The pH range at these concentrations is 14.3 – 15. It is safe to assume that the cristobalite surface is entirely composed of ≡Si-O^- sites at the OH^- concentrations used.

Figure 4.16 shows the dissolution curve of M006 cristobalite in equimolar concentrations of NaOH and KOH over 24 hours. The properties of M006 are shown in Table 3.1. Aliquots were analysed in three batches. The first batch between 0 – 6 hours, second batch between 10 – 22 hours with data collected every 4 hours and final batch at 24 and 25 hours.

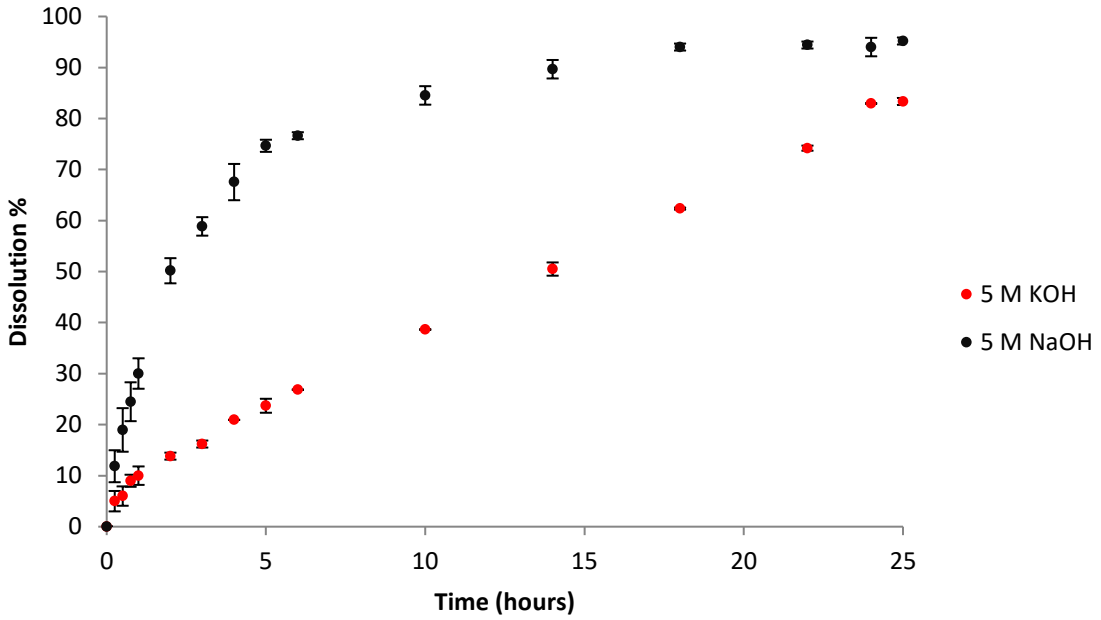

Figure 4.16 Dissolution curve of cristobalite (M006) in equimolar NaOH and KOH solutions for 25 hours at 95°C and stirrer at 300 rpm

Cristobalite dissolution in NaOH is faster than KOH at equimolar concentrations. In NaOH, the reaction seems to have two regimes – an initial period in the first 1 hour with a rapid dissolution rate followed by a steady rate decline for the remaining 23 hours. In KOH, two regimes are also observed – an initial rapid dissolution rate in the first 30 minutes followed by a constant rate for the remaining time. A likely reason for this will be explained subsequently.

To understand the effect of [OH^-] on the dissolution rate of cristobalite, solutions of NaOH and KOH at 0.5 M, 1 M, 2 M, 5 M and 10 M were prepared and reacted with cristobalite under the reflux set-up previously described. A magnetic stirrer at 300 rpm was used to agitate the solution and prevent settling of the cristobalite powder and the solution temperature was set at 95°C.

Figure 4.17 shows the dissolution curves of cristobalite M006 in different concentrations of NaOH.

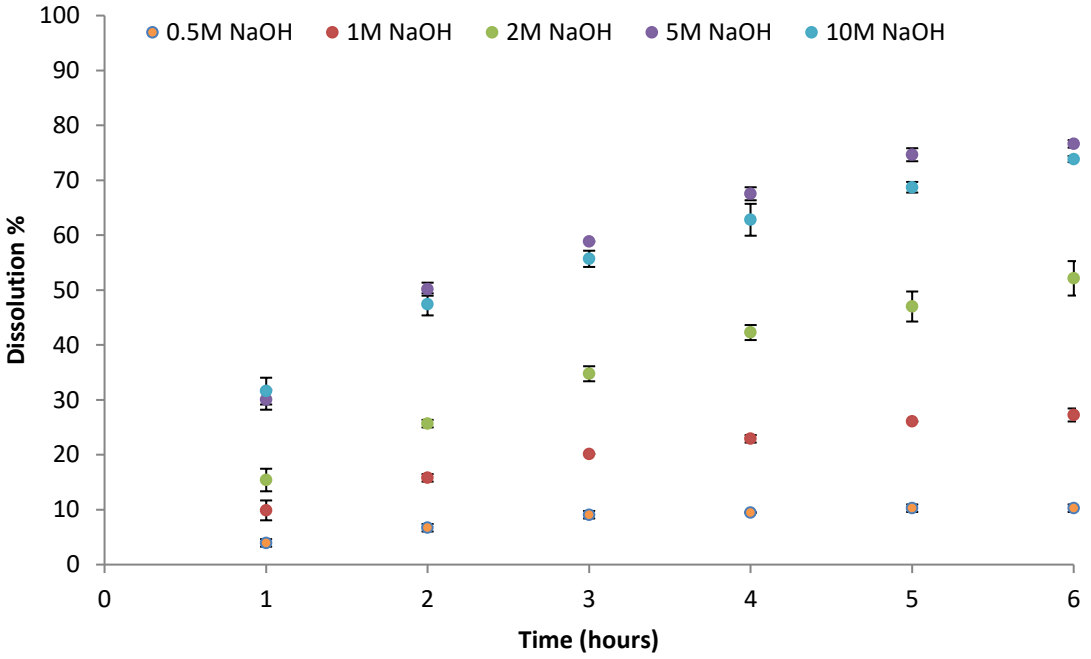

Figure 4.17 M006 cristobalite dissolution in different concentrations of NaOH

The dissolution rate in the first hour is significantly higher than the subsequent 5 hours, regardless of the initial concentration. A likely reason for this is that the M006 cristobalite supplied by Sibelco is made by iron free grinding to achieve the required particle size distribution. This could lead to the formation of a disordered amorphous layer on the cristobalite surface which is more susceptible to nucleophilic attack. A disordered cristobalite surface will have imperfections and more Q^2 and Q^1 Si atoms making it easier to form the five-fold coordinated complex before siloxane cleavage occurs. As discussed in the literature review,

the activation energy required to form this complex is larger than the energy required to break the siloxane bond and is the rate limiting step for the process.

From the literature, different dissolution curves have been observed – sigmoidal, parabolic, exponential, linear and logarithmic depending on the silica polymorph (109). Dissolution of silica aerogel in 0.8 M NaOH was reported to have a sigmoidal dissolution curve with a distinct induction period at the start of the reaction (110). In crystalline silica, no induction period has been observed and the dissolution curves shown in Figure 4.17 with a rapid initial rate are in agreement with experiments carried out by Jendoubi et al. (109).

Another important observation from the dissolution curves shown in Figure 4.17 is that the dissolution rate increases as the concentration of OH^- is increased. Determining the initial reaction rate is difficult because of the likely presence of an amorphous layer on the cristobalite surface formed during the grinding process which artificially accelerates dissolution.

Figure 4.18 shows the dissolution curves of cristobalite in KOH. A similar trend between $[OH^-]$ and dissolution % is observed in both NaOH and KOH – the dissolution rate increases as $[OH^-]$ is increased up to 5 M. At 10 M, the dissolution rate slows implying that the optimum concentration for cristobalite dissolution is between 5 M and 10 M regardless of the type of metal cation present.

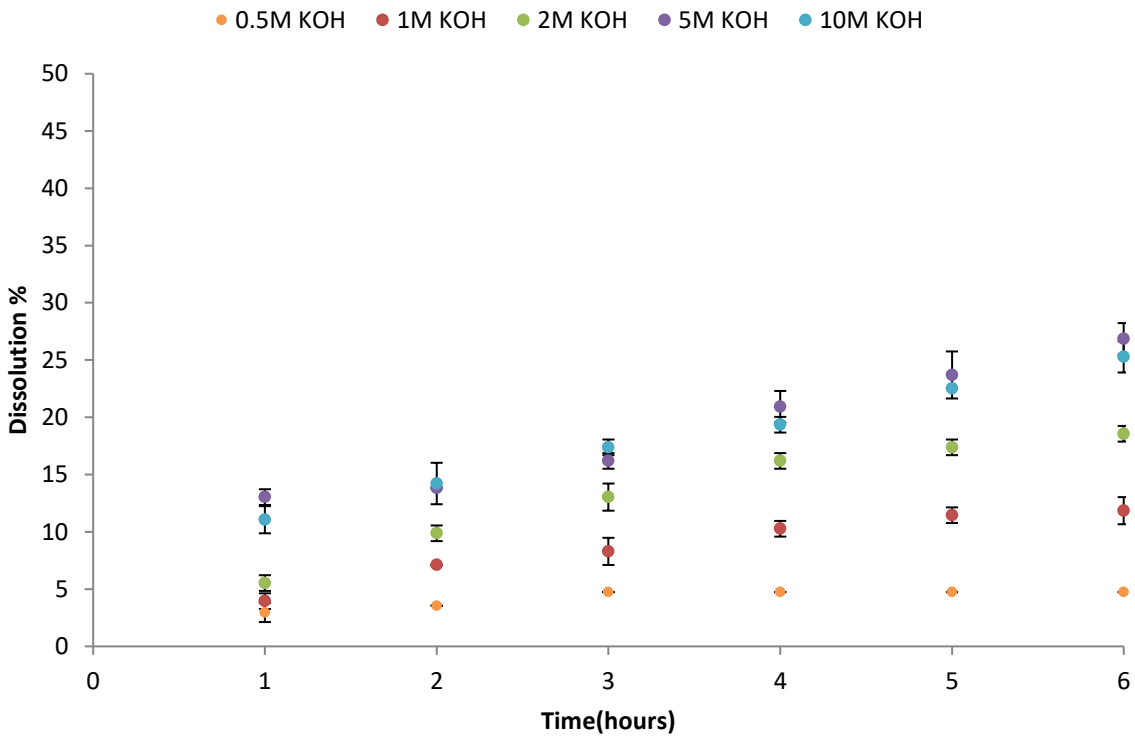

Figure 4.18 M006 cristobalite dissolution in different concentrations of KOH

In both NaOH and KOH, an optimal concentration for dissolution exists between 5 M and 10 M. Above the optimum concentration, the total amount dissolved after 6 hours actually declines as evidenced by the dissolution curve in 10 M OH^-. The reason for this is not fully understood – it was expected that beyond the optimal concentration, OH^- will be in excess relative to the available Si atoms susceptible to siloxane cleavage and the reaction rate will simply remain flat beyond this concentration. This is in agreement with dissolution experiments performed by Jendoubi et al. (109) where the dissolution rate steadily increased as [OH^-] increased from 0.5 M to 8 M whereas between 8 M and 12 M, the rate remained flat. At such high OH^- concentrations, clustering will reduce the concentration of free hydroxides which are the catalyst for silica dissolution (24).

4.3.2 Stirrer Speed and Rate Determining Step

The default stirrer speed for previous experiments was 300 rpm. In order to understand the effect of stirrer speed on cristobalite dissolution, the stirrer speed was increased to 1200 rpm.

Figure 4.19 shows the dissolution rate in 1 M NaOH and KOH solutions.

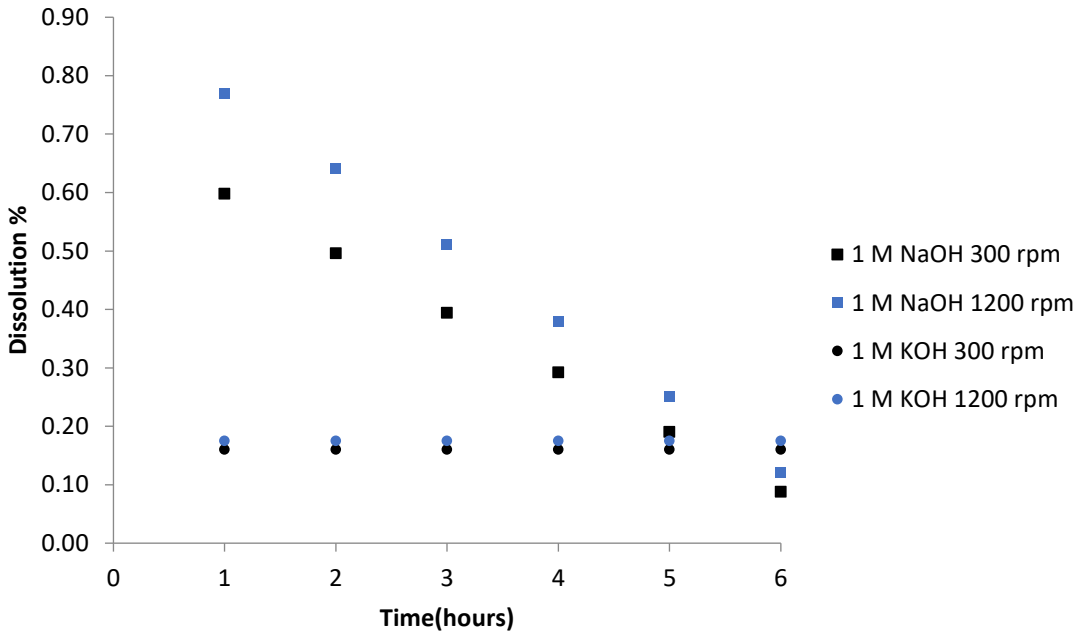

Figure 4.19 Effect of stirrer speed on cristobalite dissolution in 1 M NaOH and KOH

In NaOH, the dissolution rate at the start of the experiments is significantly faster compared to KOH, regardless of the stirrer speed. However, the rate steadily declined in NaOH whereas it remained constant in KOH. To understand why this was observed, the equilibrium of silicates in solution as well as its rheological properties needs to be understood.

As will be detailed in Section 4.4, the steady decline of the dissolution rate in NaOH occurs because of a build-up of monomeric silicates in solution. Silica dissolution produces silicate monomers in solution, which over time will form longer chain oligomers through a polycondensation reaction. ^{29}Si-NMR showed that equilibrium was shifted more to the right in KOH, i.e. in favour of more polymerised species compared to NaOH. The system responds by dissolving more silica to replace the monomers. In NaOH, a build-up of monomers in solution is hypothesised to be the reason why the rate steadily declines. This could also be the reason (as will be shown in Section 4.4.1) that NaOH loses its potency as a leachant through repeated re-use whereas KOH does not.

Increasing the stirrer speed in NaOH increased the dissolution rate by a factor of 1.3 over the entire 6 hours. In KOH, increasing the stirrer speed had no effect on the dissolution rate. This is likely caused by differences in the viscosity of the fluid film layer.

As will be explained in greater detail in Section 4.5, the viscosity of silicates is strongly dependent on the SiO_2:M_2O molar ratio. Higher ratios correspond to more siliceous solutions whereas lower ratios correspond to more alkaline solutions. At 1 M NaOH or KOH concentration, the fluid film layer will be more siliceous compared to a 5M solution because of the lower concentration of OH^-.

The dissolution rate in 1 M NaOH increased as the stirrer speed was increased because the fluid film layer viscosity was sufficiently large to be rate limiting. In KOH, the viscosity of the fluid film layer was much higher thus limiting the effect of the higher stirrer speed. This was proved correct in Section 4.5.2 which showed that potassium silicates are more viscous than sodium silicates at a high SiO_2:M_2O ratio. Sodium silicates displayed Newtonian behaviour across all SiO_2:Na_2O ratios analysed whereas potassium silicates displayed shear thinning and viscoelastic properties at high SiO_2:K_2O ratios of 3:1. More siliceous solutions of potassium silicates showed elastic solid-like behaviour which could explain why an increased stirrer speed had no effect at 1 M KOH, the viscosity of the fluid film layer may simply be too large.

The effect of a higher stirrer speed at 5 M NaOH and KOH concentrations further proves this point. From Figure 4.19, increasing the stirrer speed had a negligible effect on the dissolution rate in NaOH. In KOH however, the dissolution rate doubled at a higher stirrer speed. At a higher OH^- concentration, the fluid film layer will be more alkaline, i.e. lower SiO_2:M_2O ratios. A more alkaline fluid film layer will have a lower viscosity. In the NaOH solution, the sodium silicate fluid film layer no longer had a rate limiting effect, evidenced by the negligible change in dissolution rate at a higher stirrer speed.

In KOH, increasing the stirrer speed by a factor of 4 doubled the dissolution rate, possibly because of the lower viscosity of the potassium silicate fluid film layer

compared to the 1 M solution where it is likely that a solid-like gel formed around the cristobalite grains.

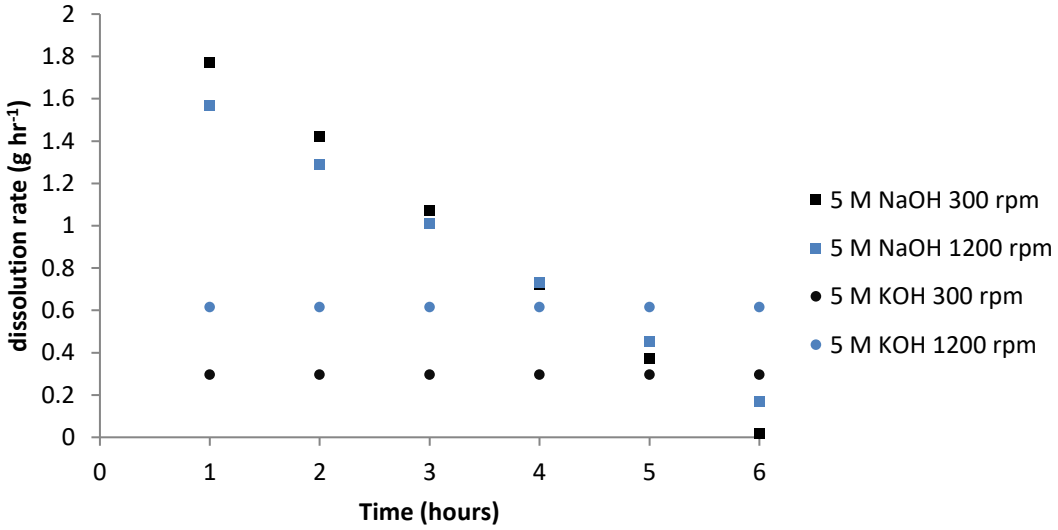

Figure 4.20 Effect of stirrer speed on cristobalite dissolution in 5 M NaOH and KOH

At a higher stirrer speed, the increase in the dissolution rate can be attributed to an increase in the rate of diffusion of OH^- through the fluid film layer which is explained through Fick's law (111):

$$N = -D_{OH}\Delta C \tag{4.8}$$

where N is molar flux (mol m^2 s^{-1}), D_{OH} is the diffusion coefficient (m^2 s^{-1}) and ΔC = concentration gradient across fluid film (mol m^{-3}).

For spherical particles moving through a viscous fluid, a good approximation of the OH^- molecule diffusing through the viscous potassium silicate fluid film layer, Stoke formulated an equation to show the relationship between the friction coefficient (f_0) and the radius (r) of the moving particle and the viscosity (μ) of the medium through which the particle moves:

$$f_0 = 6\pi\mu r \quad (4.9)$$

Einstein assumed Equation 4.9 could be applied to determine the diffusion coefficient (D_{OH}) of large molecules (112). This is known as the Stoke-Einstein relation:

$$D_{OH} = \frac{kT}{6\pi\mu r} \quad (4.10)$$

where T is the absolute temperature (K), K is Boltzmann's constant (1.38×10^{-23} m^2 kg s^{-2} K^{-1}) and r is the molecule radius (m).

In this case, diffusion occurs through a fluid film layer. According to film theory, the molar flux in Equation 4.8 at a steady state will be inversely proportional to the film thickness (113):

$$J_{OH} = \frac{D_{OH}C_e}{d} \quad (4.11)$$

where J_{OH} is diffusive flux through film layer (mol m^2 s^{-1}), C_e is equilibrium concentration of OH in film layer (mol m^{-3}) and d is film thickness (m)

Combining Equations 4.10 and 4.11, the relationship between the diffusive flux, viscosity and thickness of the fluid film layer is clear (112):

$$J_{OH} = \frac{kTC_e}{6\pi\mu rd} \quad (4.12)$$

This is however only applicable under a low Reynolds number, i.e. Re << 1 (114). In the bulk fluid, the Reynolds number is larger than 1. The action of a magnetic

stirrer in a round bottom flask is analogous to that of an impeller in a stirred tank reactor. The Reynolds number of a stirred tank is given as (115):

$$Re = \frac{ND^2\rho}{\mu} \quad (4.13)$$

where N is the stirrer velocity (m/s), D is the stirrer diameter (m), ρ and μ are the bulk solution density (kg m^{-3}) and viscosity (Pa s) respectively. The angular velocities of 300 rpm and 1200 rpm were converted into linear velocities by dividing the distance covered by the stirrer during a complete revolution by the time elapsed during that period. Applying this conversion, 300 rpm = 0.31 ms^{-1} and 1200 rpm = 1.26 ms^{-1}.

The bulk solution density and viscosity will depend on the alkaline solution concentration and the amount of silica dissolved in solution. However, to simplify the Reynolds number calculation, the solution is assumed to the pure KOH at a 5 M concentration. Density and viscosity data at 80 ^oC were obtained from Occidental (47) and Sipos et al. (45). The data at 95 ^oC was not available.

At 300 rpm:

$$Re = \frac{0.31 \times 0.02^2 \times 1127}{0.0015} = 93$$

At 1200 rpm:

$$Re = \frac{1.26 \times 0.02^2 \times 1127}{0.0015} = 379$$

According to Nienow (116), the fluid flow is laminar if the Reynolds number in a stirred tank < 10. Reynolds number > 20 x 10^4 means the flow is turbulent and Reynolds number between 10 – 20 x 10^4 means the flow is in the transition regime. For the stirred dissolution experiments described, both were in the transition regime in the bulk of the fluid. Diffusion can be assumed to be an important mechanism because even though the solution is vigorously stirred at a high rpm, the small size of the magnetic stirrer means that no turbulence is created.

The Peclet number is a product of the Reynolds number and the Schmidt number. The Reynolds number is the ratio of inertial to viscous effects while the Schmidt number is the ratio of viscous to diffusion effects (88, 117). The Peclet number is the ratio of inertial to diffusion effects. The calculation of the diffusion coefficient of OH^- is shown in equation 4.10.

$$Pe = \frac{ND^2}{D_{OH}} \tag{4.14}$$

In the bulk solution at 300 rpm, the Peclet number is:

$$Pe = 8.42 \times 10^4$$

At 1200 rpm, the Peclet number is:

$$Pe = 3.42 \times 10^5$$

In the bulk solution, inertial effects are more important than diffusion effects. It is assumed however that a no-slip boundary condition exists on the surface of the cristobalite grains. The viscosity and thickness of this fluid film boundary layer is not known.

The doubling of the dissolution rate in 5 M KOH at a higher stirrer speed can be attributed to a:

I. Reduction in fluid film layer viscosity by half
II. Reduction in fluid film thickness by half
III. Combination of I and II where the product of the fluid film viscosity and thickness is reduced by half

The three reasons listed above seem equally plausible. An increase in stirrer speed will increase the fluid velocity around the cristobalite grain which could lead to shearing of the viscous fluid film layer and a reduction in the thickness. As will be shown in Section 4.5.1, siliceous potassium silicate solutions display shear thinning behaviour so a reduction in viscosity at a higher stirrer speed is a possible explanation.

It is difficult to determine the primary cause of dissolution rate increase and a combination of a reduction in viscosity and fluid film layer thickness is possible. The increase in dissolution rate caused by a disruption of the viscous fluid film plays an important role in optimising autoclave cycle times and will be further explored in Chapter 7.

It should be noted that no specific claims about the absolute viscosity or SiO_2:M_2O molar ratios of the fluid film layer were made in this section. The exact concentration of the fluid film layer is unknown. However, at a lower OH^- concentration, it is assumed that it will be more siliceous hence more viscous. At a higher OH^- concentration, it will be more alkaline and less viscous.

The viscosity of sodium and potassium silicates as a function of SiO_2:M_2O molar ratios are discussed in Section 4.5 and support the results covered in this section.

4.3.3 Effect of Surface Area on Dissolution Rate

To determine the effect surface area had on the dissolution rate of cristobalite, initial rates were measured after 15 minutes from the dissolution curves shown in Figures 4.21 and 4.22. Previous dissolution experiments were carried out using M006 cristobalite (properties shown in Table 3.1). Cristobalite M3000 and M6000 had larger surface areas hence faster initial rates. In order to capture what occurs at the start of the reaction, initial rates were calculated at 15 minutes using a straight line fit over the first hour.

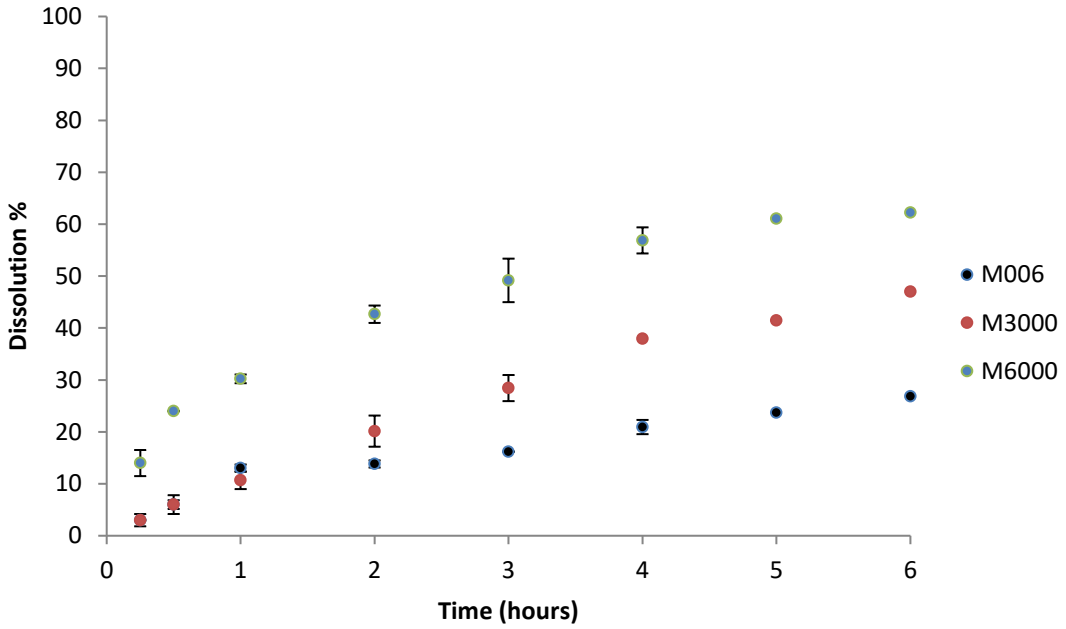

Figure 4.21 Effect of surface area on dissolution rate in 5 M KOH

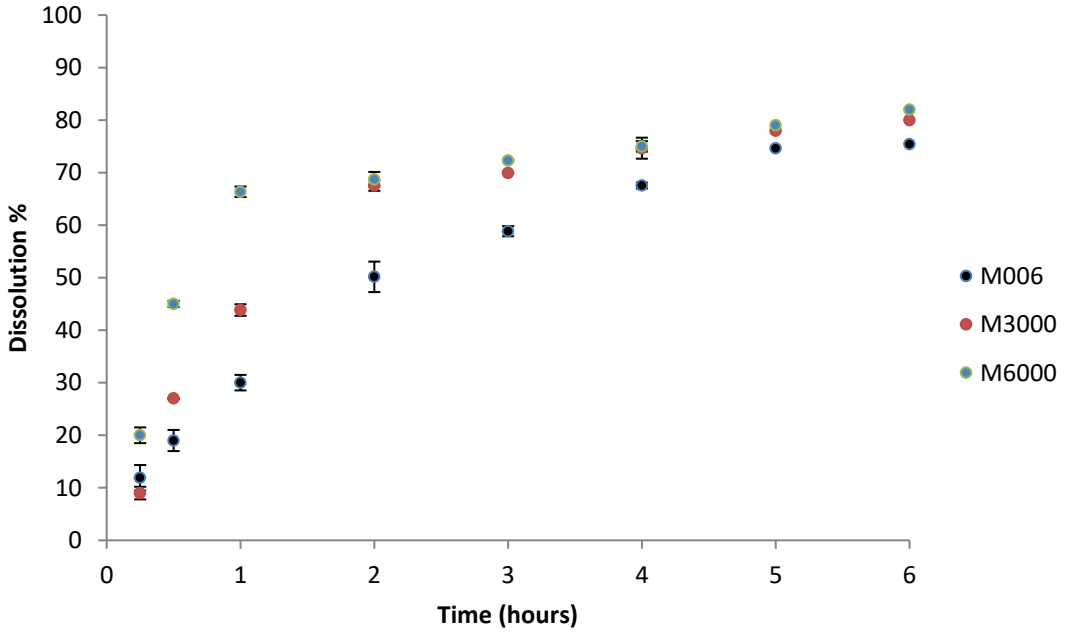

Figure 4.22 Effect of surface area on dissolution rate in 5 M NaOH

Tables 4.2 and 4.3 show the initial dissolution rates of cristobalite with different surface areas.

Table 4.2 Effect of cristobalite surface area on initial dissolution rate in 5 M KOH

Cristobalite name	**BET Surface area (m^2 kg^{-1})**	**Initial Rate (g hr^{-1})** [first derivative of dissolution equation at x =0.25 divided by 10]
M006	700	1.3
M3000	1500	1.2
M6000	5000	4.8

Table 4.3 Effect of cristobalite surface area on initial dissolution rate in 5 M NaOH

Cristobalite name	**BET Surface area (m^2 kg^{-1})**	**Initial Rate (g hr^{-1})** [first derivative of dissolution equation at x =0.25 divided by 10]
M006	700	3.9
M3000	1500	4.9
M6000	5000	8.5

Dissolution at the early stages will be dominated by the fines which explains why M006 and M3000 have similar dissolution rates in the first hour. As shown in Table 3.1, the D10 of M006 is 5 µm while M3000 is 4.5 µm.

Figure 4.22 shows the relationship between initial dissolution rates and cristobalite surface areas. In both NaOH and KOH, a two-fold increase in the surface area between 700 m^2 kg^{-1} to 1500 m^2 kg^{-1} had a negligible effect on the dissolution rate. It was expected that the initial rate wold increase proportionally to the surface area as a result of better contact with the alkaline solution and a larger area for the metal cations to adsorb onto. The reason for the initial rate decline in KOH even as the surface area approximately doubled remains unclear.

However, for surface areas between 1500 m^2 kg^{-1} and 5000 m^2 kg^{-1}, the initial rate increased by a factor of 4 in KOH and a factor of 1.7 in NaOH.

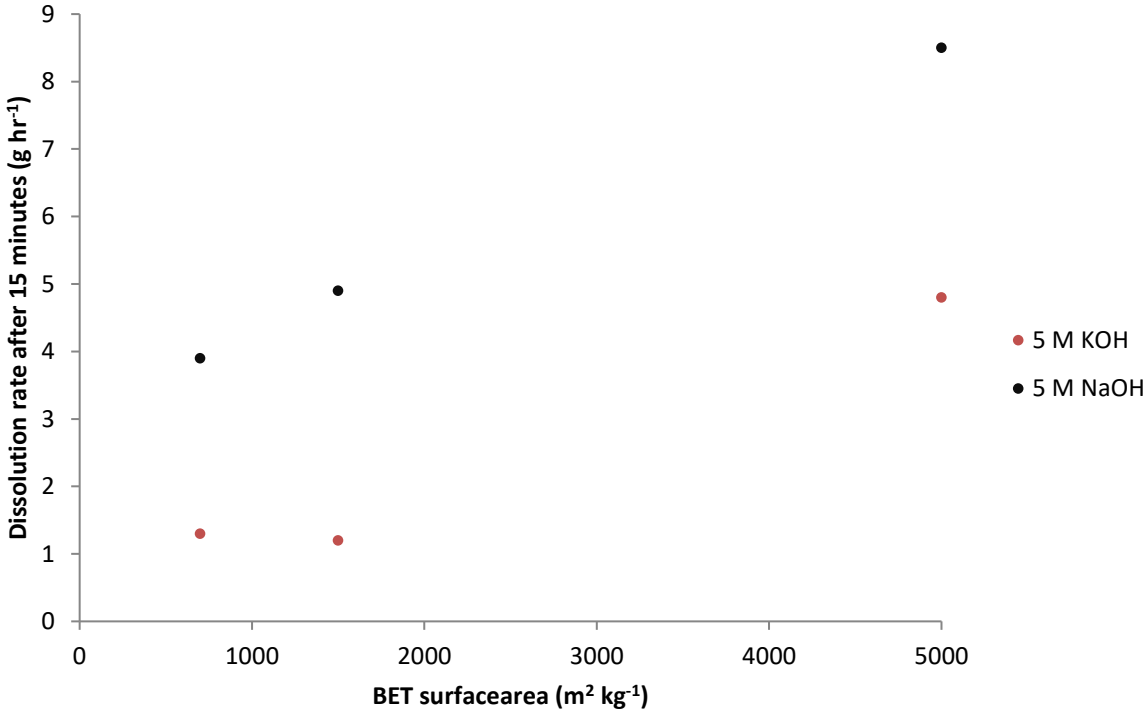

Figure 4.23 Effect of cristobalite surface area on initial dissolution rate

Dissolution in KOH is more strongly dependent on the cristobalite surface area compared to dissolution in NaOH. The only difference between the two solutions is the type of metal cation present. Therefore, any difference the dissolution rate between NaOH and KOH as a function of the surface area can be attributed to the metal cation. The metal cation affects adsorption behaviour on the cristobalite surface and rheology of the fluid film layer.

At the different surface areas considered, dissolution rates in NaOH exceeded KOH. A possible reason for this was explained in Section 4.2.1.

4.3.4 Reaction Controls

The ceramic core leaching process is a heterogeneous fluid-solid reaction. Such reactions experience different resistances which inhibit the reaction. The largest resistance experienced by the reacting species is known as the rate controlling step since the reaction rate is in essence, largely controlled by that step.

In the case of fluid – solid reactions, three main rate controlling steps are possible (88):

- Diffusion through ash layer controlled
- Diffusion through fluid film controlled
- Chemical reaction controlled

XRD analysis showed that no insoluble layer forms on the cristobalite surface when dissolved in NaOH or KOH. Therefore the rate controlling mechanism is not via diffusion through an ash layer in these solutions. This was however the case in LiOH where an insoluble layer of lithium silicates formed on the cristobalite surface and arrested the reaction.

Table 2.6 in Chapter 2 showed the different theoretical models for fluid film diffusion controlled and chemical reaction controlled reactions. Since the dissolution rate in KOH is constant, Equation 2.17 is an appropriate model describing the diffusion controlled process.

$$kt = \alpha \qquad (2.17)$$

A plot of conversion (α) against time gives a straight line as shown in Figure 4.23.

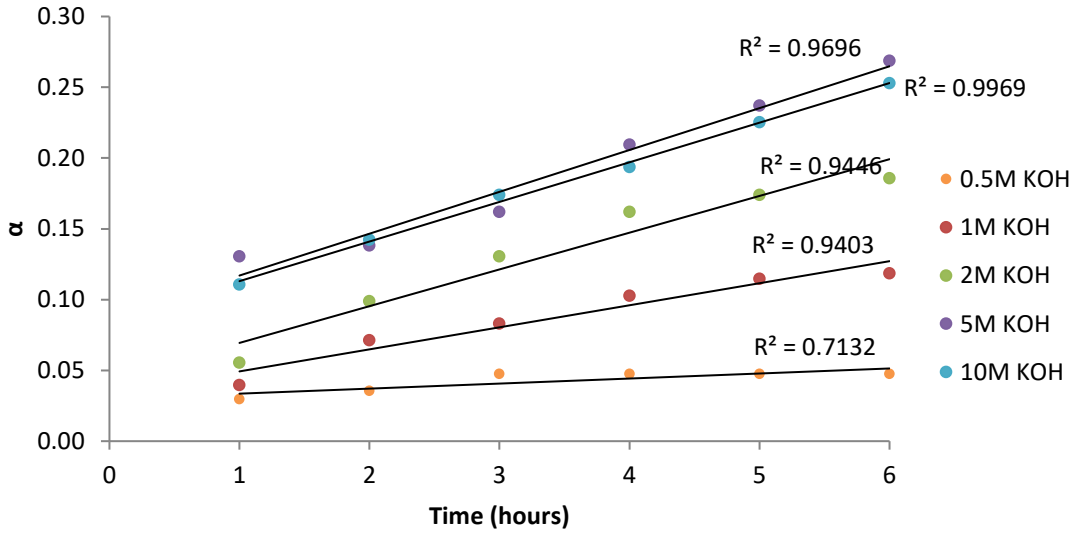

Figure 4.24 : Diffusion controlled dissolution in KOH – one dimensional model

This model is not however appropriate at the start of the reaction. When the cristobalite particles first contact OH^-, the reaction will be chemically controlled, and the rate will be constrained by the ability of OH^- to form a five-fold coordinated compound.

Also, at lower concentrations (0.5M) there is a poor fit to the trend line. This was also observed in the 0.5M NaOH solution and could be indicative of a different mechanism occurring at lower hydroxide concentrations. This is not explored further because such low concentrations are not used industrially.

Three alternative diffusion control models which have a better fit to the data and capture what occurs at the start of the reaction were detailed in Table 2.4 and are:

$$kt = (1-\alpha)\ln(1-\alpha) + \alpha \quad (2.18)$$

$$kt = \left[1-(1-\alpha)^{1/3}\right]^2 \quad (2.19)$$

$$kt = \left(1-\frac{2\alpha}{3}\right) - (1-\alpha)^{2/3} \quad (2.20)$$

All three Equations had a good fit with the experimental data however; Equation 2.19 – three dimensional diffusion control had marginally higher R^2 values. These are shown in Figure 4.24.

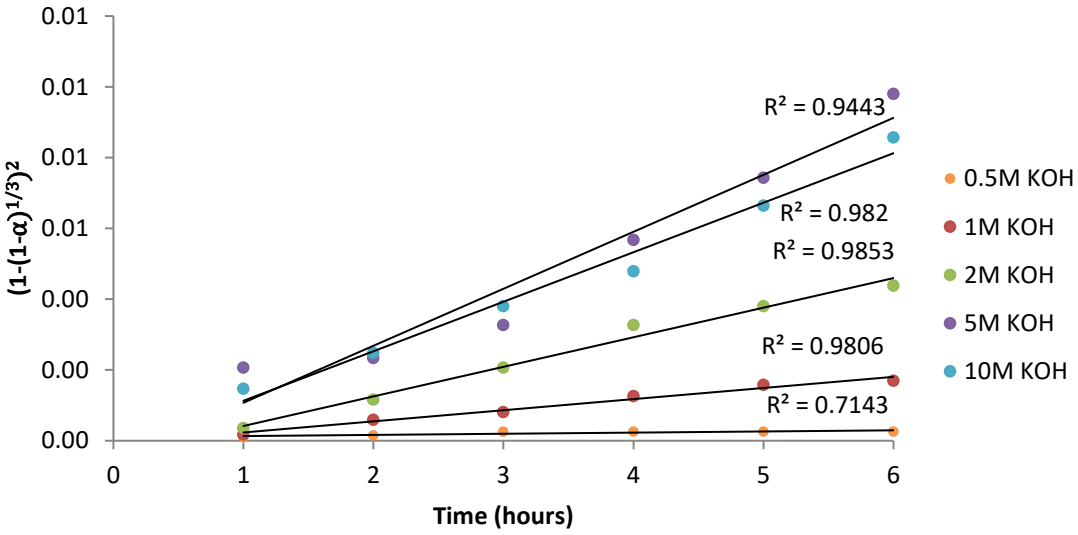

Figure 4.25 Diffusion controlled dissolution in KOH – three dimensional model

The diffusion control model is in agreement with the results discussed in Section 4.3.2 where an increase in stirrer speed had a significant effect on the dissolution rate. A diffusion controlled reaction is constrained by the diffusive flux of hydroxide ions through the viscous fluid film layer. In Section 4.5, it will be shown that more siliceous solutions of potassium silicates are more viscous than sodium

silicates, which explains why the diffusion through the fluid film is the rate controlling step in KOH. The formation of a highly viscous gel around the cristobalite particles reduces the diffusive flux of hydroxide ions onto the cristobalite surface.

In NaOH, a viscous fluid film layer does not exist and the dissolution rate showed a negligible increase at a higher stirrer speed. A slight increase was observed in 1 M NaOH but at 5 M (more representative of autoclave concentrations) increasing the stirrer speed had no effect on dissolution rate.

Figure 4.25 shows the core shrinking model for spheres described by Equation 2.29

$$kt = 1 - (1 - \alpha)^{1/3} \tag{2.29}$$

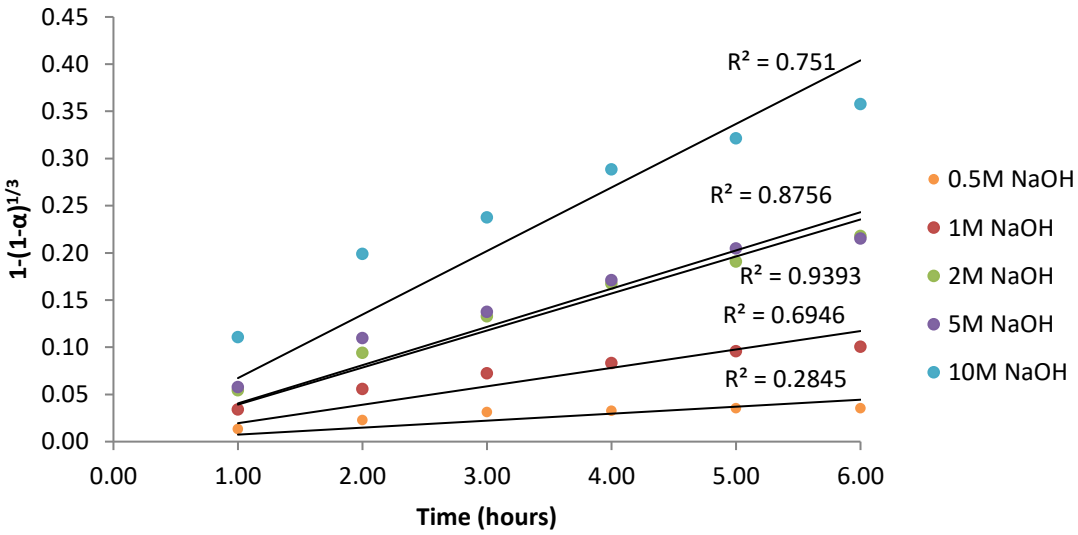

Figure 4.26 Chemical reaction controlled – core shrinking model for spheres

The model shows a best fit at 2M and 5M NaOH concentrations. At concentrations higher and below this, there is a poor fit to the model. A possible reason for this may be caused by a change in the mechanism at as the reaction progresses whereas in the 2M and 5M solution, the rate controlling mechanism remains constant. Alternative chemical reaction controlled theoretical models detailed in Table 2.4 did not show a better fit at 0.5M, 1M and 10M NaOH concentrations.

Chemical controlled reactions have large activation energies often in excess of 40 kJ mol^{-1}, i.e. strong rate dependence on temperature (88). This is discussed further in Section 4.3.5.

4.3.5 Isoconversion Model and Activation Energy

In a heterogeneous chemical process, the reaction mechanism occurring at the solid surface is in constant flux because as the reaction proceeds, the surface becomes modified leading to changes in the mechanism. The best way to accommodate for this is through an isoconversion model (76).

The constant modification of the cristobalite surface exposes Si atoms with varying siloxane bond connectivity. The basic premise is as follows: Cristobalite is a crystalline form of silica which limits the nucleophilic attack of the OH^- to the surface. Si atoms with a low connectivity will be more susceptible to the formation

of a 5-fold coordinated compound which is the preceding step before siloxane cleavage. Therefore, the activation energy of cristobalite dissolution will change as a function of the conversion (α) of the individual grains.

The converted fraction of a cristobalite grain as a function of reaction time is given by (76):

$$\frac{d\alpha}{dt} = kf(\alpha) \tag{4.13}$$

where k is the rate constant and *f*(α) is a function associated with the mechanism. Rearranging equation 4.13 and integrating both sides of the equation:

$$\int_0^{\alpha} \frac{d\alpha}{kf(\alpha)} = \int kdt \tag{4.14}$$

$$\int_0^{\alpha} \frac{d\alpha}{kf(\alpha)} = kt \tag{4.15}$$

Assigning the integral in equation 4.15 a function *g(α)*:

$$g(\alpha) = kt \tag{4.16}$$

Combining equation 4.16 with the Arrhenius equation:

$$g(\alpha) = \left(Ae^{-\frac{E_a}{RT}}\right)t \tag{4.17}$$

Rearranging for *t*:

$$ln(t) = \frac{E_a}{RT} + ln\left(\frac{g(\alpha)}{A}\right) \tag{4.18}$$

At a particular mole conversion, $ln\left(\frac{g(\alpha)}{A}\right)$ is constant therefore, the gradient of a plot of ln(t) versus 1/T gives the activation energy.

Every plot of ln(t) versus 1/T yields a straight line. The gradient is multiplied by the molar gas constant R = 8.314 J mol^{-1} K^{-1} to give the activation energy of the

reaction at a particular molar conversion. Dissolution experiments were carried out at 50 °C, 70 °C and 105 °C, to determine the activation energy. For all the temperature dependence experiments, cristobalite M6000 was used instead of the standard M006 used in Section 4.2 because the former has a larger surface area therefore took less time to reach the desired conversion.

Figure 4.26 and 4.27 shows the plot of ln(t) versus 1/T at different molar conversions in 5 M KOH and NaOH respectively.

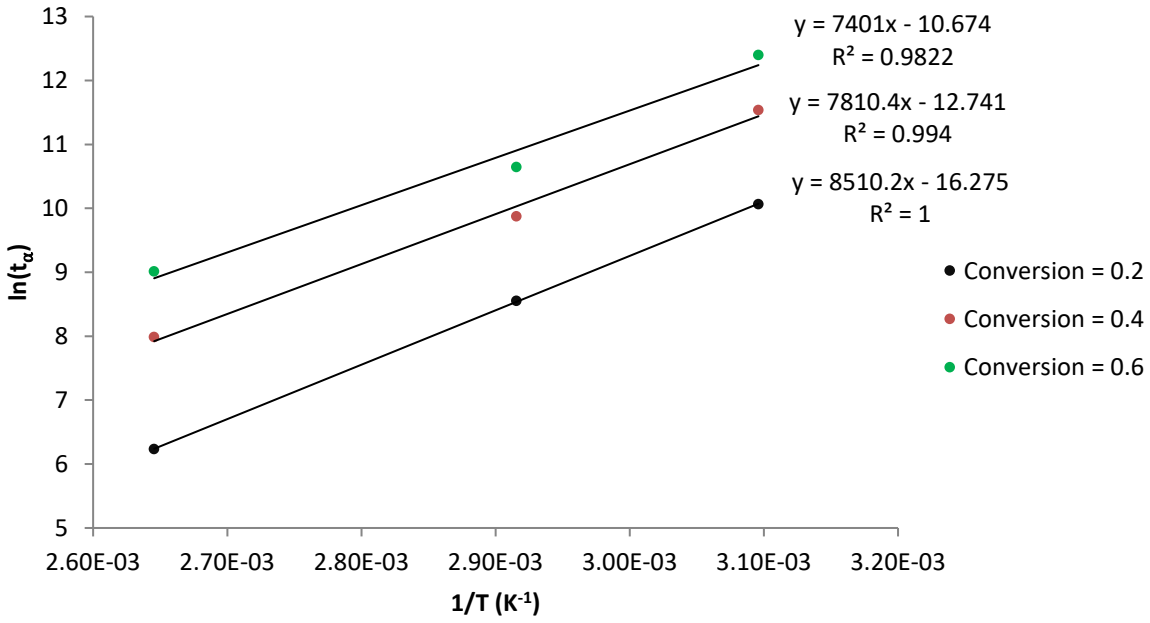

Figure 4.27 ln(tα) versus 1/T at 323 K ≤ T ≤ 378 K at different conversions in 5 M KOH

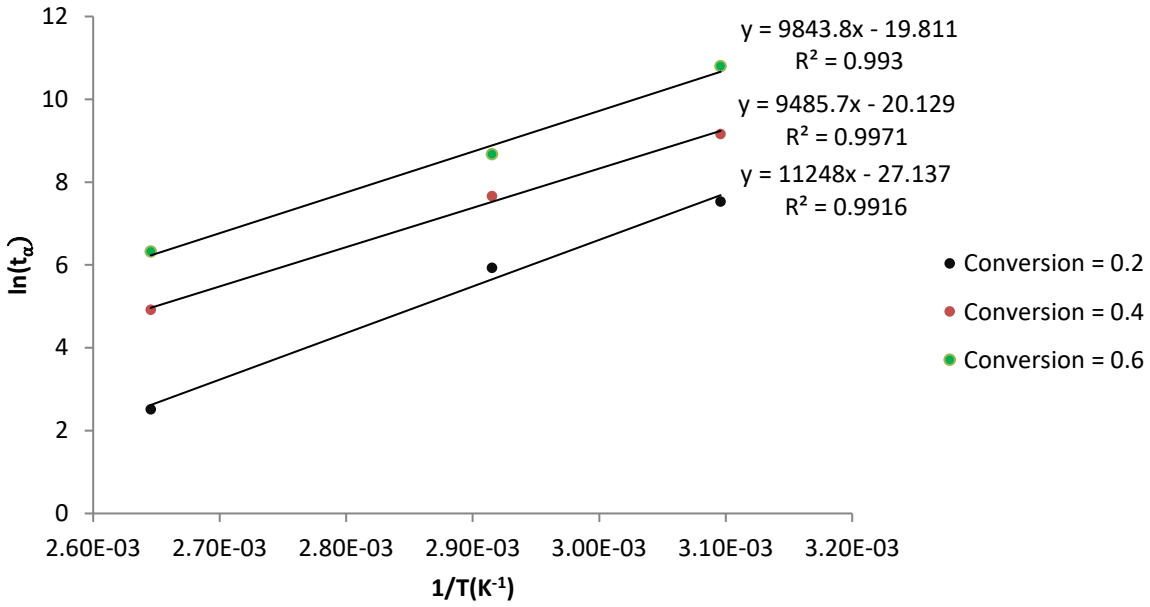

Figure 4.28 ln(tα) versus 1/T at 323 K ≤ T ≤ 373 K at different conversions in 5 M NaOH

The gradient of the plots shown in Figures 4.27 and 4.28 multiplied by the molar gas constant gives the activation energy at different conversions and is depicted in Figure 4.29.

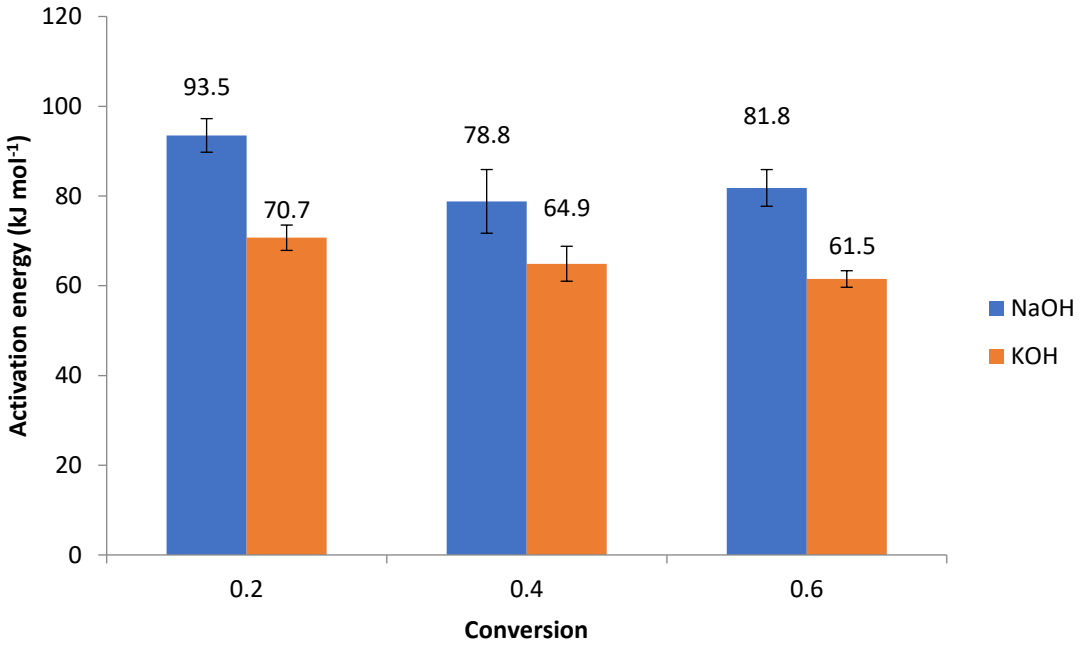

Figure 4.29 Dependence of activation energy on conversion degree based on the isoconversion model

Two important observations can be drawn from Figure 4.29. The activation energy decreased as the degree of conversion increased and the activation energy in NaOH was consistently larger than in KOH. The change in activation energy was more pronounced when the degree of conversion increased from 0.2 to 0.4 whereas between 0.4 and 0.6, the activation energy did not change as much and the error bars also show a larger standard deviation.

Lower activation energies means that it became progressively easier to form the 5-fold coordinated Si compound as the cristobalite surface was modified. This is in disagreement with experimental work carried out by Gmati (76) where the activation energy of α cristobalite in NaOH increased from 89 kJ mol^{-1} – 94 kJ mol^{-1} in the same conversion range shown in Figure 4.28. (0.2 – 0.6).

The trend for computational activation energies as a function of conversion degree shown in Table 2.4 for β cristobalite in water are in agreement with the results shown in Figure 4.28. Work done by Pelmenschikov (64) showed that the activation energy declined steadily from 205 kJ mol^{-1} for Q^4 to Q^3 transformations down to 75 kJ mol^{-1} for Q^1 to Q^0.

As discussed in the beginning of this section, in detaching a single $(SiO_4)^{4-}$ unit from the silica surface into solution, three siloxane (Si-O-Si) bonds need to be broken. In the process, three transition states are formed with an unstable five-fold coordinated Si compound.

$$Q^3 \xrightarrow[TS1]{} Q^2 \xrightarrow[TS2]{} Q^1 \xrightarrow[TS3]{} Q^0$$

At the start of the reaction, the cristobalite surface was primarily composed of Si atoms in the Q^3 configuration, i.e. three siloxane bonds connected to Si. Figures 4.29 – 4.34 show the transformation of an Si atom in the Q^3 configuration to Q^0 when it is detached from the cristobalite surface and exists as a monomer in solution.

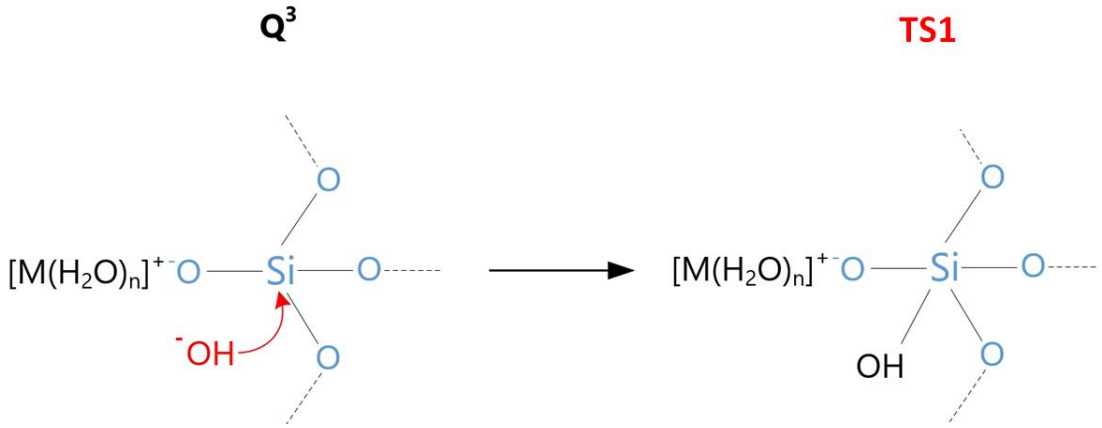

Figure 4.30 Q^3 to TS1 transformation

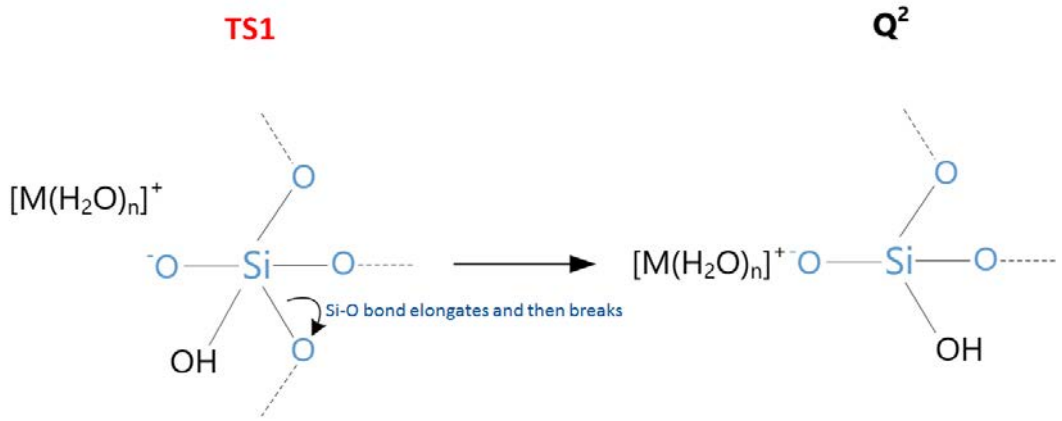

Figure 4.31 TS1 to Q^2 transformation

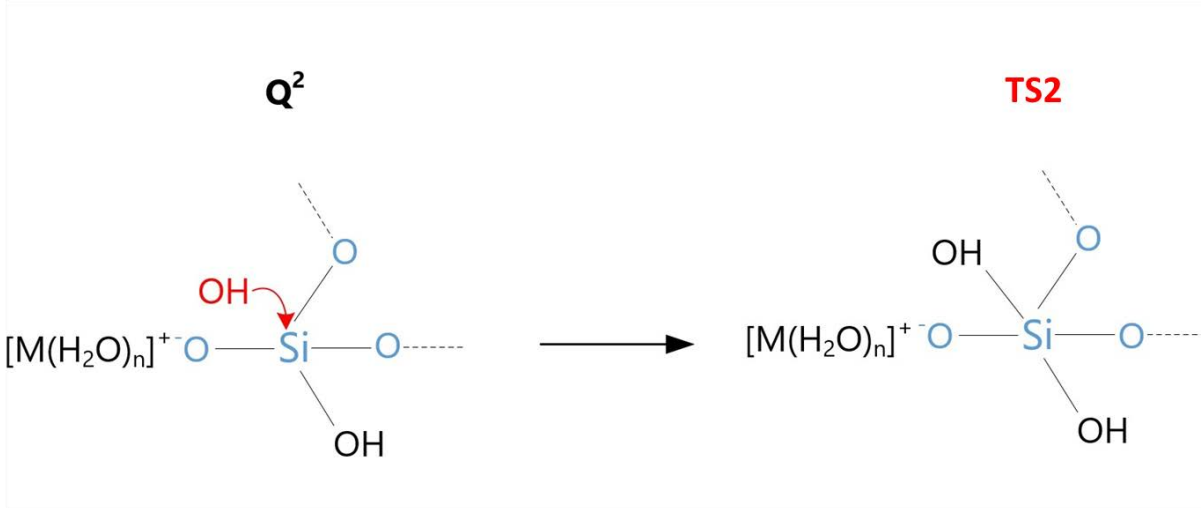

Figure 4.32 Q^2 to TS2 transformation

Figure 4.33 TS2 to Q^2 transformation

Figure 4.34 Q^1 to TS3 transformation

Figure 4.35 TS3 to Q^0 transformation

A likely reason for the decline in activation energy as the degree of conversion increased is as follows: At the start of the reaction, the cristobalite surface will be primarily composed of Q^3 Si. Any $(SiO_4)^{4-}$ group detached from the cristobalite surface will create two adjacent Si atoms in the Q^2 configuration. Nucleophilic attack of OH^- will form a five-fold coordinated compound. However because a Q^2 Si only has two siloxane bonds, it is easier for the OH^- to attack the Si atom since the silanol group (Si-OH) can reorient itself into a more favourable position.

As the reaction continues, the cristobalite surface is continuously altered and the concentration of Q^2 and Q^1 Si atoms on the surface will increase as shown in Figure 4.35. A higher concentration of Q^2 and Q^1 Si atoms will increase the ease of forming the 5-fold coordinated transition state which is a prerequisite for siloxane cleavage.

As discussed in the literature review, computational studies (52) showed that the formation of the five-fold coordinated, i.e. the first transition state (TS1) had an activation energy of 79.1 kJ mol^{-1} whereas the formation of the hydrolysed products via siloxane cleavage had an activation energy of 18.8 kJ mol^{-1}. The formation of the transition state is the rate controlling mechanism since it has a larger activation energy.

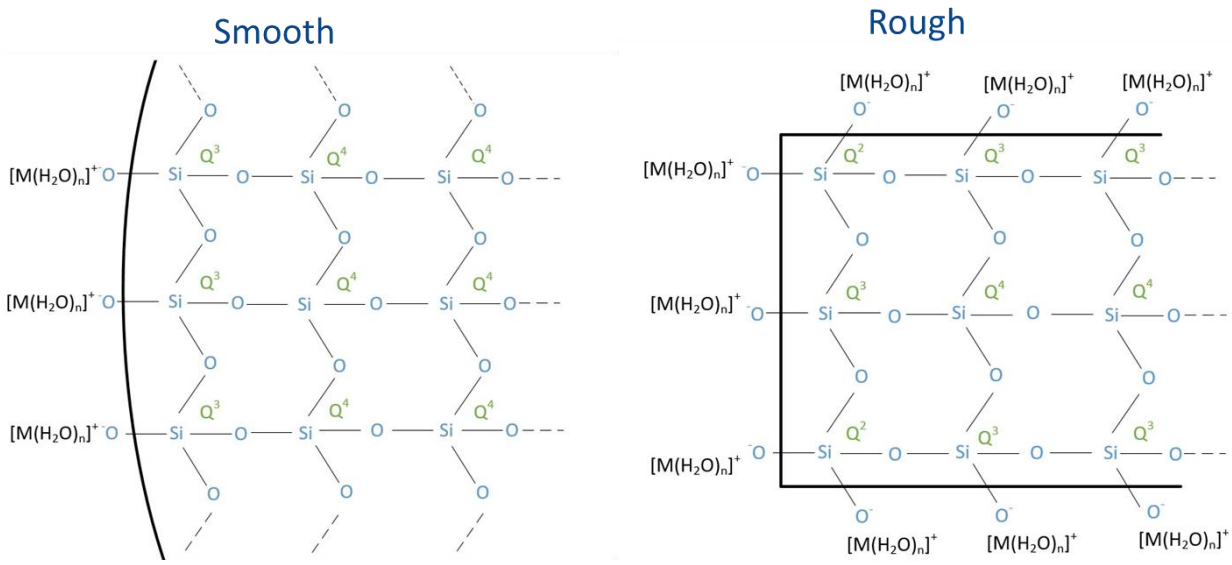

Figure 4.36 Alteration of the cristobalite surface increasing the concentration of Q2 andQ1 Si atoms

The difference in activation energies between KOH and NaOH can be attributed to the adsorption behaviour of the metal cations on the cristobalite surface. Computational studies (58) showed that cationic adsorption causes an increase in Si – O bond length making the subsequent cleavage easier to achieve. NaOH consistently had larger activation energies than KOH as shown in Figure 4.28. This reason for this is unclear since Na has a higher charge density and possibly a stronger influence on the adjacent Si – O bond lengths. In any case, the larger

activation energies in NaOH point to a kinetically controlled reaction. which is in agreement with the results discussed in Section 4.3.2, Section 4.3.4 and the rheological properties of sodium silicates. As will be shown in Section 4.5, sodium silicates have a low viscosity therefore a diffusion controlled reaction is unlikely.

4.3.6 Conclusion

The results discussed in this section show that the cristobalite dissolution is a very complex process. The optimum concentration for dissolution is between 5 M and 10 M.

The type of metal cation present also had a significant effect on the dissolution process. Only NaOH and KOH were considered, and it was shown that the amount of cristobalite dissolved in NaOH after 6 hours was approximately double the amount dissolved in KOH at equimolar concentrations.

At 5 M, which is more representative of concentrations in the autoclave, it was found that the stirrer speed had a significant effect during dissolution in KOH whereas in NaOH, its effects were negligible. A four-fold increase in stirrer speed from 300 rpm to 1200 rpm doubled the dissolution rate in KOH.

Dissolution in KOH was found to be diffusion controlled and showed a good fit with the one dimensional diffusion control equation. The limitation of this model is that it does not accurately capture what occurs within the first hour of the reaction, i.e. during the formation of the fluid film layer. The three dimensional diffusion control model showed a better fit across the entire reaction time. Dissolution in NaOH was chemical reaction controlled. A good fit with the interface contracting volume model for spherical particles was observed at 2M and 5M NaOH solutions. At other concentrations, the model showed a poor fit to the theoretical model and could be indicative of a change in mechanism as the reaction progressed.

Activation energies could not be determined using a simple Arrhenius plot because the cristobalite surface was constantly in a state of flux as the reaction proceeded. An isoconversion model was used to determine activation energies as a function of the degree of conversion. As the degree of conversion increased, the activation energy decreased since the surface became more concentrated with Q^2 and Q^1 Si atoms. Formation of the five-fold coordinated transition state became easier as the connectivity of the Si atom was reduced.

In NaOH, activation energies between 93.5 kJ mol^{-1} and 81.8 kJ mol^{-1} were observed whereas in KOH, the activation energies were in the lower range between 70.7 kJ $mol^{-1\ 1}$ and 61.5 kJ mol^{-1}. The difference is attributed to the

adsorption behaviour of the metal cations however the precise mechanism behind this remains unknown.

4.4 ^{29}Si-NMR

The ^{29}Si-NMR spectra of silicates in solution exhibit several resonances corresponding to structurally different sites of the Si atom. This is caused by a change in the local environment of the Si atom – specifically the number of siloxane bonds around it. The more siloxane bonds associated with an Si atom, the more negative the chemical shift observed (87).

As explained in the Literature Review, the standard nomenclature used in ^{29}Si-NMR used to describe the connectivity of the Si atom is Q^n where n is the number of siloxane bonds. Figure 4.37 shows some of the different silicate structures present in solution. The silicate monomer has no siloxane bond therefore the Si atom is denoted Q^0. The linear silicates consists of Q^1 and Q^2 Si atoms. Any structure with Q^3 Si atoms is potentially layered. These are found in more siliceous solutions and affect the rheology and water absorbing properties of the silicates.

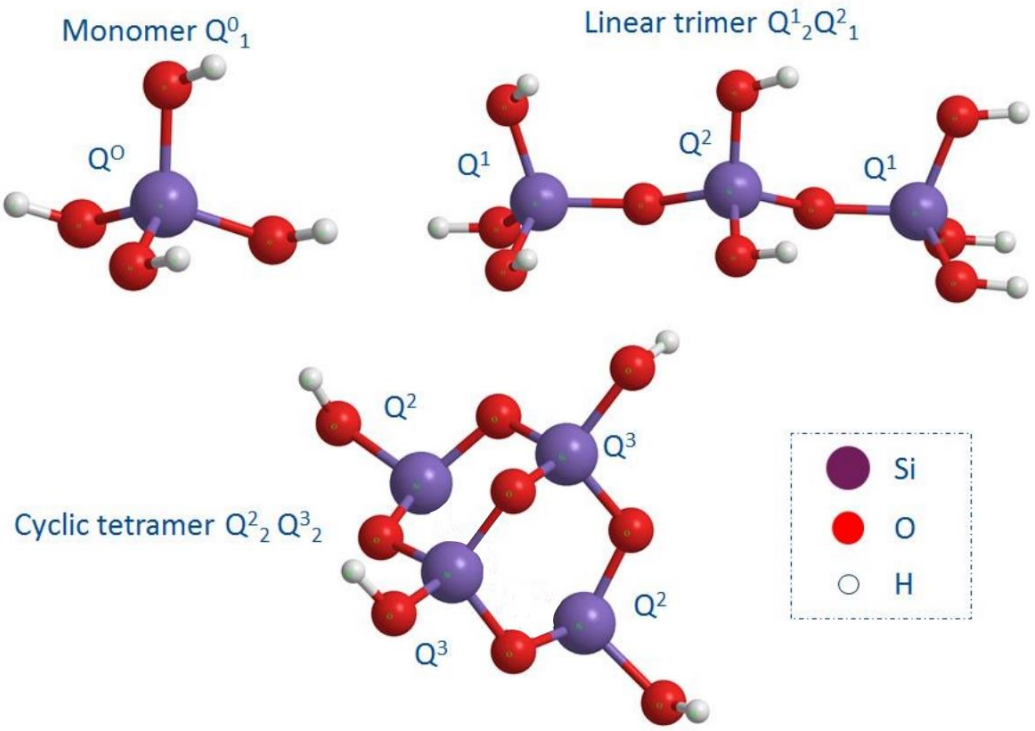

Figure 4.37 Different silicate structures and Q^n Si atoms

The subscript Q_x represents the number of Q^n Si atoms present. For example, the linear trimer structure has two Q^1 atoms and one Q^2 atom.

Table 4.4 shows the reference NMR peaks for the different Q^n sites.

Table 4.4 Reference NMR peaks (53)

Q^n site	Chemical shift ranges (– ppm)
Q^0	71.3
Q^1	79.2 – 79.8
$Q^2_{cyclical}$	81.1 – 87.3
Q^2	87.5 – 88.2
Q^3	88.4 – 98.6
Q^4	104 – 120

Q^2 can exist in a linear or cyclical form. The linear form is shown in Figure 4.36 and a cyclical form can be imagined as a triangle with each vertex representing a Q^2 Si atom connected to two other vertices. This is not largely important since Q^2 Si atoms arranged in a linear or cyclical configuration are still two dimensional.

Figures 4.37 and 4.38 shows the ^{29}Si-NMR spectra of sodium silicates at different SiO_2:Na_2O molar ratios. Figures 4.39 and 4.40 show the spectra of potassium silicates.

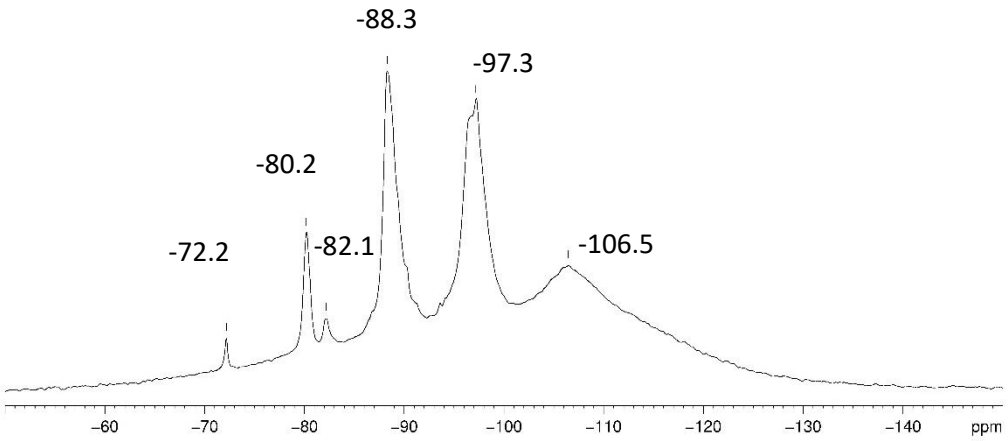

Figure 4.38 NMR spectra of SiO_2:Na_2O = 2.5:1

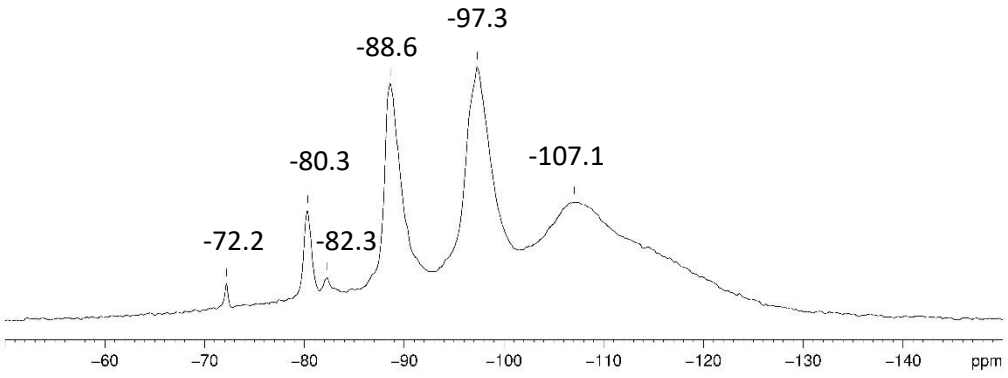

Figure 4.39 NMR spectra of SiO_2:Na_2O = 3:1

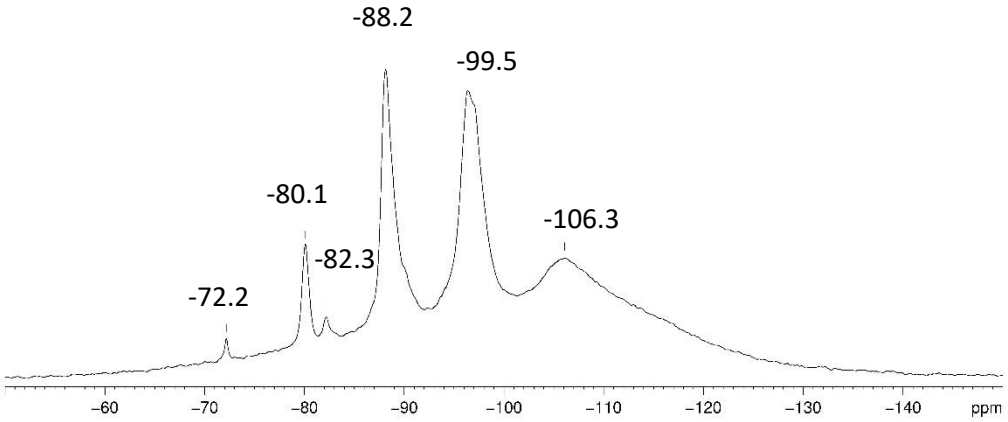

Figure 4.40 NMR spectra of SiO_2:K_2O = 2.5:1

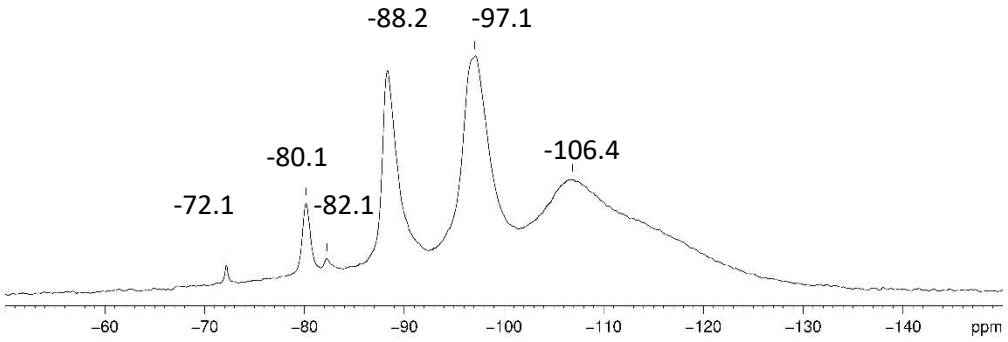

Figure 4.41 NMR spectra of SiO_2:K_2O = 3:1

The area under each peak is proportional to the concentration of Q^n Si atoms. This is indicative of the amount of linear and potentially layered silicates in the solution.

Table 4.5 shows the integral range over which the areas under each peak were calculated.

Table 4.5 Integral range for calculating area under 29Si-NMR peaks (53)

Q^n site	Integral range (-ppm)
Q^0	71.6 – 72.6
Q^1	79.0 – 81.2
$Q^2_{cyclical}$	3.0
Q^2	86 – 91
Q^3	94 – 100
Q^4	102 – 125

Figure 4.41 shows the composition of Q^n at different SiO_2:M_2O ratios and the influence of the metal cation on silicate distribution.

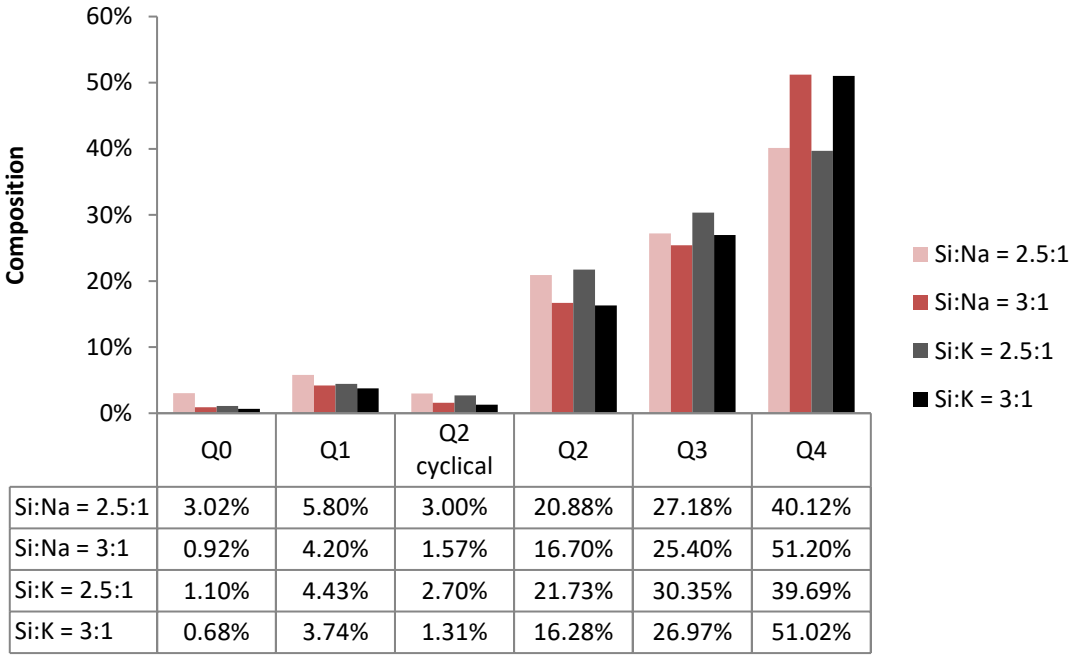

	Q0	Q1	Q2 cyclical	Q2	Q3	Q4
Si:Na = 2.5:1	3.02%	5.80%	3.00%	20.88%	27.18%	40.12%
Si:Na = 3:1	0.92%	4.20%	1.57%	16.70%	25.40%	51.20%
Si:K = 2.5:1	1.10%	4.43%	2.70%	21.73%	30.35%	39.69%
Si:K = 3:1	0.68%	3.74%	1.31%	16.28%	26.97%	51.02%

Figure 4.42 Silicate solution composition as a function of SiO_2:M_2O molar ratios and metal cation present

Two main observations from Figure 4.41:

I. As the solution became more siliceous, i.e. at a higher SiO_2:M_2O ratios, the concentration of monomers, Q^0 fell while the concentration Q^3 and Q^4

increased. This is caused by polycondensation of the monomer as the concentration of SiO_2 increased.

SiO_2 dissolution in water or alkaline solutions proceeds via the formation of monomers.

In water (53):

$$SiO_2 + H_2O \leftrightarrows Si(OH)_4 \quad (4.19)$$

In alkaline solutions a deprotonated monomer is formed:

$$SiO_2 + H_2O \leftrightarrows H_2SiO_4^{2-} \quad (4.20)$$

Three monomers can exist in solution depending on the pH: $Si(OH)_4$, $H_2SiO_4^{2-}$, $H_2SiO_3^{-}$. These can combine in 5 unique reactions to produce a dimer and a leaving group via a polycondensation reaction with water as the leaving group.

$$H_2SiO_4^{2-} + H_2SiO_4^{2-} \leftrightarrows H_2Si_2O_7^{4-} + H_2O \quad (4.21)$$

$$H_2SiO_4^{2-} + H_3SiO_4^{-} \leftrightarrows H_3Si_2O_7^{3-} + H_2O \quad (4.22)$$

$$H_2SiO_4^{2-} + H_4SiO_4 \leftrightarrows H_4Si_2O_7^{2-} + H_2O \quad (4.23)$$

$$H_3SiO_4^{-} + H_4SiO_4 \leftrightarrows H_5Si_2O_7^{-} + H_2O \quad (4.24)$$

$$H_4SiO_4 + H_4SiO_4 \leftrightarrows H_6Si_2O_7 + H_2O \quad (4.25)$$

The dimers in equation 4.23 – 4.25 have been confirmed to exist in solution (53).

These dimers undergo further polycondensation reactions to form higher order oligomers as the solution becomes more siliceous. This could explain why the concentration of Q^4 silicates increased as the SiO_2:M_2O ratio increased.

II. The metal cation had a significant effect on monomer concentration (Q^0) at equimolar silicate concentrations. Sodium silicates had approximately three times more monomer than potassium silicates at SiO_2:M_2O = 2.5:1. At SiO_2:M_2O = 3:1, the difference in monomer concentration had narrowed but sodium silicates still had a higher concentration. However the concentration of Q^4 silicates was identical in both sodium and potassium silicates which was unexpected.

^{29}Si-NMR work carried out by Wijnen et al. (87) showed that the potassium silicates had a lower Q^0 and higher Q^4 concentration than sodium silicates. This could be caused by the type of metal cation present in solution. In KOH, equilibrium shifted further to the right to produce higher order silicate oligomers.

The presence of lithium ions produced mainly monomers in solution (87). Another researcher (80) observed a similar metal cation influence on the distribution of silicates in solution. Addition of Li^+ ions was found to reduce the

concentration of Q^3 and Q^4 silicates and simultaneously increase Q^1 and Q^2. The mechanism behind this remains unknown however Wijnen (87) attributed this to the hydrated radius of the metal cations. Potassium had the lowest hydrated radius and potassium silicates were the most polymerised whereas lithium had the largest hydrated radius and was least polymerised.

At the 2.5:1 ratio, the difference in monomer concentration between sodium and potassium silicates was more significant. This solution was further explored to determine whether the higher concentration of monomer in sodium silicates would retard the dissolution process.

4.4.1 Reusability

KOH solutions have been reported to be more effective for re-use compared to NaOH solutions in Rolls Royce and other casting facilities. In order to prove the hypothesis, identical concentrations of used KOH and NaOH solution were used to dissolve cristobalite in the laboratory.

The potassium and sodium silicate solutions contained 20 wt.% SiO_2 and had a molar ratio of 2.5:1. The ^{29}Si-NMR spectra showed that the used KOH solution, i.e. potassium silicate had a lower concentration of monomer in solution. It was hypothesised that this would lead to a faster dissolution in KOH since the equilibrium was shifted more to the right.

Figure 4.43 shows the dissolution curve.

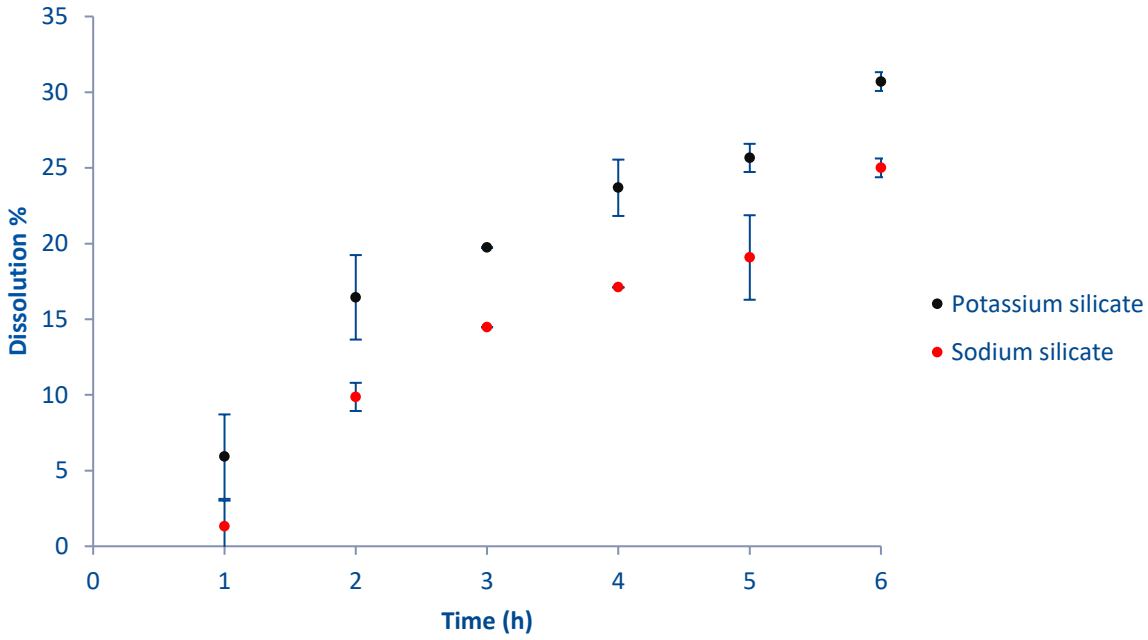

Figure 4.43 Cristobalite dissolution in 20 wt% SiO2 solution of potassium silicate and sodium silicate at SiO_2:M_2O molar ratio of 2.5:1

The used KOH solution dissolved more cristobalite after 6 hours. This is likely caused by the lower concentration of monomer in solution which causes the system to respond by dissolving more SiO_2 through Le Chatelier's principle. Since the equilibrium concentration of silicates is shifted further to the right, i.e. the rate of dimer production is faster than monomer production, more SiO_2 is dissolved to replace the monomers in an attempt to return the system to equilibrium. The error bars show that the difference in the amount of cristobalite dissolved in the used KOH and NaOH solutions is significant.

4.5 Rheology of silicates

4.5.1 Dynamic Viscosity Measurements

The viscosity of sodium and potassium silicate solutions was measured as a function of the $Si0_2$ wt. % and SiO_2:M_2O molar ratio. The results are shown in Figure 4.44 and 4.45.

Figure 4.44 shows the viscosity of sodium silicate solutions over different shear rates and the effect of SiO_2 wt. % and SiO_2:Na_2O molar ratios. Recall that a lower SiO_2:Na_2O molar ratio means the solution is more alkaline whereas a higher SiO_2:Na_2O means the solution is more siliceous. It should be noted that by mixing wt% and molar ratios in silicate solutions, there will be a difference in water content. However, using SiO_2 wt.% and SiO_2:M_2O molar ratios is widely used in the literature and is therefore a good way of comparing the properties of different silicate solutions.

Sodium silicate solutions mainly displayed Newtonian behaviour irrespective of the SiO_2 wt. % or SiO_2:Na_2O molar ratios at high shear rates. The viscosity increased progressively as the SiO_2 wt. % increased from 20wt. % to 30wt. %. As the sodium silicate solutions became more siliceous, possible shear thinning was observed in solutions at higher SiO_2 wt.% at low shear rates. This was observed in SiO_2:Na_2O ratios of 3:1 at 30 wt.% and SiO_2:Na_2O ratio of 3.3:1 at 26.5 wt.%, 28 wt.% and 30 wt.%.

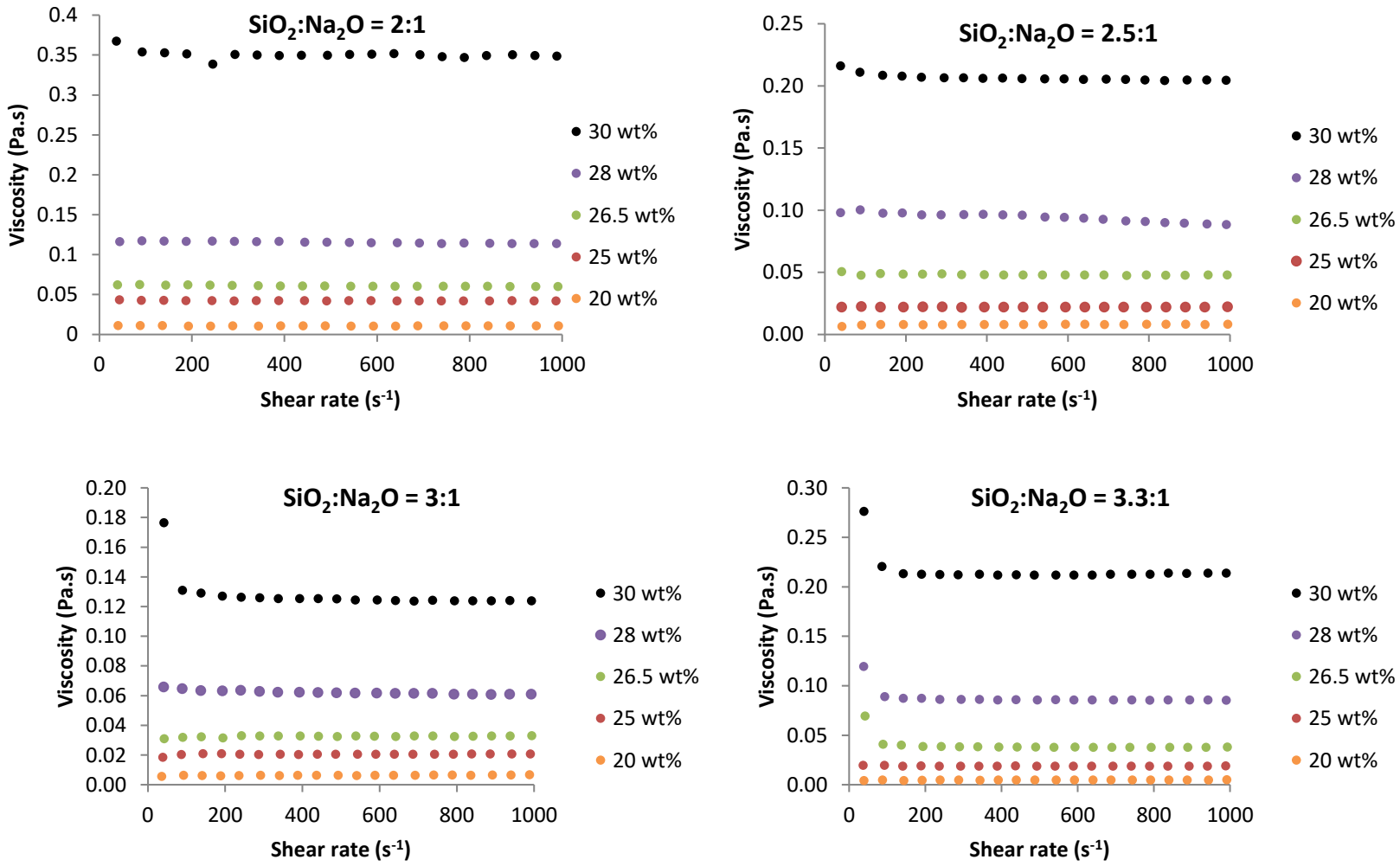

Figure 4.44 Effect of shear rate on sodium silicate viscosity at different SiO2 wt. % and SiO_2:Na_2O molar ratios

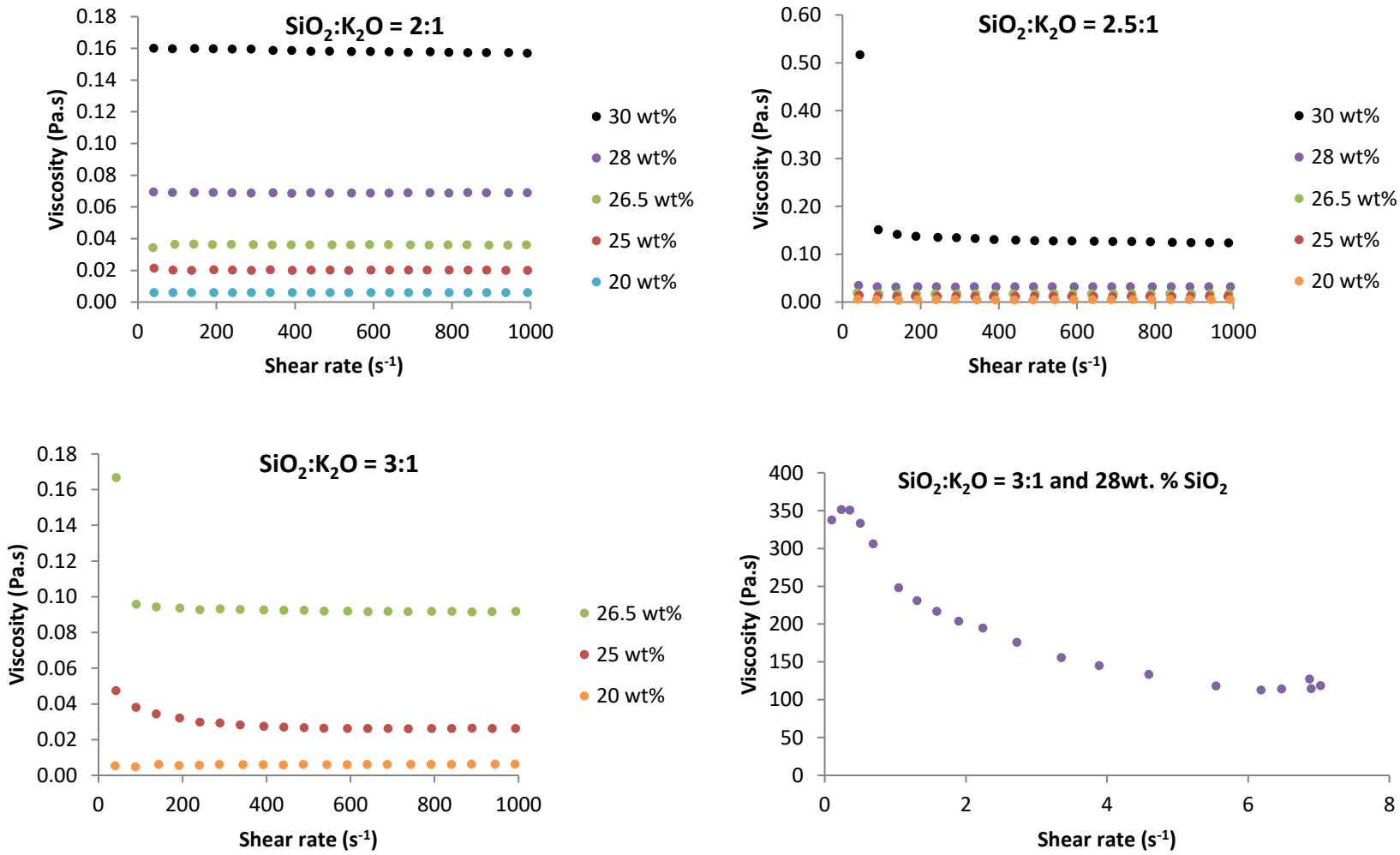

Figure 4.45 Effect of shear rate on potassium silicate viscosity at different SiO2 wt. % and SiO_2:K_2O molar ratios

Potassium silicate solutions mostly displayed Newtonian behaviour at higher shear rates. Just as in the sodium silicate solutions, as the solutions became more siliceous and at high SiO_2 wt.%, shear thinning behaviour was observed at low shear rates. These solutions could also be demonstrating a yield stress. The argument that the film thickness does not change above a certain viscosity even as the shear rate (rpm) increased, as shown in the 1 M KOH solutions in Figure 4.19, could be further indication of a yield stress that could exist at high SiO_2:K_2O ratios.

Figure 4.46 shows the viscosity as a function of the shear rate for the 30wt. % potassium silicate solution. Measuring the viscosity of this solution was very difficult because the material was sticky. At high SiO_2 wt. % and SiO_2:K_2O molar ratios, potassium silicates are used as adhesives (118). This made it particularly difficult to measure the viscosity using a rheometer. The shear rate could not exceed 0.1 s^{-1} and the parallel plates of the rheometer were stuck together after sample was analysed.

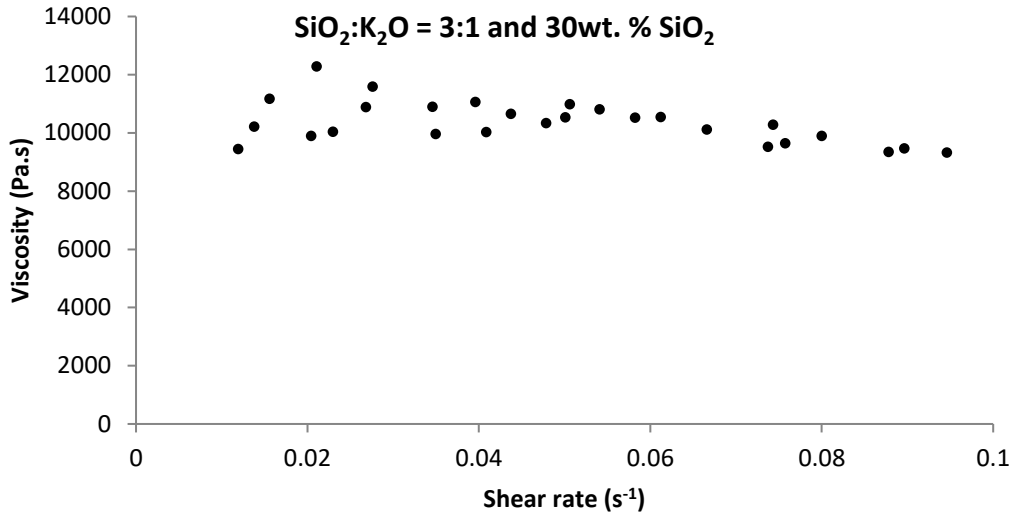

Figure 4.46 Effect of shear rate on potassium silicate viscosity at 3:1 molar ratio and 30wt. % SiO_2

For comparison, the shear rate in the laboratory dissolution experiments detailed in Section 4.3.2 at 300 rpm and 1200 rpm were 5 s^{-1} and 20 s^{-1} respectively.

There are three volume fraction regimes for spherical particles in suspension (119):

I. Dilute regime: Volume fraction ≤ 0.02, rheology is Newtonian
II. Semi dilute regime: Volume fraction ≤ 0.25, rheology is approximately Newtonian
III. Concentrated regime: Volume fraction between 0.25 – 0.45, rheology is increasingly non Newtonian, specifically shear thinning

Potassium and sodium silicate solutions were prepared on a mass fraction (weight %) basis. Since the density of a KOH or NaOH solution is approximately half the density of cristobalite, the transition to non-Newtonian behaviour at a volume fraction of 0.25 is equivalent to a mass fraction of 0.43 (assuming silica and KOH/NaOH solution densities are 2360 kg m^{-3} and 1200 kg m^{-3} respectively).

Based on this, a suspension of spherical silicates in solution is expected to display non-Newtonian behaviour at approximately 43wt. % SiO_2. However, non-Newtonian behaviour was observed from 28wt. % SiO_2. The early onset of non-Newtonian behaviour can be attributed to the presence of linear silicates consisting of Q^0, Q^1 and Q^2 Si atoms as shown by ^{29}Si-NMR results. The presence of linear silicate oligomers increased the particle interactions leading to non-Newtonian behaviour.

Siliceous potassium silicate solutions with a high solids content exhibit shear thinning behaviour at low shear rates. This was expected based on the experiments discussed in Section 4.3.2 which showed that increasing the stirrer speed increased the dissolution rate in KOH and not NaOH. The increased dissolution rate was only observed in KOH because potassium silicates are more viscous than sodium silicates therefore an increase in stirrer speed is inconsequential during dissolution in NaOH.

The hypothesis is that a fluid film layer forms on the silica surface. In both the laboratory experiments and the pilot scale trials, the fluid film layer is formed on the leach front. These two examples are illustrated in Figure 4.47.

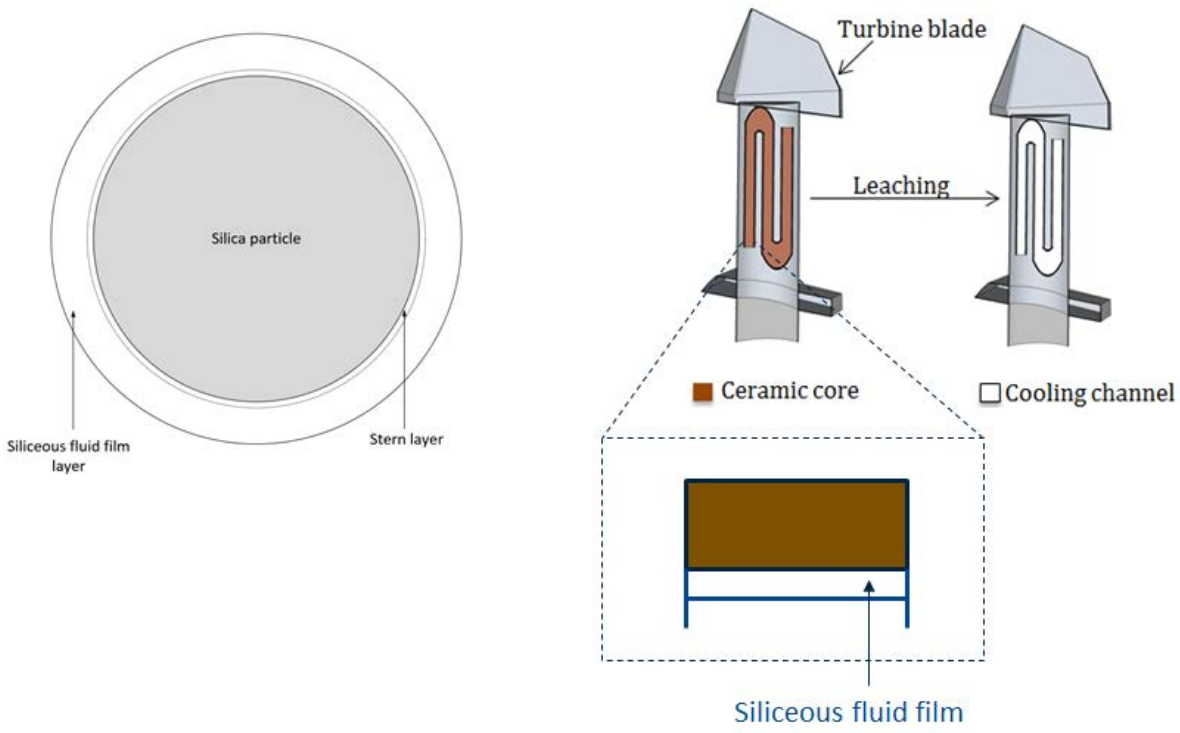

Figure 4.47 Siliceous fluid film layer forming around a silica particle and at the surface of the ceramic core

In Chapter 5, it will be shown that a siliceous fluid film layer likely forms within the porous ceramic core. The potentially layered Q^3 silicates could absorb water and expand causing the brittle ceramic core to crack which leads to further infiltration of the alkaline solution.

4.5.2 Variables Affecting Silicate Viscosity

The rheological properties of silicate solutions are complicated because they exhibit properties of a suspension and polymers (85).

The basic rheological properties detailed in Section 4.5.1 show that the viscosity of a silicate solution depends on the SiO_2wt. %, SiO_2:M_2O molar ratio and the type of metal cation present. Non-Newtonian behaviour was only observed in potassium silicates at high concentrations of SiO_2 and high SiO_2:K_2O molar ratios.

Three independent variables were observed to affect the rheological properties of sodium and potassium silicate solutions examined in this section – the SiO_2 wt. %, the SiO_2:M_2O molar ratio and the metal cation present.

The relationship between the SiO_2 wt. % and solution viscosity at different SiO_2:M_2O molar ratios is shown is shown in Figure 4.47.

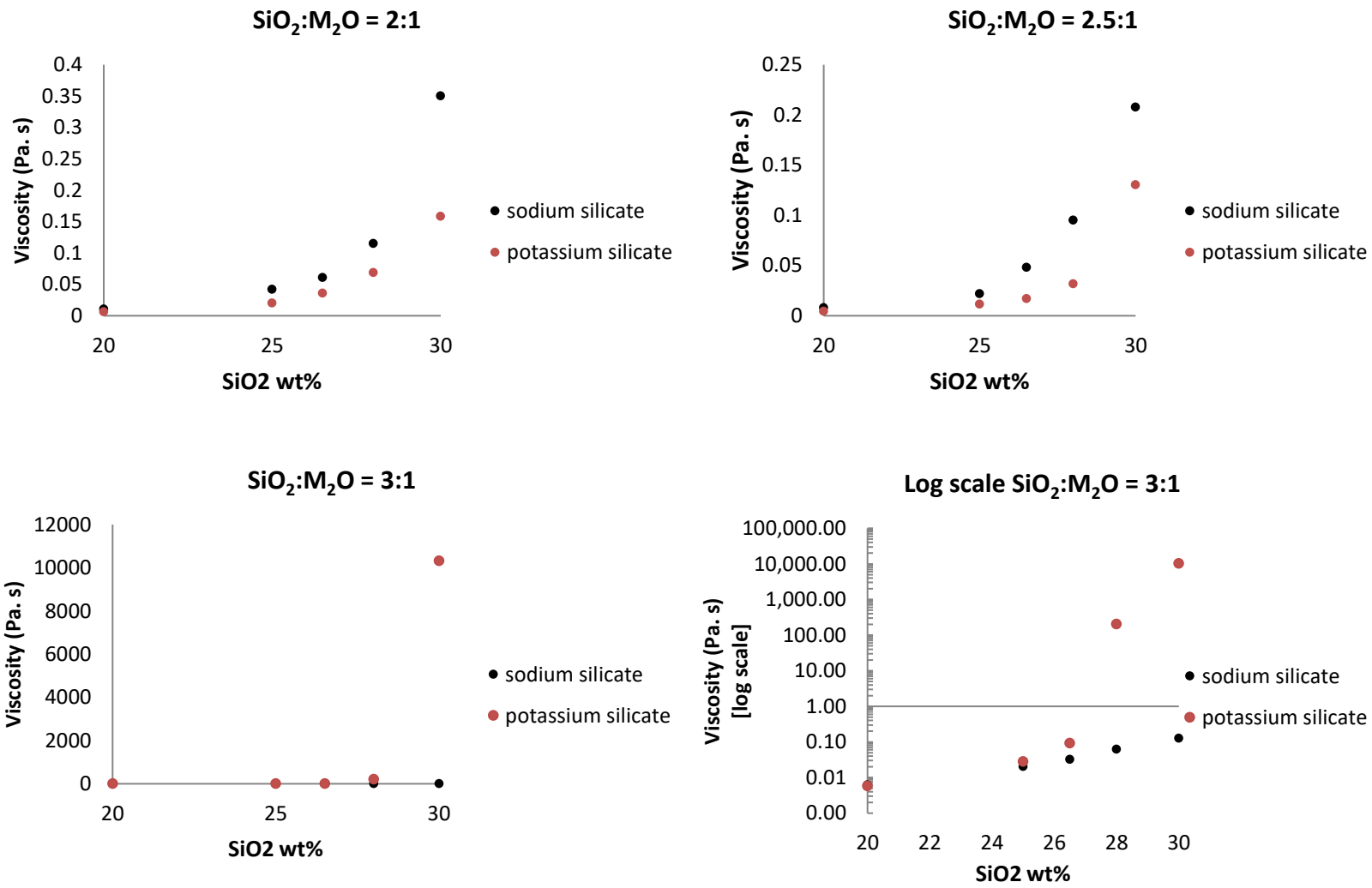

Figure 4.48 Viscosity of sodium and potassium silicates as a function of SiO2 wt. % at different SiO_2:M_2O molar ratios

At lower SiO_2:M_2O molar ratios, sodium silicate solutions were more viscous than potassium silicates at identical SiO_2wt. %. This is probably because NaOH is more viscous than KOH at equimolar concentrations. Recall that lower SiO_2:M_2O molar ratios mean the silicate solution is more alkaline therefore the viscosity of the alkaline solution has a larger impact on the overall viscosity of the suspension.

At SiO_2:M_2O = 3:1, the solution is more siliceous and potassium silicates are more viscous than sodium silicates This is likely caused by polycondensation reaction leading to the formation of higher order oligomers. This is however not supported by the ^{29}Si-NMR results shown in Section 4.4. Approximately equal amounts of Q^3 and Q^4 silicates were observed in potassium and sodium silicates when SiO_2:M_2O = 3:1. From the literature (87), ^{29}Si- NMR spectra of potassium and sodium silicates show an indistinguishable amount of Q^3 and Q^4 silicates at different SiO_2:M_2O ratios. The authors did not however measure the area under the peaks so it is impossible to quantify the results for a fair comparison.

At a high SiO_2:M_2O molar ratios, potassium silicates have been shown (84) to be more viscous than sodium silicates. The author also examined the viscosity of lithium silicates and observed that even siliceous solutions where the SiO_2:Li_2O molar ratios exceeded 4:1 had lower viscosities than sodium and potassium silicates. This was attributed to the stabilising effect of the large hydrated metal cation. Potassium, the smallest hydrated cation of the three could promote coalescence of the particles which would lead to a larger viscosity.

The relationship between the solids loading and solution viscosity is described by the Krieger Dougherty equation:

$$\eta_r = \left(1 - \frac{\phi}{\phi_{max}}\right)^{-B\phi_{max}} \quad (4.26)$$

η_r = relative viscosity (Pa)

ϕ = volume fraction

ϕ_{max} = maximum volume fraction

B = Einstein coefficient. Also referred to as the intrinsic viscosity

As the volume fraction (ϕ) of solids in the suspension approaches the maximum volume fraction (ϕ_{max}), the relative viscosity will increase asymptotically.

The higher the ϕ_{max} possible in the system, the lower the viscosity at any concentration. The viscosity of sodium silicates as a function of the SiO_2:Na_2O ratio at constant SiO_2 wt.% is shown in Figure 4.49.

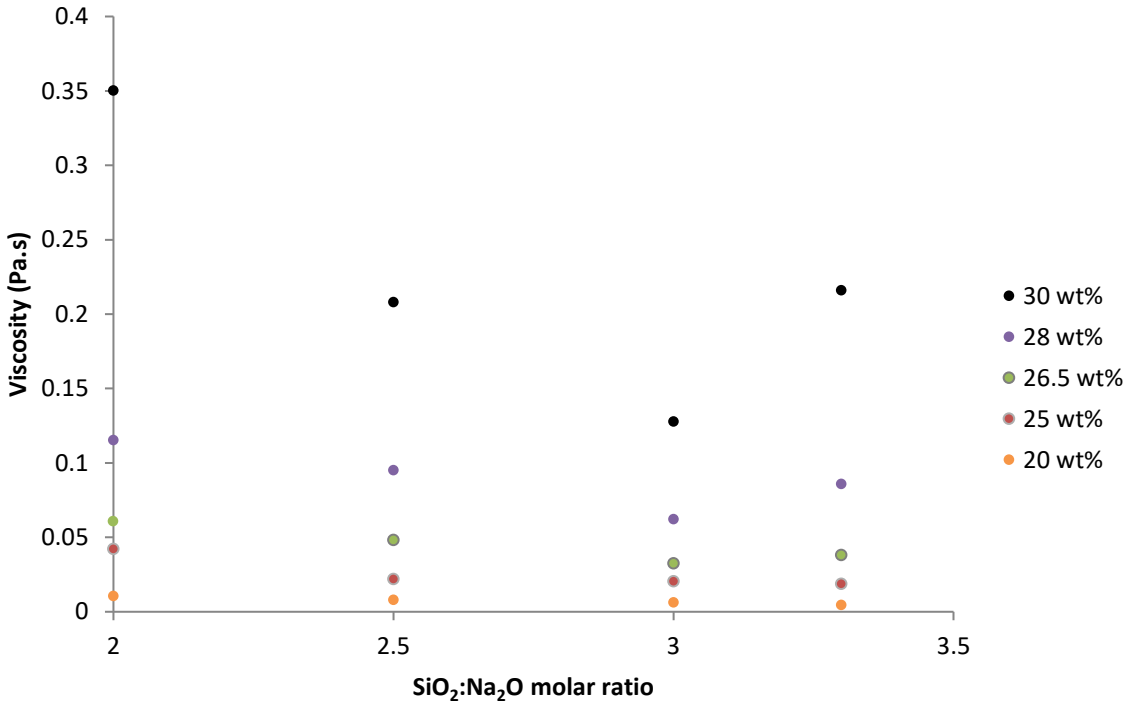

Figure 4.49 Sodium silicate viscosity as a function of SiO_2:Na_2O molar ratios at constant SiO_2 wt.%

As shown in the ^{29}Si-NMR results in section 4.4, changing the SiO_2:M_2O ratio will change the type of silicate anions present. As the SiO_2:M_2O ratio increased, the concentration of one-dimensional silicates decreased while the concentration of Q^3 and Q^4 silicates increased. The higher concentration of these increased the polydispersity of the suspension. This in turn increased the maximum volume fraction.

The one-dimensional silicates consisting of Q^0, Q^1 and Q^2 will be flexible and can be thought of as the binder in a suspension whereas the potentially layered silicates consisting of Q^3 silicates are the rigid colloidal particles.

The increased polydispersity of the suspension as the solution becomes more siliceous produced a minimum viscosity at approximately SiO_2:Na_2O = 3:1. The parabolic shaped curve shown in Figure 4.47 was also reported by other authors (84, 85). The viscosity minimum was however observed at SiO_2:Na_2O = 1.8:1 (84) and 2:1 (85). It is not clear why the minimum viscosity observed in this experiment was at a higher SiO_2:Na_2O ratio.

Polydispersity on its own does not explain why the viscosity falls to a minimum at SiO_2:Na_2O = 3:1 before increasing again. Initially, it was anticipated that the viscosity would increase as the solution became more siliceous because polycondensation would lead to the formation of longer polymer chains (53). Silicates solutions are inorganic polymers and the viscosity of a polymer is directly correlated to its molecular mass as described by the Mark Houwink equation (85).

$$B = KM^{\alpha} \tag{4.27}$$

K and α are Mark Houwink parameters which depend on the polymer-solvent system and M is the polymer molecular weight.

The intrinsic viscosity (B) shows a power law dependence to the molecular mass of the polymer. As the SiO_2:Na_2O ratio increased, polycondensation leads to the formation of polysilicate species with one author (53) observing silicates with 32 monomer units.

The existence of a minimum viscosity is therefore likely to be a combination of the Krieger Dougherty and Mark Houwink equations. As the SiO_2:Na_2O ratio increases, the suspension becomes more polydisperse which increased the maximum volume fraction and reduces the viscosity. At the same time, the molecular mass of the silicate polymers increased as the SiO_2:Na_2O ratio increased. Therefore, the minimum viscosity observed at approximately SiO_2:Na_2O = 3:1 coincides with the maximum volume fraction of the suspension. Beyond this point as the solution becomes more siliceous, the large molecular weight of the silicate polymers increased the viscosity of the solution through the Mark Houwink equation.

At a high SiO_2:M_2O ratio (which is expected at the fluid film interface) potassium silicates are more viscous than sodium silicates. The reason for this is not entirely clear because ^{29}Si-NMR at SiO_2:M_2O = 3:1 show no discernible difference in the concentration of Q^3 silicates. Since both solutions are equimolar, any difference in the rheology can be attributed to the role of the metal cation. It was expected that since potassium cations have the smallest hydrated radius, they promote coalescence of the silica particles leading to a larger viscosity. This is supported by work done by Weldes (84) which shows that at high SiO_2:M_2O ratios, equimolar concentrations of lithium and sodium silicates have a lower viscosity that potassium silicates. The larger hydrated radii of lithium and sodium cations act as a stabiliser even under highly siliceous solutions.

The complex rheological properties of silicates and its dependence on the type of metal cation explains why mixtures of NaOH and KOH were used in both the laboratory experiments (Section 4.2.3) and pilot trials (Chapter 6) in order to increase the dissolution rate of cristobalite. The NaOH/KOH mixtures did not increase the dissolution rate because there are two competing mechanisms at work.

As discussed in Section 4.4, cristobalite dissolution starts with the formation of silicate monomers until the equilibrium concentration of monomers is reached. Polycondensation reactions lead to the formation of higher order oligomers further shifting equilibrium to the right and removing monomeric silicates out of solution. ^{29}Si-NMR studies showed that potassium silicates have a lower concentration of the monomer (Q^0) indicating that the forward reaction, i.e. the production of dimers and trimers is faster in the presence of potassium.

By shifting equilibrium further to the right in the presence of potassium and reducing the concentration of monomeric silicates in the process, equilibrium shifts to the right to counteract the change and restore its equilibrium position, as described by Le Chatelier's principle. This means that more cristobalite is dissolved to make up for the loss of monomeric silicates in an attempt to re-establish equilibrium. This is a possible explanation as to why KOH is more readily re-usable than NaOH as explained in Section 4.4.1.

4.5.3 Viscoelasticity

Determining the viscoelastic properties of the non-Newtonian potassium silicate solutions which were observed at 28 wt. % and 30 wt. % SiO_2 and SiO_2:K_2O molar ratios of 3:1 involved a two-step process.

In the first step, an oscillatory strain sweep was used to determine the linear viscoelastic region of the potassium silicate solutions. In the second step, a frequency sweep below the critical strain, i.e. in the linear viscoelastic region (determined in step 1) was used to determine the storage and loss moduli as a function of the angular frequency.

Viscoelasticity is a combination of viscous and elastic behaviour represented by the loss modulus (G'') and storage modulus (G') respectively. The storage and loss modulus is indicative of the stress response of a viscoelastic fluid under oscillatory shear (120).

Figure 4.49 shows the G' and G'' as a function of oscillatory strain % ranging from 0.01% to 2%.

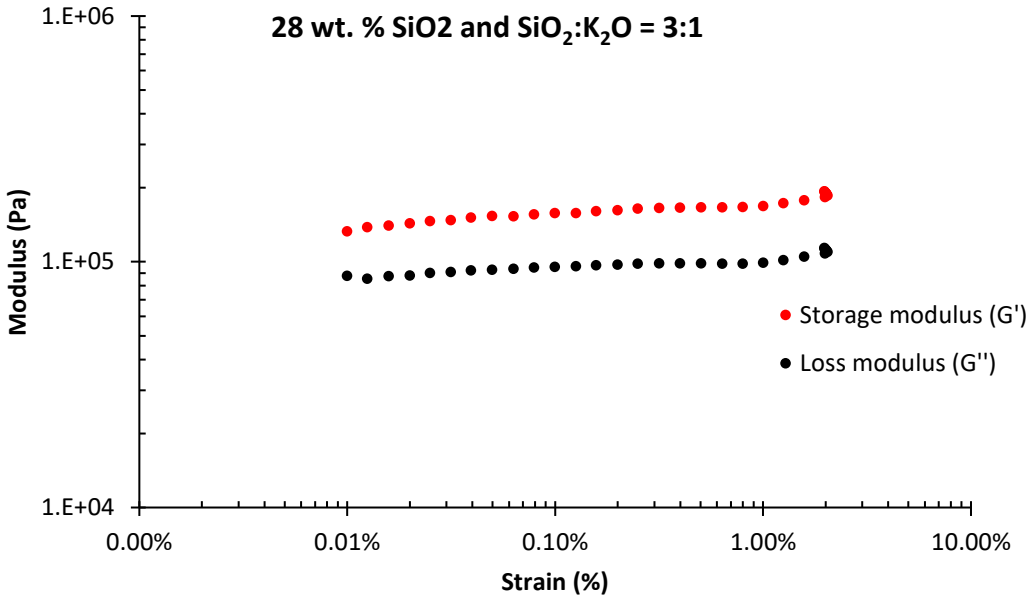

Figure 4.50 Oscillatory strain sweep (1 Hz) over linear viscoelastic region at 28 wt. % SiO_2 potassium silicate solution

Under the oscillatory strain sweep range between 0.01% to 2%, G' and G'' increase by 40% and 29% respectively therefore the fluid is not in the linear viscoelastic range.

At 28 wt. % SiO_2, the storage modulus (G') exceeded the loss modulus (G'') indicating that the material behaves more solid like. An oscillatory strain sweep range between 0.01% and 2% was also carried out on the 30 wt. % SiO_2 potassium silicate solution as shown in Figure 4.50. Under the oscillatory strain sweep range, the fluid was in the linear viscoelastic range.

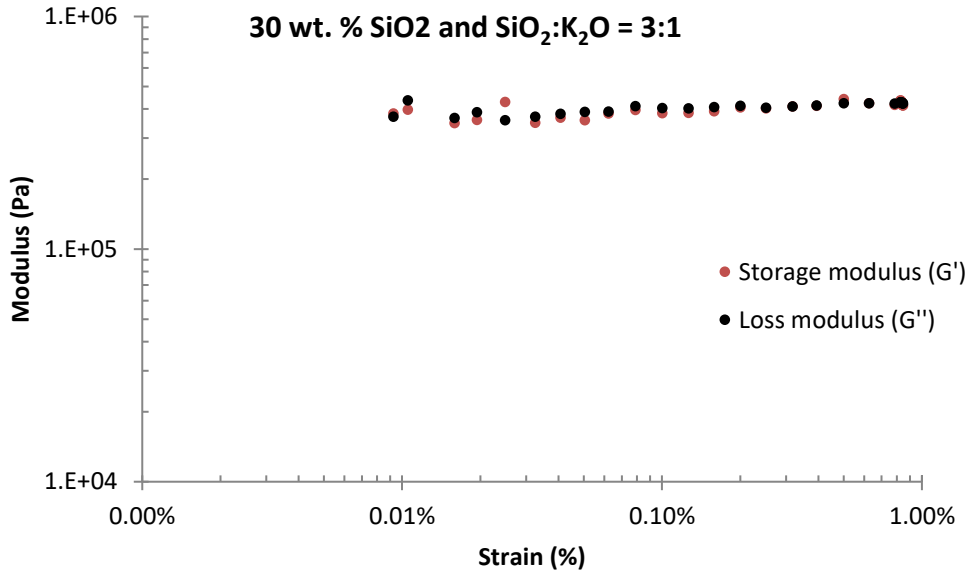

Figure 4.51 Oscillatory strain sweep (1 Hz) over linear viscoelastic region at 30 wt. % SiO_2

At 30 wt. % SiO_2, the loss modulus (G'') was approximately equal to the storage modulus (G') implying that the potassium silicate solution behaved more liquid like.

After the linear viscoelastic range was determined, an oscillatory frequency sweep was carried out to further characterise the potassium silicate structure at 30wt. % SiO_2. Below the critical strain, i.e. in the linear viscoelastic region, G' is independent of the oscillatory frequency, which is to be expected for a solid-like material (120). During the frequency sweep, the oscillatory strain was set at 1% and G' and G'' were measured as a function of the angular frequency between 0.1 rad s^{-1} – 250 rad s^{-1}. This range was chosen because similar viscoelasticity experiments were previously carried out on potassium and sodium silicates within this range (85).

At the start of the frequency sweep up to 0.8 rad s^{-1}, the loss modulus (G'') exceeded the storage modulus (G') indicative of viscous and liquid like behaviour at very low frequencies. At higher frequencies however, the storage modulus exceeded the loss modulus indicating solid-like behaviour.

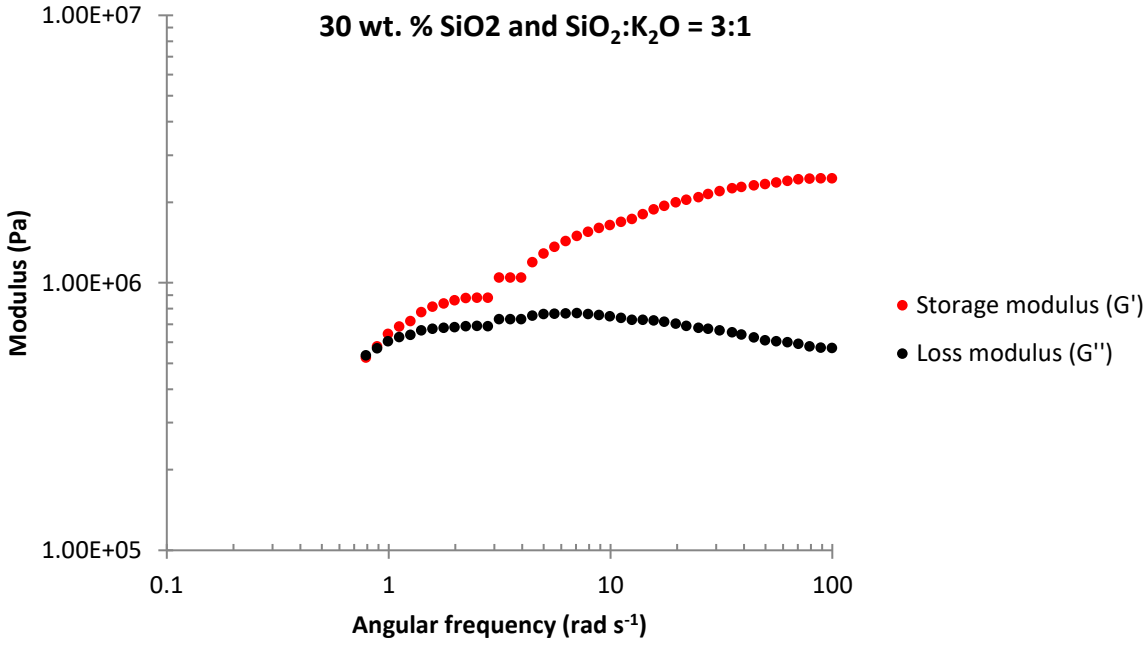

Figure 4.52 Storage and loss modulus as a function of angular frequency at 30wt. % SiO2

Up to 0.8 rad s^{-1}, the loss modulus (G'') exceeded the storage modulus (G'). The storage and loss modulus pattern observed in Figure 4.52 is typical of a rubbery material (121).

These conditions are likely to exist at the fluid film interface which explains why the dissolution in KOH is diffusion controlled. The large viscosity of the fluid film layer reduces the diffusivity of OH^- which is the catalyst for siloxane cleavage. In

Chapter 7, it will be shown how the leaching process in the autoclave can be optimised based on an understanding of silicate rheology.

4.6 Conclusion and Summary of Reaction Steps

There has been no detailed chronological description of events that occur during silica dissolution. Many authors focused on one part of the process, primarily the cleavage of siloxane bonds which is where breakdown of the silica framework actually occurs. Greenberg (49) gave a short description of what happens from the moment a silica particle comes in contact with a strong alkaline solution. It starts with deprotonation of the surface silanol groups at a high pH followed by siloxane cleavage catalysed by OH^- and ends with the diffusion of silicates into the liquid phase.

1. Hydroxyl ions deprotonate surface silanol groups
2. metal cations adsorb on –ve charged surface
3. Nucleophilic attack on Si and siloxane bond cleavage
4. Polycondensation and fluid film layer formation
5. Diffusion of silicates into the bulk liquid
6. Diffusion of M and OH^- through fluid film layer

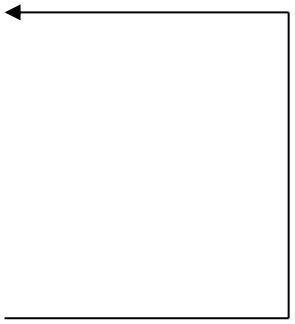

Steps 1 through 4 have been detailed in this Chapter. Step 5 is the logical next step after the formation of the fluid film layer. Some of the silicates detached from the solid surface will diffuse back in the bulk liquid. In step 6, the process repeats itself however, the hydroxide ions and metal cations must diffuse through the fluid film layer before reaching the cristobalite surface.

The next chapter will cover the physics of the core leaching process and attempt to pull together the knowledge gained from an understanding of the dissolution chemistry of cristobalite on a laboratory scale in order to understand dissolution behaviour in a simple rectangular prism ceramic core in a pressurised autoclave.

5 PHYSICS OF THE CORE LEACHING PROCESS

The core leaching autoclave used by Rolls-Royce is manufactured by LBBC Technologies and is typically run with concentrated aqueous solutions of NaOH or KOH at 160 ^{o}C. Such elevated temperatures are reached by supplying the autoclave with an external air supply which pressurises it to 600 kPag. Higher pressures supress boiling of the alkaline solution. The autoclave also operates on a pressure swing cycle where the pressure is intermittently increased and decreased. The latter is achieved by venting of the excess pressure into a dump tank as previously illustrated in Figure 3.10. When the pressure is decreased, i.e. during the venting phase, the alkaline solution boils aggressively and it was hypothesised that this was the primary physical mechanism responsible for core removal.

This chapter details the operation of the core leaching autoclave and how the pressure swing cycle aids core removal. This chapter also details the primary physical mechanism responsible for core removal and the effect of part orientation and position in the autoclave on leaching effectiveness.

5.1 Pressure Swing Cycle

As outlined in Chapter 4, the alkaline solution in the autoclave is not homogenous with respect to concentration of dissolved silica. The solution in direct contact with the silica surface – the fluid film layer, is highly concentrated in silica relative to the bulk solution in the autoclave, i.e. it is more siliceous. The viscosity of the solution in the fluid film layer is also strongly dependent on the type of leachant used and it was shown that at identical dissolved silica content (SiO_2 wt.%) and identical silica to alkali molar ratios (SiO_2:M_2O) potassium silicates are significantly more viscous than sodium silicates. This means that the diffusion of OH^- is retarded in KOH because of the viscosity of potassium silicates in the fluid film layer.

Figure 4.6 (Chapter 4) showed the effect of increased stirrer speed on silica dissolution in the laboratory set-up. As previously explained, the dissolution rate of silica in 5 M KOH was doubled by increasing the stirrer speed from 300 rpm to 1200 rpm, i.e. a four-fold increase. It was hypothesised that the doubling of the leach rate was due to shearing-off half of the viscous fluid film layer. In NaOH, doubling the stirrer speed had no effect on the leach rate. This was expected because of the much lower viscosity of sodium silicates at the fluid film layer. The same experiment was undertaken using 1 M solutions of NaOH and KOH and no change in dissolution rate was observed in either leachant as shown in Figure 4.7. The difference in leaching behaviour of silica in 1 M and 5 M KOH was likely caused by an extremely viscous potassium silicate fluid film layer formed at 1 M,

which is to be expected since the SiO_2:K_2O molar ratio is increased at a lower KOH concentration. Increasing the stirrer speed thus had no effect at the lower concentration because the viscous fluid film layer could not be removed by the applied shear.

Table 5.1 shows the autoclave parameters used to replicate the effect of agitation on core removal in an autoclave using a simple rectangular prism core geometry (Figure 3.4). For each experiment, 10 core pieces were arranged in the autoclave (as depicted in Figure 3.11) with the core opening facing down.

Table 5.1 Autoclave cycle time and total boil time for a 30 minute cycle

	High pressure dwell time – T_{hp} (s)	Vent time – T_v (s)	Low pressure dwell time – T_{lp} (s)	Total boil time –T_b (s)
Standard Cycle	60	5	60	936
Accelerated Cycle	5	5	10	1350

The total boil time (T_b) is the time is the proportion of time spent in the cycle below the vapour pressure, i.e. when the solution is boiling. It is calculated as:

$$T_b = \frac{T_V + T_{lp}}{T_{hp} + T_V + T_{lp}} \text{ x cycle time} \quad (5.1)$$

where T_v is the total vent time, T_{lp} is the low pressure dwell time and T_{hp} is the high pressure dwell time.

The accelerated cycle has shorter high pressure dwell, vent and low pressure dwell times, i.e. it is a higher frequency cycle. The total boil time of the accelerated

cycle is 44% larger than the standard cycle. This means that over the 30 minutes the experiment was run, the accelerated cycle spends 44% more time in a turbulent state. Figure 5.6 shows the effect of increased agitation on core removal in equimolar alkaline solutions.

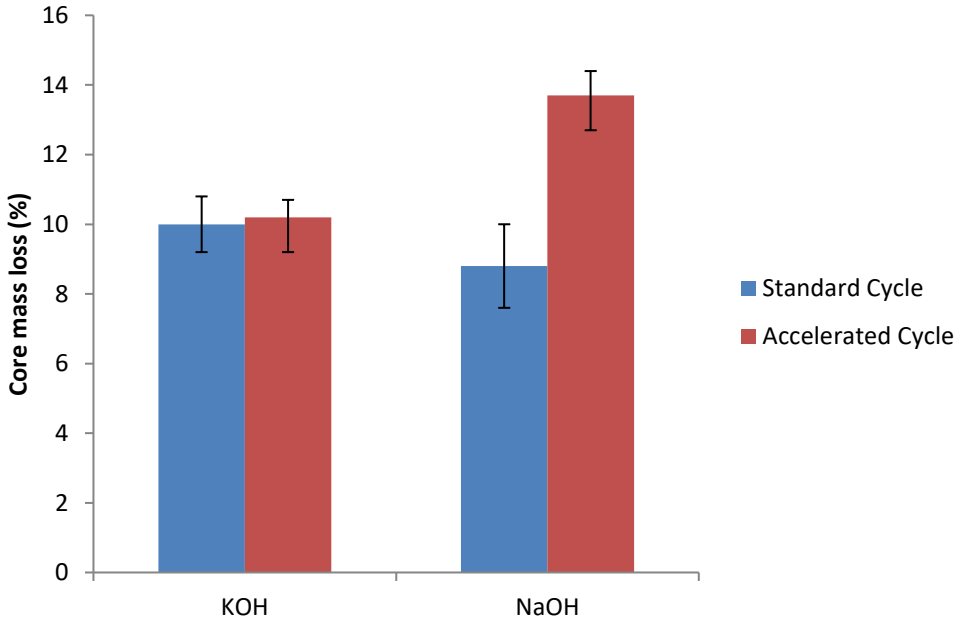

Figure 5.1 Effect of different cycle parameters on core removal in 1 M alkaline solutions

The accelerated cycle had no apparent effect on core removal using KOH. With NaOH, the standard cycle is also comparable to KOH. However, the accelerated cycle in NaOH removes approximately 56% more of the core than the standard cycle. To understand why this happens, the mechanics of the agitation process at different parts of the pressure cycle and the effects of viscosity and surface tension of silicates at the fluid film layer needs to be better understood. Figure 5.7 illustrates the detailed mechanism of what occurs at the fluid film layer during different stages of the pressure swing cycle.

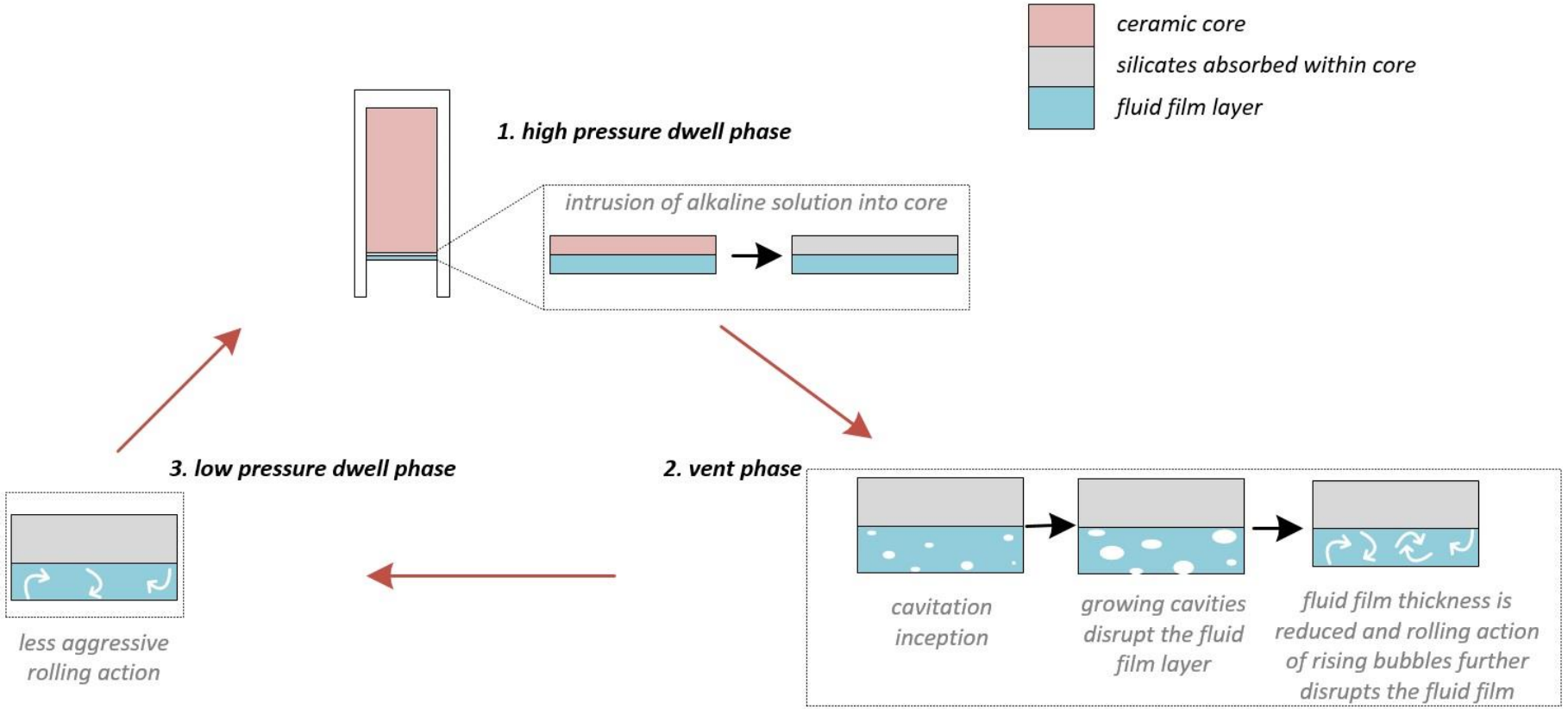

Figure 5.2 Fluid film disruption during different phases of the pressure cycle

The fluid film layer is formed as the OH^- breaks down the silica structure via siloxane bond cleavage producing silicates which are highly concentrated in the boundary layer next to the core. During the high pressure dwell phase, it was expected that the some of the alkaline solution is absorbed by the relatively porous core. The core porosity depends on the specific formulations however it is approximately 30% open porosity. The depth of penetration is difficult to predict as it depends on the viscosity of the MOH solution and the silicate solution which is not static but changes as the reaction with the silica core proceeds. It is however expected that the penetration depth will be higher in NaOH than KOH because the latter produces silicates which are more viscous. This will be expanded upon in section 5.3. During the pressure phase of the cycle, the bulk solution and the fluid film layer are in a quiescent state with no turbulence.

At the start of the vent phase, i.e. cavitation inception – vapour cavities form and grow explosively. These cavities grow explosively because the rapid pressure drop experienced during the vent phase creates large tension forces which ruptures the liquid. Unlike in boiling where the tension force is caused by an increase in temperature which is relatively slow, cavitation is rapid and explosive because the ambient pressure can almost be instantaneously decreased below the vapour pressure thereby creating large tensile forces. As the cavities grow, they disrupt the fluid film layer and increase the diffusivity of OH^- by reducing the thickness of the fluid film. The cavities also introduce turbulence into the fluid film layer and by mixing with the bulk fluid, it becomes more alkaline and less viscous.

In the accelerated cycle, there are more cavitation inception events because the cycle frequency is increased. It was therefore expected that the accelerated cycle will increase the amount of core removed in KOH because potassium silicates have been shown to be significantly more viscous than sodium silicates. However, it was observed that the accelerated cycle had no effect on the amount of core removed using KOH and increased the core loss in NaOH by 56%. In the laboratory experiments discussed in Chapter 4, increasing the stirrer speed had no effect on the dissolution rate in 1 M KOH and led to small increase in 1 M NaOH. At 5 M, a four-fold increase in stirrer speed doubled the dissolution rate in KOH. It was hypothesised that at 1 M concentration, the stirrer had no effect on silica dissolution in KOH because the large viscosity of the potassium silicates was resistant to any shearing effects observed when 5 M KOH was used. As explained in Chapter 4 – higher alkaline concentrations increase the SiO_2:M_2O ratio thereby reducing the viscosity of the silicates.

The results in Figure 5.6 are in agreement with the laboratory results and show that in 1 M KOH in the autoclave, the accelerated cycle had no effect on the amount of core removed. Apart from the effect of larger fluid film layer viscosities for silica in KOH, another reason for observing no change in the amount of core removed could be surface tension effects. The surface tension of silicates was not measured during these experiments and literature on the subject is sparse. According to Mcbain and Sharp (122) a sodium silicate solution with approximately 28 wt.% SiO_2 and SiO_2:Na_2O ratio of 3.2:1 had a surface tension

of 0.073 N m^{-1}, similar to that of water in contact with air at 25 ^{o}C. Data for potassium silicates is not available.

According to equation 2.35, an increase in the surface tension (γ) will decrease the inception pressure. This means that for solutions with a large surface tension, a lower inception pressure is required for cavities to form.

While the accelerated cycle had no effect on silica removal in KOH, it increased the amount of core removed in NaOH by 56%. This is probably because the rolling action of vapour bubbles (as shown in figure 5.7) has a larger direct impact on the core if the underlying fluid film layer is not too viscous whereas in KOH, the viscous potassium silicates act as a barrier against the turbulence created by the vapour bubbles. This is expanded upon in section 5.3.

In the latter stages of the vent phase, the solution boils and rolling action of vapour bubbles helps to dislodge and remove parts of the core that have been partially dissolved and weakened by the alkaline solution. During the low pressure dwell phase, the rolling action of the bubbles is less aggressive as shown in Figure 5.3c. The purpose of the low pressure dwell phase is to introduce agitation into the autoclave without losing any liquid. During the low pressure dwell phase, the vent valve is closed and pressure slowly starts in build-up in the autoclave. If an excessive amount of the alkaline solution is lost during venting, the turbine components in the autoclave will become exposed to air and will not leach

properly. More importantly, excessive liquid loss could lead to overheating of the autoclave if the liquid drops below the height of the knuckle band heaters because air will be heated instead of the liquid causing the autoclave to overheat (because of the lower heat capacity of air).

After the low pressure dwell phase, air is supplied to the autoclave causing the pressure to increase and the solution returns to its quiescent state. During the re-pressurisation phase, it was expected that cavitation erosion would occur as a result of the rapid and implosive collapse of vapour bubbles once the ambient pressure recovered above the vapour pressure. However, evidence of cavitation erosion on the core was not observed. This is probably because the re-pressurisation rate was too slow – it took approximately 2 seconds for the pressure to recover above the vapour pressure. To get the benefits of cavitation erosion, the re-pressurisation time needs to be reduced by an order of magnitude below the current 2 seconds. This will be explored in more detail in Chapter 8.

5.2 Silicate Gel Expansion and Cracking Mechanism

Determining the primary physical mechanism responsible for core removal was difficult because of the arbitrary line separating the chemical and physical processes. Previously, it was assumed that the alkaline solution dissolves the silica in the ceramic core formulation thereby weakening the entire core and making it more susceptible to the turbulence in the autoclave during the vent phase. This conclusion was arrived at because:

- Core removal was found to be faster using a pressurised autoclave with a pressure swing cycle
- Using water for core removal in the autoclave had no discernible effect on the core.

These two statements meant that physical agitation on its own, caused by the explosive bubble growth during the vent phase and the subsequent rolling action of the bubbles had no effect on the core. An alkaline environment is required to dissolve the silica and weaken the core.

The turbulence created during the pressure cycle helps in dislodging the partially dissolved and 'weakened' core. It was previously assumed that this weakening process was purely chemical and caused by dissolution of the silica in the core formulation which is composed of silica and zircon. While zircon is insoluble in alkaline solutions, it makes up less than a third of the core by mass therefore; dissolving the silica weakens the entire matrix allowing any insoluble zircon to simply fall out. While the process just described does indeed occur, it is aided by a physical process known as alkali silica reaction (ASR) gel expansion.

5.2.1 Test Bar Leach Profile

The test bars leached in the autoclave in 1 M KOH and NaOH were cut-up to observe the leach profile and any evidence of physical damage to the core. As previously explained, it was hypothesised that any physical damage to the core was caused by the rolling action of vapour bubbles. Figure 5.8 shows the cross-section of the test bar after 1 hour in the autoclave using 1 M KOH (a) and 1 M

NaOH (b) as the leachant. The pressure cycle used was the standard cycle shown in Table 5.1.

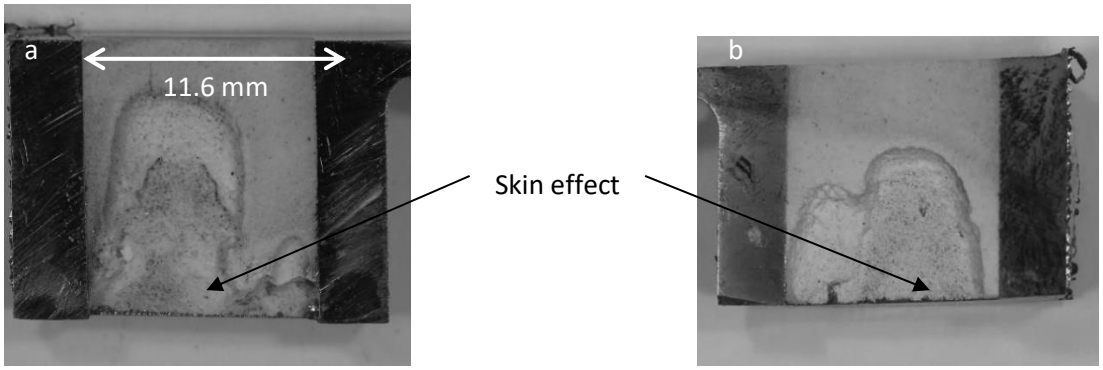

Figure 5.3 Cross-section of partially leached core in (a) KOH and (b) NaOH with core opening facing down in the autoclave

As expected, the leach profiles formed in KOH and NaOH were similar. This was expected because any turbulence that arises during the pressure cycle will be identical in both KOH and NaOH. What is more striking is the shape of the profile which was not expected. Initially, it was expected that since the core opening was facing down in the autoclave, the action of rising vapour bubbles which impact the partially dissolved and 'weakened' core surface combined with the subsequent rolling action of the vapour bubbles was responsible for this profile. This theory was however quickly discounted by simply changing the orientation of the test bar in the autoclave to see if the leach profile would change. If the rolling action of rising vapour bubbles was the cause of the leach profile observed then it shouldn't be present if the orientation of the core was altered.

Figures 5.4 and 5.5 show the cross-section of the partially leached core with the core opening facing up and on its side (horizontal).

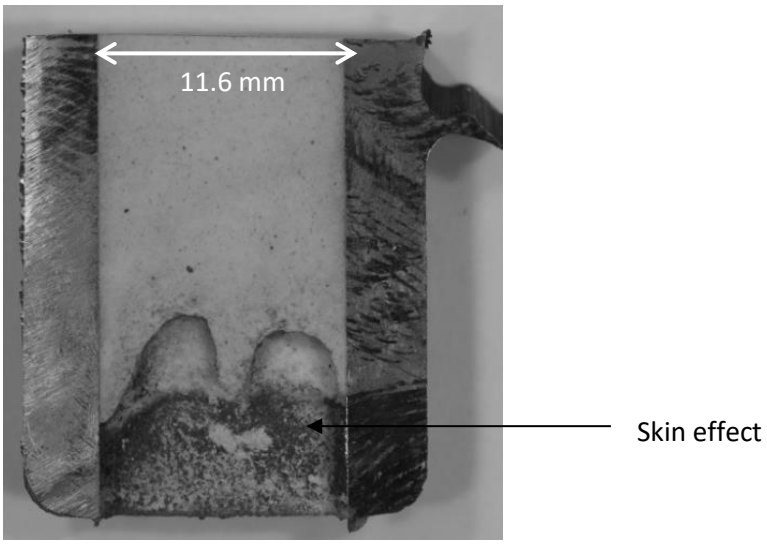

Figure 5.4 Cross-section of partially leached core leached with opening facing up (1 M KOH)

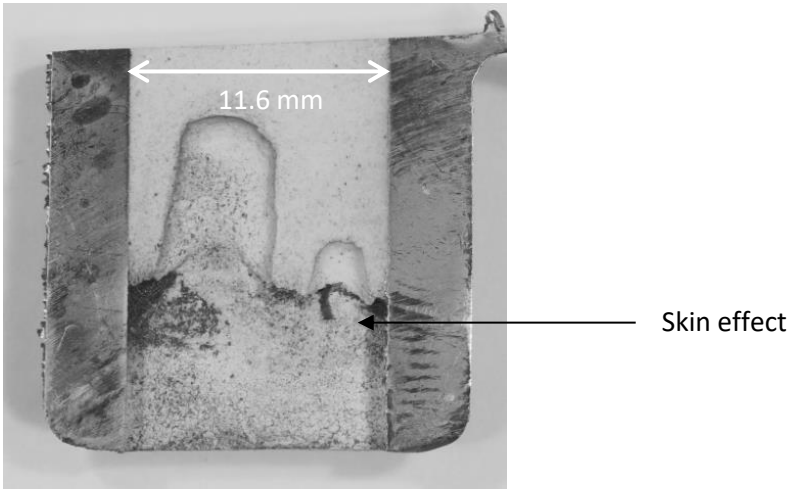

Figure 5.5 Cross-section of partially leached core leached with opening facing sideways (1 M KOH)

From Figures 5.3, 5.4 and 5.5, it can be seen that the leach profiles observed were similar regardless of the orientation of the core in the autoclave. An m-shaped symmetrical or asymmetrical leach profile was observed in each case. It should be noted that this m-shaped leach profile was not an outlier and was

observed in other core geometries and will be discussed in greater detail in Chapter 6.

Another unique pattern observed just below the leach front irrespective of the core orientation in the autoclave is the skin effect. The part of the core with the highest resistance to leaching seems to be the core in direct contact with the metal casting. This was also observed in more complex core geometries and has important implications for the process. Firstly, core in direct contact with the channel wall is more difficult to detect using an opthalmoscope or fiberscope since they do not block the channel. Secondly, this means that the core leaches from the inside out, i.e. faster in the middle of the channel and slower at the edges. This is explored in more detail in Section 5.2.2.

5.3 Effect of Part Orientation and Position on Leaching Effectiveness

5.3.1 Part Orientation

Figure 5.6 shows how the part orientation in the autoclave affects the amount of core removed in 1 M KOH after 1 hour in autoclave using the standard PVD parameters shown in Table 5.1. It was observed that the most efficient orientation for optimal core removal occurs when the core opening faces down. In this orientation, 14.6% of the core by volume was removed compared with 8.3% with the core opening facing up, i.e. a 76% increase in core volume loss. Intuitively, this was expected because if the core opening faces down, parts of the core that have been loosened because of the chemical reaction and ASR expansive gel mechanism can simply fall out due to gravity. With the core opening facing up or

on its side, any loose core within the channel simply accumulates and acts as a barrier to the dissolution reaction by limiting the contact of fresh alkaline solution with the unleached core surface.

With the core opening facing down, the rising bubbles are also more likely to have a larger impact on the core surface compared to when the core opening is facing up.

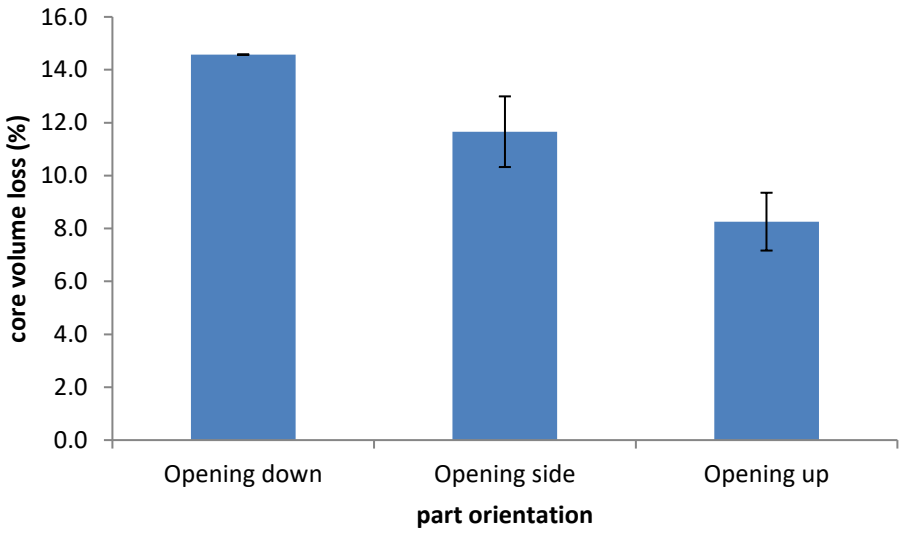

Figure 5.6 Effect of part orientation on core removal

The results shown in Figure 5.6 also highlights an important feature about core leaching. If the core test bars had two openings – one at the top and one at the bottom, the leach front will meet 64% from the bottom or 36% from the top of the core openings as shown in Figure 5.6. This however only applies to simple symmetrical geometries where the core area exposed to the alkaline solution is approximately constant from both the top and bottom. There is also a smaller standard deviation observed when the core opening facing down compared to

the other orientations. Given the role gravity plays in allowing undissolved core segments to simply drop out of the metal castings, orienting the test bars so that the core opening is on its side or facing up could lead to a larger variation in the core volume loss.

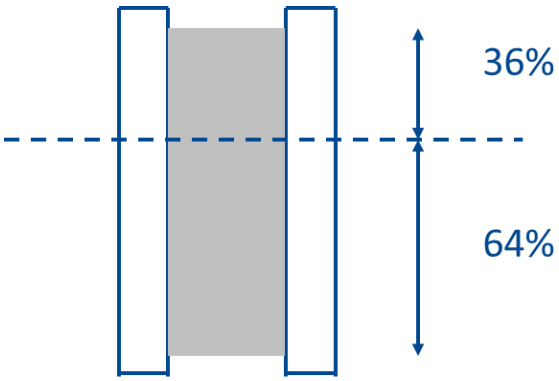

Figure 5.7 Hypothetical position of meeting leach fronts

In reality, core designs are more complex and the cross-sectional areas exposed to the alkaline solution are not constant as the reaction progresses because the geometries are asymmetrical. Thus, predicting the leach time, i.e. when the leach fronts meet, is more complicated and is covered in Chapter 6.

5.3.2 ASR Gel Expansion and Cracking Mechanism

The partially leached test bar cross-sections shown in Figures 5.8 – 5.10 were further analysed using a Jeol 6060 scanning electron microscope to explain possible causes for the m shaped profile and to highlight any defects at the core surface as a result of the pressure swing cycle.

Figure 5.13 shows the leach profile of the core which was leached with the opening facing down. Five areas of interest are highlighted which were further examined using the SEM.

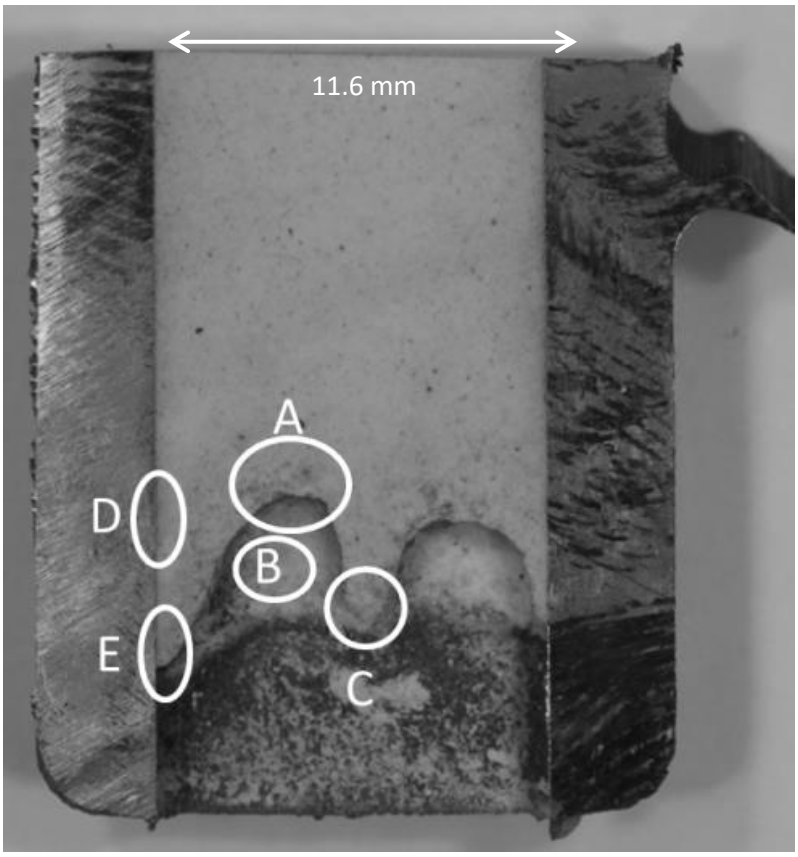

Figure 5.8 Areas of interest for SEM analysis

The outer concave section of the leach front (section A) has defects directly above the leach front. This is examined in detail in Figure 5.9.

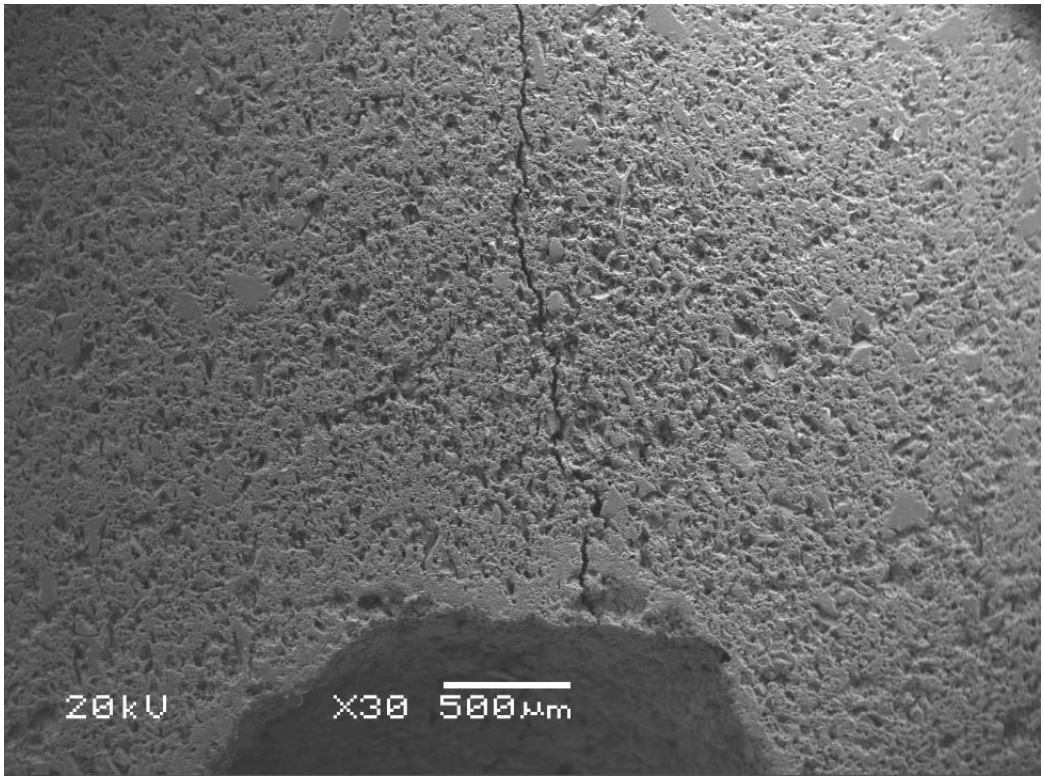

Figure 5.9 SEM of section A

A crack forms at the top of the leach front. Smaller defects next to the leach front are also observed.

The SEM image of section B is shown in Figure 5.15. This shows the inner part of the leach front which shows evidence of re-precipitation of silica which has historically been suspected of increasing the leach resistance of partially leached cores.

Figure 5.15 also shows map-cracking features. This type of cracking is also observed in concretes which are damaged as a result of alkali silica reaction (ASR) expansive gel cracking. This is caused by the hygroscopic properties of

silicates allowing them to absorb water and expand. As explained in Chapter 4, the silicates forming in the fluid film layer are likely to be highly siliceous, i.e. high SiO_2:M_2O molar ratios. ^{29}Si-NMR confirmed the presence of potentially layered silicates which primarily contain Q^3 Si atoms. It should be noted that Q^3 silicates are only potentially layered. Layered silicates can absorb water into their inner structures causing them to expand in the presence of calcium ions. Expansive ASR products requires some amount of calcium to give the gel its expansive properties (123).

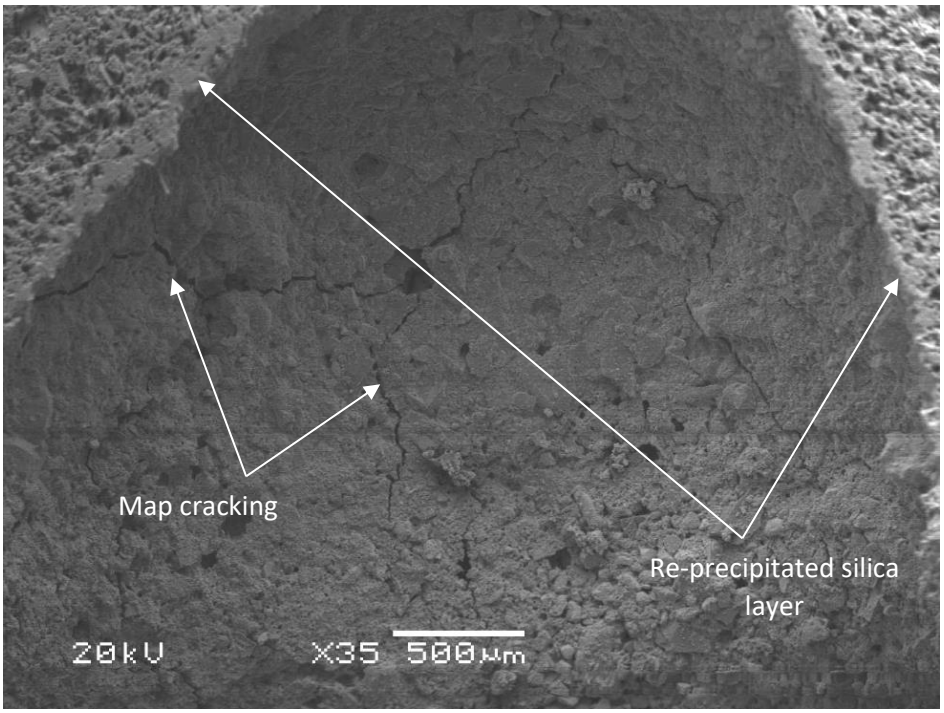

Figure 5.10 SEM of section B

The re-precipitated silica layer observed on the surface of the leach front was likely caused by the drying of the fluid film layer.

Figure 5.11 shows the ASR gel cracking phenomenon observed in concrete which bears some similarity to the map and longitudinal cracking features observed in Figures 5.10. It should be noted however that in ASR observed in concrete, map and longitudinal cracks are only surface effects. The cracks observed in the ceramic core are subsurface cracks and could arise because the large pressures of 600 kPag in the autoclave will cause some of the alkaline solution to penetrate the porous ceramic core thereby creating the potentially expansive gel beyond the surface.

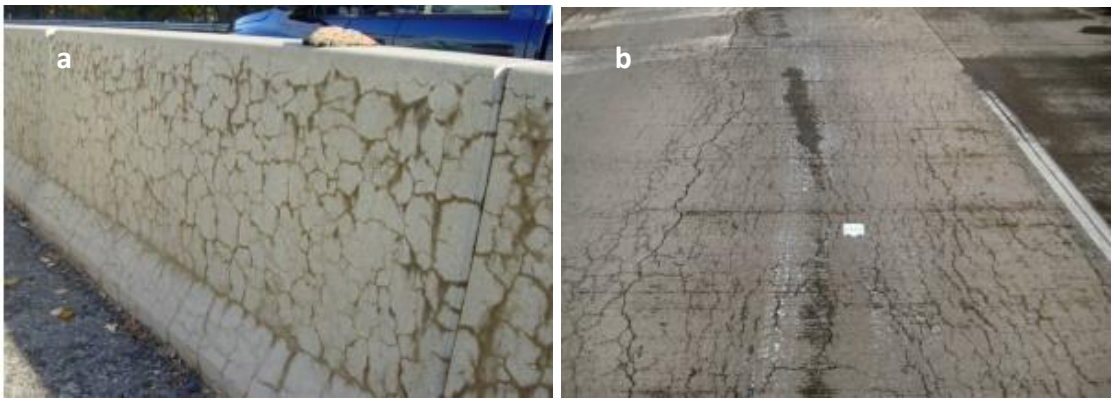

Figure 5.11 ASR gel cracking in concrete (a) Map cracking (b) Longitudinal and map cracking (124)

In concrete, the ASR gel cracking mechanism is similar albeit less aggressive than what occurs in the autoclave. Four requirements are needed for the process to occur (123, 124):

- An alkali source – Portland cement contains minor amount of Na^+, K^+ and OH^-. pH is typically 13.5
- Calcium ions

- Reactive silica present in concrete – crystalline silica (cristobalite, tridymite and quartz)
- Moisture – relative humidity above 80%

These requirements are all present and accentuated in the leaching process. There is an excess supply of Na^+ and K^+, the pH of the alkaline solution is 14.9, reactive silica comprises a majority of the core formulation and the core is constantly in contact with water. Also, the operating temperature in the autoclave is about 160 ^oC which is significantly higher than the current average world temperature. Higher temperatures increase the production rate of the siliceous fluid film layer by accelerating the dissolution rate of the silica. Finally, pressures of 600 kPag force some of the alkaline solution into the porous core (about 30% open porosity). This can be seen in Figure 5.8 where defects are present approximately 2 mm beyond the leach front. These defects also occur in concrete and are known as surface pop-outs and likely occur through the detachment of individual grains caused by the expansion of the silicate gel leaving behind a recess. Alternatively, these could simply be inert zircon grains falling out of the core.

The only requirement that may not be fully met is the presence of calcium ions since these exist as trace amounts in the core formulation – approximately 0.015 wt.%. The precise role of calcium in the formation of expansive gel products is not fully understood. While several researchers (124-126) support the idea that calcium ions are vital for ASR expansion to occur, there is no evidence to show if it is a threshold phenomenon where below a certain amount of calcium ions, no

expansive gels are produced. This does however have some implications for future core formulations since the calcium content in the cores could be hypothetically increased to enhance ASR.

Figure 5.12 shows a higher magnification SEM image of section B (Figure 5.8). A closer look at possible surface pop-outs is highlighted within the blue circles.

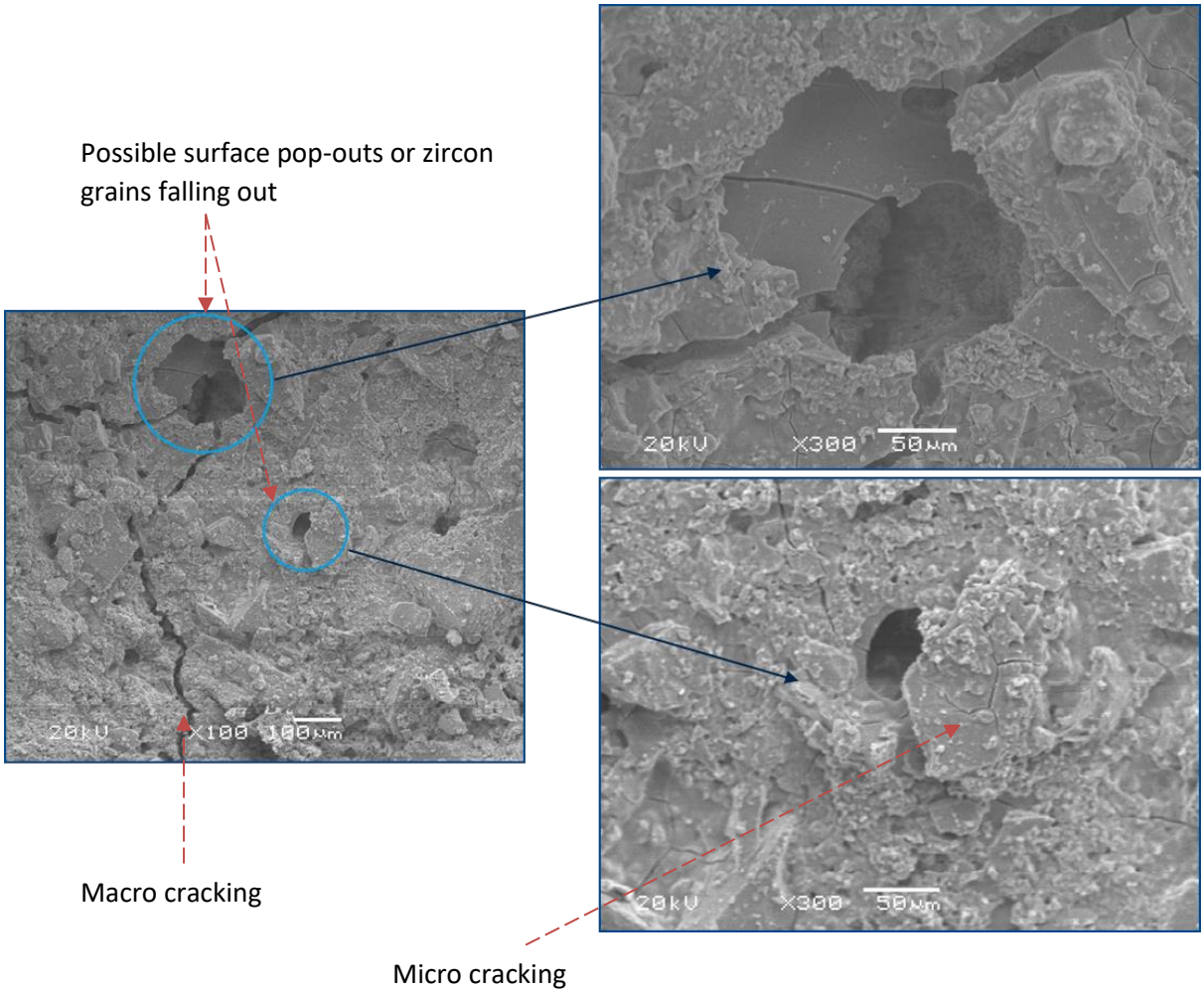

Figure 5.12 Higher magnification image of section B showing macro and micro cracking

Similar cracking features were observed in rhyolite samples immersed in NaOH at 80ºC. Rhyolite has a high silica content and in the presence of alkaline

solutions will form an calcium rich gel that leads to crack formation as shown in Figure 5.13.

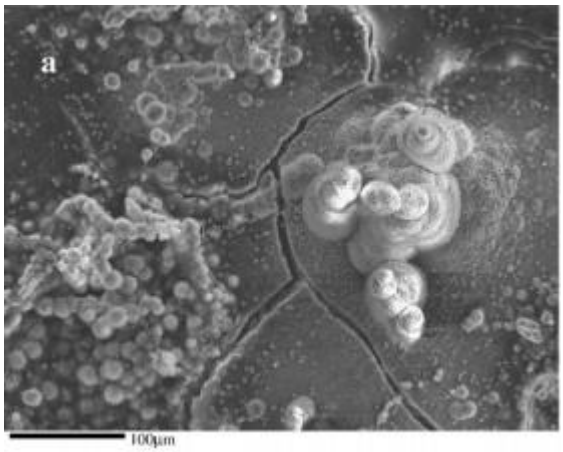

Figure 5.13 Cracks observed in rhyolite after immersion in NaOH at 80°C (79)

It is evident from these figures that both macro and micro cracking occurs as a result of the ASR expansive gel process. Macro cracking occurs between silica grains or silica and zircon grains as a result of the gel absorbing water, expanding and pushing the grains further apart. Micro cracking within the silica grain increases its surface area. This increases the concentration of Q^2 and Q^3 Si atoms, i.e. surface Si atoms which have been shown in Chapter 4 (both experimentally and from literature) to have lower activation energies for the formation of the five-fold coordinated complex which is the precursor to siloxane bond cleavage. These Q^2 and Q^3 Si atoms now exposed as a result of the micro cracks are more reactive than the Q^4 Si usually present. The micro cracks caused by the ASR expansive gel process increases the reactivity of the silica particle (via a reduction in activation energy) which in turn increases the production of the

siliceous fluid film layer. The physics and chemistry of the process are thus self-reinforcing on each other.

Section C of Figure 5.13 shows a portion of the core that seemed to have a larger resistance to leaching and was responsible for the m shaped leach profile previously described. Figure 5.19 shows a magnified version of section C. Initially, it was expected that the localised resistance to leaching was a result of a higher concentration of insoluble zircon particles in that region. From Figure 5.14 however, it is not possible to tell which grains are zircon.

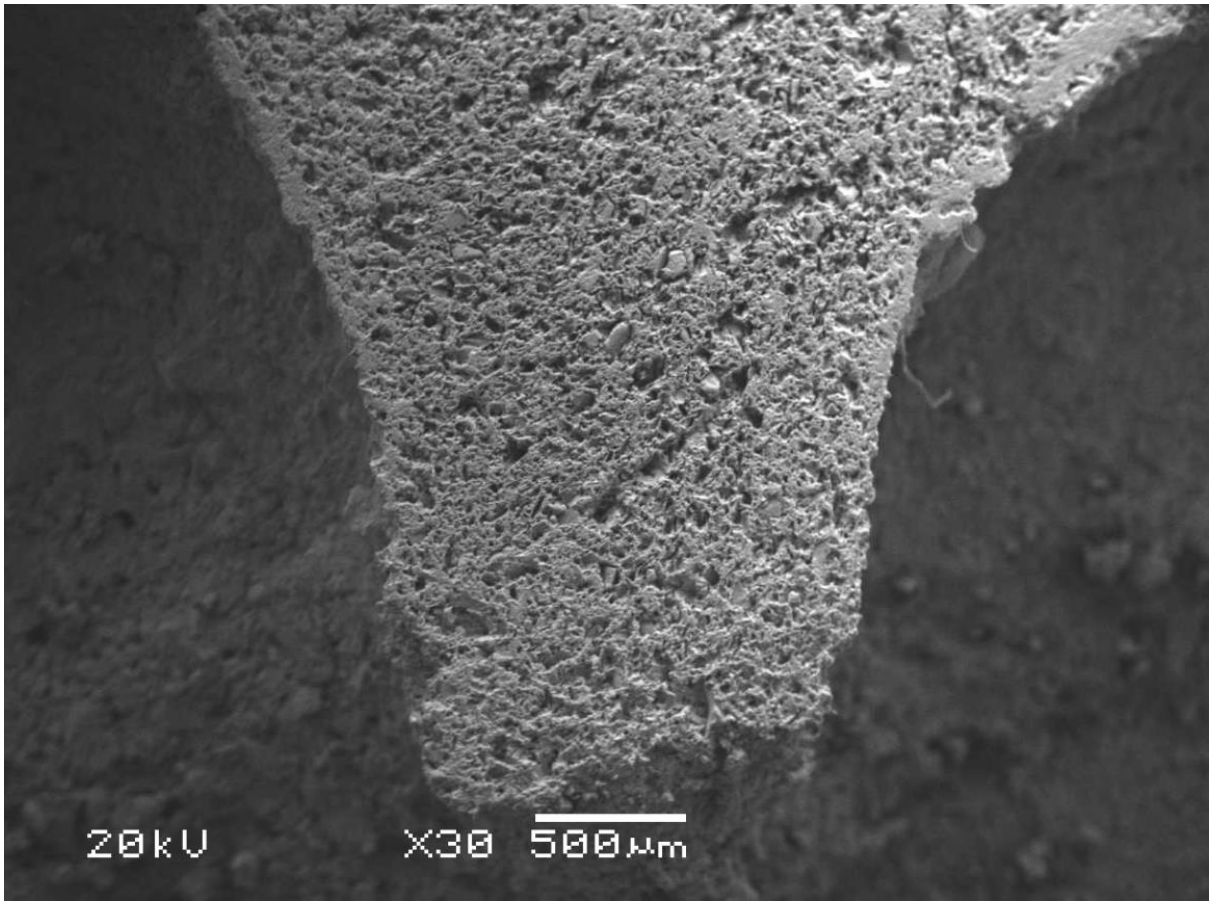

Figure 5.14 SEM of section C

A more likely cause of the m shaped profile could be caused that localised differences in core porosity. As previously explained, the alkaline solution is absorbed into the porous core structure and reacts with the silica particles forming an expansive silicate gel. However, localised regions of lower porosity may be less pervious to the alkaline solution thereby arresting the ASR expansive gel process.

It is hypothesised that any difference in porosity across the core arises because of an uneven particle size distribution caused by the injection process. Ceramic cores are injected into a die forming the shape of the desired core geometry. During injection, it is possible that localised pockets of high and low porosity are formed which promote or restrict the infiltration of the alkaline solution respectively. Areas of higher porosity will be more susceptible to the ASR expansive gel cracking process.

High porosity areas are formed by a higher concentration of larger silica and zircon grains whereas low porosity areas are formed either by a higher concentration of smaller silica and zircon grains or evenly distributed regions where the smaller particles fill up the interstitial spaces between the larger particles. These three possibilities are shown in Figure 5.15.

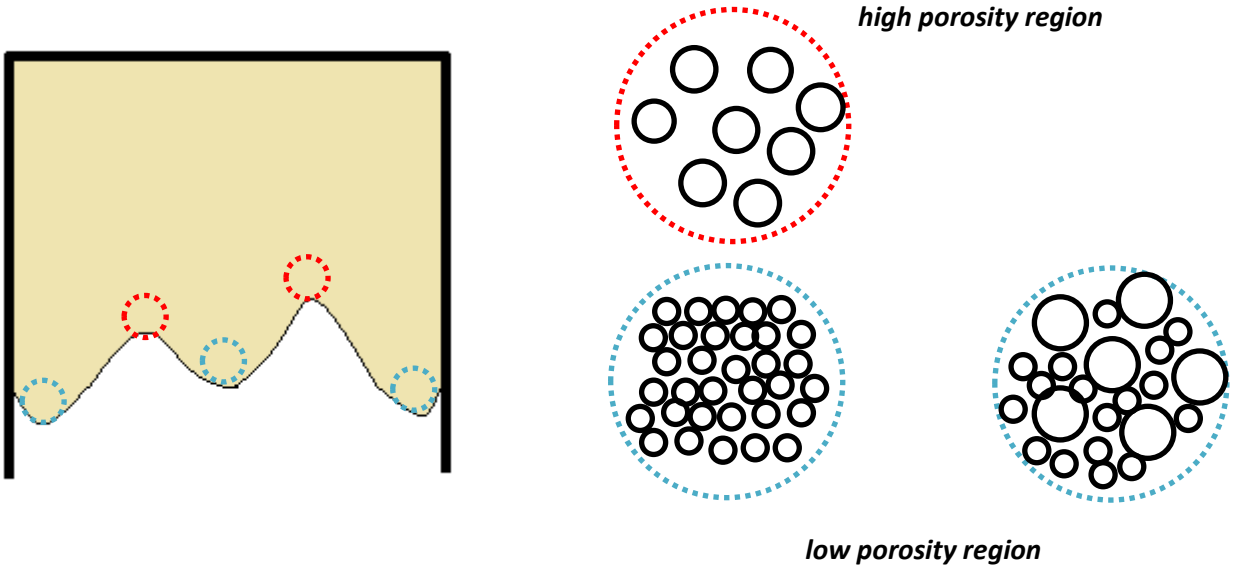

Figure 5.15 Possible porosity variation at different sections of the core

The flow of liquid into the pores is governed by the Washburn equation which describes the penetration length of a liquid into a capillary pore as shown in Equation 5.2:

$$l = \sqrt{\frac{\gamma r t \cos\emptyset}{2\mu}} \qquad (5.2)$$

where *l* is the penetration depth, γ is the surface tension, r is the pore radius, t is time, ∅ is the contact angle between the liquid and particle and μ is the viscosity. Longer penetration depths are expected as the pore radius is increased. Larger viscosities will also limit the penetration depth. Calculating a precise value of the penetration depth is very difficult because the viscosity of the penetrating fluid will not be constant. As the alkaline solution penetrates the porous core structure, it will react with the silica grains to form viscous silicate products.

It is suggested that the m shaped leach profile (shown in Figures 5.8 – 5.10) is caused by a backflow of larger particles during the injection process as illustrated in Figure 5.21. The arrows point to the flow of larger particles which create localised regions with a higher porosity.

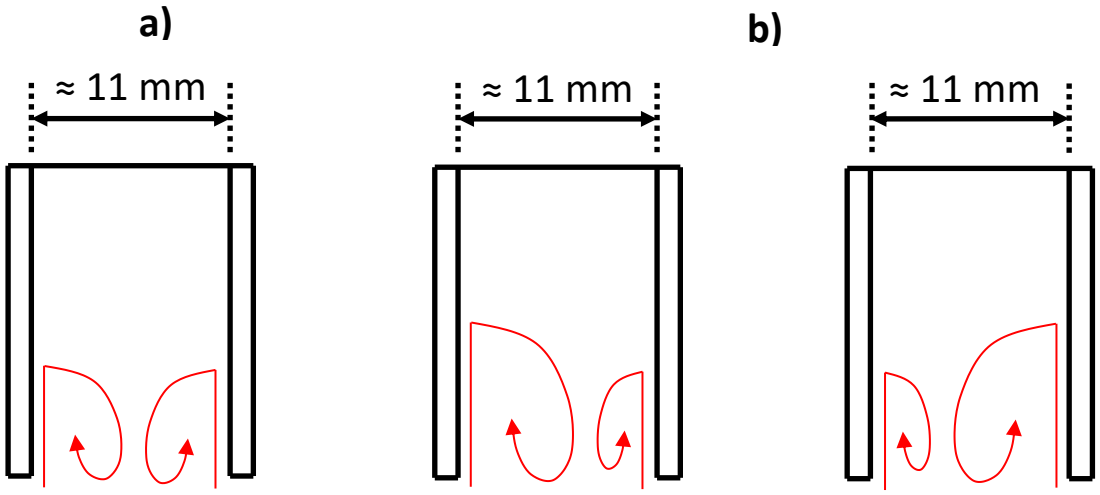

Figure 5.16 Backflow during core injection – a) symmetrical backflow b) asymmetrical backflow

Particle orientation during injection moulding could also lead to differences in porosity across the channel width. During injection moulding, the ceramic core undergoes shearing, compression and cooling. The shear stresses have been reported to cause grain orientation of plate like particles in the direction of the flow (127). Differences in particle orientation across the channel width could cause variations in porosity and hence susceptibility to the ASR cracking mechanism.

In narrower channels, the m shaped leach profile was not observed. Instead, a simple parabolic profile was formed as shown in Figure 5.17. This could imply that in narrower channels (≈5 mm) no backflow occurs during core injection and larger grains aggregate at the centre of the channel as shown in Figure 5.18.

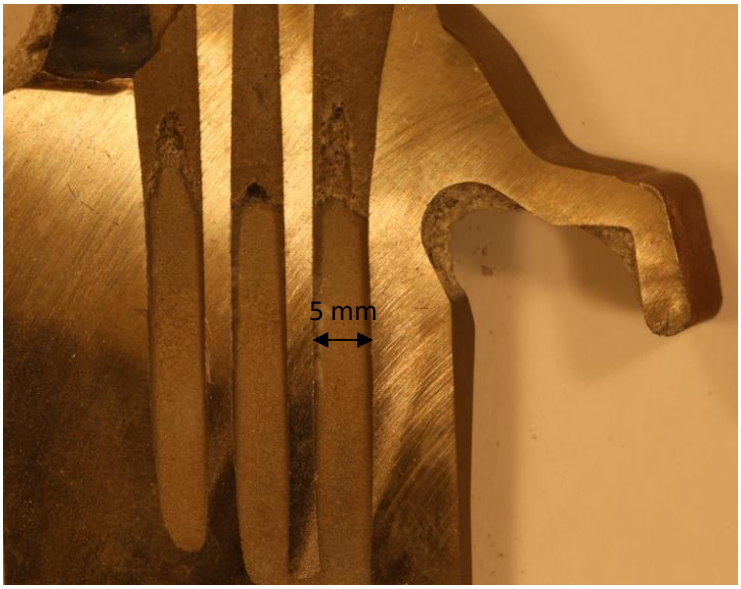

Figure 5.17 Single parabolic leach front observed in narrow channels

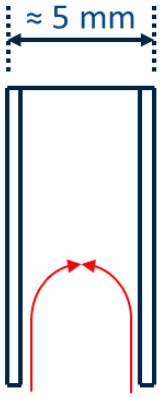

Figure 5.18 No backflow during core injection

An alternative explanation is that these leach profiles are simply a product of rising bubbles during boiling in the autoclave. This is unlikely to be the cause because the same patterns were observed irrespective of the orientation of the parts in the autoclave as shown in Figures 5.8 – 5.10. The impact of rising bubbles hitting the core surface will have a different effect on a test bar with its opening facing down compared to a test bar with its opening facing sideways.

From Figures 5.8 – 5.10, it was observed that the core in direct contact with the metal casting was more resistant to leaching. This led to the skin effect previously described and was also observed in more complex core geometries used in actual blades which will be covered in Chapter 6. Initially, it was hypothesised that this was caused by diffusion of the metal casting into the porous core surface it comes in contact with thereby giving it a stronger ‘grip’ on the ceramic core. This was however discounted as shown in Figure 5.24 which shows no intrusion of the metal casting into the core surface.

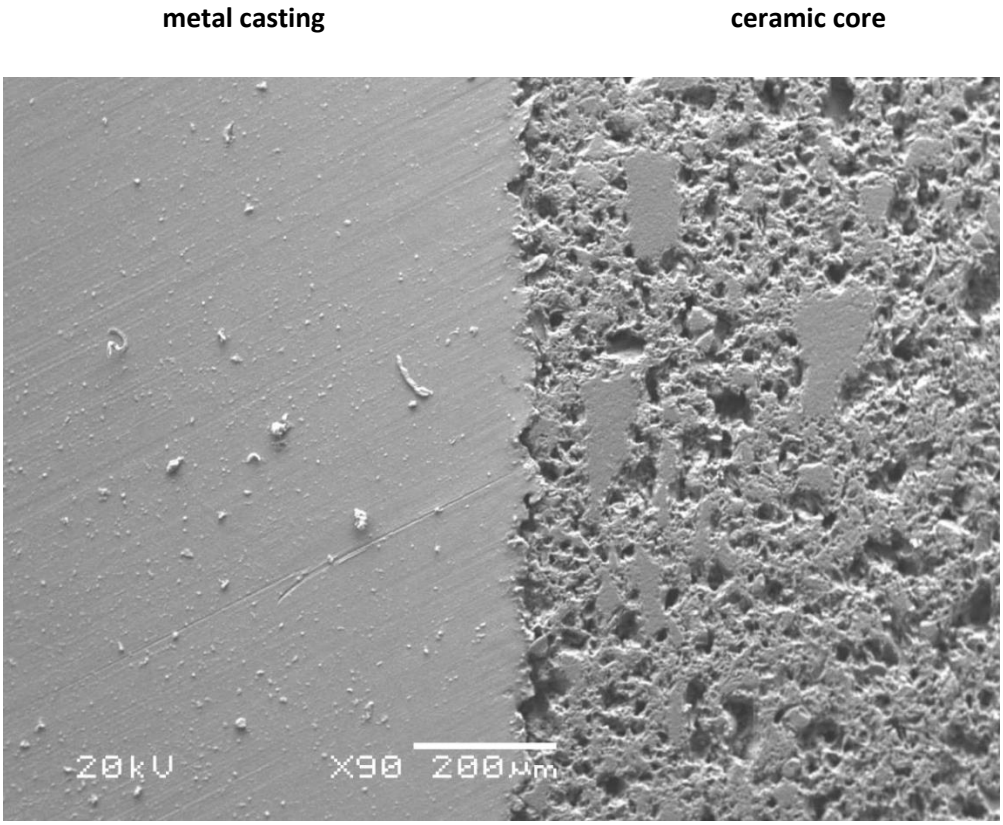

Figure 5.19 SEM of section D

A more likely explanation is that lower porosity regions exist near the core surface (i.e. the part of the core in direct contact with the metal casting) which limits the intrusion of the alkaline solution thereby restricting the subsequent ASR expansive gel process.

Lower porosity regions near the core surface could arise because:

I. Direct contact with the metal casting exposes the core surface to high temperatures (up to 1400 °C) which could cause additional sintering of the particles
II. A higher concentration of smaller particles near the core surface or evenly distributed regions as shown in Figure 5.20
III. Particle orientation aligned with the flow during injection moulding

IV. A combination of I and II and III

5.3.3 Part Position

The relative position of the test bars in the autoclave had a negligible effect on the amount of core removed. Figure 5.26 shows the arrangement of the test bars in the autoclave and the numbering system used to record their position in the autoclave. These were leached for 15 minutes in 1 M KOH using the PVD parameters shown in Table 5.1. All the parts were oriented with the core opening facing down.

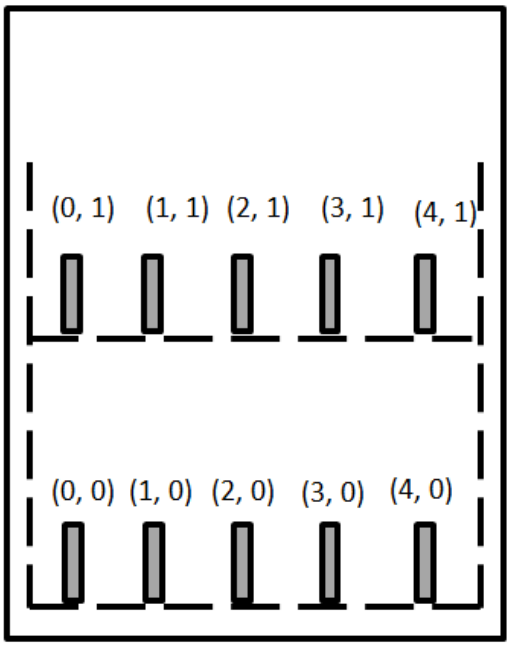

Figure 5.20 Part positioning in the autoclave

It was found that test bars in the top basket had a core volume loss of 6.3% ± 1.3% compared to parts in the bottom basket which had a core volume loss of

5.8% ± 1.3%. This is not a statistically significant result. Also, batch to batch variation of core volume loss was less than 2% of the mean.

5.4 Conclusion

The pressure swing cycle used in the autoclave is technically a cavitation cycle since vapour bubble formation is preceded by a drop in autoclave pressure at approximately constant temperature. However, bubble collapse is unlikely to occur because re-pressurisation after the low pressure dwell phase is unlikely because air is not supplied rapidly enough to the autoclave.

The explosive bubble growth experienced once the autoclave pressure drops below the vapour pressure helps in disrupting the viscous fluid film layer. However, fluids with large viscosities and surface tensions may be resistant to this as evidenced by leaching carried out in 1M KOH solution which showed no improvement under an accelerated cycle.

The ASR cracking mechanism is the likely physical phenomenon responsible for core removal in the autoclave. It is caused by the formation of a siliceous fluid film layer consisting of potentially layered silicates which absorb water, swell and cause cracks to form. Potential layering was observed from the ^{29}Si-NMR data which showed the presence of Q^3 silicates in both NaOH and KOH. It has however not been proven if the Q^3 silicates are indeed layered. Trace amounts

of calcium present in the core also make it a possibility that the potentially layered silicates have an expansive property. However, it is not known whether the amount of calcium present in the core is sufficient to cause the damaging effects of ASR observed in concrete.

Leaching of simple rectangular core samples showed an ‘m’ shaped leach profile for wider channels (≈11 mm) while a parabolic leach front was observed in narrower channels (≈5 mm). This is unlikely to be caused by boiling action and rising bubbles impacting the core surface because the same pattern was observed irrespective of the orientation of the core in the autoclave. A more likely explanation is localised variation of porosity across the channel width which either promotes or limits the penetration of the alkaline solution.

The orientation of the core opening in the autoclave had a significant effect on the amount of core removed. The optimal orientation was with the core opening facing down because weakened pieces of core could simply fall out due to gravity. Also, the impact of rising bubbles hitting the core surface will be more aggressive with the core opening facing down.

Finally, the effect of the test bar position in the autoclave did not have a significant effect on the amount of core removed.

6 PILOT SCALE TRIALS

The aim of this chapter is to explain the leaching mechanism of ceramic cores in actual turbine blade geometries. These are complex, asymmetrical geometries with non-regular cross-sections. This chapter will also detail a method to predict leach times for turbine blades.

The operating conditions of the pilot-scale trials were designed to be closer to reality. In Chapter 5, the rectangular core test bars were leached in 1 M alkaline solutions. These conditions were used because it was expected that higher concentrations would completely dissolve the small core volume leaving nothing behind for analysis.

Cores used in turbine geometries have larger volumes therefore the alkaline solution concentration used was 5 M which is closer to the actual concentrations used on an industrial scale. A new blade was used for each run and a 5 M KOH solution was used as the leachant. The standard cycle parameters were used as shown in Table 5.1 for every trial described in this section.

The leaching mechanism of ceramic cores in simple rectangular prism geometries was examined in Chapter 5 and it was found that the rate of core removal was approximately constant over a 3 hour period. Turbine blade geometries exhibit more complex leach rates because the ceramic core

geometries have constrictions and dilations across their axial sections leading to a decrease and increase (respectively) in the cross-sectional area (CSA) directly exposed to the alkaline solution.

6.1 Leach Rate Across Different Channels

The turbine blades used in these experiments had a total of four channels as shown in figure 6.1.

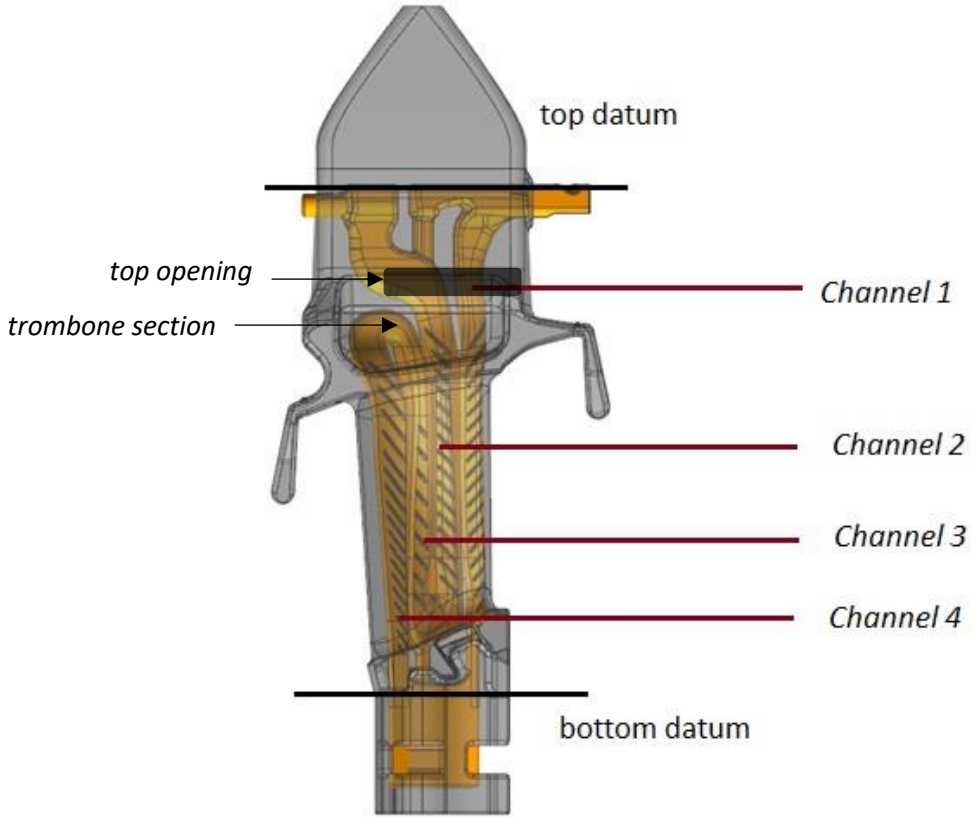

Figure 6.1 Core geometry of Trent 1000 HP blade (128)

Channels 1 and 2 have dual openings – one at the bottom datum and another near the top datum as indicated in Figure 6.1. These two channels are simultaneously leached from both openings whereas channels 3 and 4 only have

a single opening at the bottom. Channels 3 and 4 have another peculiar feature not present in the other channels – the presence of a trombone section connecting the two channels together.

As explained in section 3.14.1, the amount of core removed from each channel was measured by inserting a 1 mm diameter steel wire into each channel and measuring the depth of penetration. The leach depth across each channel was then used to measure the corresponding volume loss using the CAD file of the blade. The limitation of this method is that it systematically overestimates the leached volume because of the non-linear leach front of the core as shown in Figure 6.2a and 6.2b.

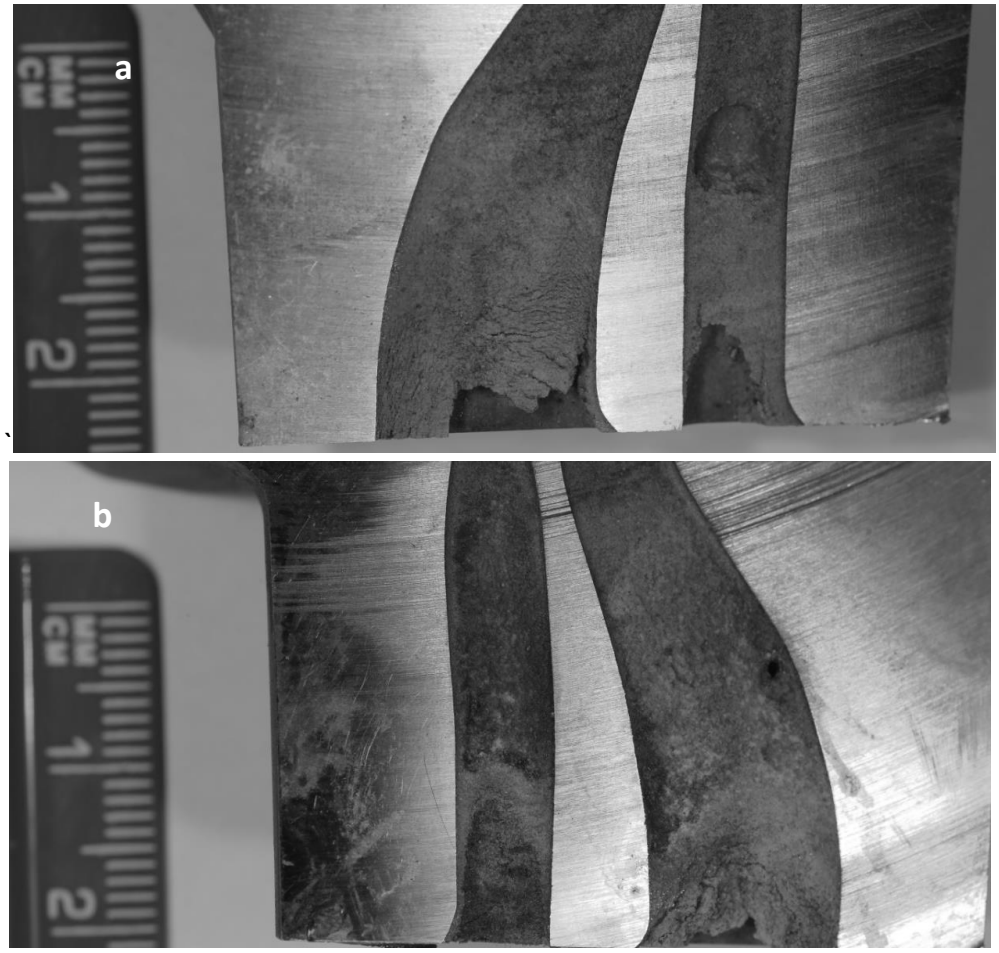

Figure 6.2 Non-linear leach front of two halves from the root section of a Trent 1000 HP blade

Similar non-linear leach fronts were also observed in the rectangular core bars discussed in Chapter 5.

The metal wire is inserted at approximately the midpoint of each channel as shown in Figure 6.3.

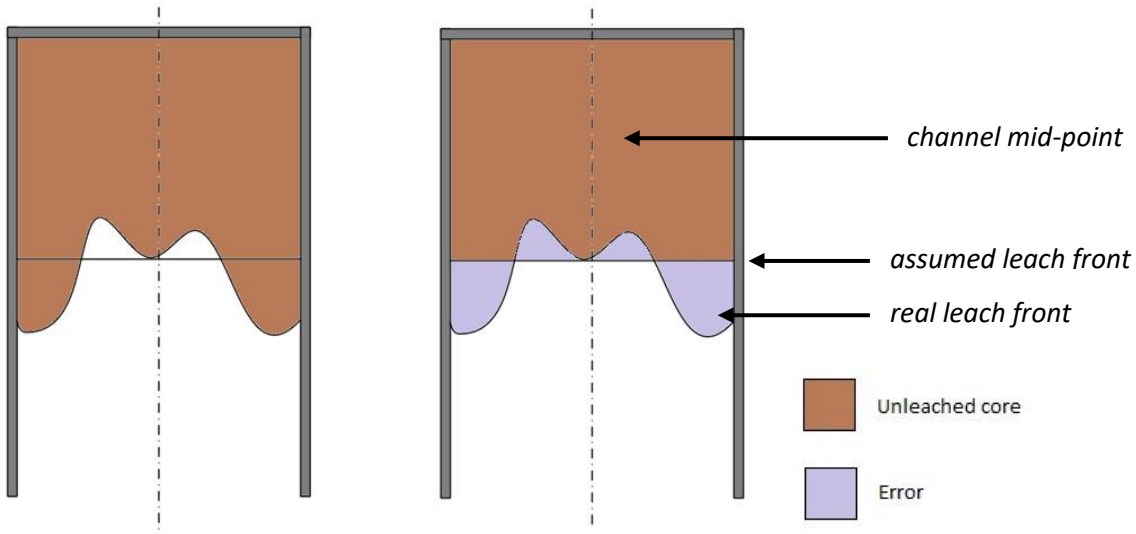

Figure 6.3 Leach depth measurement

There is some random error involved with this method because the centre of the core does not actually represent the depth of the leach front. The centre of the core often leaches at different rates to the edges therefore some measurements will overestimate or underestimate the depth of penetration.

X-ray imaging was also carried out to accurately detect the leach front and measure the core volume loss. This proved unsuccessful because the ceramic core was undetectable under X-rays.

The core volume loss in the rectangular prism geometry described in Chapter 5 is shown in Figure 6.4.

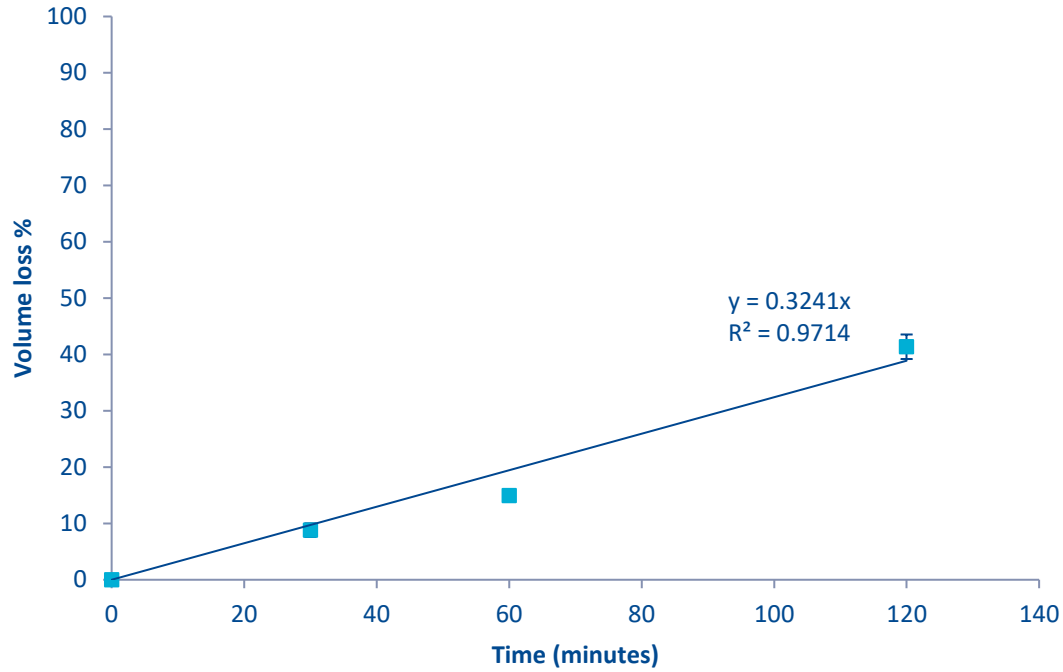

Figure 6.4 Core volume loss in rectangular prism geometry (1 M KOH)

In the simple rectangular prism geometry, the cross sectional area of the metal casting is constant. However, the cross-sectional area exposed to the alkaline solution is not constant because of the non-linear leach front.

Figure 6.5 shows the progression of the core volume loss % for an actual core geometry. The total cross-sectional area (CSA) over which the core volume loss was registered is also shown. This is the approximate CSA of the core which exposed the alkaline solution and was calculated using the method described in Section 3.11.1.

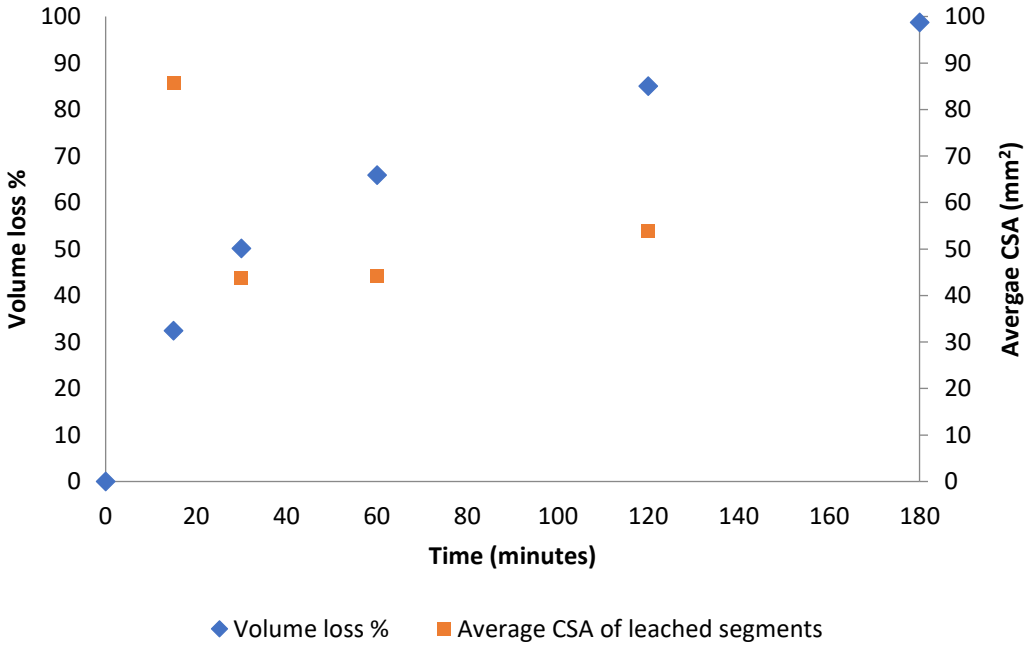

Figure 6.5 Core volume loss and average CSA exposed in Trent 1000 HP

After 180 minutes, 99% of the core (by volume) was leached. In the first 15 minutes, 41% of the entire core was leached. This rapid initial rate is likely due to the large core section exposed to the alkaline solution at the start of the reaction. In the first 15 minutes, the total core CSA exposed is 86 mm^2. In the next 15 minutes, the constrictions in the individual core channels reduce the total CSA exposed to 44 mm^2, an approximate 50% reduction in CSA. This reduction in the cross-sectional area reduces the dissolution rate of the silica-based core.

Since the average CSA exposed to the alkaline solution was calculated by averaging the top and bottom CSA from the CAD file, error bars were not used on the average CSA of leached segments.

Figure 6.6 shows how the amount of unleached core material in the turbine changes with time. The rate of core loss from the turbine component seems to follow an exponential decay curve.

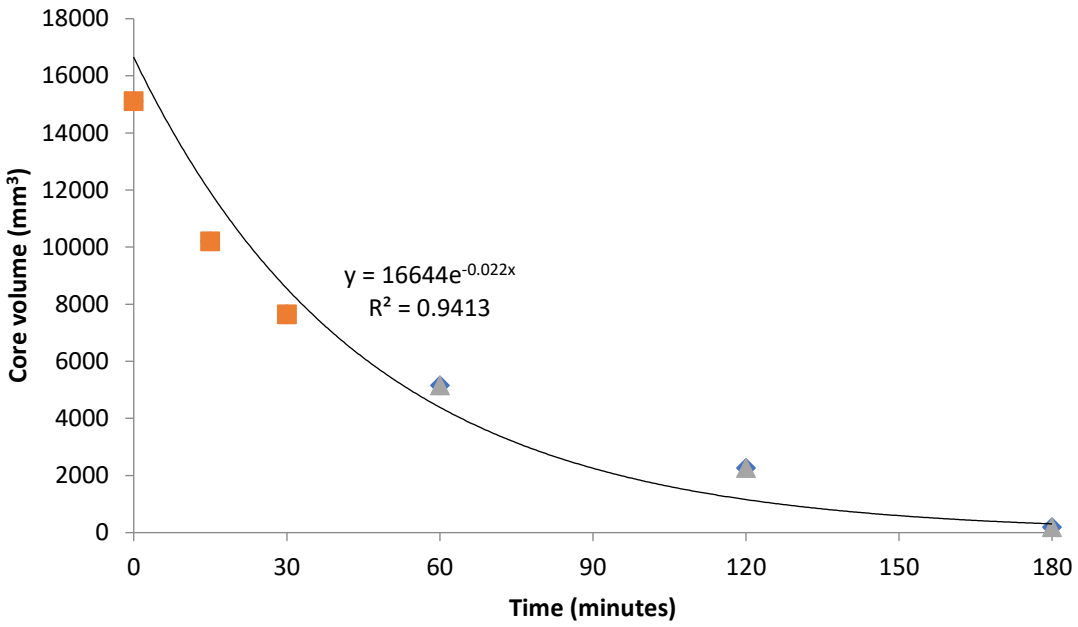

Figure 6.6 Unleached core volume as a function of time

One possible explanation for the exponential decay curve is that the build up of silicates in the autoclave slows down the rate of core removal. This was explained in Chapter 4 and occurs because the different silicate species exist in equilibrium with each other and any build-up in monomeric silicates in solution (which is the first product when silica reacts with OH^-) will slow down the reaction. This certainly occurred in the laboratory experiments where 10 g of silica was dissolved in 100 mL of alkaline solution – there was a noticeable retardation of the reaction because the silica concentration in solution was approximately 10 wt.% once fully dissolved.

However, the pilot scale trials described in this chapter take place on a much larger scale. For each trial, two turbine blades were used. Each core weighs approximately 35 g and the total autoclave volume is 30 L (approximately 30 kg of liquid). The total core mass is 70 g and the dissolvable mass (amount of silica in the core) is approximately 2/3rd of 70 g = 47 g. Therefore, the silica concentration in solution once all the core is dissolved is only about 0.16 % (0.047 kg of core in 30 kg solution). This is a negligible concentration of silica in solution and is likely to have no effect on the dissolution rate.

Alternatively, the trend observed in Figure 6.6 could be explained by an initial rapid rate in the first 30 minutes. During this time, large sections of the core were exposed to the alkaline solution thereby increasing the rate of siloxane cleavage and the ASR cracking process. After the initial rapid rate, the rate of core removal decelerates because of constrictions in the core channels as shown in Figure 6.5.

The different channels have different volumes so a better way to show leaching progress is as a percentage of the channel volume as shown in Figure 6.7.

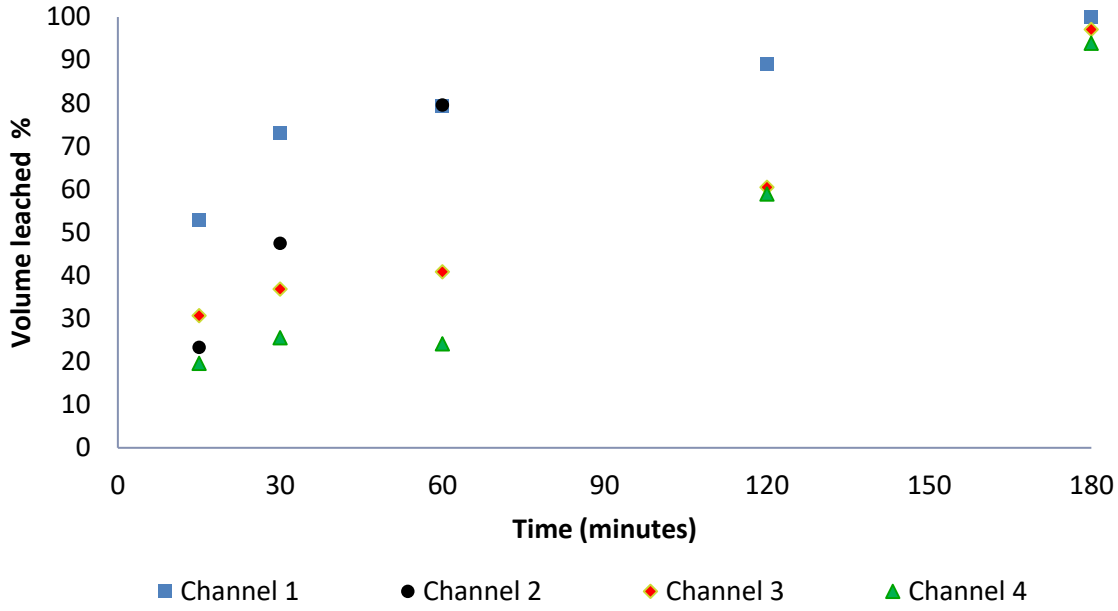

Figure 6.7 Volume loss % across different channels

Channel 2 is the fastest and is fully leached after 120 minutes. Channel 1 is close behind with 90% leached after 120 minutes while channels 3 and 4 are the slowest. In the first 30 minutes, almost 70% of the core was leached out of channel 1. Channel 2 quickly catches up and overtakes channel 1 after 120 minutes. These results were not surprising considering channels 1 and 2 have dual openings as shown in Figure 6.1 while channels 3 and 4 only have a single opening each.

Another reason why channels 1 and 2 leach faster than 3 and 4 is because the former have larger cross-sectional areas as shown in Figure 6.9. The core CSA exposed was calculated using the CAD file of the core geometry as explained in section 3.11.1.

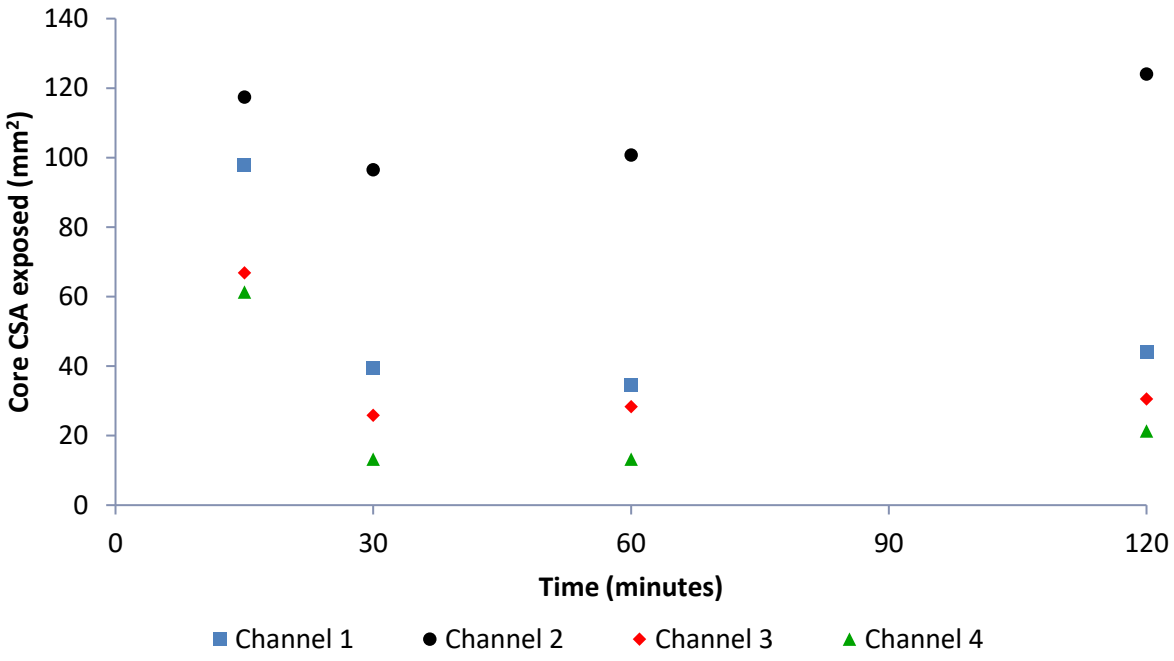

Figure 6.8 Core CSA exposed at different times across the four channels

Initially, all channels start with a large CSA exposed to the alkaline solution but subsequent constrictions in the geometry reduces the CSA across channels 1, 3 and 4. Channel 2 has the largest CSA which would explain why it leaches the fastest whereas channel 4 was the slowest and had the smallest CSA.

6.2 Correlation between Leached Volumes and Average Cross-Sectional Area

In total, 14 leached segments were analysed to show the relationship between the core volume loss of different core segments and the average cross-sectional area over which that loss was registered. The results are shown in Figure 6.10.

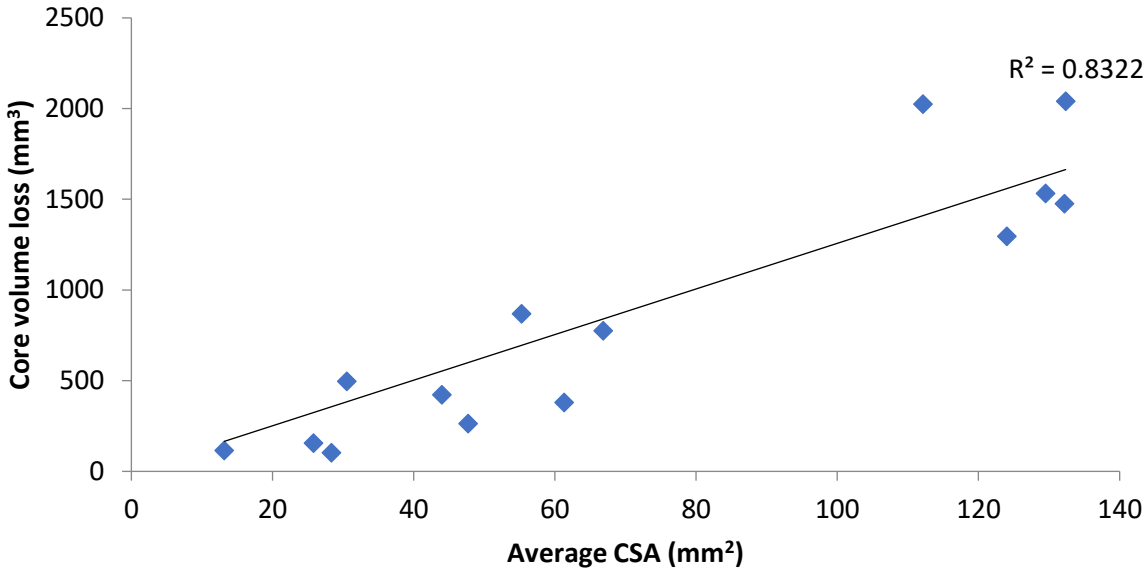

Figure 6.10 Correlation between core volume loss and average CSA over which loss was registered (y intercept set at 0)

There is a reasonable correlation between the volume of individual segments leached and the average cross-sectional area of that segment. The problem with this analysis is that there are two clusters of average cross-sectional areas – one less than 70 mm^2 and another greater than 100 mm^2 with nothing in between.

In Chapter 5, it was shown that the orientation of parts in the autoclave significantly affects the amount of core removed. Core openings facing down were found to remove about 76% more core material compared with core openings facing up (identical geometries and core formulations in both orientations). This was attributed to gravity – any loose core can easily fall down with a downward facing core opening but accumulates in an upward facing core

opening. Also, the impact of rising bubbles during the vent phase will have a larger impact when the core opening faces down.

This factor was used to adjust the cross-sectional areas of core segments in channels 1 and 2 (which had both upward and downward facing core openings as shown in Figure 6.1). Adjustments were made by dividing the upward facing core cross-sections by 1.76.

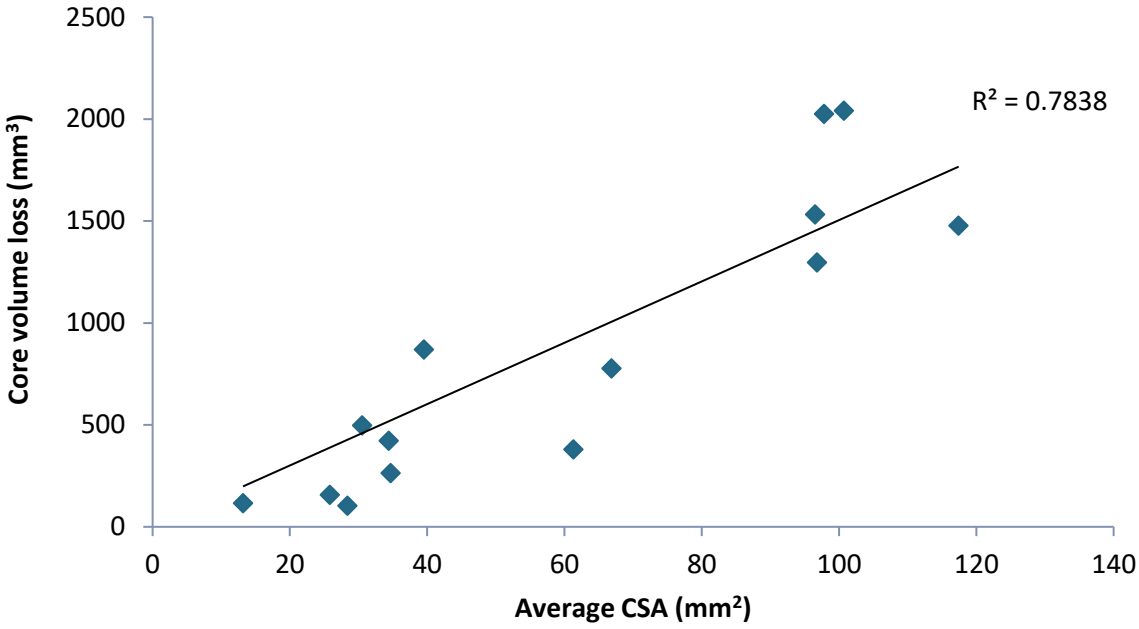

Figure 6.11 Correlation between core volume loss and average adjusted CSA over which loss was registered (adjusted CSA is the actual CSA divided by 1.78 for upward facing core segments)

The R^2 value after adjusting for the orientation effects was 0.78, slightly lower than the 0.83 R^2 value obtained without considering orientation effects. This was unexpected because the upper sections of channels 1 and 2 should leach at a slower rate because of the reasons previously highlighted, i.e. with the core opening facing up, gravity does not aid the process and rising bubbles have a

weaker impact on the core surface. Therefore, adjusting for the orientation effects should have shown a stronger correlation between the core volume loss and average CSA over which the loss was registered.

One possible explanation for this is that the ASR cracking mechanism could be more aggressive in larger channels. In channels 1 and 2, the larger segments of the core are near the top opening and these may be more susceptible to the ASR mechanism because of their larger cross sectional areas.

While there is a reasonably strong linear correlation between the core segment volume leached and the CSA over which that loss was registered, the data is partially flawed because it does not consider the range of cross sectional areas between 70 mm^2 to 100 mm^2. Intuitively, it was expected that the larger exposed areas would correlate to larger segments of core leached since there is increased contact between the alkaline solution and the ceramic core.

6.3 Predicting Leach Times

In section 6.2, it was shown that the leach rate across the different channels had the following trend (from fastest to slowest): channel 2 > channel 1 > channel 3 > channel 4. The leach time will however be a function of the core volume and the leach rate as shown in equation 6.1.

$$Predicted\ leach\ time\ (\text{min}) = \frac{Core\ volume\ (mm^3)}{leach\ rate\ (mm^3 min^{-1})} \quad (6.1)$$

Applying a margin of safety to the predicted leach time can be used to estimate how long it would take to completely leach any geometry. As a result of the skin effect discussed in Chapter 5, the predicted leach time underestimates how much core has actually been leached therefore applying a large margin of safety is key.

Figure 6.12 shows the core volume and average cross-sectional area of the four channels.

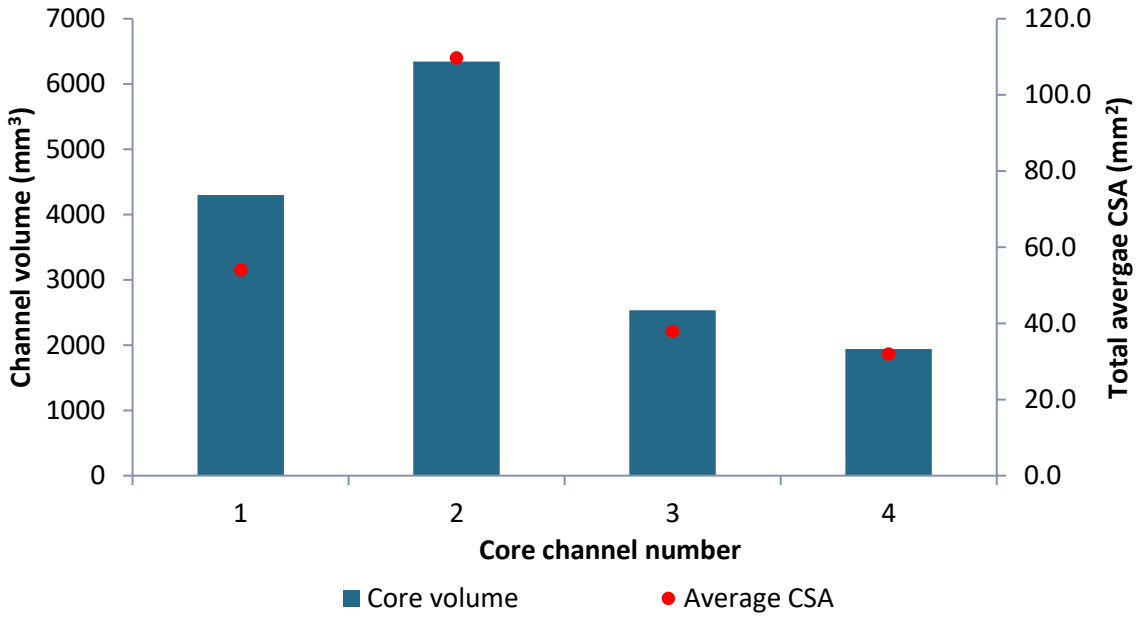

Figure 6.12 Core volume and average CSA of channels in Trent 1000 HP

Channel 2 has the largest volume and the largest average CSA whereas channel 4 has the smallest volume and smallest average CSA. It should be noted that channels 1 and 2 have a larger total average CSA because of their dual openings.

The leach rate of each channel is however independent of the volume and only depends on the cross-sectional area exposed to the alkaline solution. Figure 6.13 shows the core volume and leach rate for each channel.

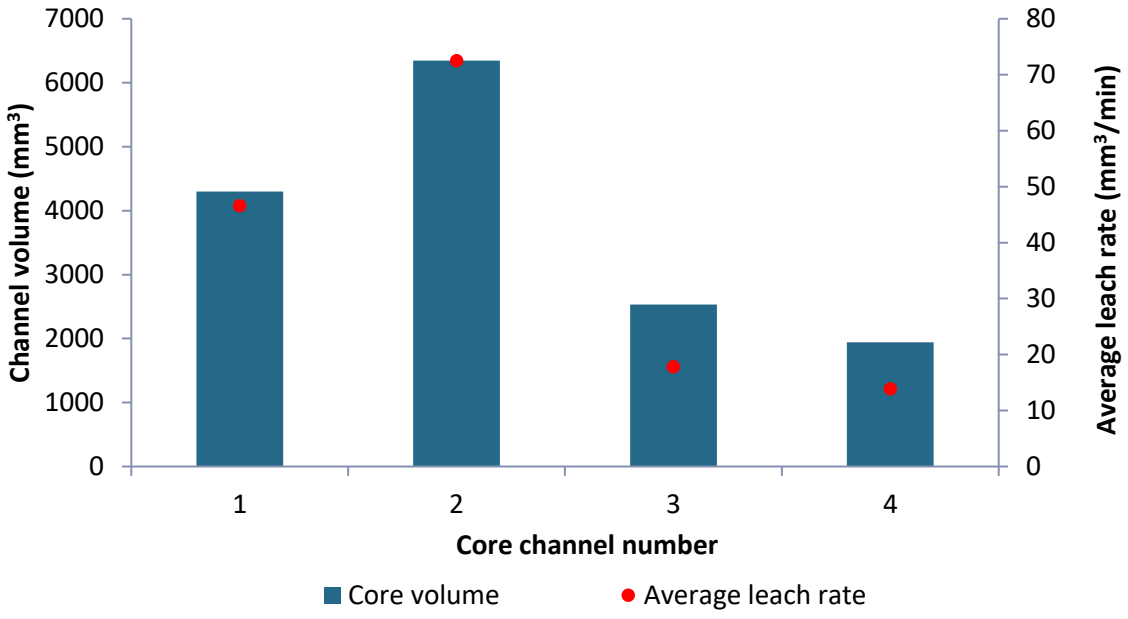

Figure 6.13 Core volume and average leach rate of channels in Trent 1000 HP

As expected, the average cross-sectional area and leach rate follow the same trend; larger cross-sections leach at a faster rate and vice-versa. The proportionality is however not = 1, i.e. a 50% decrease in the average cross-sectional area does not equal a 50% decrease in the average leach rate as shown in Figure 6.14.

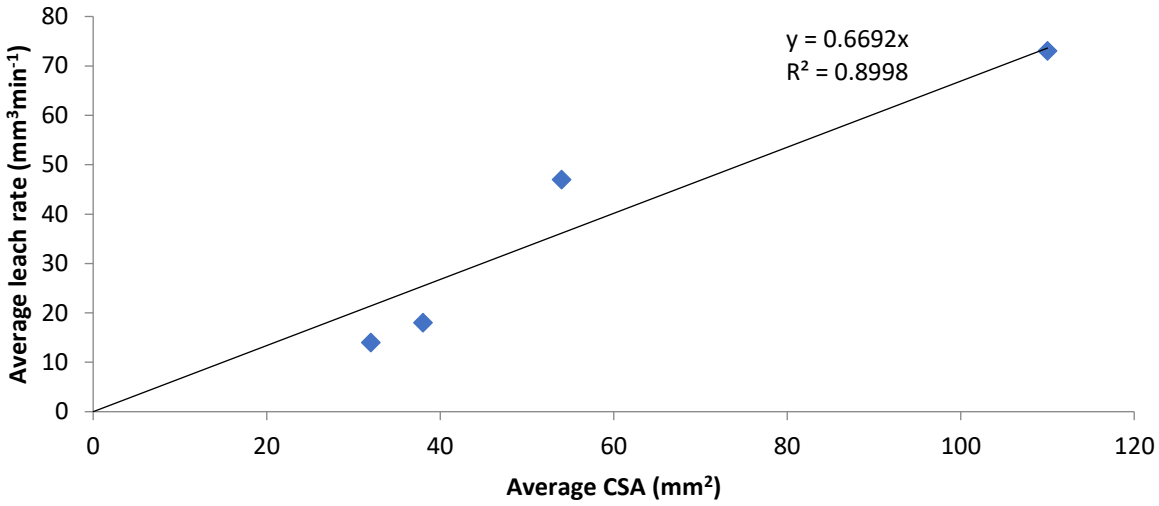

Figure 6.9 Dependence of leach rate on average CSA

The proportionality constant is 0.67 which implies that average leach rate of any channel can be found by multiplying the total average CSA by 0.67. This of course only applies to the core formulation used in this core. Any change in formulation will likely change this relationship.

A possible reason for a non-integer constant is that the ASR expansive gel mechanism plays an important role in core leaching. As previously explained, this process leads to micro and macro cracking which breaks down the brittle ceramic core in a non-predictable way. The pressure swing cycle in the autoclave causes intermittent absorption and desorption of the alkaline solution within the porous ceramic core. This can be thought of as a fatigue cycle loading where the tensile forces caused by the expansive silica gel within the cracks break down the core through repeated stress cycles. This will inevitably lead to some randomness in the leach rate depending on how the cracks propagate in the ceramic core.

The predicted leach time for individual channels can then be calculated as shown in Equation 6.1. Predicted leach times for the different channels are shown in Figure 6.16.

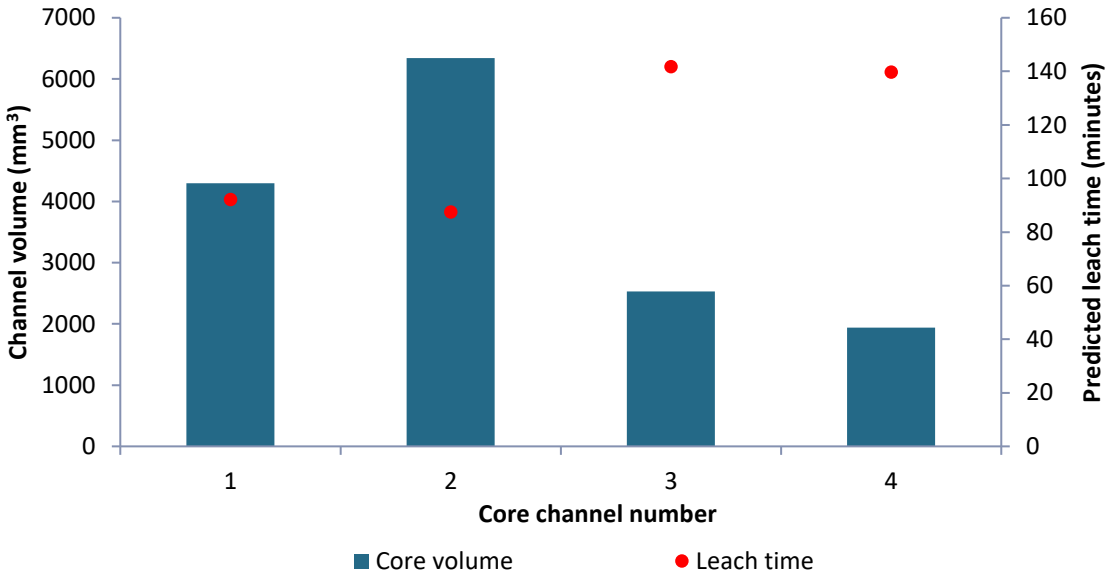

Figure 6.10 Core volume and predicted leach time of channels in Trent 1000 HP

Channels 3 and 4 have the longest predicted leach times - approximately 140 minutes and are the rate limiting channels. Therefore, the entire blade can be assumed to be fully leached after 140 minutes based on the predicted leach time of the rate limiting channels.

The prediction that the entire core is fully leached after 140 minutes compares reasonably well with reality. As explained in Section 6.2, approximately 99% of the core by volume is leached after 180 minutes (3 hours). This means that

predicting the leach time based on the average CSA and volume of each channel is 78% accurate.

An accuracy of 78% has a large error of 22%. This combined with the fact that residual core next to the channel wall is not measured when calculating the actual volume leached. To compensate for the 22% prediction error and the skin effect, applying a large margin of safety should give a reliable leach time for the Trent 1000 HP blade.

A 200% margin of safety based on the predicted leach time implies that the blade will be fully leached after 420 minutes (7 hours). Non-destructive evaluation using a fiberscope and an ophthalmoscope at the Advanced Blade Casting Facility (ABCF) in 2014 showed that Trent 1000 HP blades were fully leached after only 4 hours in the autoclave (128). The conditions were not identical, however. Stronger concentrations of OH^- were used in the casting facilities along with different pressure swing parameters.

A large margin of safety is required because of the difficulty of detecting residual core within the channels after leaching. Residual core within the cooling channels will reduce the heat transfer properties of the blade during operation because of the low thermal conductivity of ceramics. Any residual core could also block the exit holes at the blade surface which form a protective barrier against the high temperature combustion gases driving the turbines as explained in Chapter 1.

6.4 Leach Profile and Evidence of ASR in Complex Geometries

In Chapter 5, the leach profile of a simple rectangular prism geometry was shown to be ‘m’ shaped for channels approximately 11 mm in diameter. This shape was attributed to non-uniform porosity of the ceramic core. Lower porosity areas arise because of a higher local concentration of large silica and zircon particles which have larger interstitial spaces. These spaces allow for the infiltration of the alkaline solution which leads to dissolution of the silica grains and the production of an expansive silica gel. The silica gel is composed of mainly layered Q^3 silicates (as confirmed by ^{29}Si-NMR). These are potentially layered and can absorb water causing expansion of the gel and cracking of the brittle ceramics. It must be noted that the expansive property of the gel has not been proven and requires calcium ions of which there is only a trace amount in the cores.

In actual channel geometries, the same phenomenon was expected to occur. Figures 6.17 – 6.21 shows the cut through of the root section of a Trent 1000 HP blade leached at different times in the pilot scale autoclave.

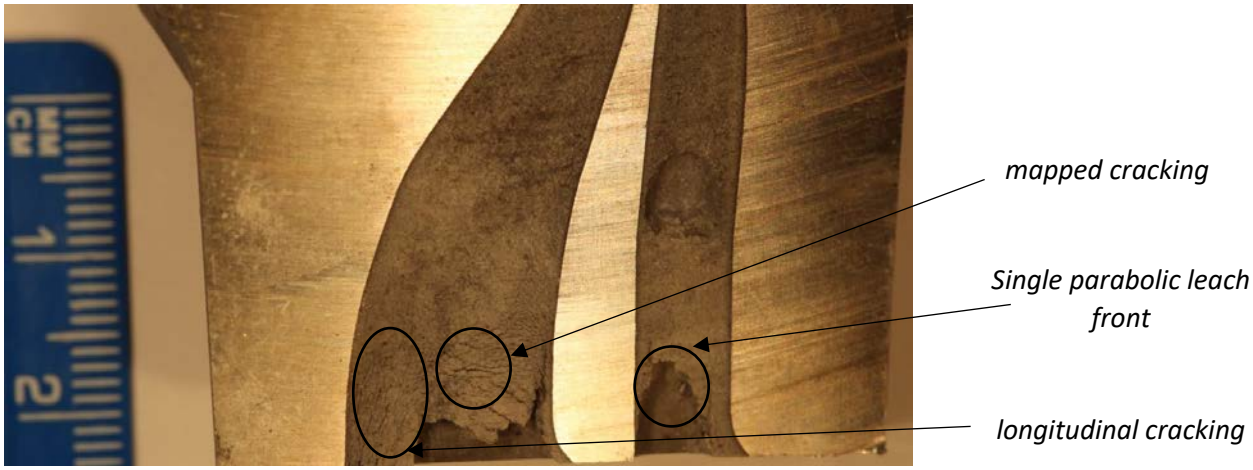

Figure 6.11 Root section cut-through after 15 minutes leach

After 15 minutes, the larger channel which is approximately 11 mm at its base developed an asymmetrical ‘m’ shaped leach front. There is also evidence of mapped and longitudinal cracks forming beyond the leach front. These 2 features were also observed in the rectangular prism core pieces as shown in Figure 5.12 and 5.13. In the smaller channel, a parabolic leach front was also observed.

Figure 6.12 Root section cut-through after 30 minutes leach

After 30 minutes, the outline of the leach profile becomes less obvious. Two longitudinal cracks forming at the top of the concave leach profile are observed. Similar longitudinal cracks were observed in the rectangular prism core

geometries as shown in Figure 5.12. This supports the hypothesis that larger silica and zircon grains are present at the centre of the channel. These larger grains have a higher interstitial volume making it easier for the alkaline solution to infiltrate and cause cracks to form via the ASR expansive gel mechanism.

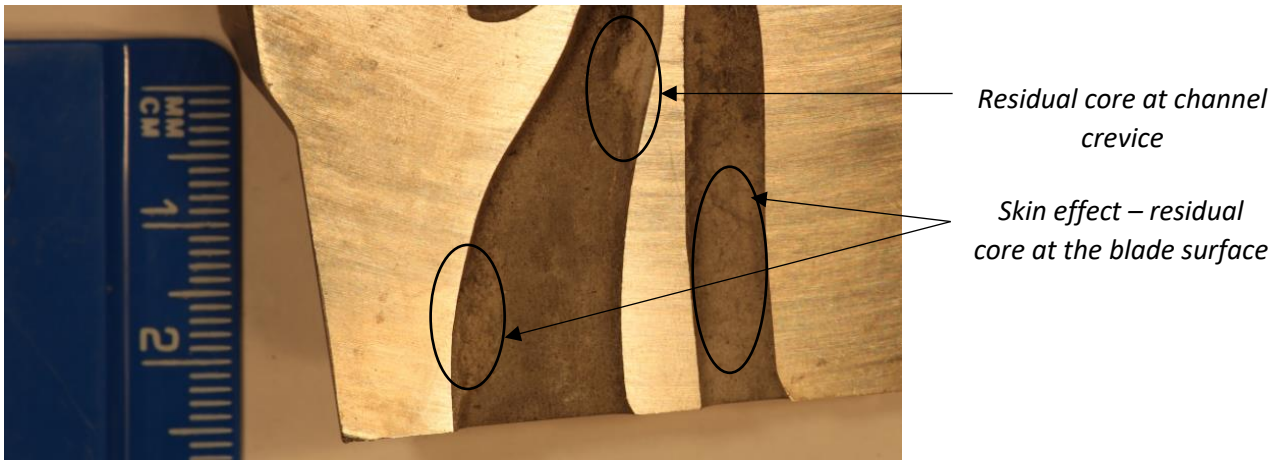

Figure 6.13 Root section cut-through after 1 hour leach

After 1 hour, the bulk of the core in the root section was leached out. Residual core still remained on the channel surface. This skin effect was also observed in the rectangular prism geometries detailed in Chapter 5. This skin effect persists even after 2 hours as shown in Figure 6.20

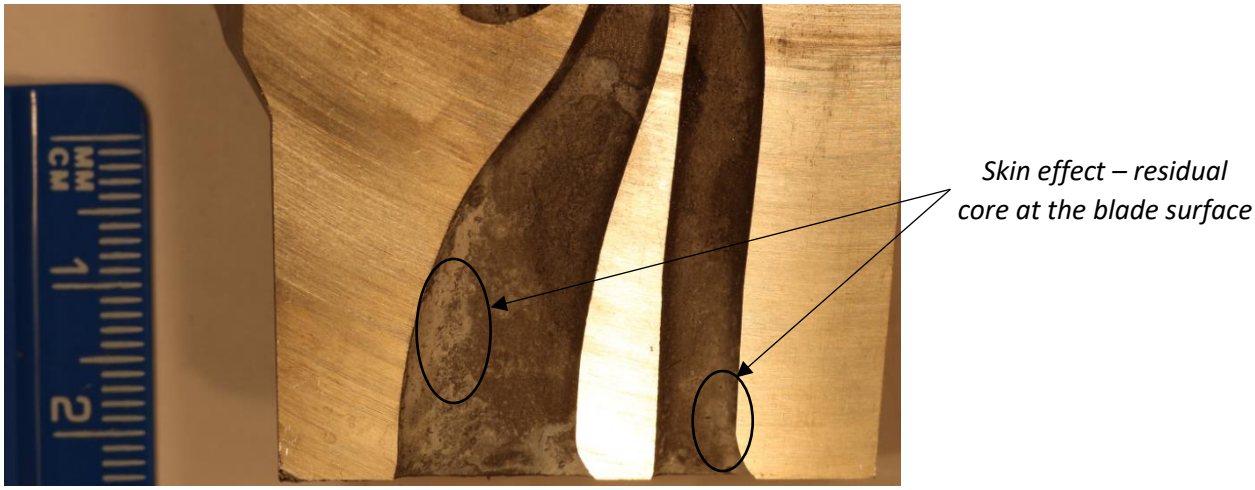

Figure 6.14 Root section cut-through after 2 hour leach

After 3 hours, 99% of the core by volume was removed but a very small amount of residual core remained at the channel crevice as shown in Figure 6.21.

Figure 6.15 Root section cut-through after 3 hour leach

It has been observed that in wider channels (approximately 11 mm wide) an irregular 'm' shaped leach front was formed whereas in smaller channels (approximately 5 mm wide) a single parabolic leach front was formed.

Another blade geometry – the Trent 1000 IP has narrower channels (approximately 5 mm in diameter) as shown in Figure 6.22

Figure 6.16 Trent 1000 IP tip section leach front

All three channels are approximately 5 mm in diameter and have a parabolic leach front. The reason for this single parabolic leach front forming in narrower channels was explained in Chapter 5. To recap, it was hypothesised that a non-linear leach front exists because of localised variations of porosity. Highly porous regions will be more susceptible to the ASR expansive gel cracking mechanism. A high concentration of large grains in a localised area will have a larger porosity because of the larger interstitial volume between the grains. In narrower channels, it is hypothesised that a single parabolic leach front is formed because there is no backflow of material during core injection whereas in larger channels (≈11 mm) there is a backflow of material.

A lack of backflow could mean that larger grains are likely to be deposited in the centre of the channel during the core injection process whereas smaller grains or a combination of large and small grains (which have a lower porosity because of the lower interstitial volume between the grains) are deposited at the edges of

the channel. This would explain the skin effect where the core in direct contact with the metal is very difficult to leach. The skin effect was observed in both the rectangular prism and actual cooling channel geometries. A lower porosity at the edge of the core is more resistant to the ASR expansive gel process and hence leaches slower. A rapid leach rate at the centre of the channel combined with slower rates closer to the metal surface forms a parabolic leach front.

6.5 Conclusion

Leach rates in turbine geometries showed a strong dependence with the average cross sectional area exposed to the alkaline solution with a 0.9 coefficient of determination. Channels with larger cross sectional areas leached faster than narrower channels. This was expected because the rate of siloxane cleavage is dependent on the surface area exposed to the alkaline solution.

The entire core was expected to leach at a rate constrained by the rate of the slowest channel. Channels 3 and 4 were the slowest and hence rate limiting channels. The predicted leach time was determined by dividing the core channel volume by the leach rate. This method of predicting leach times was found to be 78% accurate.

A non-linear leach profile was also observed in the turbine geometries. In narrower channels (≈5 mm) a parabolic leach profile was observed while in wider channels (≈11 mm) a non-linear pattern was observed. This was likely caused by localised variations in porosity which promoted or limited the ASR cracking mechanism.

7 PROCESS IMPROVEMENTS

From our understanding of the fundamental chemistry and physics of the core leach process outlined in preceding chapters, it is clear that improvements can be made to the process to reduce the leach times. This chapter examines the effect of different leachants and pressure swing parameters to determine ideal operating conditions of the core leaching autoclave.

Sourcing turbine blades for these experiments was difficult and unpredictable because it is expensive to manufacture blades solely for leaching. As a result of this, the ideal leachant and pressure swing parameters were determined using two different blade geometries and core formulations.

7.1 Trent 1000 IP

Table 7.1 shows the pressure swing cycle parameters for a standard cycle, extended low pressure dwell and extended vent used in leach experiments on the Trent 1000 IP blade. The definitions of these phases of the pressure swing cycle are illustrated in Figure 2.25.

Table 7.1 Cycle parameters for Trent 1000 IP leaching experiments

	Standard cycle	Extended low pressure dwell	Extended vent
High Pressure dwell (s)	60	30	30
Vent (s)	5	5	5
Low pressure dwell (s)	60	90	30
High Pressure dwell %	48	24	46
Vent %	4	4	8
Low pressure dwell %	48	72	46

Figure 7.1 shows the volume loss observed under the cycle parameters outlined in Table 7.1. The effectiveness of different leachants using the standard cycle was also evaluated. All blades were leached for 1 hour in the autoclave and two blades were used per cycle. A small variation of ± 5% volume loss between blades in the same cycle was observed.

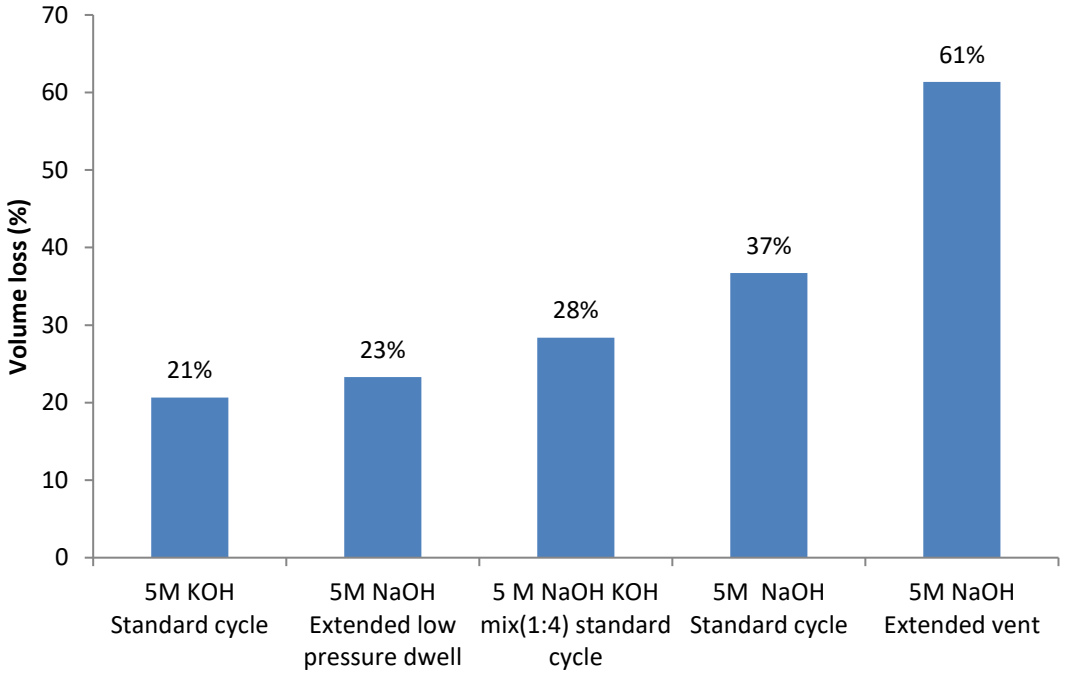

Figure 7.1 Trent 1000 IP volume loss % as a function of cycle parameters in different alkaline solutions

The least effective leachant was the 5 M KOH solution which removed about 21% of the core by volume. A mixture of NaOH/KOH in a 1:4 mole ratio removed 28% of the core while the 5 M NaOH solution was the most effective with a 37% volume loss. These results follow the same trend as the cristobalite dissolution in the laboratory discussed in Chapter 4. In NaOH, the absence of a viscous fluid film layer means the diffusive flux of OH^- is not reduced whereas in KOH, the viscous

fluid film layer with a large storage modulus behaves like a solid and slows down the diffusion of OH^-.

The effects of cycle parameters were only used in comparing the effectiveness of NaOH because of the limited blade samples available. From Figure 7.1, it can be seen that the most effective pressure cycle for NaOH was the extended vent while the least effective was the extended low pressure dwell.

Based on the understanding of the fluid film layer viscosity discussed in Chapter 4, the ASR mechanism discussed in Chapter 5 and an overview of the different phases of the pressure swing cycle, it is clear to see the extended vent was most effective while extended dwell was the least effective.

In the extended vent cycle, the percentage of the total cycle time spent in the high pressure dwell phase was 46% - identical to the standard cycle but almost double that of the extended low pressure dwell cycle. The low viscosity and Newtonian behaviour of sodium silicates at the fluid film layer means that diffusion of OH^- is not rate limiting. Reaction control results discussed in Section 4.3.4 also showed that dissolution in NaOH was chemical reaction controlled.

A long pressure time likely caused the alkaline solution to penetrate deeper into the ceramic core and promote the ASR cracking process. The extended vent

cycle also had an 8% vent time – double that of the other cycles. As explained in Chapter 5, explosive bubble growth caused by a rapid drop in autoclave pressure below the vapour pressure of the alkaline solution during the vent phase could dislodge any loose core that has already been damaged by the depolymerisation reactions with OH^- and the ASR cracking mechanism.

In the extended low pressure dwell cycle, the percentage of the total cycle time spent in the low pressure dwell phase was 72%. During this part of the cycle the solution boils lightly creating vapour bubbles that can disrupt or prevent the formation of the fluid film layer since there is constant mixing. This is however inconsequential for leaching in NaOH since the fluid film viscosity is negligible. Using an extended low pressure dwell cycle meant less time was spent at a higher pressure where the ASR cracking process could have accelerated core removal.

In NaOH, maximum core removal is achieved by increasing the percentage of the cycle time spent at a high pressure dwell and vent phase. The low pressure dwell phase is not important for core removal using NaOH.

7.2 Trent 1000 HP

Table 7.2 shows the pressure swing cycle parameters for a standard cycle, extended high pressure dwell, extended low pressure dwell and extended vent.

Table 7.2 Cycle parameters for Trent 1000 HP leaching experiments

	Standard cycle	Extended high pressure dwell	Extended low pressure dwell 1	Extended low pressure dwell 2	Extended vent
High Pressure dwell (s)	60	60	30	5	30
Vent (s)	5	5	5	5	5
Low pressure dwell (s)	60	5	90	26	30
High Pressure dwell %	48	86	24	14	46
Vent %	4	7	4	14	8
Low pressure dwell %	48	7	72	72	46

Figure 7.2 shows the core volume loss observed under the different cycles. All blades were leached for 2 hours.

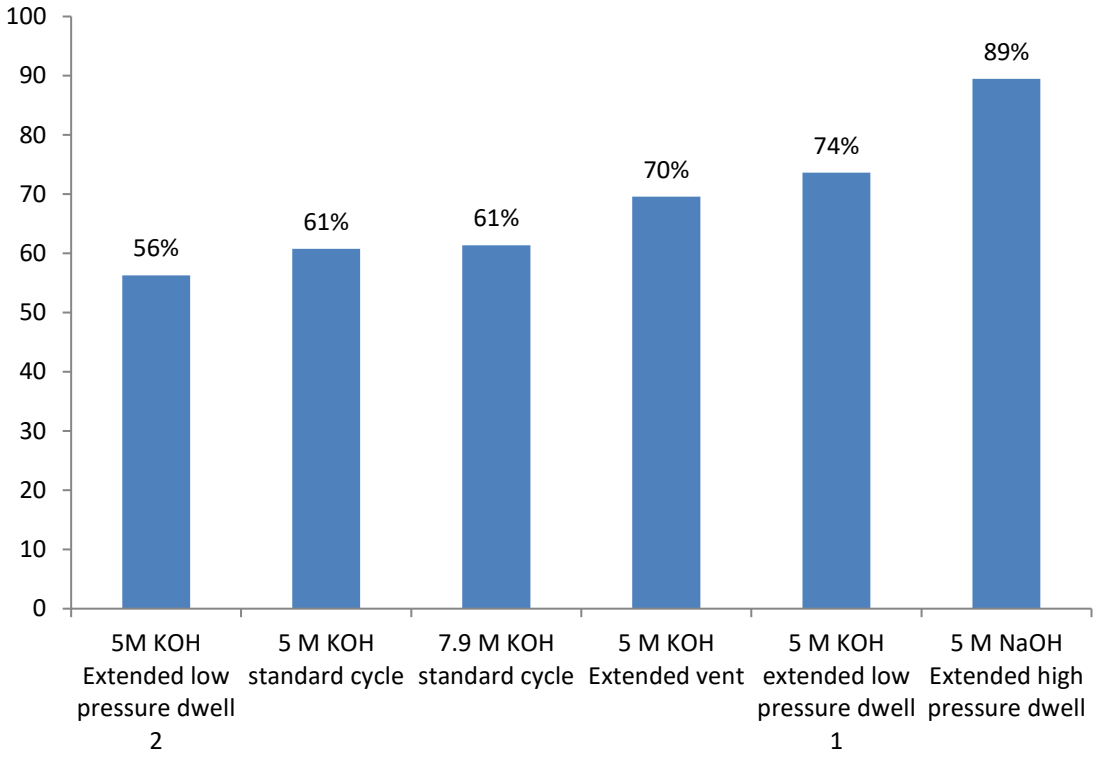

Figure 7.2 Trent 1000 HP core volume loss % as a function of cycle parameters

The ideal pressure cycle was observed in the 5 M NaOH extended high pressure cycle. This further supports the hypothesis discussed in Section 7.2 – core removal in NaOH is enhanced by having a long high pressure dwell phase.

For KOH, there were insufficient parts available to determine the core volume loss under an extended high pressure cycle. However, the extended vent cycle had the next longest high pressure dwell time – 46% of the leach cycle. This cycle was the second best for core removal. An increased high pressure dwell time likely led to improved penetration of the alkaline solution and enhanced the ASR cracking mechanism.

The best cycle for KOH was the extended low pressure dwell 1. This is because of a combination of long low pressure dwell % (light boiling) which disrupts the viscous fluid film layer and a relatively long high pressure dwell time % (increased ASR gel cracking).

The worst cycle for KOH was the extended dwell 2. This had the same low pressure dwell time % as extended dwell 1 (72%) however; the high pressure dwell time % was shorter hence decreased ASR cracking.

Higher OH^- concentration had no effect on core removal – 61% of the core by volume was removed in 5 M KOH and 7.9 M KOH under the standard cycle.

7.3 Conclusion

In KOH, the formation of a viscous fluid film layer slows down the diffusion rate of OH^- towards the cristobalite surface. In order to reduce the leach time, this layer needs to be removed. The ASR expansive gel cracking mechanism also aids core removal. The leach time can be reduced by increasing the percentage of the cycle time spent under the high pressure dwell phase and the vent phase. The former promotes ASR gel cracking and the latter disrupts the fluid film layer thereby increasing the diffusive flux of OH^- towards the cristobalite surface.

In NaOH, a combination of long high pressure dwell and long vent times (as a percentage of the cycle time) was ideal. The low viscosity and Newtonian

behaviour of sodium silicates at the fluid film layer meant that the diffusive flux of OH^- was not affected by the lack of turbulence during the high pressure dwell phase.

Increasing the percentage of the cycle time spent in vent increased the amount of core removed in both NaOH and KOH. The explosive bubble growth during the vent phase can dislodge some of the loose core already weakened by the ASR process. Overall, NaOH was more effective than KOH during core leaching in the autoclave. This is in agreement with the experimental work carried out in Chapter 4.

8 CONCLUSION AND FUTURE WORK

This project had 3 primary aims:

I. To develop an understanding of the chemistry of silica dissolution in highly alkaline environments
II. To develop an understanding of the underlying physics of the core removal process for complex geometries in an autoclave utilising a pressure-swing system
III. To utilise the knowledge gained from I. and II. to drive improvements in the industrial core leach process

8.1 Chemistry of Silica Dissolution

Silica dissolution is the depolymerisation of the three dimensional covalent silica network. Dissolution rates depend on the pH and strong alkaline solutions speed up dissolution because an excess of hydroxide ions leads to deprotonation of the surface silanol groups creating a negatively charged surface. The metal cation from an alkali metal hydroxide solution adsorbs onto the negatively charged silica surface creating an electrically neutral stern layer. Hydroxide ions act as a catalyst for silica dissolution by forming a five-fold coordinated compound which is unstable and breaks down via cleavage of a siloxane bond. This process repeats itself until the $(SiO_4)^{4-}$ unit is detached from the silica surface.

The type of metal cation present in solution had a significant effect on dissolution behaviour. The influence of four Group IA metal cations on cristobalite dissolution was studied at equimolar concentrations of alkali metal hydroxide solutions. XRD analysis of the supposedly cristobalite had in fact been transformed into lithium silicates.

In the presence of CsOH, no caesium silicates were observed on the cristobalite surface however, dissolution was retarded in the presence of Cs^+ relative to Na^+ and K^+. This was likely caused by the influence of charge density on adsorption behaviour. Cations with a large charge density like Li^+ adsorb strongly onto the surface thereby forming an insoluble complex of lithium silicates. Further down the group, cations with a larger ionic radius will have a lower charge density and weakly adsorb onto the silica surface. It was hypothesised that the optimal dissolution rates reported in Na^+ and K^+ likely occur because they adsorb with sufficient strength to cause elongation of the siloxane bonds making it easier for the hydroxide ion to form the five-fold coordinated compound which is a prerequisite to siloxane cleavage. This hypothesis could be tested by carrying out Ab initio quantum mechanical studies to show the effect of Group IA metal cations on siloxane bond elongation.

The type of metal cation present also influenced the properties of the reaction products. ^{29}Si-NMR showed that lower concentration of monomers was observed in potassium silicates compared to sodium silicates at equimolar concentrations.

In potassium silicates, equilibrium of the polycondensation reaction is shifted more to the right relative to sodium silicates. Since the different silicates exist in equilibrium, a lower concentration of monomers in potassium silicates allowed for more SiO_2 to be dissolved returning the system back to equilibrium. This could explain why KOH is more effective than NaOH after repeated use as was shown in the laboratory and is in agreement with anecdotal evidence from foundries.

The rheology of the reaction products was also affected by the metal cation. Sodium silicates displayed Newtonian behaviour irrespective of the SiO_2 wt. % or SiO_2:Na_2O molar ratios at higher shear rates. Siliceous concentrations of potassium silicates at SiO_2:K_2O = 3:1 displayed shear thinning and viscoelastic properties at 30 wt. % SiO_2. At these concentrations, the storage modulus exceeded the elastic modulus which is indicative of a solid like behaviour. The viscosity of potassium silicates at these concentrations was also several orders of magnitude larger than that of sodium silicates. This was likely caused by the larger molecular weights of potassium silicates however was not confirmed. The molecular weights of sodium and potassium silicates as a function of SiO_2:M_2O molar ratios should be determined to prove this hypothesis.

Dissolution in NaOH was shown to be chemically controlled while in KOH it was diffusion through the fluid film controlled. A viscous fluid film layer formed on the cristobalite surface and reduced the diffusive flux of the hydroxide ions. This partly explains why the amount of core dissolved during laboratory experiments

in NaOH was almost twice as large as that dissolved in KOH at equimolar concentrations. The three dimensional diffusion controlled model showed a good fit with the experimental data for cristobalite dissolution in KOH. In NaOH, the theoretical model with the closest fit to the experimental data was the chemical reaction controlled core shrinking model for spherical particles.

An isoconversion model was used to determine the activation energy of cristobalite dissolution in NaOH and KOH solutions as a function of the degree of conversion. It was found that in NaOH, activation energies ranged between 81.8 kJ mol^{-1} and 93.5 kJ mol^{-1}. In KOH, lower activation energies were observed between 61.5 kJ mol^{-1} and 70.7 kJ mol^{-1}.

8.2 Physics of Core Leaching

The core leaching autoclave operates on a pressure swing cycle. Vapour cavities are formed once the autoclave pressure drops below the vapour pressure of the alkaline solution. The critical inception pressure is the vapour pressure less surface tension effects which acts as an external force that prevents cavities from growing. This is important in the fluid film layer because viscous potassium silicates could prevent cavitation inception. The surface tension of sodium and potassium silicates as a function of the SiO_2:M_2O molar ratio should be measured to elucidate the effect of large surface tensions on cavitation inception.

There was no evidence of cavitation erosion caused by bubble collapse on the core surface after leaching. This is probably because the autoclave did not re-pressurise fast enough to cause implosion of the vapour bubbles. It took approximately 2 seconds for the pressure to recover above the vapour pressure. Rapid re-pressurisation could lead to cavitation erosion which should speed up the leaching process. Methods to decrease the re-pressurisation time should be developed and timescales required for cavitation erosion also need to be better understood.

The main physical mechanism responsible for core removal in the autoclave is likely to be the Alkali Silica Reaction (ASR) cracking mechanism. Sodium and potassium silicates form an expansive gel around the cristobalite. The expansivity of this gel has not been proven and relies on the presence of calcium ions which exist in the core formulation in trace amounts. This gel is likely to be very siliceous and contains potentially layered silicates which can absorb water, expand and cause cracking in the brittle ceramic core. The depth of penetration of the alkaline solution in the autoclave is also not fully understood but is likely to be governed by the Washburn equation. Coloured dye mixed with NaOH or KOH solutions could be used to determine the penetration depth of the alkaline solution in the ceramic core. From this, this viscosity of the siliceous fluid film layer could also be determined.

Non-linear leach profiles were observed in both rectangular test bars and turbine blade geometries. In narrower channels (≈ 5 mm) a single parabolic leach front was observed whereas in wider channels (≈ 11 mm) an ‘m’ shaped profile was observed. This was likely caused by localised variations in porosity which promoted or limited the ASR cracking mechanism. To confirm this hypothesis, the porosity at different sections across the core channel width should be determined.

The orientation of parts in the autoclave had a significant effect on the amount of core removed in rectangular core prism geometry. The amount of core removed when the core opening faced down was 76% larger compared to when the core opening faced up. This was largely due to gravity and the turbulence created by rising vapour bubbles.

8.3 Improvements

One of the aims of this project was to understand the leaching mechanism in complex core geometries and to suggest improvements based on the knowledge developed from an understanding of the chemistry and physics of the leaching process.

The leach time in a Trent 1000 HP blade was predicted with 78% accuracy by assuming the time taken to leach an entire core is constrained by the rate of the

slowest channel. An R^2 value of 0.9 showed a strong relationship between the average leach rate and the average cross-sectional area over which the core volume loss was registered. This experiment was carried out using only one type of core geometry and should be repeated across more geometries to confirm repeatability.

Increasing the calcium content in the core formulation could improve the expansive properties of the gel thereby making the ASR process more aggressive and potentially speeding up the leaching process.

In both NaOH and KOH, the amount of core leached in the autoclave was increased by increasing the high pressure dwell and vent times. The former promotes ASR gel cracking and the latter disrupts the fluid film layer thereby increasing the diffusive flux of OH^- towards the cristobalite surface.

The limited sample size of turbine blades meant that a thorough statistical analysis of the variables affecting the core volume loss could not be carried out. A multiple regression analysis with the leached core volume as the dependent variable and the high pressure dwell, vent and low pressure dwell times as the independent variables in both KOH and NaOH should be carried out. This could quantify the variables affecting core leaching in the autoclave.

9 REFERENCES

1. Rolls-Royce Holdings financial statements from 2006-2016 [Internet]. Thomson Reuters 2017 [cited 18th November 2017].
2. Rolls-Royce markets [press release]. https://www.rolls-royce.com/country-sites/singapore/markets/civil-aerospace.aspx. : Rolls-Royce plc. , 17th February 2017.
3. Rolls-Royce. The Jet Engine: Wiley; 2015.
4. The story so far…. [press release]. http://lbbctechnologies.com/about/history/: LBBC Technologies [17th November 2017].
5. Thomas R. Investment cast operation times. In: Adetunji D, editor. 2017.
6. Glasser LS, Kataoka N. The chemistry of 'alkali-aggregate' reaction. Cement and Concrete Research. 1981;11(1):1-9.
7. Cengel Y, Boles M. Thermodynamics: An engineering approach. New-York: McGraw-Hill publishers; 2008.
8. Quested P, Brooks R, Chapman L. Measurement and estimation of thermophysical properties of nickel based superalloys. Materials Science and Technology. 2009;25(2):154-62.
9. Xu L, Bo S, Hongde Y, Lei W. Evolution of Rolls-royce Air-cooled Turbine Blades and Feature Analysis. Procedia Engineering. 2015;99:1482-91.
10. Bell C, Clarkson PJ, Dawes WN. Improving the Turbine Cooling Conceptual Design Process. 2008(43161):2631-40.
11. Rolls-Royce. Large civil engine schematic. In: Adetunji D, editor. 2015.
12. Prasad R. Progress in Investment Castings http://cdn.intechopen.com/pdfs/39309/InTech-Progress_in_investment_castings.pdf . [13th November 2013].
13. Jade-Trading. Investment casting / lost wax casting 2016 [13th November 2013].
14. Reed R. Superalloys Fundamentals and Applications: Cambridge University Press; 2006.
15. Versnyder FI, Shank ME. The development of columnar grain and single crystal high temperature materials through directional solidification. Materials Science and Engineering. 1970;6(4):213-47.
16. Jockey N. Shell removal process: Rolls-Royce; 2010.
17. Wilson P. Investigating the formulation of silica-based ceramic core materials for investment casting. Birmingham: University of Birmingham; 2011.
18. Heaney P. Structure and chemistry of the low-pressure silica polymorphs . Reviews in Mineralogy. 1994;29(1):1-40.
19. Thomas R. Cristobalite firing cycle. In: Adetunji D, editor. 2015.
20. Pickard H, Eastwood J. Ceramic Core Leaching Autoclave Systems. New Pudsey: LBBC Technologies; 2012.
21. Pataki L, Zapp E. Basic analytical chemistry. Oxford: Pergamon; 1980.
22. UCSB. Table of Acids with Ka and pKa Values http://www4.ncsu.edu/~franzen/public_html/CH201/data/Acid_Base_Table.pdf [1st June 2015].

23. NCSU. Table of acid and base strength http://www4.ncsu.edu/~franzen/public_html/CH201/data/Acid_Base_Table.pdf [1st June 2015].
24. Sharma SK, Kashyap SC. Ionic interaction in alkali metal hydroxide solutions — A raman spectral investigation. Journal of Inorganic and Nuclear Chemistry. 1972;34(12):3623-30.
25. Tansel B. Significance of thermodynamic and physical characteristics on permeation of ions during membrane separation: Hydrated radius, hydration free energy and viscous effects2011.
26. Birk JP. Metal Ions in Solution (Burgess, John). Journal of Chemical Education. 1979;56(10):A324.
27. Kinrade SD. Oxygen-17 NMR Study of Aqueous Potassium Silicates. The Journal of Physical Chemistry. 1996;100(12):4760-4.
28. E Conway B. Ionic hydration in chemistry and biophysics / B. E. Conway2019.
29. Shannon R. Revised effective ionic radii and systematic studies of interatomic distances in halides and chalcogenides. Acta Crystallographica Section A. 1976;32(5):751-67.
30. David F, Vokhmin V, Ionova G. Water characteristics depend on the ionic environment. Thermodynamics and modelisation of the aquo ions. Journal of Molecular Liquids. 2001;90(1):45-62.
31. Essington M. Soil and water chemistry. Florida: CRC Press; 2015.
32. Nightingale ER, Jr. Phenomenological theory of ion salvation. Effective radii of hydrated ions. J Phys Chem. 1959;63:1381-7.
33. Volkov A, Paula S, Deamer D. Two mechanisms of permeation of small neutral molecules and hydrated ions across phospholipid bilayers. Bioelectrochemistry & Bioenergetics. 1997;42(2):153-60.
34. Shackelford J, Alexander W. CRC materials science and egineering handbook. Florida: CRC Press; 2001.
35. Binder H, Zschörnig O. The effect of metal cations on the phase behavior and hydration characteristics of phospholipid membranes. Chemistry and Physics of Lipids. 2002;115(1):39-61.
36. Whitten K. Chemistry. California: Cengage Learning; 2013.
37. Kiriukhin MY, Collins KD. Dynamic hydration numbers for biologically important ions. Biophysical Chemistry. 2002;99(2):155-68.
38. Degrève L, Vechi SM, Junior CQ. The hydration structure of the Na+ and K+ ions and the selectivity of their ionic channels. Biochimica et Biophysica Acta (BBA) - Bioenergetics. 1996;1274(3):149-56.
39. Klein C. Manual of Mineral Science. 23rd ed. New York: Wiley; 2007.
40. Wells A. Structural inorganic chemistry. Oxford: Clarendon; 1984.
41. Lyklema J. Fundamentals of interface and colloid science. London: Academic Press; 1991.
42. Webb T. On the Free Energy of Hydration of Ions. Proceedings of the National Academy of Sciences. 1926;12(8):524.
43. Jenkins H, Thakur P. Journal of Chemical Education. 1979;56(9):576.
44. Marcus Y. The Standard Partial Molar Volumes of Ions in Solution. Part 5. Ionic Volumes in Water at 125–200 °C. The Journal of Physical Chemistry B. 2012;116(24):7232-9.

45. Sipos PM, Hefter G, May PM. Viscosities and Densities of Highly Concentrated Aqueous MOH Solutions (M+ = Na+, K+, Li+, Cs+, (CH3)4N+) at 25.0 °C. Journal of Chemical & Engineering Data. 2000;45(4):613-7.
46. Solvay. Liquid caustic soda viscosity http://www.solvay.com/en/markets-and-products/markets/index.html2004 [6th July 2015].
47. Corporation OC. Caustic potash handbook http://www.oxy.com/ourbusinesses/chemicals/products/documents/causticpotash/kohhandb.pdf.2013 [6th July 2015].
48. Papirer E. Adsorption on Silica Surfaces: Taylor & Francis; 2000.
49. Greenberg SA. The Depolymerization of Silica in Sodium Hydroxide Solutions. The Journal of Physical Chemistry. 1957;61(7):960-5.
50. Iler RK, K IR. The Chemistry of Silica: Solubility, Polymerization, Colloid and Surface Properties and Biochemistry of Silica: Wiley; 1979.
51. Xiao Y, Lasaga AC. Ab initio quantum mechanical studies of the kinetics and mechanisms of silicate dissolution: H+(H3O+) catalysis. Geochimica et Cosmochimica Acta. 1994;58(24):5379-400.
52. Xiao Y, Lasaga AC. Ab initio quantum mechanical studies of the kinetics and mechanisms of quartz dissolution: OH− catalysis. Geochimica et Cosmochimica Acta. 1996;60(13):2283-95.
53. Sjöberg S. Silica in aqueous environments. Journal of Non-Crystalline Solids. 1996;196:51-7.
54. White Arthur F, Brantley Susan L. Chemical Weathering Rates of Silicate Minerals2018.
55. Dove PM, Icenhower J, editors. Kinetic and thermodynamic controls on silica reactivity: an analog for waste disposal media. CEA/Valrho summer session Glass scientific research for high performance containment; 1997; France.
56. Alexander GB, Heston WM, Iler RK. The Solubility of Amorphous Silica in Water. The Journal of Physical Chemistry. 1954;58(6):453-5.
57. Belton DJ, Deschaume O, Perry CC. An overview of the fundamentals of the chemistry of silica with relevance to biosilicification and technological advances. The FEBS Journal. 2012;279(10):1710-20.
58. Tamada O, Gibbs G, Monte B JB, Donald Rimstidt J. Silica dissolution catalyzed by NaOH: Reaction kinetics and energy barriers simulated by quantum mechanical strategies. 2012;107:87-98.
59. Schwartzentruber J, Fürst W, Renon H. Dissolution of quartz into dilute alkaline solutions at 90°C: A kinetic study. Geochimica et Cosmochimica Acta. 1987;51(7):1867-74.
60. Brady PV, Walther JV. Kinetics of quartz dissolution at low temperatures. Chemical Geology. 1990;82:253-64.
61. Dove PM, Crerar DA. Kinetics of quartz dissolution in electrolyte solutions using a hydrothermal mixed flow reactor. Geochimica et Cosmochimica Acta. 1990;54(4):955-69.
62. Gratz AJ, Bird P. Quartz dissolution: Negative crystal experiments and a rate law. Geochimica et Cosmochimica Acta. 1993;57(5):965-76.
63. Nangia S, Garrison B. Reaction Rates and Dissolution Mechanisms of Quartz as a Function of pH †. 2008;112:2027-33.
64. Pelmenschikov A, Strandh H, Pettersson LGM, Leszczynski J. Lattice Resistance to Hydrolysis of Si−O−Si Bonds of Silicate Minerals: Ab Initio

Calculations of a Single Water Attack onto the (001) and (111) β-Cristobalite Surfaces. The Journal of Physical Chemistry B. 2000;104(24):5779-83.
65. Criscenti L, Kubicki J, Brantley S. Silicate Glass and Mineral Dissolution: Calculated Reaction Paths and Activation Energies for Hydrolysis of a Q3 Si by H3O+ Using Ab Initio Methods2006. 198-206 p.
66. Walsh TR, Wilson M, Sutton AP. Hydrolysis of the amorphous silica surface. II. Calculation of activation barriers and mechanisms. The Journal of Chemical Physics. 2000;113(20):9191-201.
67. Pelmenschikov A, Leszczynski J, Pettersson LGM. Mechanism of Dissolution of Neutral Silica Surfaces: Including Effect of Self-Healing. The Journal of Physical Chemistry A. 2001;105(41):9528-32.
68. Cypryk M, Apeloig Y. Mechanism of the Acid-Catalyzed Si−O Bond Cleavage in Siloxanes and Siloxanols. A Theoretical Study. Organometallics. 2002;21(11):2165-75.
69. Kagan M, Lockwood GK, Garofalini SH. Reactive simulations of the activation barrier to dissolution of amorphous silica in water. Physical Chemistry Chemical Physics. 2014;16(46):25649-.
70. Wallace AF, Gibbs GV, Dove PM. Influence of Ion-Associated Water on the Hydrolysis of Si−O Bonded Interactions. The Journal of Physical Chemistry A. 2010;114(7):2534-42.
71. Tester J, Worley W, Robinson B, Grigsby C, Feerer J. Correlating quartz dissolution kinetics in pure water from 25 to 625°C. Geochimica et Cosmochimica Acta. 1994;58(11):2407-20.
72. Rimstidt JD, Barnes HL. The kinetics of silica-water reactions. Geochimica et Cosmochimica Acta. 1980;44(11):1683-99.
73. G. Worley W, W. Tester J, Grigsby C. Quartz Dissolution Kinetics from 100-200°C as a Function of pH and Ionic Strength. AIChE Journal. 1996;42:3442-57.
74. Dove PM. The dissolution kinetics of quartz in aqueous mixed cation solutions. Geochimica et Cosmochimica Acta. 1999;63(22):3715-27.
75. Bennett PC. Quartz dissolution in organic-rich aqueous systems. Geochimica et Cosmochimica Acta. 1991;55(7):1781-97.
76. Fertani-Gmati M, Jemal M. Thermochemistry and kinetics of silica dissolution in NaOH aqueous solution. Thermochimica Acta. 2011;513(1):43-8.
77. Allen L, Matijevíc E, Meites L. Exchange of Na^+ for the silanolic protons of silica. Journal of Inorganic and Nuclear Chemistry. 1971;33(5):1293-9.
78. Dove PM, Nix CJ. The influence of the alkaline earth cations, magnesium, calcium, and barium on the dissolution kinetics of quartz. Geochimica et Cosmochimica Acta. 1997;61(16):3329-40.
79. Feng X, Thomas MDA, Bremner TW, Folliard KJ, Fournier B. Summary of research on the effect of LiNO3 on alkali–silica reaction in new concrete. Cement and Concrete Research. 2010;40(4):636-42.
80. Kim T, Olek J. The effects of lithium ions on chemical sequence of alkali-silica reaction. Cement and Concrete Research. 2016;79:159-68.
81. Leemann A, Lörtscher L, Bernard L, Le Saout G, Lothenbach B, Espinosa-Marzal RM. Mitigation of ASR by the use of LiNO3—Characterization of the reaction products. Cement and Concrete Research. 2014;59:73-86.

82. Bickmore BR, Nagy KL, Gray AK, Brinkerhoff AR. The effect of Al(OH)4− on the dissolution rate of quartz. Geochimica et Cosmochimica Acta. 2006;70(2):290-305.
83. Ali AM, Padmanabhan E, Baioumy H. Characterization of Alkali-Induced Quartz Dissolution Rates and Morphologies. Arabian Journal for Science and Engineering. 2017;42(6):2501-13.
84. Weldes HH, Lange KR. Properties of soluble silicates. Industrial & Engineering Chemistry. 1969;61(4):29-44.
85. Yang X, Zhu W, Yang Q. The Viscosity Properties of Sodium Silicate Solutions. Journal of Solution Chemistry. 2008;37(1):73-83.
86. Mitchell LD, Grattan-Bellew PE, editors. Quantitative petrographic analysis of concrete - The damage rating index (DRI) method, a review. Symposium on AAR in Concrete; 2006.
87. Wijnen PWJG, Beelen TPM, de Haan JW, Rummens CPJ, van de Ven LJM, van Santen RA. Silica gel dissolution in aqueous alkali metal hydroxides studied by 29Si□NMR. Journal of Non-Crystalline Solids. 1989;109(1):85-94.
88. Levenspiel O. Chemical reaction engineering. New-York: Wiley; 1999.
89. Pegg J. Understanding the chemistry and physics of the investment casting core removal process to enhance its industrial application. Birmingham: University of Birmingham; 2012.
90. Brennen C. Fundamentals of multiphase flow. Cambridge: Cambridge University Press; 2009.
91. Eisenberg P, Research USOoN, Hydronautics i. Cavitation and Impact Erosion: Concepts, Correlations, Controversies. California: Hydronautics, Incorporated; 1969.
92. Sibelco. Cristobalite technical data sheet. In: Sibelco, editor. 2010.
93. Banks C, John D, Melnick L, Musgrave J. Treatise on Analytical Chemistry: Analytical Chemistry of the Elements: Interscience Publishers; 1962.
94. Yu. Tretinnik V, V. Terlikovskii E, P. Skorobogach L. Potentiometric determination of the silica content in solutions of alkali silicates. New-York: Plenum publishing corporation; 1993. 317-20 p.
95. Brevard C, Granger P. Handbook of high resolution multinuclear NMR. New-York: Wiley; 1981.
96. Derwent. CAD model of 5 cavity aluminium die. In: Adetunji D, editor.: Derwent Valley Tooling; 2016.
97. Goudouchaouri O. V200 test bar assembly. In: Adetunji D, editor. 2016.
98. Pickles K. Pilot scale autoclave specifications. In: Adetunji D, editor. 2015.
99. Berger G, Cadore E, Schott J, Dove PM. Dissolution rate of quartz in lead and sodium electrolyte solutions between 25 and 300°C: Effect of the nature of surface complexes and reaction affinity. Geochimica et Cosmochimica Acta. 1994;58(2):541-51.
100. Chappex T, Scrivener KL. The influence of aluminium on the dissolution of amorphous silica and its relation to alkali silica reaction. Cement and Concrete Research. 2012;42(12):1645-9.
101. Ahrens LH. The use of ionization potentials Part 1. Ionic radii of the elements. Geochimica et Cosmochimica Acta. 1952;2(3):155-69.
102. Parsonage MW. Facts and Practice for A-Level Chemistry: Maxinterax, Limited; 2007.

103. Koning E, Gehlen M, Flank AM, Calas G, Epping E. Rapid post-mortem incorporation of aluminum in diatom frustules: Evidence from chemical and structural analyses. Marine Chemistry. 2007;106(1):208-22.
104. Harouiya N, Oelkers EH. An experimental study of the effect of aqueous fluoride on quartz and alkali-feldspar dissolution rates. Chemical Geology. 2004;205(1):155-67.
105. Krauss D, Eisenberg B, Gillespie D. Selectivity sequences in a model calcium channel: role of electrostatic field strength. European Biophysics Journal. 2011;40(6):775-82.
106. Downs T, Palmer C. The pressure behavior of alpha cristobalite. AMCSD. 1994;79:9-14.
107. Cruz D, Bulbulian S. Synthesis of Li4SiO4 by a Modified Combustion Method. Journal of the American Ceramic Society. 2005;88(7):1720-4.
108. Gui X, Chen S, Yun Z. Continuous production of biodiesel from cottonseed oil and methanol using a column reactor packed with calcined sodium silicate base catalyst. Chinese Journal of Chemical Engineering. 2016;24(4):499-505.
109. Jendoubi F, Mgaidi A, El Maaoui M. Kinetics of the dissolution of silica in aqueous sodium hydroxide solutions at high pressure and temperature. The Canadian Journal of Chemical Engineering. 1997;75(4):721-7.
110. Okunev AG, Shaurman SA, Danilyuk AF, Aristov YI, Bergeret G, Renouprez A. Kinetics of the SiO2 aerogel dissolution in aqueous NaOH solutions: experiment and model. Journal of Non-Crystalline Solids. 1999;260(1):21-30.
111. Comsol. Diffusion Coefficient https://www.comsol.com/multiphysics/diffusion-coefficient2015 [10th August 2017].
112. Edward JT. Molecular volumes and the Stokes-Einstein equation. Journal of Chemical Education. 1970;47(4):261.
113. Nptel. Theories of mass transfer https://nptel.ac.in/courses/103103035/module3/lec5.pdf2015 [10th August 2017].
114. Ha C, Kim S-J, Pak HK. Experimental study of the Stokes-Einstein relation by using oscillating optical tweezers and a position tracking method. Journal of the Korean Physical Society. 2013;62(4):564-8.
115. Raju R, Balachandar S, Hill DF, Adrian RJ. Reynolds number scaling of flow in a stirred tank with Rushton turbine. Part II — Eigen decomposition of fluctuation. Chemical Engineering Science. 2005;60(12):3185-98.
116. Nienow A. Scale-Up, Stirred Tank Reactors. Ullmanns Encyclopedia of Industrial Chemistry. 7: Wiley-VCH; 2010.
117. Rapp BE. Chapter 9 - Fluids. In: Rapp BE, editor. Microfluidics: Modelling, Mechanics and Mathematics. Oxford: Elsevier; 2017. p. 243-63.
118. PQ-Corporation. Bonding And Coating Applications of PQ Soluble Silicateshttps://www.pqcorp.com/docs/default-source/recommended-literature/pq-corporation/sodium-silicate-liquids/bulletin_12-31.pdf?sfvrsn=87e8e494_32006 [10th August 2017].
119. Mueller S, Llewellin EW, Mader HM. The rheology of suspensions of solid particles. Proceedings of the Royal Society A: Mathematical, Physical and Engineering Sciences. 2010;466(2116):1201-28.

120. Texas Instruments. Understanding Rheology of Structured Fluids. http://www.tainstruments.com/pdf/literature/AAN016_V1_U_StructFluids.pdf 2016 [2nd June 2018].
121. Blackburn S. Loss and storage modulus of a rubbery material. In: Adetunji D, editor. 2018.
122. McBain JW, Sharp ER. A Comparative Study of Surfaces of Solutions with the Film Balance and Surface Tension Equipment. Journal of the American Chemical Society. 1941;63(5):1422-6.
123. Aquino W, Lange DA, Olek J. The influence of metakaolin and silica fume on the chemistry of alkali–silica reaction products. Cement and Concrete Composites. 2001;23(6):485-93.
124. USFHA. Alkali-silica Reactivity Field Identification Handbook: U.S. Department of Transportation, Federal Highway Administration; 2011.
125. Wang H, Gillott JE. Mechanism of alkali-silica reaction and the significance of calcium hydroxide. Cement and Concrete Research. 1991;21(4):647-54.
126. Bleszynski RF, Thomas MDA. Microstructural Studies of Alkali-Silica Reaction in Fly Ash Concrete Immersed in Alkaline Solutions. Advanced Cement Based Materials. 1998;7(2):66-78.
127. Zhang T, Blackburn S, Bridgwater J. The orientation of binders and particles during ceramic injection moulding. Journal of the European Ceramic Society. 1997;17(1):101-8.
128. Thomas R. Rolls-Royce internal technical report. Rolls-Royce Plc; 2014. Contract No.: NSX152.